

Design of High-Speed, Meso-Scale Nanopositioners Driven by Electromagnetic Actuators

by

Dariusz S. Golda

S.M. Mechanical Engineering  
Massachusetts Institute of Technology, 2003

B.S. Mechanical Engineering  
Rutgers University, 2001

Submitted to the Department of Mechanical Engineering  
in Partial Fulfillment of the Requirements for the Degree of

Doctor of Philosophy in Mechanical Engineering

at the

Massachusetts Institute of Technology

February 2008

© 2008 Massachusetts Institute of Technology  
All rights reserved

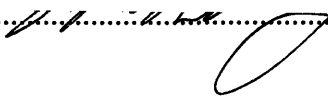
A .

Signature of Author.....



Department of Mechanical Engineering  
January 15, 2008

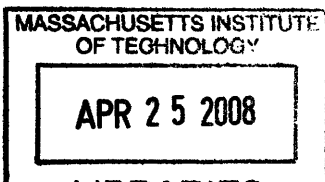
Certified by.....



Martin L. Culpepper  
Associate Professor of Mechanical Engineering  
Thesis Supervisor and Committee Chair

Accepted by.....

Lallit Anand  
Professor of Mechanical Engineering  
Chairman, Department Committee on Graduate Students



ARCHIVES

This page intentionally left blank.

# Design of High-Speed, Meso-Scale Nanopositioners Driven by Electromagnetic Actuators

by

Dariusz S. Golda

Submitted to the Department of Mechanical Engineering  
on January 15, 2008 in Partial Fulfillment of the  
Requirements for the Degree of  
Doctor of Philosophy in Mechanical Engineering

## ABSTRACT

The purpose of this thesis is to generate the design and fabrication knowledge that is required to engineer high-speed, six-axis, meso-scale nanopositioners that are driven by electromagnetic actuators. When compared to macro-scale nanopositioners, meso-scale nanopositioners enable a combination of greater bandwidth, improved thermal stability, portability, and capacity for massively parallel operation. Meso-scale nanopositioners are envisioned to impact emerging applications in data storage and nanomanufacturing, which will benefit from low-cost, portable, multi-axis nanopositioners that may position samples with nanometer-level precision at bandwidth of 100s of Hz and over a working envelope greater than  $10 \times 10 \times 10$  micrometers<sup>3</sup>. This thesis forms the foundation of design and fabrication knowledge required to engineer meso-scale systems to meet these needs.

The design combines a planar silicon flexure bearing and unique moving-coil microactuators that employ millimeter-scale permanent magnets and stacked, planar-spiral micro-coils. The new moving-coil actuator outperforms previous coil designs as it enables orthogonal and linear force capability in two axes while minimizing parasitic forces. The system performance was modeled in the structural, thermal, electrical, and magnetic domains with analytical and finite-element techniques. A new method was created to model the three-dimensional permanent magnet fields of finite magnet arrays. The models were used to optimize the actuator coil and flexure geometry in order to achieve the desired motions, stiffness, and operating temperature, and to reduce thermal error motions.

A new microfabrication process and design-for-manufacturing rules were generated to integrate multilayer actuator coils and silicon flexure bearings. The process combines electroplating for the copper coils, a silicon dioxide interlayer dielectric, and deep reactive-ion etching for the silicon flexures and alignment features. Microfabrication experiments were used to formulate coil geometry design rules that minimized the delamination and cracking of the materials that comprise the coil structure. Experiments were also used to measure the previously-unreported breakdown strength of the unannealed, PECVD silicon dioxide interlayer dielectric.

The results of this research were used to design and fabricate a meso-scale nanopositioner system. The nanopositioner was measured to have a range of motion of 10 micrometers in the lateral directions, a range of 2 micrometers in the out-of-plane direction, an angular range of 0.5 degrees, and a first mode resonant frequency at 900 Hz. Open-loop calibration has been shown to minimize parasitic in-plane motion to less than 100 nm over the range of motion.

This page intentionally left blank.

# ACKNOWLEDGEMENTS

---

This research was made possible by all the wonderful people who have helped, guided, and supported me through the tumultuous journey that embodied my PhD. I have been inspired by many amazing people whose impact on my life and career is immeasurable.

My utmost gratitude goes to Professor Marty Culpepper for his gracious support of my research and his exceptional guidance as supervisor of my PhD research. He gave me the freedom to create and pursue a project that spiked my research interests. In addition, thanks to the NSF for providing funding support for this project.

Thanks to my doctoral committee for their invaluable inputs and insight into my work, without whom this research would still be floundering. Professors Jeffrey Lang, Carol Livermore-Clifford, David Trumper, and Dr. William Plummer have provided timely help at critical junctures during my course of my research. They have also provided me with first-class professional and career guidance.

Thanks to all those who have donated the use of their equipment including: Professor Dennis Freeman for use of his MMA system, Jack Danieli of Polytec for use of the laser vibrometer, Prof. Lang for use of his microscope room, Prof. Trumper for use of his Gauss meter, Lorenzo Pires for use of his impedance analyzer, and Brian Chow for use of the Media Lab laser cutter. Special thanks to Gerry Wentworth and the staff of the LMP Machine Shop for all their help and patience in manufacturing parts for experiments.

Microfabrication of the device was done at the MTL. Thanks to all the great researchers, staff, and students of the MTL for their invaluable help and countless discussions in the fab. Special thanks to Vicky Diadiuk, Donal Jamieson, Dave Terry, Gwen Donahue, and Tim Turner. Very special thanks to Dennis Ward for keeping it real in- and out- of the fab. I also want to thank Hanqing Li. His knowledge, wisdom, patience, and mentorship are exemplary. Finally, I must thank my fellow students for all their help during my time in the fab: Alexis Weber, Joyce Wu, Niamh Waldron, and anyone else I might be forgetting.

Thanks to Zhen Liu of Nexx Systems for graciously donating time and valuable resources in order to electroplate my wafers.

Thanks to all my PCSL labmates, past and present, for their outstanding support, kindness, and willingness to help in times of need. In addition, thanks to the LMP staff and students for all of their wonderful support.

Special thanks to all the friends that I've made while at MIT. The fantastic people make MIT special. The friendships forged over the years will last a lifetime. My great friends helped to ease the pain during the difficult times of my research, and were there to celebrate the good times. Very special thanks to the CSC for helping to put everything in perspective, for listening to the countless stories of research failures, and for the time spent sharing the waves of the great oceans.

Finally and most importantly, I must pay special thanks to my family. Without them, I would not be completing my doctoral degree and none of this would be possible. They are truly the light that guides my way. Thank you Mom, Dad, Jeff, and Renata. Your love has inspired and moved me in ways that words cannot describe. I am proud to be your son, brother, and significant other. Thank you.

# CONTENTS

---

CHAPTER 1. INTRODUCTION.....	19
1.1 Motivation.....	19
1.1.1 Nano-scale Electro-machining.....	21
1.1.2 Data Storage.....	24
1.1.3 Biomedical Research and Manufacturing.....	26
1.1.4 Synopsis.....	27
1.2 Prior Art.....	27
1.2.1 Macro-scale Nanopositioners.....	27
1.2.2 Meso-scale Nanopositioners.....	29
1.2.3 Microactuators.....	34
1.2.3.A Electrostatic Microactuators.....	34
1.2.3.B Overview of Electromagnetic Microactuators.....	36
1.2.3.C Variable Reluctance Microactuators.....	38
1.2.3.D Moving-Magnet Microactuators.....	38
1.2.3.E Moving-Coil Microactuators.....	39
1.2.3.F Electromagnetic Microactuator Summary.....	39
1.2.3.G Thermal Microactuators.....	40
1.2.3.H Piezoelectric Microactuators.....	40
1.2.3.I Microactuator Summary.....	41
1.2.4 Flexure Concept Background.....	42
1.2.5 Summary.....	43
1.3 Research Challenges.....	43
1.4 Contributions.....	44
1.5 Thesis Summary.....	45
CHAPTER 2. DESIGN CONCEPT.....	47
2.1 Functional Requirements.....	47
2.2 Constraints.....	48
2.3 Flexure Concept.....	49
2.4 Flexure Bearing Concept.....	53
2.5 Microactuator Concept.....	55
2.5.1 Functional Requirements.....	55
2.5.2 Microactuator Species Selection.....	56
2.5.3 First-Order Coil Sizing.....	59
2.5.4 Two-Axis Moving-Coil Concept Selection.....	60
2.6 Nanopositioner Concept.....	65
2.7 First Order Design Equations and Scaling Laws.....	68
2.8 Design and Characterization of a Bench-level Prototype.....	72
2.8.1 Design of the Bench-level Prototype.....	72
2.8.2 Experimental Results.....	74
2.9 Summary.....	79
CHAPTER 3. MODELING AND ANALYSIS.....	80

3.1	Fourier Solution to the Permanent Magnet Fields .....	80
3.1.1	Introduction.....	80
3.1.2	Modeling.....	83
3.1.2.A	Model Setup and Boundary Conditions.....	83
3.1.2.B	Model Solution.....	85
3.1.2.C	Model Limitations.....	88
3.1.3	Three-Pole Actuator Magnet Array .....	89
3.1.4	Numerical Analysis.....	90
3.1.5	Comparison of Predicted and Measured Field Characteristics .....	91
3.2	Lorentz Coil Force .....	95
3.3	Electrical Circuit Model.....	97
3.3.1	Coil Resistance.....	98
3.3.2	Self-Inductance .....	98
3.3.3	Mutual Inductance .....	99
3.3.4	Mutual Capacitance .....	99
3.4	Kinematic and Dynamic Model.....	99
3.4.1	Model Setup and Boundary Conditions.....	100
3.4.2	Flexural Rigidity .....	101
3.4.3	Torsional Rigidity .....	102
3.4.4	Single-Sided Bent-Beam Unit Flexure .....	102
3.4.5	Double Bent-Beam Flexure .....	105
3.4.6	Six-Axis Nanopositioner Flexure .....	108
3.4.6.A	X-Axis Stiffness and Modal Frequency.....	108
3.4.6.B	Y-Axis Stiffness and Modal Frequency.....	109
3.4.6.C	$\theta_z$ -Axis Stiffness and Modal Frequency.....	110
3.4.6.D	$\theta_x$ -Axis Stiffness and Modal Frequency.....	111
3.4.6.E	$\theta_y$ -Axis Stiffness and Modal Frequency.....	111
3.4.6.F	Z-Axis Stiffness and Modal Frequency.....	112
3.5	Thermomechanical Model .....	113
3.5.1	Model Setup and Boundary Conditions.....	113
3.5.2	One-Dimensional Steady State Heat Conduction.....	115
3.5.3	Thermomechanical Out-of-Plane Displacement.....	118
3.6	Modeling Summary .....	119
CHAPTER 4. DESIGN AND OPTIMIZATION.....		121
4.1	System-Level Design.....	121
4.2	Actuator Design .....	125
4.2.1	Coil Winding Cross-Section and Pitch .....	127
4.2.2	Actuator Footprint and Magnet Size.....	128
4.2.3	Force and Power Optimization .....	129
4.2.4	Electrical Circuit.....	137
4.3	Double Bent-Beam Flexure Design Method.....	139
4.3.1	Nonlinear System of Equations .....	139
4.3.2	Thermal “Rigidity” of the Actuator Paddle .....	141
4.4	System-Level Performance Optimization.....	141
4.5	Mask Design Geometry .....	146
4.6	Package Design.....	148



4.7	Summary .....	150
CHAPTER 5. MICROFABRICATION DEVELOPMENT.....		152
5.1	Introduction.....	152
5.2	Process Overview.....	155
5.3	Mask Designs.....	159
5.4	Copper Electroplating .....	160
5.4.1	Top-down filling in Silicon molds.....	161
5.4.2	Bottom-up filling in photoresist molds.....	163
5.5	Copper CMP .....	165
5.6	Silicon Dioxide Thermomechanical Stress Experiments.....	166
5.7	Silicon Dioxide Electrical Design and Experiments.....	170
5.8	Nested Via Structure .....	173
5.9	Deep Reactive-Ion Etching .....	174
5.10	Oxygen Plasma cleaning with Exposed Copper .....	175
5.11	Integrated Fabrication Results .....	175
5.12	Summary .....	176
CHAPTER 6. EXPERIMENTAL RESULTS.....		177
6.1	Assembled Meso-Scale Nanopositioner .....	177
6.2	Electrical Experiments .....	179
6.2.1	Resistance and Sustainable Current.....	179
6.2.2	Self-Inductance .....	183
6.2.3	Mutual Capacitance .....	185
6.3	Mechanical Measurements.....	186
6.3.1	Experiments using the MEMS Motion Analyzer.....	186
6.3.1.A	Experimental Setup .....	186
6.3.1.B	Pre-Calibrated Input Command Signals .....	189
6.3.1.C	In-Plane Frequency Response.....	189
6.3.1.D	Quasistatic In-Plane Motion .....	191
6.3.1.E	Calibration procedure.....	196
6.3.1.F	Calibrated Quasistatic In-Plane Motion.....	197
6.3.1.G	Quasistatic Out-of-Plane Motion .....	199
6.3.1.H	Calibrated Quasistatic Out-of-Plane Motion .....	203
6.3.1.I	In-Plane Repeatability.....	204
6.3.2	Experiments using the Polytec MSA-400.....	205
6.3.2.A	Out-of-Plane Frequency Response .....	205
6.3.2.B	Out-of-Plane Step Response .....	207
6.4	Summary .....	208
CHAPTER 7. CONCLUSIONS AND FUTURE WORK.....		210
7.1	Summary and Conclusions .....	210
7.2	Future Work .....	214
7.2.1	Near-Term Motion Experiments.....	214
7.2.2	Thermal Error Compensation .....	216
7.2.3	Capacitive Sensing.....	216
7.2.4	Integration into a Nanomanufacturing System .....	217
REFERENCES .....		218
APPENDIX A. PHOTOMASKS.....		231

A.1	Mask 1 – Trenches for Buried Copper Coils .....	231
A.2	Mask 2 – Interlayer Silicon Dioxide .....	232
A.3	Mask 3 – Photoresist Mold for Upper Copper Coils .....	233
A.4	Mask 4 – Backside Silicon Cavities.....	233
APPENDIX B. PART DRAWINGS.....		235
B.1	Alignment Plate .....	235
B.2	Back Iron.....	236
B.3	PCB Frame.....	237
B.4	PCB Lead Board .....	238
APPENDIX C. CURRENT AMPLIFIER .....		239
APPENDIX D. MICROFABRICATION PROCESS DETAILS.....		242
D.1	Approved Microfabrication Process .....	242
D.2	Process Details .....	246
D.3	Copper CMP Process Suggestions and Run Data.....	255
D.4	AZ9260 Photoresist Experiment Data .....	259

# FIGURES

---

Figure 1.1. Image of the completed nanopositioner. The dime is included for size reference...	20
Figure 1.2. Schematic of the nano-scale electro-machining process. ....	22
Figure 1.3. a) Schematic representation of the flexure-guided nanopositioner in a nano-EM system. b) Solid model of a planar compliant flexure system that could be actuated in a manner that generates six-axis motion at the stage. ....	24
Figure 1.4. Schematic representation of the IBM probe-based data storage concept [12]. © 2000 IEEE. ....	25
Figure 1.5. First-order flexure-guided nanopositioner performance model. ....	32
Figure 1.6. Stroke vs. first resonant frequency for state-of-the art meso-scale nanopositioners.	33
Figure 2.1. Six-axis meso-scale nanopositioner concept.....	50
Figure 2.2. Actuation scheme with two independent and orthogonal actuator forces at each paddle. ....	52
Figure 2.3. Orthogonal 6-axis motion deformations of the nanopositioner flexure bearing mechanism due to forces applied at the actuator paddles.....	52
Figure 2.4. Nanopositioner flexure concepts: a) single-bent beam, b) double-bent beam, and c) bow-flexure.....	54
Figure 2.5. Schematic illustration of a magnet-coil actuator with planar spiral coil. ....	58
Figure 2.6. Cross-section schematic representations of two-axis planar coil actuator concepts that use a permanent magnet field source and enable in-plane and out-of-plane forces: a) alternating pole magnet array with stacked actuator coils; b) single magnet and yolk with stacked actuator coils; c) symmetric semi-Halbach magnet array with nested actuator coils; d) symmetric semi-Halbach magnet array with stacked actuator coils.....	62
Figure 2.7. Comparison of the a) x-component and b) y-component of the magnetic flux-density at a height $h/a = 0.5$ above the magnet array for each actuator concept.....	63
Figure 2.8. a) Cross-section schematic of the two-axis moving-coil actuator architecture and b) individual schematic plan views of the stacked coil actuator architecture.....	64
Figure 2.9. Solid model nanopositioner concept. ....	66
Figure 2.10. Cross-section schematic of the nanopositioner multi-layer flexure beams (not drawn to scale).....	66
Figure 2.11. First-order design models for a flexure-guided nanopositioner with suspended coil actuator: a) displacement due to linear beam-bending; b) dynamic mass-spring representation; c) coil power dissipation through the flexure bearing resulting in thermal growth.....	69
Figure 2.12. a) Bench-level prototype nanopositioner. b) Cross-section A-A of the nanopositioner showing actuator components.....	73
Figure 2.13. First mode of the prototype nanopositioner at 125Hz as computed using FEA.....	74
Figure 2.14. Bench-level nanopositioner with capacitance probes and measurement target. ....	75
Figure 2.15. Measured vs. commanded displacement in the a) x-direction and b) z-direction. .	75
Figure 2.16. Dynamic response in the z-direction without probe target.....	76

Figure 2.17. Nanopositioner response to a 600nm step input in the x-direction with six-axis capacitance probe target. ....	76
Figure 2.18. Nanopositioner response to a 10nm step in the z-direction without the capacitance probe target. ....	77
Figure 2.19. Nanopositioner response to a 100nm step in the z-direction, without the capacitance probe target. ....	77
Figure 2.20. Nanopositioner response to a 1000nm step in the z-direction, without the capacitance probe target. ....	78
Figure 2.21. Measured trajectory of the nanopositioner when commanded to follow a 3-loop spiral trajectory with diameter and total traversed height of 1000nm. ....	78
Figure 3.1. An actuator with a periodic array a) and an actuator with a non-periodic array b)...	81
Figure 3.2. A meso-scale, six-axis nanopositioner. ....	81
Figure 3.3. Generalized in-plane magnet arrangement with equivalent surface magnetic charge distribution $\sigma(x,y)$ at $z = (1/2)c$ (a) and side view with detail of charge distribution on upper and lower surfaces (b). ....	83
Figure 3.4. Schematic representation of the example three-pole magnet arrangement. ....	90
Figure 3.5. Computation time vs. normalized RMS error for each component of the flux density at $z = c/2$ above the example magnet surface as computed by the Fourier transform and superposition integral (SPI) methods. ....	91
Figure 3.6. Schematic of the Equipment used to acquire data (a) and corresponding experimental setup (b). ....	92
Figure 3.7. Comparison of predicted (surface) vs. measured (points) values of the x (a), y (b), and z (c) components of the magnetic flux density. Cross-sections of the x surface at $y = 0$ mm (d), y surface at $y = 12.7$ mm (e) and z surface at $y = 0$ mm (f). ....	94
Figure 3.8. Measured vs. predicted bench-level prototype displacement in the z-direction. ....	97
Figure 3.9. a) Electrical circuit model of an actuator coil. b) Planar-spiral coil model for approximating the inductance. ....	98
Figure 3.10. Schematic model of the double bent-beam flexure with cross-section of the multi-layer beam. ....	100
Figure 3.11. Schematic model of the single-sided bent-beam flexure. ....	103
Figure 3.12. Lumped parameter stiffness model of the double-bent beam flexure. ....	105
Figure 3.13. Lumped-parameter half model for X-axis translation. ....	109
Figure 3.14. Lumped-parameter half model for Y-axis translation. ....	109
Figure 3.15. Lumped-parameter half model for $\theta_z$ rotation. ....	110
Figure 3.16. Lumped-parameter half model for $\theta_x$ rotation. ....	111
Figure 3.17. Lumped-parameter half model for $\theta_y$ rotation. ....	112
Figure 3.18. Lumped-parameter half model for Z translation. ....	112
Figure 3.19. Thermomechanical model schematic of the double bent-beam flexure and actuator paddle. ....	114
Figure 3.20. One-dimensional heat conduction model for the transverse temperature distribution across the multilayer flexure beams. ....	115
Figure 3.21. One-dimensional model of heat conduction along the flexure beams. ....	116
Figure 3.22. Comparison of the steady-state temperature along the double-bent flexure beam as computed by FEA and the one-dimensional model. ....	118
Figure 4.1. Solid model of the proposed nanopositioner system. ....	122

Figure 4.2. Assembled a) and exploded view b) of the two-axis moving-coil microactuator and double bent-beam flexure. ....	123
Figure 4.3. Solid model a) and detailed cross-section view along A-A b) of the moving-coil microactuator. ....	124
Figure 4.4. Actuator magnet and coil geometric parameters. ....	126
Figure 4.5. X-actuator a) and Z-actuator b) coils superimposed upon the z-component a) and x-component of the simulated magnetic flux density that exists along the plane of the coils. ....	127
Figure 4.6. Simulated force output of the x- and z-actuators versus coil footprint. ....	129
Figure 4.7. Simulated actuator forces and moments versus coil segment spacing, $d$ . The x-actuator forces and moments are presented in a) and c), while the z-actuator forces and moments are presented in b) and d). ....	131
Figure 4.8. Simulated force efficiencies versus coil segment spacing, $d$ , for the a) x- and b) z-actuators. ....	132
Figure 4.9. Simulated actuator forces and moments versus coil height, $h$ . The x- actuator forces and moments are shown in a) and c), while the z-actuator forces and moments are shown in b) and d). ....	134
Figure 4.10. Simulated actuator forces versus vertical coil position relative to $h = 150 \mu\text{m}$ . The x- actuator x-directed force is shown in a) and the z-actuator z-directed force is shown in b). ....	135
Figure 4.11. Simulated actuator forces versus lateral position of the actuator coil. The x-actuator's, x-directed force is shown in a) and the z-actuator's z-directed force is shown in b). ....	136
Figure 4.12. Skin depth for copper coil windings as a function of excitation frequency. ....	139
Figure 4.13. Iterative loop for the design of the nanopositioner. ....	142
Figure 4.14. a) Exaggerated deformation of the nanopositioner FEA model that was caused by power dissipation in the coils; b) close-up view of the solid mesh used in the FEA model. ....	143
Figure 4.15. Simulated transient thermally-induced error motion of the nanopositioner. ....	145
Figure 4.16. Qualitative representation of the nanopositioner system dynamics in the thermal, mechanical, and electrical domains. ....	146
Figure 4.17. Plan view of the front side of the nanopositioner chip. ....	147
Figure 4.18. Mask geometry of the stacked actuator coils that shows the vias and jumper architecture that route current to the coils. ....	148
Figure 4.19. a) Solid model representation of the assembled nanopositioner chip and alignment package; b) exploded view of the complete nanopositioner assembly. ....	149
Figure 4.20. Schematic representation of the method that was used to align the chip to the actuator magnets. ....	149
Figure 5.1. Cross-section schematic of the meso-scale nanopositioner chip and magnet array	155
Figure 5.2. Cross-section schematics of the microfabrication process that was used to realize the nanopositioner. ....	156
Figure 5.3. Optical image of the completed nanopositioner die. ....	159
Figure 5.4. Mask designs for the nanopositioner process: a) mask 1, buried copper coil trenches; b) mask 2, silicon dioxide vias and DRIE mask; c) mask 3, photoresist mold for upper copper coil, leads, bond pads, and dummy features; and d) mask 4, backside cavity and trenches. ....	160

Figure 5.5. Optical image a buried coil after CMP that shows voids in the copper deposits. ...	162
Figure 5.6. SEM cross-section images of buried copper coils with void defects from different wafers. The cross-sections were created by cleaving the wafers and fracturing the copper in tension.....	162
Figure 5.7. Optical image a void-free buried coil after CMP. ....	163
Figure 5.8. SEM cross-section images of void-free buried copper coils after partial CMP. ....	163
Figure 5.9. SEM images of the a) cross-section of the resist-molded coil winding and b) coil corner before DRIE flexure etching. ....	164
Figure 5.10. SEM image of cracked silicon isolators after deposition and patterning of PECVD oxide. Wet-etched oxide is visible around the perimeter of the silicon isolator ...	166
Figure 5.11. Optical image of a crack-free copper coil embedded in silicon with 1 $\mu\text{m}$ of PECVD oxide. ....	167
Figure 5.12. Delaminations in silicon dioxide after etching of the seed layer for upper copper coil layer. ....	167
Figure 5.13. In-plane and cross-sectional buried copper coil geometric parameters. Thermal oxide and Ti/Cu seed are not shown for clarity.....	168
Figure 5.14. Mechanical defect rate of the silicon dioxide versus copper and silicon line widths. The defect rate was measured after completion of the double coil process. ....	169
Figure 5.15. Simulated copper concentration vs. depth in silicon dioxide for various times at $T = 300^\circ\text{C}$ . A 1 $\mu\text{m}$ PECVD silicon dioxide was deposited in approximately 0.3 hours at $300^\circ\text{C}$ . ....	171
Figure 5.16. Cross-section schematic of the capacitor test structure that was used to measure the electrical breakdown strength of unannealed silicon dioxide.....	172
Figure 5.17. Measured electrical breakdown field for 1 $\text{mm}^2$ un-annealed PECVD silicon dioxide capacitors. ....	173
Figure 5.18. a) Optical image of nested vias etched through the oxide to the underlying copper coils. b) Inclined SEM image of a via after seed layer deposition. ....	174
Figure 5.19. SEM images of the a) composite flexure beam and b) edge of the actuator paddle .....	175
Figure 5.20. Optical images of the stacked double coil structure a) before and b) after etching, release, and cleaning of the flexure structure. ....	176
Figure 5.21. SEM image of a stacked-coil actuator paddle after completion of the fabrication process. The outline of the buried copper coils is visible under the oxide.....	176
Figure 6.1. Image of the assembled meso-scale nanopositioner: a) silicon chip that was mounted on the magnet fixture; b) chip and magnet fixture that was assembled to the PCB electrical lead frame. ....	177
Figure 6.2. Optical image of a completed actuator paddle from an assembled nanopositioner. The magnets are visible under the paddle. ....	178
Figure 6.3. a) Measured static I-V characteristics for a suspended x-actuator coil and b) calculated average static coil temperature versus input current. ....	180
Figure 6.4. a) Measured static I-V characteristics for a suspended z-actuator coil and b) calculated average coil temperature versus input current.....	181
Figure 6.5. a) Measured static I-V characteristics for a test coil and b) average coil temperature calculated from the change in resistivity of the copper coil windings. ....	182
Figure 6.6. Measured self-inductance of the a) x-actuator and b) z-actuator coils.....	183
Figure 6.7. Measured self-inductance of the test coil. ....	184

Figure 6.8. Measured mutual capacitance between the x- and z- actuator coils.....	185
Figure 6.9. a) Schematic diagram and b) image of the MMA experiment setup.....	187
Figure 6.10. Optical image of the MMA target showing the regions of interest used for calculation of: a) in-plane translations and rotation; and b) out-of-plane translations and rotation. ....	188
Figure 6.11. Measured frequency response of the nanopositioner for pre-calibrated actuation in the a) x- and b) y-directions.....	190
Figure 6.12. Measured frequency response of the nanopositioner for pre-calibrated actuation in the $\theta_z$ direction. ....	190
Figure 6.13. Pre-calibrated, in-plane quasistatic response versus input current for commanded motion in the x-direction: a) measured and predicted x-motion and parasitic y-motion; b) measured $\theta_z$ parasitic motion. ....	192
Figure 6.14. Pre-calibrated, in-plane quasistatic response versus input current for commanded motion in the y-direction: a) measured and predicted y-motion and parasitic x-motion; b) measured $\theta_z$ parasitic motion. ....	192
Figure 6.15. Pre-calibrated, in-plane quasistatic response versus input current for commanded motion in the $\theta_z$ -direction: a) measured parasitic x- and y-motion; b) measured and predicted $\theta_z$ motion. ....	193
Figure 6.16. Pre-calibrated in-plane static response versus input current for commanded motion in the z-direction: a) measured parasitic x- and y-motion; b) measured and predicted $\theta_z$ motion. ....	194
Figure 6.17. Pre-calibrated, in-plane static response versus input current for commanded motion in the $\theta_x$ -direction: a) measured parasitic x- and y-motion; b) measured parasitic $\theta_z$ motion. ....	195
Figure 6.18. Pre-calibrated, in-plane static response versus input current for commanded motion in the $\theta_y$ -direction: a) measured parasitic x- and y-motion; b) measured parasitic $\theta_z$ motion. ....	195
Figure 6.19. Calibrated, in-plane static response versus input current for desired motion in the x-direction: a) measured x-motion and parasitic y-motion; b) $\theta_z$ parasitic motion. .	197
Figure 6.20. Calibrated, in-plane static response versus input current for desired motion in the y-direction: a) measured y-motion and parasitic x-motion; b) $\theta_z$ parasitic motion. .	198
Figure 6.21. Calibrated, in-plane static response versus input current for desired motion in the $\theta_z$ -direction: a) measured parasitic x- and y-motion; b) measured $\theta_z$ motion. ....	198
Figure 6.22. Out-of-plane static response versus input current for calibrated motion in the x-direction: a) measured parasitic motion in the z-direction; b) measured parasitic motion in the $\theta_x$ - and $\theta_y$ -direction. ....	200
Figure 6.23. Out-of-plane static response versus input current for calibrated motion in the y-direction: a) measured parasitic motion in the z-direction; b) measured parasitic motion in the $\theta_x$ - and $\theta_y$ -direction. ....	200
Figure 6.24. Out-of-plane static response versus input current for commanded motion in the $\theta_x$ -direction: a) measured parasitic motion in the z-direction; b) measured motion in the $\theta_x$ -direction and parasitic motion in the $\theta_y$ -direction. ....	201
Figure 6.25. Out-of-plane static response versus input current for commanded motion in the $\theta_y$ -direction: a) measured parasitic motion in the z-direction; b) measured motion in the $\theta_y$ -direction and parasitic motion in the $\theta_x$ -direction. ....	202

Figure 6.26. Out-of-plane static response versus input current for commanded motion in the z-direction: a) measured motion in the z-direction; b) measured parasitic motion in the $\theta_x$ - and $\theta_y$ -direction. ....	202
Figure 6.27. Calibrated, out-of-plane static response versus input current for commanded motion in the z-direction: a) measured motion in the z-direction; b) measured parasitic motion in the $\theta_x$ - and $\theta_y$ -directions. ....	203
Figure 6.28. Calibrated static in-plane response versus input current for multiple trials of commanded motion: a) commanded motion in the x-direction; b) commanded motion in the y-direction. ....	205
Figure 6.29. Measured out-of-plane frequency response of the nanopositioner for input into one z-actuator. ....	206
Figure 6.30. Measured out-of-plane response for a pre-calibrated, square wave input signal to the z-actuator coils: a) one z-actuator excited by a signal with 1 sec period; and b) three z-actuators excited by a signal with 10 sec period. ....	207
Figure 7.1. Six-axis capacitive sensing concept. ....	216
Figure 7.2. a) Schematic illustration of a bench-top, probe-based nanomanufacturing and metrology system; b) schematic illustration of arrayed nanomanufacturing on macro-scale substrates. ....	217



# TABLES

---

Table 1.1. Mismatch in scale of conventional precision machines and nano-scale features.....	21
Table 1.2. High-speed nanopositioner functional requirements for use in nano-electro-machining. ....	23
Table 1.3. Probe-based data storage performance comparison.....	26
Table 1.4. Macro-scale nanopositioner performance comparison.....	29
Table 1.5. Comparison of state-of-the-art small-scale multi-axis nanopositioners.....	31
Table 1.6. Electrostatic actuator species performance comparison.....	36
Table 1.7. Summary of electromagnetic actuator applications.....	38
Table 1.8. Electromagnetic actuator species performance comparison.....	40
Table 1.9. Summary comparison of micro-actuator types.....	41
Table 2.1. Nanopositioner functional requirements.....	48
Table 2.2. Nanopositioner constraints.....	49
Table 2.3. Simulation parameters used for flexure concept comparison.....	54
Table 2.4. Nanopositioner flexure concept performance metric comparison.....	55
Table 2.5. Two-axis actuator functional requirements.....	56
Table 2.6. Microactuator species qualitative comparison.....	57
Table 2.7. Typical dimensions and material properties for magnet-coil microactuators.....	59
Table 2.8. Parameters used for first-order actuator coil sizing.....	60
Table 2.9. Two-axis moving-coil microactuator concept comparison.....	64
Table 2.10. Relevant flexure material properties for high-speed electromagnetically-driven nanopositioners.....	67
Table 2.11. First-order nanopositioner model parameter sensitivities.....	71
Table 2.12. Nanopositioner scaling laws.....	72
Table 3.1. Dimensions and material properties of the experiment.....	93
Table 3.2. Bench-level prototype coil actuator design parameters.....	97
Table 3.3. Parameters used to compare double bent-beam model to FEA.....	107
Table 3.4. Comparison of unit flexure stiffness as predicted by the model and FEA.....	108
Table 3.5. Parameters used to compute the transverse temperature distribution across the multilayer beam.....	116
Table 4.1. Comparison of interlayer dielectric materials properties.....	125
Table 4.2. Magnet geometry that was used to compute the flux density contours for the example coil geometry.....	127
Table 4.3. Magnet and coil geometry characteristics that were used to compute force for variable actuator footprint.....	128
Table 4.4. Magnet and coil geometry characteristics that were used to compute force and power for variable coil spacing $d$ .....	130
Table 4.5. Magnet and coil geometry that was used to compute force and power for variable coil height $h$ .....	133
Table 4.6. Design geometry for the two-axis moving coil actuator.....	137
Table 4.7. Model parameters were used to compute the resistance, self-inductance, and electrical time constant.....	137

Table 4.8. Mutual capacitance model parameters.....	138
Table 4.9. Flexure geometry of the optimized nanopositioner. ....	143
Table 4.10. Predicted resonant modes of the optimized nanopositioner. ....	144
Table 4.11. Predicted static motion, thermally-induced error motion, and maximum operating temperature. ....	144
Table 5.1. Experimental parameters for the oxide delamination study. ....	169
Table 6.1. Measured magnetic gaps for each actuator coil in the meso-scale nanopositioner. .	179
Table 6.2. Comparison of measured and predicted coil resistance.....	182
Table 6.3. Comparison of the measured and predicted inductance and $L$ - $R$ frequency.....	184
Table 6.4. Relative command inputs for motion along each axis of the nanopositioner prior to calibration. ....	189
Table 6.5. Comparison of predicted and measured in-plane resonant modes. ....	190
Table 6.6. Comparison of predicted and measured out-of-plane resonant modes.....	206
Table 7.1. Summary comparison of the functional requirements and measured performance of the meso-scale nanopositioner.....	214

## INTRODUCTION

---

### 1.1 Motivation

The purpose of this thesis is to generate the design and fabrication knowledge that is required to engineer high-bandwidth, six-axis, meso-scale (HSM) nanopositioners that are driven by electromagnetic actuators. The fundamental issues to be addressed in this work include: 1) conceptualization and design of a HSM nanopositioner architecture 2) design of electromagnetic actuators that are capable of driving the positioner in 6-axes with sufficient force, range, and bandwidth; 3) parametric, physics-based modeling and optimization of the actuator and nanopositioner input-outputs responses; 3) microfabrication and assembly of a prototype nanopositioner that contains actuators and bearings that are integrated into its structure and designed for high-bandwidth probe-based nanomanufacturing; 4) experimental investigation of the nanopositioner performance limits and the accuracy of the parametric performance models; and 5) physics-based design principles for future concept design activities. The impact of this work is that the new nanopositioner could be used to improve the throughput, accuracy, and repeatability of nano-scale metrology and tip-based nanomanufacturing.

The results of this research were used to design and fabricate a meso-scale nanopositioner system. The nanopositioner was measured to have a range of motion of 10 micrometers in the lateral directions, a range of 2 micrometers in the out-of-plane direction, an angular range of 0.5 degrees, and a first mode resonant frequency at 900 Hz. Open-loop calibration has been shown to minimize parasitic in-plane motion to less than 100 nm over the range of motion. Figure 1.1 shows an image of the completed nanopositioner next to a dime.

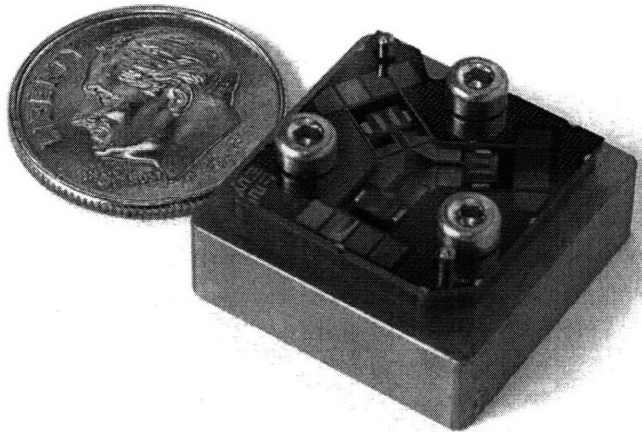


**Figure 1.1. Image of the completed nanopositioner. The dime is included for size reference.**

Nanopositioners – be they nano-, micro- or macro-scale in physical size – enable us to move large or small parts with nanometer-level or better precision. They therefore set the limits on our ability to measure/understand and manipulate/affect physical systems. Nanopositioners often operate in multiple axes, thereby controlling position and/or orientation in one to six degrees-of-freedom (DOF). Although nanopositioners may be of any size scale, several common performance characteristics scale favorably as the size of the nanopositioner decreases. Multi-axis, macro-scale nanopositioners are common and the engineering knowledge that is required design them is well-understood. HSM nanopositioners are not common and lack the body of knowledge that may be readily used to design them. This thesis is a first step in laying the foundation for high-speed, meso-scale nanopositioner design. Once realized, HSM nanopositioners will enable high-bandwidth, precise positioning and measurement in the biological sciences, data storage, probing instruments for nano-scale measurements, and equipment for nanomanufacturing processes [1-8]. Emerging applications in these fields would benefit from portable, multi-axis, nanopositioners with tens-of-microns range, bandwidths of hundreds to thousands of Hertz, and Angstrom-level resolution.

Conventional nanopositioners are often tens of centimeters in size and have positioning time constants on the order of tens to hundreds of milliseconds. In contrast, nano-scale phenomena typically occur on time scales that are less than tens of microseconds, as illustrated in Table 1.1.

**Table 1.1. Mismatch in scale of conventional precision machines and nano-scale features.**

Parameter	Conventional Machines	Nano-scale Features
Length	10s cm to 1m	10s nm
Time Constant	100s msec	10s $\mu$ sec

The mismatch between the length scales and time scales of macro-scale positioners and nano-scale phenomena limits the use of state-of-the-art nanopositioners in future small-scale applications. For example, process throughput is important in many of these applications. The size scale of macro-scale nanopositioners limits their throughput since they are not amenable to massively parallel operation and their positioning response time is slow. It may be possible to bridge the length and time scale gaps by using millimeter- or meso-scale nanopositioners that operate at higher bandwidth and retain nanometer-level precision. Meso-scale systems take advantage of length scaling to attain higher mechanical bandwidth than macro-scale machines. This is due to reduction in mass and increased resonant frequencies that typically accompany reduced size. Meso-scale nanopositioners also exhibit less thermal growth per unit temperature change, and therefore they exhibit better thermal stability.

One important emerging application that requires high-bandwidth nanopositioners is probe-based nanomanufacturing. Conventional nanopositioners have been used in these systems to control the position of probe tips for surface modification by deposition, removal, or manipulation of material. Tseng and Notargiacomo provide a review of these techniques [9]. The following sub-sections describe several types of probe-based processes that could benefit from an HSM nanopositioner.

### **1.1.1 Nano-scale Electro-machining**

One example, called nano-scale electro-machining (nano-EM), selectively removes conductive material from a surface [8]. Figure 1.2 shows a schematic representation of the process. An electrical potential is applied across a 10-20nm gap between a probe tip and conductive work surface. The gap is filled with a suitable dielectric. The potential is set high enough to cause breakdown of the dielectric, thereby resulting in a high current density that leads to local material removal from the work surface. Material is typically removed to a depth and diameter of tens of nanometers. Nano-EM is a serial process that requires several hundred microseconds to remove several cubic-nanometers of material.

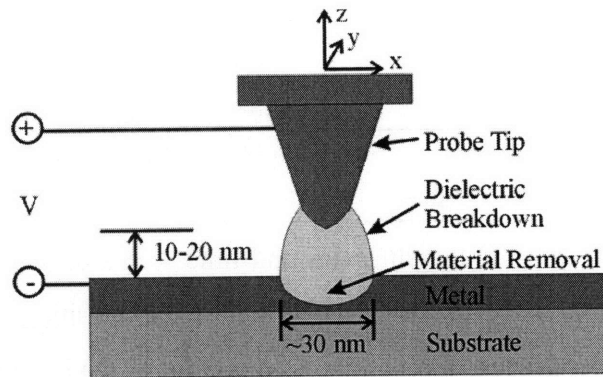


Figure 1.2. Schematic of the nano-scale electro-machining process.

Nano-EM may enable the manufacturing of nano-scale circuitry, precision mask edits, and research-level prototyping. In order to make this technique practical, sample moves of several microns should be executed in milliseconds and with nanometer-level or better resolution and repeatability. Conventional lithographic patterning of one metal surface on a silicon wafer typically takes on the order of 2-5 hours. An arrayed set of meso-scale nanopositioners that is fitted with nano-EM probe-tips could be designed to have a similar production rate, yet be capable of 20nm feature size as opposed to the current 90nm semiconductor node. Consider the following:

- 1) An HSM nanopositioner system with a  $10\ \mu\text{m} \times 10\ \mu\text{m}$  X-Y work area.
- 2) The nanopositioner operates on a chip that is  $10\ \text{mm} \times 10\ \text{mm}$  in size.
- 3) An array of these nanopositioners may be translated by a coarse X-Y stage.

In order to completely cover the chip area, the nanopositioner array should scan through its range at  $10^6$  locations on the chip. It may be shown that the nanopositioner should be capable of scanning at roughly 10 kHz with a scan pitch of 20 nm to make nano-EM comparable to lithography in terms of processing time. This is optimistic for an HSM nanopositioner given the state-of-the-art in micro-actuation technology. The performance of comparably-sized systems, as reported in the literature, indicates that a realistic performance target would include a resonant frequency of 1 kHz, a  $10\ \mu\text{m}$  workspace in x-y-z, and a repeatability of 10 nm. Table 1.2 lists the design requirements and specifications by row: functional requirements, capability of a state-

of-the-art nanopositioner (Physike Instrumente 3-axis system), and a realistic set of requirements for the proposed nanopositioner system.

**Table 1.2. High-speed nanopositioner functional requirements for use in nano-electro-machining.**

	Natural Frequency (Hz)	Stroke ( $\mu\text{m}$ )	Axes	Precision (nm)	Size (mm)	Cost
Functional Requirements	1000	10	6	10	10	NA
Current Capability	220	100	3	25	40	\$5k
Proposed System	1000	10	6	10	20	~\$20

In nano-EM, the positioner must control the probe-tip location relative to the surface in six degrees of freedom:  $x$ ,  $y$ ,  $z$ ,  $\theta_x$ ,  $\theta_y$ , and  $\theta_z$ . The probe-substrate gap must be held to less than 10-20 nm during the machining operation. Angular control of the probe tip is necessary when operating the system in open-loop because angular motion of a finite-length probe tip would result in gap error and lateral tip error at the surface. An HSM nanopositioner that uses suitable microactuators, and operates in open-loop, could correct these rotation errors. This type of machine could also enable fast moves with high precision. They may also be arrayed for parallel processing. Closed-loop control in six axes could improve system bandwidth, reduce steady-state error, and improve disturbance rejection capability. The implementation of closed-loop control would require extensive research in order to integrate microfabricated, on-chip sensing for a meso-scale nanopositioner system.

A closed-loop, HSM nanopositioner will require a combination of advances in actuation, flexure sensing, electronics and control technologies. The proposed research will address the core flexure and actuator modules that may be used in open loop. The focus on these modules will make it possible to create a prototype that operates in open-loop and which may be used to demonstrate the feasibility of the design. This initial work will provide the foundation to conceptualize, model, simulate, design, and fabricate the meso-scale nanopositioners. Given this body of work, the resulting prototype may then serve as a platform upon which research in sensing, electronics, and controls will build to realize feedback control.

Figure 1.3a shows a schematic representation of a six-axis flexure-guided nanopositioner that is integrated into a nano-EM system. The flexure elements are represented by vertical and

horizontal springs of stiffness  $k$ . A probe tip is mounted upon the stage. The stage is deflected from its neutral position by an actuation force,  $F$ , that acts upon the center of stiffness on the positioner stage. Figure 1.3b shows a meso-scale flexure and stage arrangement that could enable six-axis motion when the stage is subjected to the appropriate actuator inputs,  $F_1$ ,  $F_2$ , etc., in the schematic. The three-way symmetric, planar flexure concept is adapted from the HexFlex compliant mechanism that was designed for use in low-cost nanopositioners [10]. The planar configuration is amenable to lithographic fabrication, thereby making it suitable for a microfabricated meso-scale nanopositioner system.

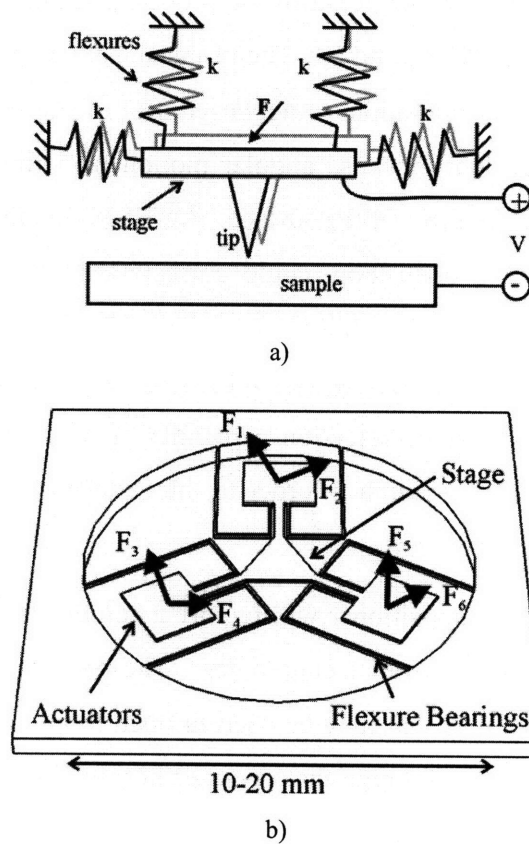


**Figure 1.3. a) Schematic representation of the flexure-guided nanopositioner in a nano-EM system. b) Solid model of a planar compliant flexure system that could be actuated in a manner that generates six-axis motion at the stage.**

### 1.1.2 Data Storage

In addition to nanomanufacturing, probe-based data storage could benefit from the HSM nanopositioner. Probe-based data storage systems write and read data with an array of probe tips



that locally deform a movable polymer media surface [11-13]. Figure 1.4 shows a schematic representation of the probe-based data storage concept. A pit that was written into the surface represents a “1” bit, and the original surface represents a “0.” In the state-of-the-art research prototypes, data bits are approximately 15 nm in diameter and they are written at a pitch of 30 nm. Portable, probe-based data-storage systems can read and write data bits at kilohertz frequencies with area densities that approach terabits per square inch, but they require the translation of a media shuttle over distances of several tens-of-microns [7].

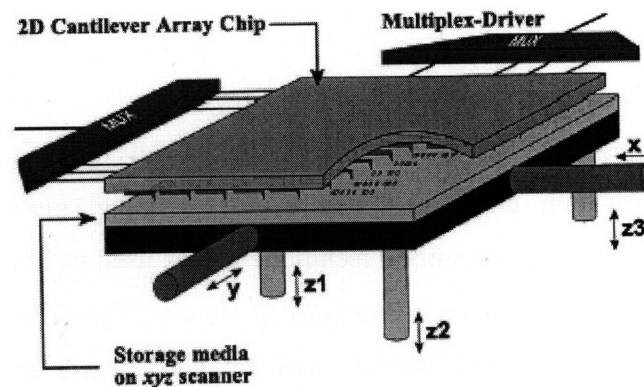


Figure 1.4. Schematic representation of the IBM probe-based data storage concept [1]. © 2000 IEEE.

These systems use meso-scale positioners to control the media shuttle motion [1, 3, 7]. Table 1.3 compares the proposed HSM nanopositioner and state-of-the-art meso-scale positioners that have been developed for probe-based data storage. The proposed system could improve data transfer rates up to 10X by increasing the mechanical bandwidth to 1 kHz. Six-axis open-loop motion control of the media sled could be used to compensate for mapped parasitic errors of the motion stage and this would eliminate the need for external actuation and feedback control of probe height. In addition, storage density could be increased to 2-5 Tbits/in<sup>2</sup> by improving accuracy to better than 10 nm, which would result in closer packing of the bits. Closed-loop control could improve disturbance rejection and steady state error, but this would require integration of on-chip sensing. Although sensor integration and closed-loop feedback position control could improve system performance, an initial prototype operating in open-loop would demonstrate the concept and serve as a test-bed for future integration of sensing and feedback control.

**Table 1.3. Probe-based data storage performance comparison**

Author	Year	Natural Frequency (Hz)	Stroke ( $\mu\text{m}$ )	Axes	Precision (nm)	Power (mW)	Size (mm)
Rothuizen	2000	60	240	5	NA	200	30
Rothuizen	2002	80	160	5	NA	8	15
Pantazi	2004	124	120	2	4 (CL)	NA	17
Lantz	2007	168	120	2	NA	170	17
<b>Golda</b>	<b>2008</b>	<b>1000</b>	<b>10</b>	<b>6</b>	<b>&lt;10 OL</b>	<b>300</b>	<b>15</b>

### 1.1.3 Biomedical Research and Manufacturing

The HSM nanopositioner has the potential to impact several biological applications that require nano-scale fabrication or measurement. For example, massively-parallel dip-pen nanolithography (DPN) is a scanning probe technique that is used in biological research where there is a need to write molecule-level amounts of materials on a substrate [14]. In this method, arrayed probe tips are mounted on cantilevers, functionalized with a compound, positioned in close proximity to a substrate, and then pulled across the surface after making contact. DPN is anticipated to enable high-throughput molecular functionalization when combined with recently developed, ordered arrays of DNA [15]. Obtaining a suitable throughput with DPN is a central challenge for those who use the technique. This has been partially addressed by arraying tens to thousands of microfabricated tips upon a chip. The chip is then scanned over the substrate and through a range, 20 – 90  $\mu\text{m}$ , which is equal to the tip spacing. The maximum speed and repeatability of the positioning system combine to impose an upper limit on the throughput and the parallelization of this process. The HSM nanopositioner could improve pen raster-scan bandwidth and enable multiple chips to process a substrate, thereby improving throughput.

In light of these applications, it is desired to develop HSM nanopositioning systems that are capable of operating at 100s to 1000s of Hertz, with stroke of tens-of-microns, and with precision that is better than 10 nm. As will be shown in the literature review, the combination of actuators, flexures, and microfabrication process research have expanded the performance envelope of state-of-the-art multi-axis positioning systems.

### **1.1.4 Synopsis**

In this section, the utility of open loop, electromagnetically-driven, flexure-based HSM nanopositioners have been identified as a possible solution for positioning applications that require kHz bandwidth, tens-of-microns stroke, six-axes of motion, and nanometer-level precision. Applications such as portable probe-based data-storage and nano-electrical discharge machining would benefit from improvements in positioning bandwidth, precision, and accuracy. Several design and fabrication challenges must be addressed in order to achieve the target performance goals and realize microfabrication of the system. The results of the following literature review will be used to identify specific challenges.

## **1.2 Prior Art**

Nanopositioners may be divided into micro-, meso-, and macro-scale classes. Conventional macro-scale nanopositioners use a variety of bearings, operate over large distances (100s microns to centimeters), exert large forces (N-kN), and exhibit low bandwidth (a few Hz) and high precision (nanometers). Macro-scale nanopositioners often operate under closed-loop control. Meso-scale systems often use flexure bearings, operate over microns, exert mN-level forces, and exhibit 100s-1000s Hz bandwidth and nm-level precision. Unfortunately, meso-scale systems typically operate in open-loop due to the complexity of adding sensing at the meso-scale. As a result, meso-scale system performance is usually actuator-limited. It is therefore important to understand micro-actuation technology and how this affects the performance of meso-scale system relative to their better-known macro-scale counterparts. The following presents a review of macro- and meso-scale positioners, with emphasis on understanding how micro-actuation affects the performance of meso-scale nanopositioning.

### **1.2.1 Macro-scale Nanopositioners**

Macro-scale nanopositioners can position large or small objects over 100+ microns travel and with nanometer-level precision in up to six degrees-of-freedom. The relatively large mass of these systems limit their natural frequencies and bandwidth to 10-100 Hz. Table 1.4 summarizes the performance of selected macro-scale Cartesian nanopositioning systems. Magnetic levitation systems that exhibit two to six axis motion have been developed primarily for semiconductor manufacturing equipment and scientific instruments [16-22]. These systems operate with approximately 100 Hz bandwidth over several millimeters of travel in-plane, and with hundreds

of microns out-of-plane. Magnetic levitation systems require sensing and feedback in order to stabilize their motion. This limits system repeatability to ~50 nm and adds design and control complexity and cost to the systems. Air bearings have been implemented to stabilize out-of-plane motion and thereby reduce the control burden, but they further add to system design complexity [23-24]. Flexure bearings do not require feedback for stabilization, and so they provide an attractive alternative to magnetic and air bearings. The use of flexure motion bearings can reduce system complexity and increase repeatability, but then mechanical resonances and limited range of motion become important issues. Although flexure bearings have been used frequently in precision machines, especially in one-axis applications, recent work has led to motion guidance in three to six axes over hundreds of micrometers [10, 25-27]. Many of these macro-scale devices operate under closed-loop control, require high-voltage power supplies, dissipate several Watts of power, and cost several thousands of dollars. The high power dissipation also leads to temperature changes that may result in large position errors within macro-scale machines.

The force and stroke capabilities of large nanopositioners grossly exceed the positioning requirements of small-scale samples, such as probe tips, cells, thin-film samples, and micro-optics. These applications would benefit from the high bandwidth and precision of micro- or meso-scale systems at the expense of force and stroke.

**Table 1.4. Macro-scale nanopositioner performance comparison.**

Author	Year	Actuation	Scale	Stroke ( $\mu\text{m}$ )	Bandwidth or Nat Freq (Hz)	Precision (nm)	Feed-back	Description
Trumper	1996	EM	cm	200000	NA	<30	yes	2-axis levitated stage
Wang	1996	EM	cm	700	NA	300	yes	5-axis flexure-guided stage
Lee	1997	Piezo	cm	NA	NA	20	yes	X-Y- $\theta$ flexure-guided fine stage mounted on coarse stage
Ku	2000	Piezo	cm	5	1200	2	yes	3-axis flexure-guided stage
Lee	2000	EM	cm	40	NA	25	yes	3-axis air bearing stage
Kim	2001	EM	cm	50000	100	30	yes	6-axis levitated stage
Chen	2002	EM	cm	160	85	50	yes	X-Y- $\theta$ flexure-guided stage
Jung	2002	EM	cm	NA	NA	100	yes	6-axis levitated stage
Compter	2004	EM	cm	NA	NA	NA	yes	6-axis levitated stage
Gao	2004	EM	cm	40000	NA	200	yes	X-Y- $\theta$ levitated stage
Culpepper	2004	EM	cm	100	100	200	no	6-axis flexure-guided stage
Verma	2004	EM	cm	300	NA	5	yes	6-axis levitated stage
Burleigh FR-3000	-	NA	cm	25000	NA	0.1	NA	Commercial 6-axis inchworm
PI F-206	-	Piezo	cm	10000	100	30	NA	Commercial 6-axis hexapod

## 1.2.2 Meso-scale Nanopositioners

State-of-the-art micro-fabricated micro- and meso-scale nanopositioners illustrate the improved performance of meso-scale systems relative to macro-scale systems when tens to hundreds of micrometers of motion are acceptable. Table 1.5 compares the performance of state-of-the-art, small-scale nanopositioners with two or more axes of motion. The review of these devices is limited to systems with two or more axes of motion because most practical systems operate in at least two axes. Meso-scale nanopositioners most often use flexure-guided stages that are driven by electrostatic or electromagnetic actuation. Classic comb-drive and parallel-plate electrostatically-actuated systems have been used for data storage [28], scanning-probe microscopy [29], and cellular manipulation [4]. Although these systems exhibit some excellent performance characteristics, they are limited to in-plane motion due to the geometry of the parts within the actuators. In other work, a dipole surface-driven x-y stage demonstrated improved performance for in-plane actuation at the expense of elaborate microfabrication [30, 31]. Fan et al [32] have used comb-drives to drive a three-axis optical alignment system in- and out-of-the plane, with the use of low-precision elements including sliding hinges and scratch-drive actuation. Microfabricated hinges limit repeatability and resolution due to the free clearance fit at the bearing surfaces that is required for motion. Surface stiction and non-repeatable friction-

related effects limit the performance of scratch-drives to micron-level repeatability when operating in open-loop.

Magnet-coil systems are an alternative technology and have been developed for data storage applications that require 50-100  $\mu\text{m}$  linear motion in the x- and y-directions [1,3, 33]. These systems suffer from limited bandwidth, on the order of 100s of Hz, and complex fabrication and assembly. Rothuizen et al. [1] used copper flexure springs with low stiffness characteristics in order to achieve large displacements in five axes. Eight coils were packed onto a central stage of large mass, and this resulted in a low natural frequency [1, 3]. Stage-mounted coils also resulted in detrimental heating of the stage and the attached polymer sample. More recent work has yielded a simpler two-axis design for a x-y positioner that is driven by hand-wound coils. This system exhibited improved force output and slightly higher bandwidth at the expense of costly and tedious manual winding of the coil and assembly of the magnet and coil [6, 34]. Microfabricated coil-magnet actuators provide an attractive alternative to electrostatic actuation because of their capacity to operate in multiple axes and exert moderate force output on the order of 10 mN. The resonant frequency and range-of-motion of systems driven by magnet-coils may be increased by improving actuator force density and optimizing the flexure bearing.

Recently, a thermally-driven six-axis micro-scale nanopositioner, called the  $\mu\text{HexFlex}$ , was developed for micro-optical and fiber optic alignment [35]. The device demonstrated 10nm open loop resolution and 10 $\mu\text{m}$  stroke via the use of several two-axis thermal actuators. These actuators exhibit a bandwidth of approximately 100 Hz. The small size,  $\sim 1 \text{ mm}^2$  footprint, leads to a fragile device upon which it is difficult to mount samples. In this regard, most practical applications are limited to active micro-optics positioning, where the stage serves as a mirrored surface.

**Table 1.5. Comparison of state-of-the-art small-scale multi-axis nanopositioners.**

Author	Year	Natural Frequency (Hz)	Stroke (um)	Axes of Motion	Precision (nm)	Size (mm)	Actuation	Application
Rothuizen	2000	61	200	5	NA	30	Electromagnetic	data storage
Rothuizen	2002	80	160	5	NA	15	Electromagnetic	data storage
Lee	2000	240	160	2	NA	15	Electrostatic	NA
Lantz	2007	168	120	2	NA	17	Electromagnetic	data storage
Pantazi	2004	124	120	2	4 (CL)	17	Electromagnetic	data storage
Fan	1997	NA	120	3	NA	3	Electrostatic	optics alignment
Hoehn	2003	131	100	2	4	3	Electrostatic	NA
Choi	2001	325	42	2	NA	13	Electromagnetic	data storage
Kim	2003	164	36	2	NA	17	Electrostatic	data storage
Wang	1995	NA	12	2	NA	2	Electrostatic	AFM
Chen	2006	150	10	6	10	3	Thermal	fiber alignment
Sun	2002	750	4	2	10 (CL)	3.2	Electrostatic	cellular manipulation
<b>Golda</b>	<b>2008</b>	<b>1000</b>	<b>10</b>	<b>6</b>	<b>10</b>	<b>13</b>	<b>Electromagnetic</b>	<b>Nanomanufacturing</b>

Table 1.5 provides a summary comparison of multi-axis meso-scale nanopositioners that are guided by flexure bearings. The stiffness of a flexure bearing sets upper limits on the bearings resonant frequency and it leads to situations wherein the stroke is fundamentally due to force-limited actuation. For a given actuator force output and a given moving mass, a stiffer flexure would increase resonance frequency, but this would occur at the expense of stroke. As range and bandwidth are primary requirements, actuator force density and system mass are recognized as important design considerations.

Normalization of the device size and stiffness better captures the impact of actuation force density and also provides a more fair comparison across actuation domains. Figure 1.5 shows a simplified, first-order lumped-parameter model for static displacement and dynamic response. The model consists of a flexure bearing in the form of a beam, actuator mass,  $m$ , and actuator force,  $F$ . This model may be used to investigate the trends between performance characteristics and design variables.

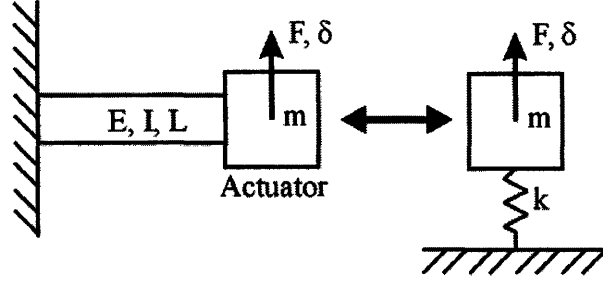


Figure 1.5. First-order flexure-guided nanopositioner performance model.

The static displacement and resonant frequency of the system are given by the following equations:

$$F = k\delta \quad (1.1)$$

$$f = \frac{1}{2\pi} \sqrt{\frac{k}{m}}. \quad (1.2)$$

Equations (1.1) and (1.2) may be combined to eliminate the flexure stiffness,  $k$ , and thereby arrive at a relation between the resonant frequency and static displacement:

$$\delta = \frac{1}{(2\pi)^2} \frac{F}{m} \frac{1}{f^2}. \quad (1.3)$$

The displacement is normalized with respect to the characteristic length of the device,  $L_c$

$$\frac{\delta}{L_c} = \frac{1}{(2\pi)^2} \frac{F}{mL_c} \frac{1}{f^2}. \quad (1.4)$$

The normalized displacement is related to the resonant frequency of the device through the force density constant  $F/mL_c$ . It may be shown that this metric affects several nanopositioner performance characteristics. The normalized displacement and resonant frequency of the systems from Table 1.5 are plotted on a log-log scale in Figure 1.6. Contours of constant  $F/mL_c$  are plotted for reference. Devices with constant force output and variable stiffness are located along these contours. In the figure, performance improvements correlate to moving upwards and to the right in the plot.



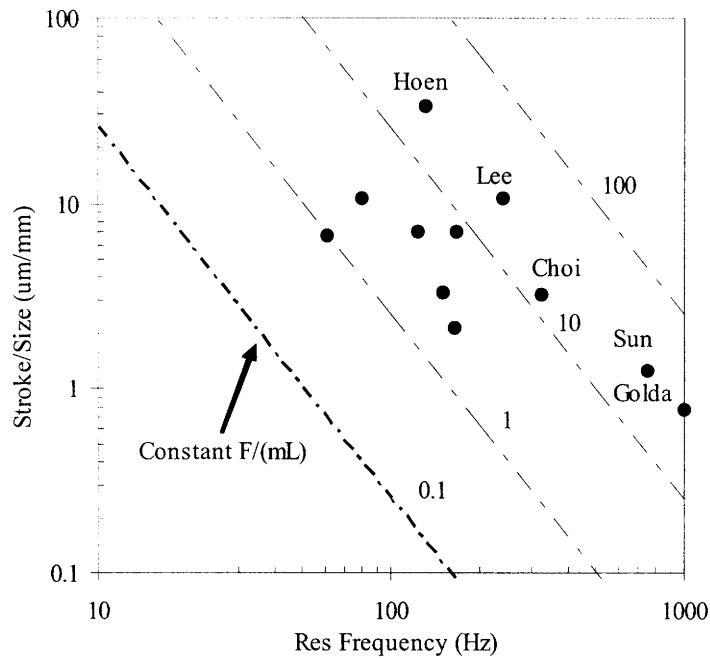


**Figure 1.6. Stroke vs. first resonant frequency for state-of-the art meso-scale nanopositioners.**

Table 1.5 and Figure 1.6, may be used to deduce how far the systems are from satisfying the stroke and bandwidth requirements that are listed in Table 1.2. In review, these functional requirements include a resonant frequency of 1 kHz, 10  $\mu\text{m}$  stroke in each axis, and approximately 10 nm repeatability. The table and figure indicate that it may be possible to use electromagnetic actuation in a device with high resonant frequency at the expense of stroke.

This may also be viewed as a motivation for improving the performance quantities so as to reduce the tradeoff. This need was a motivating factor for design decisions that were made in the process of optimizing microfabricated electromagnetic (EM) actuators and supporting flexure bearings. As will be discussed in section 1.2.3.B, this combination will enable a system that meets or exceeds the performance envelope of state-of-the-art HSM nanopositioners. The flexure and actuator combination will also enable six-axis motion with improved precision (10 nm). Novel micro-actuation schemes, within the constraints of microfabrication processes, must be created in order to realize the improvements in performance that have been laid out in the preceding sections. The following section provides a review of micro-actuator technology with emphasis on performance capability and fabrication complexity

### **1.2.3 Microactuators**

A review of the literature indicates that the present micro-actuator technology does not meet the target performance criteria that this work has set for a HSM nanopositioner. Many types of actuators have been investigated for micro-electromechanical systems (MEMS) and meso-scale electromechanical systems, including electrostatic, electromagnetic, thermal, piezoelectric, shape-memory alloy, and electro-active polymer. Shape-memory and polymeric actuators are well-known to be unsuitable for precision positioning due to poor repeatability and low bandwidths, and so they are not included in this review.

The relative merits of the other types of actuator species will be discussed in relation to the performance criteria in Table 1.2. Emphasis is placed upon electrostatic and electromagnetic actuation as these species are most often employed in the types of nanopositioners under consideration. The following is a concise review. For additional information, reviews of macro-scale actuator technology may be found in Huber et al. [36], while reviews of several micro-actuators may be found in Zupan et al. [37] and Bell et al. [38].

#### **1.2.3.A Electrostatic Microactuators**

The seminal paper by Tang, et al [39], led to the development of the MEMS electrostatic comb-drive actuator. Several variations of the classic comb-drive actuators have been developed for applications that range from positioning mirrors to data storage [28, 40-47]. For example, a comb drive X-Y stage that was equipped with a probe tip was integrated into an atomic force microscopy (AFM) system. The device exhibited a first resonant mode of 16 kHz but limited motion of only 3  $\mu\text{m}$  [29]. A variety of parallel-plate configurations have been designed for optical systems, positioning of memory read heads, micro-pumps and micro-valves, hard drive heads, micro-relays, and inchworm-type motors [48-61]. Comb drive-based and parallel plate-based devices are generally one- or two degree-of-freedom systems, and the magnitude of their flexure stiffness limits either stroke or bandwidth.

Major problems with electrostatic devices include gap-field breakdown, gap contamination, and the need to use command voltages that are on the order of tens- to hundreds-of-Volts. Comb drives have the advantage of simple fabrication processes that require only 1-2 masks and constant actuation force. They are commonly used for in-plane translation [28, 29, 62], in-plane rotation [41,43], or for pure out-of-plane motion [47, 63, 64]. Comb-drives cannot

be used in a practical way to control in- and out-of-plane motion over useful distances. This limits their utility in applications that require more than two degrees-of-freedom. Comb drives are also problematic because useful force output requires micron-level gaps between the comb fingers. This precludes their use in systems where the combs must move in directions other than along the long axis of the combs. A fitting example is a six-axis positioning system. It may be possible to integrate comb drives into a six-axis system if the displacements are limited to a fraction of the comb spacing, that is less than 500nm, but this is not useful for most applications including the motivating applications that were discussed in previous sections.

Parallel-plate actuators are used for either planar motion [4, 49, 54, 55, 65], or out-of-plane motion [52, 53, 59], but not both. Several systems use parallel plates for single axis rotation [51] or two-axis tip-tilt [60]. Parallel plate devices also suffer from gap-limited range of motion that is on the order of a few microns at most. These devices can operate with several kHz bandwidth due to the high force output that correlates with small gaps. Recently, electrostatic zipping actuators have improved the force and range characteristics of electrostatic actuators. These actuators have been used effectively in switches [66-68]. Although they have excellent force-displacement characteristics and a range of tens of microns, zipping actuators are limited to motion that is purely normal or parallel to the wafer plane. Other electrostatic configurations have been developed to enable longer travel at lower Voltage supply levels. Hoen, et. al. [30, 31], have developed a unique X-Y electrostatic dipole surface drive positioner that is capable of 50 micron travel and 4nm open-loop repeatability with mechanical resonant frequencies near 130 Hz . The system only delivers in-plane motion, and it suffers from a relatively complicated fabrication process that requires a multitude of masks and post-processing assembly of multiple chips.

Other electrostatic configurations have been developed to overcome gap- and comb-limited displacements. Inchworm-type electrostatic stepper actuators enable travel of approximately 100  $\mu\text{m}$  in one axis for optics positioning [65, 69]. Some problems for precision applications include wear and repeatability. Scratch drives have been used to achieve three-axis motion at the expense of complex fabrication and device wear [32]. The device uses hinges which necessitates an inherent clearance in each joint. The clearance and sliding contact limits motion resolution and repeatability to a few microns. These designs are suitable for applications such as mirror positioning that require long travel and coarse repeatability.

Table 1.6 presents a qualitative comparison of the electrostatic actuator species. Actuation axes refer to the maximum number of axes through which the actuator could operate. Although comb drive and dipole drive may operate in two axes, none of the actuators can meet the functional requirements that are listed in Table 1.2.

**Table 1.6. Electrostatic actuator species performance comparison.**

Species	Speed	Force	Range	Actuation Axes	Fabrication
Parallel Plate	Fast	Moderate	Low	1	Easy
Comb Drive	Fast	Moderate	Moderate	2	Easy
Zippering	Fast	Moderate	High	1	Moderate
Dipole Drive	Fast	Moderate	High	2	Difficult

### 1.2.3.B Overview of Electromagnetic Microactuators

Electromagnetic micro-actuation was first investigated in the early 1990s. The earliest works on integrated electromagnetic micro-actuation resulted in micro-coils that interacted with permanent magnets that were bonded to silicon flexures [70, 71]. Previous work has shown that electromagnetic scaling laws are favorable for micro-coils with respect to attainable current density and long working distances [72]. Heat transfer, as normalized by characteristic device size, is improved as coil size is reduced to the micro-scale. The rate of heat transfer away from the coils depends on the ratio of surface area to volume, and this increases as devices are scaled down. As a result, micro-coils have achieved current densities in excess of  $1000 \text{ A/mm}^2$  ( $10^9 \text{ A/m}^2$ ) as compared to  $5 - 10 \text{ A/mm}^2$  at the macro scale.

Electromagnetic actuators that use permeable materials may store more energy per unit volume than electrostatic actuators for gap distances that are greater than approximately  $2 \text{ }\mu\text{m}$  [73]. For example, at a gap distance of  $10 \text{ }\mu\text{m}$ , magnetic micro-actuators can store approximately 100 more energy than electrostatic actuators. As a result, electromagnetic micro-actuators show better promise for high-force, high-stroke applications at the expense of relatively large size (mm) and the requirement of external field sources, such as permanent or electromagnets. These actuators are suitable for larger, mm-scale systems that require several microns of travel. They are easily designed to exhibit a high degree of linearity in current response and have favorable dynamic and electromagnetic scaling characteristics. For these reasons, electromagnetic (EM) actuators have been used in several high-performance MEMS devices. An overview of these systems may be found in [72, 73].

An advantage of electromagnetic systems is that they require low command voltages. This enables portability and compatibility with CMOS electronics and this makes electromagnetic systems attractive for applications such as portable data storage [1, 3, 5, 11-13, 33, 34]. Other applications include high-bandwidth AFM heads [74], fluid pumps [75], mirrors for optical scanning and switching [76-91], and micro-relays and micro-switches [92-100]. These devices leverage the capability of EM actuators to produce fine resolution displacements on the order of nanometers with small response times on the order of milliseconds. Recently, systems that consist of micro-coils and magnetic materials have been used in rotating micro-machinery for power generation [101-107]. These examples illustrate the potential of EM-based devices in demanding applications at the meso-scale. They also illustrate how micro-actuator design perspective differs from a macro-scale design perspective. The assembly and fabrication methods that are used to realize macro-scale EM actuators cannot be used in general to build micro- and meso-scale actuators. In addition, lithographically-fabricated micro-coil structures are limited to stacked 2-D planar geometry which limits the use of complex 3D actuator geometries as are used at the macro-scale. In addition, the micro-fabrication of permanent magnet structures is a high-risk area of research [73, 108-114]. These fabrication limitations place constraints on the geometric designs that are available for micro-coil actuators. Consequently, limited work has been done on the design theory for micro-fabricated coil-driven actuators.

Table 1.7 presents an applications summary of the three main electromagnetic actuator species.

**Table 1.7. Summary of electromagnetic actuator applications.**

Actuation Species	Application	Author / Year
Variable Reluctance	Micro-relays and switches	Rogge 1995; Ren 1997; Fullin 1998; Taylor 1998; Tilmans 1999; Wright 1997, 1999; Sadler 2000; Gray 2005
	Optical scanning	Yalcinkaya 2007
	Optical switching	Judy 1997; Ko 2002; Horsley 2005; Huang 2006;
	Linear Motors	Feldmann 2007
	Hearing Aid	Rehder 2002
Moving Magnet	Power Generation	Koser 2001, 2006; Arnold 2006; Cros 2006
	Portable Data Storage	Lantz 2007
	Optical scanning	Cho 2002, 2003;
	Linear Motors	Fohse 2003; Shutov 2005
	Power Generation	Das 2005, 2006; Achotte 2006; Arnold 2006
Moving Coil	Other	Wagner 1991; Kruusing 2002
	Portable Data Storage	Lutwyche 1998; Choi 2001; Rothuizen 2000, 2002
	Micro-pumps and valves	Kim 2005
	AFM scanning	Lee 2000
	Optical scanning	Ferreira 1999; Asada 2000; Miyajima 2001, 2003; Ahn 2004; Bernstein 2004; Oliveira 2006; Yalcinkaya 2006;
	Optical switching	Han 2002, 2004; Taylor 2004

### 1.2.3.C Variable Reluctance Microactuators

Variable reluctance devices exhibit high force output but they only operate in one axis. Microsystems that use permeable materials in magnetic circuits and hand-wound inductor coils have achieved actuator force outputs of hundreds of milli-Newtons [115]. Despite fabrication difficulties, researchers have developed microfabricated hard- and soft magnetic materials that are integrated into variable reluctance actuators in relays [92, 93, 95, 96, 98, 100, 116, 117], scanning mirrors [118], hearing aids [119], and linear micro-motors [120, 121]. A notable and relevant advance may be found in a long-travel linear motor that consists of integrated permeable materials that were placed upon an assembled stator and rotor. This device demonstrated travel of greater than 500  $\mu\text{m}$  [122]. The disadvantages of variable reluctance devices with soft magnetic materials include low saturation flux densities, fabrication complexity, and actuation that is typically limited to a single axis.

### 1.2.3.D Moving-Magnet Microactuators

Meso-scale permanent magnets that require directed assembly are more commonly used in MEMS than are microfabricated permanent magnets. Meso-scale permanent magnets provide

high flux density at the expense of relatively large size. Moving magnet actuators that use fixed coils exhibit single- to multi-axis capability, and they have been used for data storage and optical scanning [34, 70, 71, 118]. In these devices, the magnets are either fabricated or bonded onto flexure bearings. Fixing the coils results in advantageous thermal dissipation and therefore higher operating currents and forces. In a fixed coil configuration, permanent magnetic materials must be integrated onto the traveler. This increases the degree of complexity that is required to micro-fabricate the actuator. In addition, the integration of meso-scale permanent magnets also introduces large suspended masses and thereby leads to lower resonant frequencies.

#### **1.2.3.E Moving-Coil Microactuators**

Moving coil systems are simpler to assemble than moving magnet systems, and they can exert moderate force levels. Typical systems consist of a planar coil that is suspended on a flexure bearing within close proximity to a permanent magnet field source. The two major drawbacks of this configuration include: 1) fabrication integration and 2) power dissipation from the moving coils through the flexures. The second drawback must be addressed in order to design motion systems that exhibit sufficient precision. Moving coil actuators that use fixed external magnets have been used for many applications that range from data storage to fluid pumps [1, 33, 75, 84]. Prior work has enabled a) flexure-guided electromagnetic moving-coil systems to operate in 2-5 axes for data storage [1, 3, 33], b) others to achieve high bandwidths (~1 kHz, primarily as tilting mirrors) [77, 78, 82-84, 90, 123], and c) others to achieve large deflections in one axes [71, 75, 80]. Unfortunately, all of the preceding may not be achieved simultaneously. Large strokes of 50+  $\mu\text{m}$  in multiple axes were obtained at the cost of lower bandwidths (10-100s of Hz) and large sizes. Magnet-coil actuators may be combined with rolling or sliding element bearings to create linear motors. The actuators exhibit a range of motion in one axis that is limited only by the size of the machine. Large stroke comes at the expense of size and complex assembly [124, 125].

#### **1.2.3.F Electromagnetic Microactuator Summary**

Table 1.8 summarizes the relative merits of the electromagnetic actuator species that were discussed in the preceding sections. The table is useful for qualitative comparison and understanding the tradeoffs that may be required for each species. For example, the data in the table indicates that moving coil actuators may be suitable for high-bandwidth, moderate force,

six-axis nan positioning systems. The tradeoffs are the heat dissipation in the coils that limits sustainable current and therefore force, and potential fabrication difficulties. Moving magnet and variable reluctance devices may sustain greater current and thereby output higher force than moving coil systems. Moving coil systems exhibit a better combination of ease of fabrication and assembly which are important in realizing a practical device.

**Table 1.8. Electromagnetic actuator species performance comparison.**

Species	Speed	Force	Multi-axis	Heat dissipation	Fabrication	Assembly
Variable Reluctance	Fast	High	No	Low	Difficult	NA
Moving Magnet	Moderate	High	Yes	Low	Moderate	Difficult
Moving Coil	Fast	Moderate	Yes	Moderate	Moderate	Moderate

### **1.2.3.G Thermal Microactuators**

Thermal actuators make use of Joule heating and thermal expansion of materials to generate displacements. Although they experience small strains, the force output may be high in silicon devices. Resolution on the order of tens of nanometers is possible with fine current control. Several configurations have been implemented to amplify the strain, including chevron beams, differentially heated beams, and bimorph beams [126-130]. Mirror positioning systems, linear drive systems, rotary drive systems, and micro-relays [127, 128, 131] have been made using these types of systems. Nested bimorph hinges have enabled some devices to achieve large displacement over hundreds of microns and optical scan angles that exceed 30° [132]. They have been used to drive a six-axis nan positioner for fiber alignment [35] over a 10 μm range and with actuator-limited bandwidth of 100 Hz. Compared to electromagnetic and electrostatic devices, thermal actuator bandwidth is limited by thermal heating and cooling time constants. Thermal actuators continually dissipate heat and operate at high temperatures, on the order of 600°C, that may be too high for temperature-sensitive nan positioning applications such as biological manipulation or probe-based data storage.

### **1.2.3.H Piezoelectric Microactuators**

Piezoelectric thin films have been used in MEMS devices as actuators and sensors. Recent micro-fabrication research shows promise for producing reliable films [133], however fabrication complexity and low reproducibility remain major problems. The most common type



of actuator is the bimorph cantilever beam, which has been used in several applications [134-137]. Typical piezoelectric film strain is less than 0.1%, and so it is necessary to amplify the resulting displacements in order to achieve useful motions. The structure of bimorph beams amplifies the displacements that are caused by the piezoelectric film strain and thereby produces useful displacements of several microns to tens of microns. Several other devices have been developed in addition to the bimorph beam, including tunable optical gratings, linear drive systems, rotary motors, and 2D mirror scanners [138-143]. Piezoelectric devices generally exhibit high bandwidths on the order of 10s of kHz and small strokes on the order of microns or less. The inherent hysteresis and steady-state drift seen in piezoelectric actuators are problems that affect precision nanopositioning applications, but they may be addressed via the use of closed-loop feedback control. Given the preceding issues, piezoelectric actuators are not yet suitable for multi-axis nanopositioners that must operate in open-loop.

### 1.2.3.I Microactuator Summary

The four most often used micro-actuator types include electrostatic, electromagnetic, thermal, and piezoelectric. Table 1.9 qualitatively compares the actuator classes with respect to nanopositioning metrics.

**Table 1.9. Summary comparison of micro-actuator types.**

Species	Speed	Force	Stroke	Heat Dissipation	Fabrication
Electrostatic	Fast	Low	Low	Low	Easy
Thermal	Slow	High	Moderate	High	Easy
Piezoelectric	Fast	High	Low	Low	Difficult
Electromagnetic	Fast	Moderate	Moderate	Moderate	Difficult

Piezoelectric actuators suffer from difficult and unreliable film fabrication, hysteresis and steady state drift, which preclude them from use in precision positioning applications. Thermal actuators operate with suitable precision and high force output. Their high operating temperatures, heat dissipation, and slow thermal time constants limit their utility in high-bandwidth nanopositioning, particularly in temperature sensitive applications. Electrostatic actuators dissipate negligible heat, and have found use in a variety of one- to two-axis precision positioning applications. Electrostatic actuation is limited to two Cartesian axes, which is unsuitable for a six-axis nanopositioner. Electromagnetic actuators can exert moderate forces

over long distances, but they dissipate more heat and require more complex fabrication when compared to electrostatic systems. In summary, electromagnetic moving-coil actuators are most suitable for larger millimeter-scale systems that require moderate forces, linear responses in open loop, and strokes of several microns in multiple axes.

Several challenges must be addressed when using moving-coil actuators for high-bandwidth nanopositioners, including: (1) the minimization of parasitic motions; (2) improvements of actuator force density; (3) power dissipation through the flexure bearing elements; and (4) microfabrication and magnet assembly. The problem of generating high-stroke, high-speed, parasitic-free motion in multiple axes while managing heat dissipation has yet to be solved. In addition, little work has been done on the performance modeling of linear micro-coil-magnet systems [124, 144-146].

#### **1.2.4 Flexure Concept Background**

Compliant flexure bearings may be coupled with electromagnetic micro-actuators to precisely guide nanopositioner motion. Flexures act as constraining elements that guide and stabilize motion in certain directions and as spring-like transmissions that tune actuator motion in other directions. Flexures possess several advantages: 1) stable, predictable, and repeatable motion in open-loop operation; 2) motion amplification; 3) mechanical filtering; 4) ease of micro-fabrication; and 5) ease of integration with actuators. The addition of flexures as machine elements introduces limitations on bandwidth and maximum stroke for a given actuator force output. As a result, flexure bearings must be carefully designed for each actuation system in order to optimize this tradeoff. Several planar compliant flexure mechanisms have been used for Cartesian motion ( $x$ - $y$ ) [147], planar ( $x$ - $y$ - $\theta_z$ ) [26, 148], or spherical ( $\theta_x$ - $\theta_y$ ) [149]. Three-dimensional assemblies of planar mechanisms and conventional joints have enabled devices to operate in six axes ( $x$ - $y$ - $z$ - $\theta_z$ - $\theta_x$ - $\theta_y$ ) [150, 151]. Recent work has led to the development of a six-axis planar compliant flexure bearing, called the HexFlex, for macro-scale nanopositioners [10]. The planar architecture was then adapted for a six-axis micro-scale nanopositioner that is driven by thermal actuators [35]. Planar flexure bearings have also been used for three-axis motion at the micro-scale [152]. Some advantages of the planar flexure element include low-cost, thermo-centric design, and compatibility with two-dimensional fabrication techniques such as

lithography. The type of flexure bearing could be easily integrated into a HSM nanopositioner and yield useful results if it is matched with a suitable actuator.

### **1.2.5 Summary**

Nanopositioners are used to precisely position and orient samples that range from wafers to scanning probe tips. Macro-scale nanopositioners can operate over long distances with high force output in multiple axes. Device scaling yields benefits for meso-scale nanopositioners in terms of bandwidth, thermal sensitivity, portability, and cost. A review of the literature has indicated that current meso-scale nanopositioners do not satisfy the requirements of future applications. Typical meso-scale nanopositioners are guided by flexure bearings, but the limitations of micro-actuators place limits upon the performance of these devices. A review of state-of-the-art micro-actuators yields the observation that moving-coil magnetic actuators are most suitable for high-speed six-axis nanopositioning when coupled with a suitable flexure motion bearing.

## **1.3 Research Challenges**

Several challenges must be addressed to enable the design and fabrication of high-bandwidth, high-stroke, precision electromagnetic nanopositioner systems that operate in multiple axes:

1. Optimal concept and layout – It is necessary to generate integrated actuator and bearing combinations that enable 6-axis motion. The resulting geometries must be compatible with micro-fabrication techniques.

2. Multi-axes actuation – It is necessary to design electromagnetic micro-actuator arrangements that are capable of generating in- and out-of-plane forces. This enables the maximum decoupling of actuator inputs and motion kinematics in six-axis machines [10]. Force density in electromagnetic micro-actuators is limited by magnetic flux density and coil current density. Improvements in force density require the optimization of magnetic flux density and coil current. The latter is limited by heat transfer effects [72].

3. Flexure bearing design – Compliant flexure bearings provide open-loop stability (no need for feedback), mechanical filtering or amplification, pathways for heat dissipation, and precision motion guidance. Mechanical resonances introduced by the use of flexure bearings

(kHz) are generally orders of magnitude lower in frequency than the electrical resonances of EM microactuators (MHz). As a result, flexures must be designed to permit sufficiently high bandwidth and stroke for a given actuator force density. In addition, flexure bearings that are used with moving-coil actuators must be able to dissipate heat at a rate that minimizes thermal errors to an acceptable level.

4. Open-loop precision – Manufacturing tolerances, thermal transients, parasitic forces, and noise in input commands will affect the precision of a nanopositioner in open-loop operation. These disturbances should be minimized through proper design concepts, analytic techniques, calibration, and compensation techniques. Parasitic forces that arise in linear EM actuators should be minimized in order to operate with sufficient open-loop precision.

5. Micro-fabrication and constraints. Micro-fabrication is a layered 2D process, and places geometric constraints upon device design decisions. As a result, the design space for micro-scale EM actuators is limited and only the simplest of micro-scale EM actuators have been realized. Few devices have been fabricated that are capable of in- and out-of-plane and in-plane motion [1, 3, 146]. Although planar coils that yield pure out-of-plane motion are easily fabricated [75, 84, 123], the fabrication of coils for pure in-plane motion has yet to be developed. In addition, coils should be fabricated to minimize heat generation and to maximize heat transfer from the structure. This requires large cross-section coil windings and materials that exhibit high thermal conductivity.

## **1.4 Contributions**

The original contributions of this work include the following:

(1) System-level concept for a microfabricated, high-speed, six-axis, electromagnetically-driven meso-scale nanopositioner that uses small-scale permanent magnets, and a stacked coil architecture to produce designs that minimize actuator parasitic errors

(2) A moving-coil actuator architecture that combines two stacked, independently controlled planar coils that are capable of simultaneously exerting pure in- and out-of-plane forces when combined with a set of three alternating pole permanent magnets

(3) First order design rules that link actuator design parameters and performance characteristics at a level which is appropriate for conceptual machine design

(4) A three-dimensional Fourier Transform solution to the magnetic fields that are due to non-periodic planar permanent magnet arrays. The solution enables efficient computation of the fields along planes parallel to the arrays and thereby enables fast computation of planar-coil actuator forces

(5) Parametric, physics-based numerical models which incorporate the characteristics of the flexure bearing, moving-coil actuator, and the magnetic field into an accurate performance model that may be used for multi-parameter optimization (e.g. efficiency, energy density, force, etc...)

(6) A geometry-based design optimization method for minimizing the magnitude of parasitic forces and moments on the planar actuator coils for a given level of desired force output

(7) A flexure design method that may be used for minimizing thermal parasitic errors that are due to heat dissipation from the moving-coil actuators

(8) A micro-fabrication that process which produces a six-axis nanopositioner which utilizes moving-coil actuators and flexure bearings that are integrated into the device structure.

(9) Proof of concept via a prototype of a six-axis nanopositioner that has a measured work volume of  $10 \times 10 \times 2$  micron<sup>3</sup>, nm-level resolution, and a first resonant mode of 900 Hz

The contributions of this thesis will enable the deterministic design of micro-actuators for nanopositioning systems that are capable of multi-axis, sub-nanometer motion at hundreds to thousands of Hz. The nanopositioner is envisioned to enable bench-top high-bandwidth probe-based nanomanufacturing systems. For example a nano-electrical discharge machining system would be able to make use of a low-cost, six-axis nanopositioner. Other applications that may benefit from this technology include high-bandwidth, low-cost video-rate scanning for scanning-probe microscopes, and portable scanning-probe based data storage.

## **1.5 Thesis Summary**

Chapter 2 presents the conceptual design of a two-axis magnetic moving-coil actuator, a six-axis nanopositioner, and complimentary first order analysis and design rules. A bench-level six-axis nanopositioner is used to validate the actuation concept.

Chapter 3 covers physics-based modeling of the nanopositioner performance in the electromagnetic, mechanical, electrothermal, and thermomechanical domains. A Fourier Transform-based solution to permanent magnet field characteristics in 3D is developed and compared to measurements from an experiment. This field solution is then used to model the forces on the coil actuator. A mechanical model of the flexure elements is developed for use in predicting static displacement and resonant frequency of the system. This model is then coupled with an electrothermal model of the coil and flexure to predict static thermal error.

Chapter 4 covers detailed design methods for the actuator coil, flexure elements, and the entire six-axis system. The methods enable the design of the system to meet a given set of functional requirements. Actuator force optimization and parasitic error minimization are presented. A new flexure bearing topology is generated with the aim of minimizing actuator-induced thermal errors.

Chapter 5 provides a detailed discussion of the microfabrication process development including coil geometry limitations and dielectric design considerations. The required lithography mask patterns are provided.

Chapter 6 includes experimental measurements of the meso-scale system performance. Model predictions are compared with the measured values from the experiment.

Chapter 7 summarizes the work, draws conclusions, and presents possibilities for future work.

## DESIGN CONCEPT

---

This chapter introduces the nanopositioner and actuator design concepts. The flexure and actuator concepts are evaluated and then chosen based upon the performance metrics that were developed in Chapter 1. The actuator design concept is discussed in detail, and first order design equations are developed to help size the actuator and estimate parameter sensitivity for the design metrics – static displacement, 1<sup>st</sup> mechanical resonant frequency, and thermal error. Scaling laws are derived from the first order design equations. A centimeter-scale bench-level prototype is also developed as part of an experiment that is used to assess the six-axis flexure and actuation concept. Open-loop positioning results in the  $x$ -,  $y$ -, and  $z$ - directions demonstrate the design concept.

### 2.1 Functional Requirements

The nanopositioner functional requirements that were developed in Chapter 1 were based on target applications that include nanomanufacturing, probe-based data storage, and probe-based microscopy. The functional requirements:

- 1) Linear range of motion of 10  $\mu\text{m}$  in the  $x$ -,  $y$ -, and  $z$ -directions;
- 2) Angular range of motion of approximately  $3^\circ$  about each axis;
- 3) Absolute precision in open-loop of less than 10 nm;
- 4) First resonance mode near 1 kHz.

A second order mass-spring-damper system with a 1 kHz first mode resonance would have a -3dB bandwidth greater than 1 kHz and enable high-bandwidth operation. Table 2.1

summarizes the functional requirements for the nanopositioner. The following section discusses the constraints on the design.

**Table 2.1. Nanopositioner functional requirements**

Functional Requirement	Value	Units
Linear Stage Translation		
X	10	$\mu\text{m}$
Y	10	$\mu\text{m}$
Z	10	$\mu\text{m}$
Angular Stage Rotation		
X	3	deg
Y	3	deg
Z	3	deg
1st Mode Resonant Frequency	1000	Hz
Absolute Precision	10	nm

## 2.2 Constraints

The nanopositioner system design is subject to design constraints as discussed in Chapter 1. The system should be scalable to the millimeter and micrometer-level in order to leverage the force, mass, and thermal benefits that correlate with scaling. Maximum linear dimensions should be less than 20 mm for arrayed operation and portability. The system should be designed for lithographic microfabrication in order to manufacture a nanopositioner at the meso-scale with components that range from micrometers to millimeters. This constraint limits the design to a stacked 2-D planar geometry. In addition, the maximum operating temperature at the sample stage should be no higher than 50°C in order to be compatible with sensitive samples, such as those used in probe-based data storage [146]. The system must operate in open-loop, as integrated six-axis sensing has yet to be developed for multi-axis meso-scale nanopositioners. In addition, the cost of the nanopositioner's mechanical sub-system should be sufficiently low, several hundred dollars, to enable its use in large arrays and in portable devices. Table 2.2 summarizes the nanopositioner system design constraints.



**Table 2.2. Nanopositioner constraints**

Constraints	Value	Units
2-D Planar Geometry	-	-
Open-loop Operation		
Maximum Dimension	20	mm
Max Operating Temperature	50	°C
Cost (Mechanical system)	20	\$

## 2.3 Flexure Concept

Flexure bearings and flexure mechanisms enable precise motion guidance over a small range-of-motion. The yield stress threshold limits the usable range-of-motion to a few percent of the characteristic flexure length. A flexure-guided nanopositioner that operates over tens-of-microns range should then have flexure bearings on the order of hundreds of microns to a few millimeters. Operation within the linear elastic bending regime enables deterministic motion guidance that is free of the contact and sliding errors that are inherent to prismatic and rotational kinematic joints. In addition, mono-crystalline flexure materials, such as silicon, enable nanometer-level repeatability as a consequence of their low defect densities that mitigate microslip, and plastic deformations via high-energy dislocation motion at low stress levels.

A microfabricated, planar silicon flexure mechanism will be shown to satisfy the size and microfabrication constraints of the proposed nanopositioner system, and this enables the device scaling which will be discussed later. The flexure mechanism acts as a linear spring over small displacements and results in stable positioning when combined with a suitable actuator. This eliminates the need for feedback stabilization. In addition, the transmission ratio of flexure mechanisms may be designed to enable motion de-amplification for high resolution application. A flexure-guided nanopositioner acts as a mass-spring system and stores potential energy, and therefore the mechanical resonance of the nanopositioner will limit its bandwidth. The stiffness of the springs also limits the range-of-motion when the flexure is combined with a force-limited actuator. An important practical concern is that the stiffness of a flexure mechanism is sensitive to fabrication errors, which may lead to significant errors in the range-of-motion and bandwidth.

The six-axis flexure concept is adapted from the HexFlex planar compliant mechanism that was developed for use in conventional nanopositioners [10]. Figure 2.1 shows a schematic

representation of the planar flexure concept. The flexure consists of a three-way symmetric arrangement of actuator paddles around a central sample stage and a set of six flexure bearings that link the actuator paddles to ground. The flexure bearings may be considered as three pairs of symmetric sets of beams. The double-bent-beam flexure design that is shown in the figure will be discussed later. At least six actuator inputs are required to impart force on the flexure mechanism in order to achieve six-axis motion control. The figure also illustrates six generalized, independent actuator forces that are applied to the compliant flexure mechanism at the actuator paddles. The actuator forces must act in- and out-of-plane for in-plane and out-of-plane stage motions to manifest as a result of beam deformation. Combinations of vertical, or  $z$ -directed forces, and tangential in-plane forces result in linear and angular stage motions that are in- and/or out-of-plane. The geometry decouples the in-plane and out-of-plane forces and reduces the effect of parasitic actuator forces on the stage.

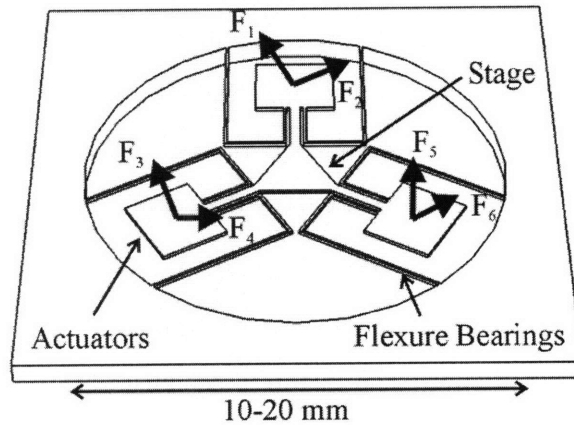


Figure 2.1. Six-axis meso-scale nanopositioner concept

The actuator input is related to stage motions through the stiffness matrix,  $K$ , of the flexure bearing. The assumptions for this analysis are as follows: 1) linear beam bending, 2) small displacements, and 3) constant actuator force over the range of motion. The six-axis stage displacement vector  $\mathbf{x}$  ( $6 \times 1$ ) is then related to the actuator force vector  $\mathbf{F}$  acting on the stage by

$$\mathbf{F} = K\mathbf{x}. \quad (2.1)$$

The actuator force is related to the actuator input vector,  $\mathbf{i}$  (voltage, current, pressure, etc.), through the actuation matrix,  $K_a$ , and the force transformation matrix,  $T$ , by

$$\mathbf{F} = TK_a\mathbf{i}. \quad (2.2)$$

The actuation matrix relates the actuator inputs to the force outputs at the actuator paddle, while the transformation matrix transforms the forces acting on the paddle to forces that act on the stage. Equations (2.1) and (2.2) are then equated and this relationship is manipulated to obtain the actuator inputs,  $\mathbf{i}$ , that are required to achieve some desired stage motion,  $\mathbf{x}$ :

$$\mathbf{i} = (TK_a)^{-1} K\mathbf{x}. \quad (2.3)$$

In order to solve for the actuator inputs, the matrix  $TK_a$  must be invertible and its rows must be linearly independent. In general, each  $n^{\text{th}}$  actuator input results in six output forces at the paddle:  $F_{nx}$ ,  $F_{ny}$ ,  $F_{nz}$ ,  $M_{nx}$ ,  $M_{ny}$ , and  $M_{nz}$ . Six actuator inputs lead to a generalized 36 x 6 actuator matrix and 36 x 1 actuator paddle force vector. The actuation matrix is then multiplied by the transformation matrix. This matrix transforms the actuator forces at the paddles to forces that operate on the stage. The resulting  $TK_a$  matrix is a 6 x 6 square matrix and may be inverted if the rows are linearly independent. Assuming a lumped stage mass and damping, the linear system dynamics can be represented by

$$M\ddot{\mathbf{x}} + B\dot{\mathbf{x}} + K\mathbf{x} = TK_a\mathbf{i} \quad (2.4)$$

where  $M$ ,  $B$ , and  $K$  are the mass, damping, and stiffness matrices of the system.

The proposed flexure mechanism requires appropriate actuator inputs so that the force transformation matrix is invertible. The required inputs may then be solved for a given set of desired outputs. Figure 2.2 shows an actuation scheme that meets these requirements. The z-axis of the stage coordinate system is directed upward and orthogonal to the device plane, but this is omitted from the figure for clarity.

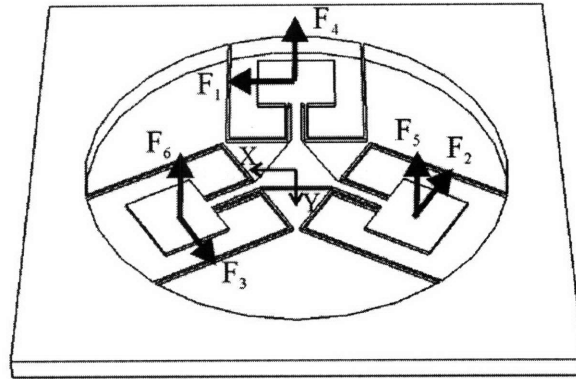


**Figure 2.2. Actuation scheme with two independent and orthogonal actuator forces at each paddle.**

Two independent and orthogonal actuator forces are applied to each of the paddles. An in-plane actuator force operates in the tangential direction, while the out-of-plane force operates normal to the device plane. Figure 2.3 illustrates the basis flexure motions that result from appropriate combinations of actuator inputs. The flexure deformations were modeled using finite-element analysis (FEA) in COSMOSWorks. Actuator force inputs are denoted by arrows at the actuator paddles, and the resulting stage motions are indicated by arrows at the stage. Six different combinations of force inputs result in six independent motions.

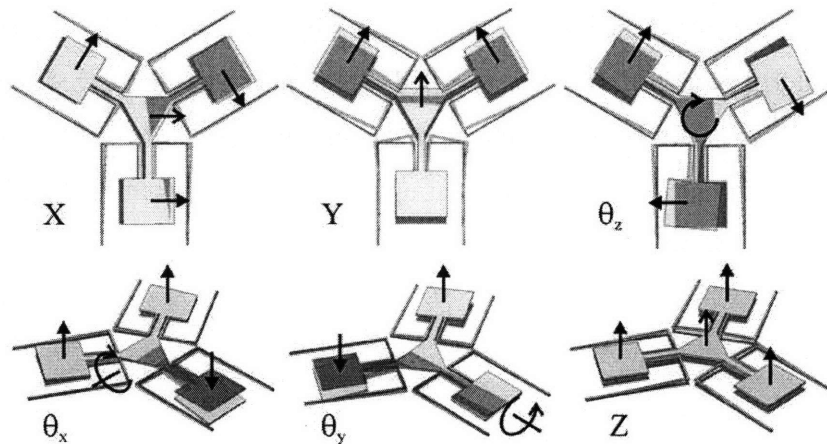


**Figure 2.3. Orthogonal 6-axis motion deformations of the nanopositioner flexure bearing mechanism due to forces applied at the actuator paddles.**

The actuator inputs are related to the forces that are applied to the stage through the matrix  $TK_a$ . This transformation matrix is invertible for the proposed actuation scheme. Two assumptions are made for this flexure system:

- 1) The flexure that joins the paddles and stage is 10X stiffer than the suspension beams.

2) The distance from the center of each paddle to the center of the stage is  $L$ .

The forces acting on the stage due to the inputs are defined in equation (2.2), which expands to

$$\begin{bmatrix} F_x \\ F_y \\ M_z \\ F_z \\ M_x \\ M_y \end{bmatrix} = \begin{bmatrix} k_{a1} & -k_{a2}/2 & -k_{a3}/2 & 0 & 0 & 0 \\ 0 & -\sqrt{3}k_{a2}/2 & \sqrt{3}k_{a3}/2 & 0 & 0 & 0 \\ Lk_{a1} & Lk_{a2} & Lk_{a3} & 0 & 0 & 0 \\ 0 & 0 & 0 & k_{a4} & k_{a5} & k_{a6} \\ 0 & 0 & 0 & -Lk_{a4} & Lk_{a5}/2 & Lk_{a6}/2 \\ 0 & 0 & 0 & 0 & \sqrt{3}Lk_{a5}/2 & -\sqrt{3}Lk_{a6}/2 \end{bmatrix} \cdot \begin{bmatrix} i_1 \\ i_2 \\ i_3 \\ i_4 \\ i_5 \\ i_6 \end{bmatrix}. \quad (2.5)$$

In this matrix equation, each  $n^{\text{th}}$  actuator input is related to its output force at the paddle by the actuator constant  $k_{an}$ . The actuator inputs  $i_1$ ,  $i_2$ , and  $i_3$  correspond to the in-plane actuator force at each paddle, while the inputs  $i_4$ ,  $i_5$ , and  $i_6$  correspond to the out-of-plane forces at each paddle as illustrated in Figure 2.2. In the idealized case, all in-plane actuators would have equivalent force output, so that  $k_{a1}$  through  $k_{a3}$  are equal. The same is true for the out-of-plane actuators. In this case, the matrix rows in equation (2.5) are linearly independent and the matrix is invertible. As a result, the combination of three-way symmetric flexure mechanism, tangential in-plane forces, and orthogonal out-of-plane forces results in a linear mapping of input forces to output motions. The required actuator inputs may be obtained for a desired set of motion outputs without the need for redundant actuation. This leads to an actuator design functional requirement that each actuator must output two independent linear forces at the paddle:

- 1) An in-plane force tangent to the radial line joining the paddle and stage.
- 2) An orthogonal force normal to the device plane.

An important advantage of this actuator and flexure configuration is that stage motions that are due to parasitic forces may be compensated in six axes by appropriate calibration of the force inputs. Force calibration will be discussed in more detail in Chapters 4 and 6.

## 2.4 Flexure Bearing Concept

Several flexure bearing arrangements may be implemented in the overall system topology is presented in Figure 2.2. The three flexure concepts presented in Figure 2.4 were selected for comparison.

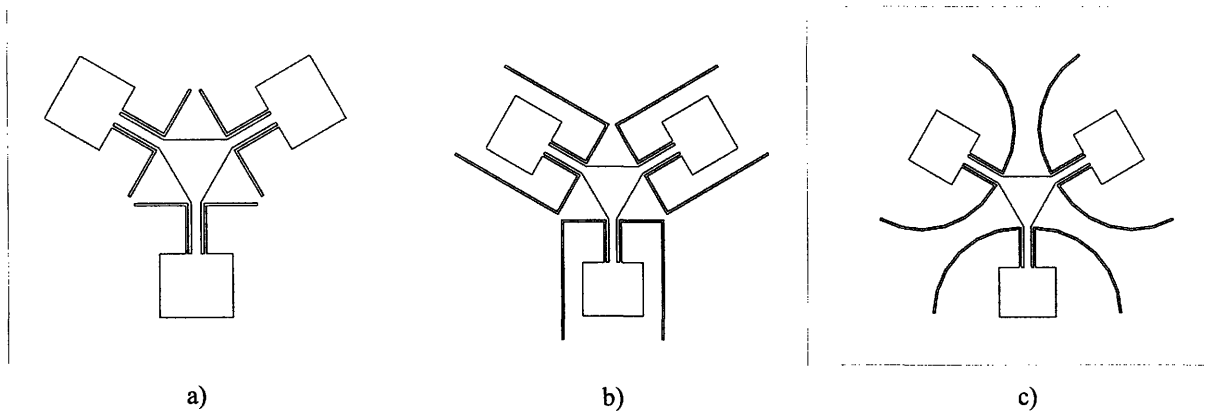


**Figure 2.4. Nanopositioner flexure concepts: a) single-bent beam, b) double-bent beam, and c) bow-flexure.**

Each concept shares the common characteristics of symmetry about the actuator paddle in order to minimize parasitic thermal drift in the plane. Each unit flexure is also composed of at least two beams in series in order to permit orthogonal in-plane motion without stress stiffening. The flexures' stiffness, resonant frequency, and transmission ratio were obtained from simulation using finite element analysis. Linear-elastic static analysis and modal analysis were performed in COSMOSWorks. The flexure thickness, beam width, footprint, actuator geometry, and paddle geometry were fixed for all three concepts. Flexure stiffness and transmission ratio were determined from the static analysis, while the resonant frequency was determined from the modal analysis. Table 2.3 lists the fixed simulation parameters used for each flexure concept. The geometry that is common to each of the concepts, such as beam thickness and width, is discussed in more detail in Chapter 4.

**Table 2.3. Simulation parameters used for flexure concept comparison**

Parameter	Value	Units
Thickness	100	$\mu\text{m}$
Beam Width	80	$\mu\text{m}$
Stage Width	2000	$\mu\text{m}$
Paddle Dimensions	2292 x 2000	$\mu\text{m}$
Paddle-Stage Distance	3855	$\mu\text{m}$
Connector Width	300	$\mu\text{m}$
Footprint Diameter	12	mm
Modulus	165	GPa

The coordinate system used in this analysis follows from Figure 2.2. The flexure stiffness was determined by applying a constant force and then measuring the resultant stage displacement.

The transmission ratio was determined by measuring the ratio of stage to paddle displacement in the given direction. The results are presented in Table 2.4.

**Table 2.4. Nanopositioner flexure concept performance metric comparison.**

Design Concept	Resonant Frequency (Hz)	Stiffness X-Direction (N/m)	Stiffness Z-Direction (N/m)	Transmission Ratio X-Direction	Transmission Ratio Z-Direction
Single-Bent Beam	1980	2758	848	0.60	0.38
Double-Bent Beam	1251	527	102	0.92	0.89
Bow Flexure	1176	594	92	0.89	0.88

Geometric constraints limit the total length of the beams in the single-bent beam concept, which results in higher stiffness, higher resonant frequency, and lower transmission ratio when compared to the other concepts. As a result, the double-bent beam and bow flexure are better suited for larger displacement motions. The data in Table 2.4 indicates that the double-bent beam and bow flexure share similar transmission ratios, resonant frequencies, and stiffness characteristics. The double-bent beam flexure is amenable to passive thermal compensation. This is important as the flexure mechanism will be combined with moving-coil actuators that dissipate heat at the paddles. Thermal compensation is discussed in Chapter 4. As a result, the double-bent beam flexure concept was selected for the nanopositioner system.

## 2.5 Microactuator Concept

The following sections develop the functional requirements for the microactuator system, compare several actuation species, discuss selection criteria, provide first-order actuator sizing, and outline the moving-coil actuator architecture. The final section discusses actuator concept selection and the challenges that are associated with the realization of the selected concept.

### 2.5.1 Functional Requirements

The microactuator functional requirements for orthogonal in-plane and out-of-plane were derived with consideration of the flexure concept in Section 2.3. The actuator functional requirements are summarized in Table 2.5. The actuator should exhibit a biaxial linear range of motion of approximately 20  $\mu\text{m}$ , which is double the desired stage motion in order to accommodate flexure transmission ratios as low as 0.5. Actuator bandwidth should be more than ten times the target 1000 Hz resonant mode of the nanopositioner system so that actuator dynamics are negligible over the operating bandwidth of the nanopositioner. The actuator should

also exert sufficient force to deflect the flexure mechanism by half the required system range of motion. The required force is estimated by considering the one degree-of-freedom (DOF) system model that was presented in Chapter 1. Equations (1.1) and (1.2) may be combined to eliminate the stiffness,  $k$ , and to obtain the force in terms of the moving mass,  $m$ , resonant frequency,  $f$ , and static displacement,  $\delta$ :

$$F = (2\pi f)^2 m\delta. \quad (2.6)$$

The mass is estimated by assuming a meso-scale silicon sample stage with side length of 5 mm x 5 mm and 200  $\mu\text{m}$  thickness. The density of silicon is 2400  $\text{kg}/\text{m}^3$ . This results in a mass of  $m = 0.01$  g. The computed mass is combined with a resonant frequency of 1 kHz and static displacement of 5  $\mu\text{m}$  to yield the required force of  $F \approx 2.4$  mN. The required force is rounded up to 10mN in order to accommodate a 300% increase in mass due to extra moving mass of the paddles and potential variations in the stage size and stiffnesses of the flexure. The paddles are assumed to have the same size as the stage for this calculation. The actuator input-output response must also be linear to within at least 1 % so as to enable open-loop linear calibration and control. The microactuator must also be compatible with current microfabrication technology so that it is possible to integrate it within a microfabricated nanopositioner system.

**Table 2.5. Two-axis actuator functional requirements.**

Functional Requirement	Value	Units
In-plane (X) Force	10	mN
Out-of-plane (Z) Force	10	mN
Range of Motion	20	$\mu\text{m}$
Bandwidth	10000	Hz
Full-scale linearity	1%	-

## 2.5.2 Microactuator Species Selection

The actuator functional requirements require that the appropriate actuator possess the following characteristics: moderate force on the order of 10 mN, range-of-motion of 20 $\mu\text{m}$ , multi-axis capability, high-bandwidth, input-output linearity to within 1%, and microfabrication compatibility. Many possible microactuators schemes meet some of the requirements, but not all of them are met simultaneously. Microactuator species that are relevant to nanopositioning include electrostatic, electromagnetic, electrothermal, and piezoelectric. A detailed review of these species, with highlights of their benefits and drawbacks, was presented in section 1.2.3.



Table 2.6 summarizes this review into a qualitative comparison of the microactuator species as related to the functional requirements for the six-axis nanopositioner. The electrostatic comb-drive is used as the baseline for comparison. The performance metrics include force density, range of motion, bandwidth, repeatability, input-output linearity, multi-axis capability, and microfabrication complexity.

**Table 2.6. Microactuator species qualitative comparison.**

Species	Electrostatic: comb drive	Electrostatic: parallel plate	Electrostatic: zipping	Electro- magnetic	Electro- thermal	Piezoelectric
Force density	0	0	0	0	+	+
Range of Motion	0	-	+	+	-	-
Bandwidth	0	0	0	0	-	+
Repeatability	0	0	0	0	0	-
Linearity	0	-	-	0	0	0
Multi-axis Capability	0	-	-	+	0	0
Fabrication	0	0	0	-	0	-
Total	0	-3	-1	1	-1	-1

Table 2.6 indicates that electromagnetic actuators are most suitable for use in a high-speed, multi-axis nanopositioner with functional requirements as outlined in Table 2.1. Force densities (force output per unit device area) for field-driven devices such as magnetic and electrostatic devices are typically on the same order of magnitude. Electromagnetic microactuators may operate over several tens- to hundreds-of-micrometers, as opposed to a) comb-drives that typically may operate over 10 – 20  $\mu\text{m}$ , or b) parallel plate actuators that operate over a couple micrometers at high voltages. The main drawback of electromagnetic actuators is the microfabrication complexity that is associated with integrating inductor coils and magnetic materials into the device. Zipping electrostatic actuators may also achieve long strokes, but only along a single axis of motion. Likewise, comb-drive actuators operate only along the comb fingers with micrometer gaps in the transverse direction, which thereby limits multi-axis motion. The comparison table indicates that the comb-drive and electromagnetic actuators may have similar performance. Electromagnetic actuators have the advantage of multi-axis capability. As a result, electromagnetic actuation was selected for the HSM nanopositioner system.

The various electromagnetic microactuator schemes include gap-closing or reluctance actuators, and Lorentz force actuators. Lorentz actuators include moving magnet and moving

coil devices. Table 1.8 compares the relative merits for each actuator species in regards to the actuator functional requirements. Variable reluctance actuators may operate at higher force densities than Lorentz force actuators, but they are nonlinear and typically limited to one-axis. Variable reluctance devices also require elaborate microfabrication of integrated inductors and permeable magnetic materials, which is a high-risk area of research. Magnet-coil microactuators require only planar-spiral coils and permanent magnets. Planar-spiral coils are amenable to lithographic microfabrication, and millimeter-scale permanent magnets may be manufactured and assembled using conventional techniques. Magnet-coil actuators also permit multi-axis actuation over large working distances. As a result, magnet-coil actuators using planar-spiral coils were selected for the nanopositioner. Figure 2.5 shows a schematic illustration of a magnet-coil actuator in which a planar-spiral coil interacts with the permanent magnet field.

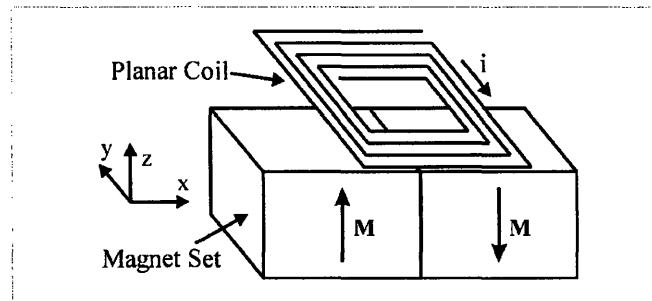


**Figure 2.5. Schematic illustration of a magnet-coil actuator with planar spiral coil.**

Magnet-coil actuators may be configured as moving-magnet or moving-coil devices when using a flexure mechanism for motion guidance. Moving magnet devices dissipate less power into the flexure because the heat-generating coils may be thermally grounded. A moving coil system dissipates heat through the flexure system to ground. Moving coil systems that use planar-spiral coils take advantage of reduced moving mass to improve mechanical bandwidth. In this configuration, large permanent magnets are fixed to ground, while a thin planar-spiral coil is mounted on the flexure. Assuming constant force output and spring stiffness, the ratio of natural frequencies for both configurations scales as the square root of the ratio of moving masses:

$$\frac{f_{coil}}{f_{magnet}} = \sqrt{\frac{A_m (\rho_m t_m + \rho_{Si} t_{Si})}{A_c (\rho_c t_c + \rho_{Si} t_{Si})}} \quad (2.7)$$

where  $\rho$  is the material density,  $t$  is the thickness, and  $A$  is the footprint area. The subscript  $c$  refers to moving coil,  $m$  refers to moving magnet, and  $Si$  refers to the silicon platform upon which the moving coil or magnet is fixed. Table 2.7 provides typical magnet-coil microactuator

dimensions and densities that were used to estimate the natural frequency ratio. The properties of the silicon platform were presented in the previous section. The resulting ratio is

$$\frac{f_{coil}}{f_{magnet}} \approx 3.5. \quad (2.8)$$

In addition to reduced bandwidth, moving magnet microactuators require the fabrication or assembly of magnets onto the moving flexure system. The integration of magnets onto delicate microfabricated flexural elements poses several challenges that are eliminated by grounding the magnets and moving the coils. Moving coils were selected over moving magnets for improved mechanical bandwidth and ease of permanent magnet assembly. Power dissipation imposes limits on the maximum force output of moving-coil actuation.

**Table 2.7. Typical dimensions and material properties for magnet-coil microactuators.**

Parameter	Symbol	Units	Moving Coil	Moving Magnet
Density	$\rho$	$\text{g/cm}^3$	8.9	7.5
Thickness	$t$	mm	0.025	1
Footprint	$A$	$\text{mm}^2$	4	3

### 2.5.3 First-Order Coil Sizing

The moving-coil actuator size was estimated before designing the actuator architecture in order to ensure that a micro-coil can output sufficient force. The Lorentz force acting on a planar spiral coil that is suspended in a permanent magnet's field is approximated by

$$F = J\bar{B}pA_{coil}t_{coil} \quad (2.9)$$

where  $J$  is the current density in the coil,  $A_{coil}$  is the coil footprint area,  $p$  is the coil winding packing factor,  $\bar{B}$  is the mean magnetic flux density, and  $t_{coil}$  is the thickness of the coil windings. The coil packing factor represents the percent coil footprint that is occupied by windings. This equation is combined with Equations (1.1) and (1.2) to arrive at a relation for the actuator coil footprint that is required to deflect a spring-mass system with mass,  $m$ , resonant frequency,  $f$ , to a desired target static displacement,  $\delta$ :

$$A_{coil} = \frac{(2\pi f)^2 m\delta}{pJ\bar{B}t_{coil}}. \quad (2.10)$$

Table 2.8 presents the parameters that were used to estimate the area given by Equation (2.10). The flux density above a permanent magnet is estimated for remnance  $B_r = 1$  T, and a height above the magnet of approximately 20 % of the magnet thickness, or  $h/c = 0.2$ . The maximum reported current density for micro-coil inductors is assumed to be  $1000$  A/mm<sup>2</sup> [72]. The calculation assumes a conservative estimate of 25 % of the maximum current density. The required area is then  $A = 3.5$  mm<sup>2</sup>, which fits within the size constraints of a meso-scale device and the design space of previously microfabricated coils. This indicates that meso-scale moving coil microactuators may satisfy the nanopositioner functional requirements. In order to achieve sufficient winding packing density and force output, the coil windings and spacing must be on the order of tens-of-micrometers. Realization of this requires lithographic microfabrication of the actuator coils. Previous reported micro-coils range in size from several hundred micrometers to several millimeters per side, with winding pitches that are on the order of tens of micrometers.

**Table 2.8. Parameters used for first-order actuator coil sizing.**

Parameter	Symbol	Value	Units
Resonant Frequency	$f$	1000	Hz
Static Displacement	$\delta$	10	$\mu\text{m}$
Stage Mass	$m$	0.01	g
Mean Flux Density	$B$	0.2	T
Current Density	$J$	250	A/mm <sup>2</sup>
Coil Winding Thickness	$t$	30	$\mu\text{m}$
Coil Packing Factor	$p$	0.75	-
Required Coil Area	$A$	3.5	mm <sup>2</sup>

#### 2.5.4 Two-Axis Moving-Coil Concept Selection

The microactuator must have the capability to output independently-controllable forces in-the-plane and normal to the plane of the coil. This functional requirement may be fulfilled by suspending two stacked planar-spiral coils that are electrically insulated from each other. The coils operate based upon the Lorentz force phenomena via interaction of the coil current with the permanent magnet field. The Lorentz force on a current density in a magnetic field is given by:

$$\mathbf{F} = \mathbf{J} \times \mathbf{B} \quad (2.11)$$

where  $\mathbf{J}$  is the current density vector and  $\mathbf{B}$  is the local flux density vector. Figure 2.5 illustrates the coordinate system used to explain the actuation concept. Consider only the coil segments directed along the y-axis in the regions of highest flux density above the magnet poles. The

other coil segments are in regions of relatively low flux density and contribute negligible force to coil. A y-directed current in the region above the poles combined with a z-directed magnetic flux density results in an x-directed force. Likewise, a y-directed current and x-directed flux density results in a z-directed force. Therefore, appropriate design of the coil segments and the magnetic flux density above a planar magnet set may result in a configuration that enables in-plane and out-of-plane forces.

Figure 2.6 presents the cross-sectional schematics of actuator concepts that use stacked or nested coil structures that are suspended above a set of fixed permanent magnets. The cross-sections are taken through the mid-plane of the coil and magnet arrangements. The figures show qualitative representations of the permanent magnet field lines, coil currents directed along the y-axis, and resulting Lorentz force vectors. Each concept shares the common characteristics of a two-lobed field above the permanent magnet structure and two independent planar-spiral coils. Coil segments have current that is directed into and out of the figure. These current flows are represented by crosses and circles, respectively. The magnet configurations include (a) 3-pole alternating array, (b) magnet and yoke, (c) symmetric semi-Halbach array with nested coils, and (d) symmetric semi-Halbach array with stacked coils. The semi-Halbach is a variation of the repeating Halbach array [153].

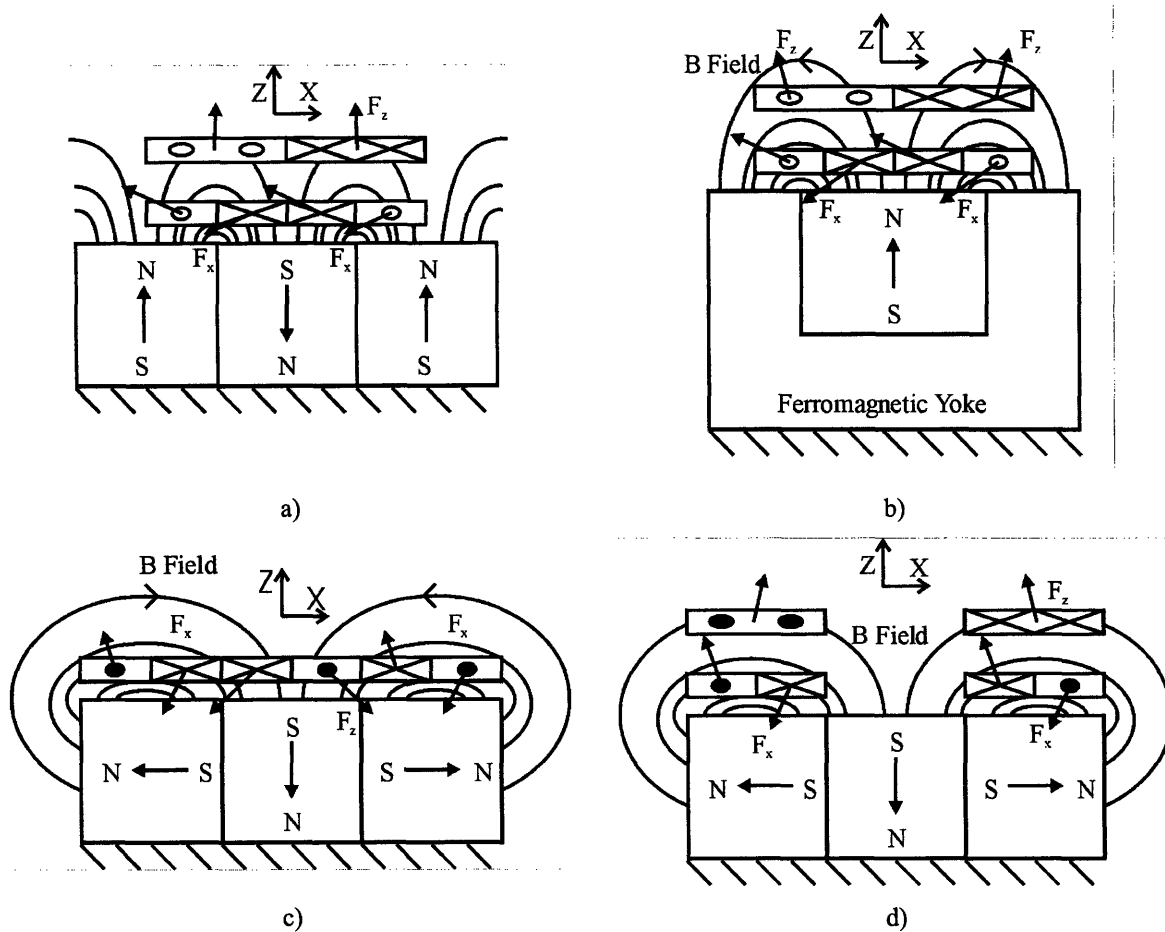


**Figure 2.6. Cross-section schematic representations of two-axis planar coil actuator concepts that use a permanent magnet field source and enable in-plane and out-of-plane forces: a) alternating pole magnet array with stacked actuator coils; b) single magnet and yolk with stacked actuator coils; c) symmetric semi-Halbach magnet array with nested actuator coils; d) symmetric semi-Halbach magnet array with stacked actuator coils.**

Each actuator concept contains 1) a “racetrack” coil that is centered upon the magnet array and which creates a net z-directed force, and 2) a “figure-eight” coil that creates a net x-directed force. A fair comparison of the actuator concepts may only be found if a) the force output is estimated by computing the magnetic flux density at a fixed height above the magnet structure and b) the actuators are constrained to fit within the same envelope. The important metrics for selecting a concept include 1) force output, 2) coil footprint, and 3) ease of assembly. The coil force is proportional to the flux density and therefore the concept with highest flux density maximizes the coil force. The flux density along the mid-plane of the structure and at a height,  $h$ , above the magnets was computed in two dimensions using a Comsol Multiphysics FEA package. The flux density is computed for square permanent magnets with side length  $a = 1$

mm, remnance of  $B_r = 1$  T, and a height of  $h = 500$   $\mu\text{m}$  above the magnet surface. Figure 2.7 plots the x and z flux density components versus the ratio of lateral position to magnet dimension.

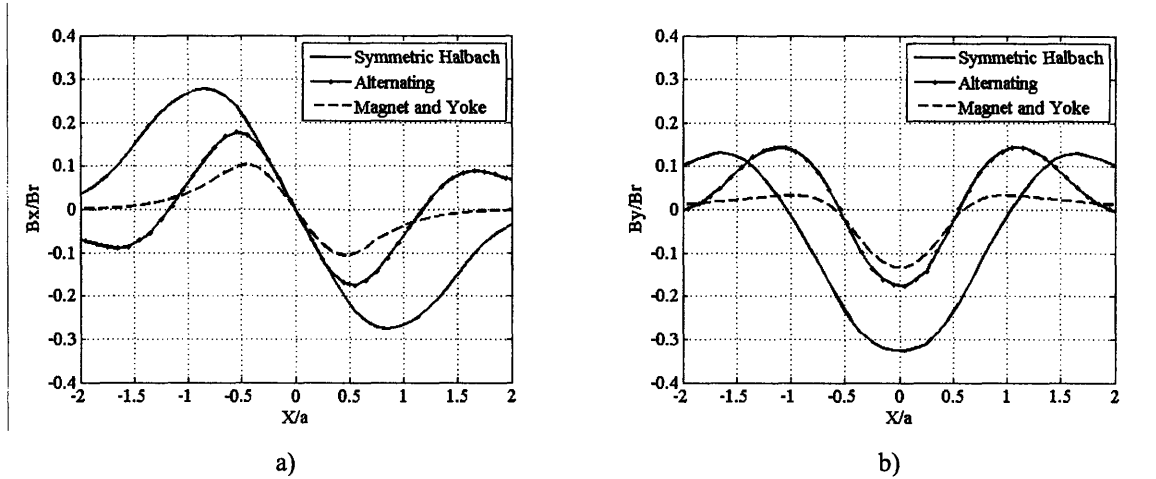


**Figure 2.7. Comparison of the a) x-component and b) y-component of the magnetic flux-density at a height  $h/a = 0.5$  above the magnet array for each actuator concept.**

The simulated data in Figure 2.7 shows that symmetric semi-Halbach array has the highest flux density, while the magnet-yoke concept possesses the lowest flux density. The magnet-yoke concept is therefore least attractive for a HSM nanopositioner. Although the semi-Halbach magnet array may yield the highest force output, the alternating pole concept has several advantages. Given equivalent magnet dimensions, Figure 2.6 shows that the semi-Halbach geometry requires a wider coil than the alternating pole concept. This translates into an increased moving mass which leads to a reduced natural frequency. Another advantage includes ease of assembly. The alternating pole concept is a stable arrangement of magnets, whereas the semi-Halbach arrangement is unstable and must be held together in a fixture or with adhesive. Although the alternating pole actuator has lower flux density when compared to the semi-Halbach configuration, the alternating-pole concept was chosen for its ease of practical assembly. Table 2.9 summarizes the actuator comparison in a Pugh chart.

**Table 2.9. Two-axis moving-coil microactuator concept comparison.**

Parameter	Alternating Pole	Magnet and Yoke	Halbach and Nested Coil	Halbach and Stacked Coil
Coil Footprint	0	0	-1	-1
Force	0	-1	1	1
Ease of Assembly	0	0	-1	-1
Total	0	-1	-1	-1

Figure 2.8a shows a cross-section of the alternating-pole concept with stacked racetrack and figure-eight coils. The upper racetrack coil creates a net z-directed force, while the figure-eight coil creates a net x-directed force. The actuator coils are electrically isolated, fixed together, and suspended above the fixed magnet array via the springs that represent the flexure mechanism. This architecture has been published by the author in [154].

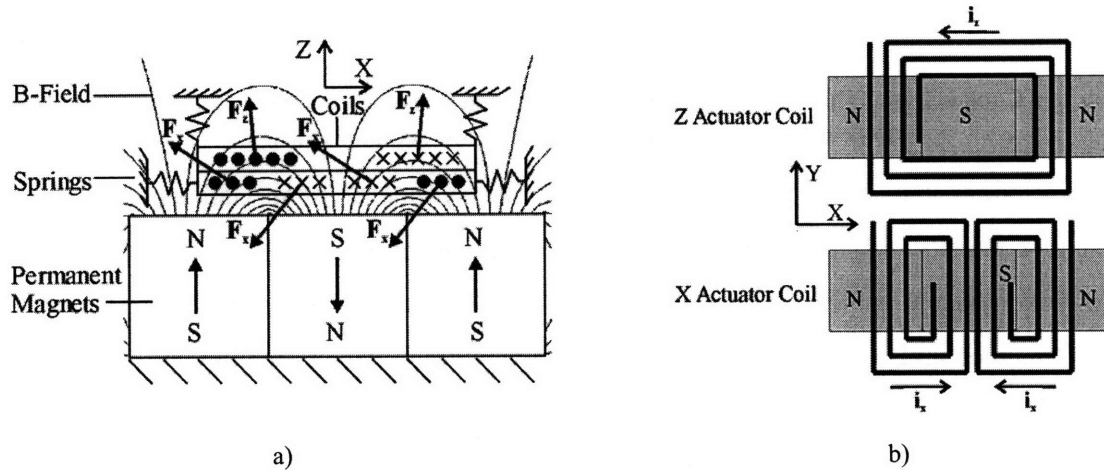


**Figure 2.8. a) Cross-section schematic of the two-axis moving-coil actuator architecture and b) individual schematic plan views of the stacked coil actuator architecture.**

Although the actuator should exert the desired orthogonal forces when energized, the in-plane actuator develops a parasitic torque about the y-axis that runs through its geometric center. The torque is due to the vertical component of the Lorentz forces that are generated by coil segments in the curving magnetic field. All planar-spiral coils that are suspended above a 2-pole alternating magnet array are subject to this parasitic torque. This torque (i) may lead to unwanted parasitic motions of the nanopositioner stage and (ii) wastes energy by doing work on the nanopositioner that could have been used to extend the range of the desired motion. The racetrack configuration uses side-by-side coils that enable minimization of this torque by



adjusting the geometry of the coils. This will be shown in Chapter 4. As a result, the actuator may be designed as a pure two-axis actuator.

Figure 2.8b shows a plan view of the actuator coils that are superimposed on the three-pole alternating magnet array. The schematics show the individual coils over the magnet array to avoid the clutter caused by superimposed coils. The segments of the coils that are parallel to the  $y$  direction and that are directly above the magnets will generate the desired  $x$ - and  $z$ -directed forces. The segments of the coils that are parallel to the  $x$  direction are in regions of negligible field so their contribution to the net exerted force is negligible. The actuator in Figure 2.8 can exert independently-controllable  $x$ - and  $z$ -directed forces as long as the coils are separated by a dielectric material. The interlayer dielectric should also provide means for electrical vias and jumpers in order to route the current into, and out of, the coils. This current is brought to the actuators by lead traces that must be integrated into the flexure system. Coil windings should also be fabricated with sufficient cross sectional area to minimize power dissipation in the leads so as to minimize thermal errors in the flexure mechanism. The design challenges associated with the two-axis actuator design are summarized below:

- 1) Minimization of the parasitic torque that results from  $x$ -directed actuation
- 2) Integration of a dielectric insulator that electrically isolates the stacked coils
- 3) Maximization of winding cross-section area in order to minimize power dissipation
- 4) Control of magnetic-coil gap height and alignment of coils to magnets

These design challenges will be addressed in Chapters 4 and 5.

## **2.6 Nanopositioner Concept**

The HSM nanopositioner concept is shown in Figure 2.9 with an integrated planar flexure mechanism, two-axis moving coil microactuators, and permanent magnets that are fixed to an alignment package. The solid model concept shows three sets of permanent magnets that must be aligned to the integrated flexure-coil structure via an alignment fixture.

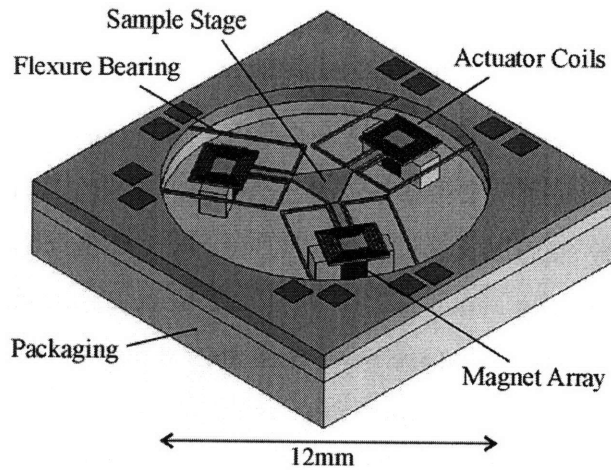


Figure 2.9. Solid model nanopositioner concept.

In this concept, the electrical connection is made to coils via the flexure bearings. The beams therefore must consist of a structural material and conductor lead wires. Figure 2.10 shows a concept for the cross-section of a flexure bearing. The multi-layer beam consists of a structural material, two conductors, and a dielectric that insulates the conductors from the structural material. Copper has been chosen as the conductor material for its low electrical resistivity, high thermal conductivity, and microfabrication compatibility. In this concept, power dissipation from the moving coil actuator through the flexure bearings may result in thermal bimorph-like bending of the beams. This is due to the mismatch in the coefficient of thermal expansion between the conductors and the structural material. The thermal bending may lead to parasitic motion of the stage. This error poses a design challenge as the flexure bearing geometry must be tuned to cancel out thermally-induced bending motions of the bearings.

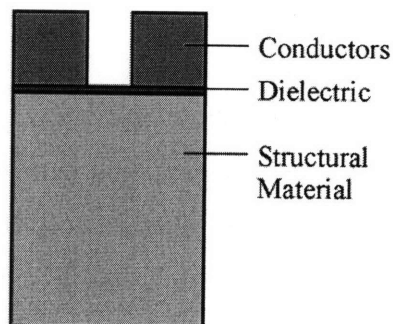


Figure 2.10. Cross-section schematic of the nanopositioner multi-layer flexure beams (not drawn to scale).

As discussed in the actuator concept section, the flexure-coil structure should be microfabricated so that sufficient coil packing density and force output may be achieved. This

leads to the choice of silicon as the flexural material, because it may be easily microfabricated using deep-etch processes. Other advantages of using silicon flexure bearings in a moving-coil nanopositioner include:

- a) Excellent repeatability due to its low-defect single-crystal structure;
- b) High flexure ratio, or ratio of yield stress to elastic modulus;
- c) High thermal diffusivity;
- d) High stiffness to density ratio.

Table 2.10 compares these properties for silicon and other common flexure materials. The flexure ratio is computed from the useful material strength,  $\sigma_y$ , and the elastic modulus,  $E$ . The thermal diffusivity is computed from the thermal conductivity,  $k$ , specific heat capacity,  $C_p$ , and density,  $\rho$ .

**Table 2.10. Relevant flexure material properties for high-speed electromagnetically-driven nanopositioners.**

Property	Symbol	Units	Silicon	Aluminum	Titanium
Flexure Ratio ( $\times 10^{-3}$ )	$\sigma/E$	-	12.0	0.7	2.1
Thermal Diffusivity ( $\times 10^{-6}$ )	$k/\rho C_p$	$m^2/s$	91	98	9
Stiffness-to-weight Ratio ( $\times 10^6$ )	$E/\rho$	$N\text{-m/kg}$	69	26	24

The data in the table indicates that silicon is a superior flexure material in terms of its ability to undergo large strain before failure. This may be seen by comparing the flexure ratio. Silicon and aluminum share similar thermal diffusivities, which is a measure of how well the material diffuses heat and thereby minimizes the time constant of the thermal errors. Silicon also possesses the ability to operate with higher resonant frequency due to its superior stiffness-to-weight ratio. These advantages coupled with microfabrication compatibility lead to the decision to use silicon as the structural material.

In summary, the design and fabrication challenges associated with the prototype HSM nanopositioner include:

- 1) Microfabrication of the silicon flexure with stacked micro-coil actuators
- 2) Alignment of the flexure-coil structure to permanent magnet arrays
- 3) Flexure bearing design with lead traces to supply power to the actuators

- 4) Control of the actuator paddle height above the magnets
- 5) Power dissipation from the coils through the flexure to ground
- 6) Parasitic motion due to thermal bimorph bending of the multi-layer beams

The strategies for dealing with these challenges will be covered in Chapters 4 and 5.

## **2.7 First Order Design Equations and Scaling Laws**

A set of first-order design equations was developed in order to understand the physics that govern the performance of the electromagnetically-driven nanopositioner. These equations may be used to a) guide system-level design to meet a set of functional requirements, b) perform sensitivity analysis, and c) generate scaling laws that provide insight into the performance as a function of device size. The performance metrics of importance include natural frequency, static range-of-motion, and parasitic thermal error. Figure 2.11 shows a set of first order models that represent a flexure-guided nanopositioner's moving actuator or stage mass that is supported by a cantilever beam that represents the supporting flexure mechanism.

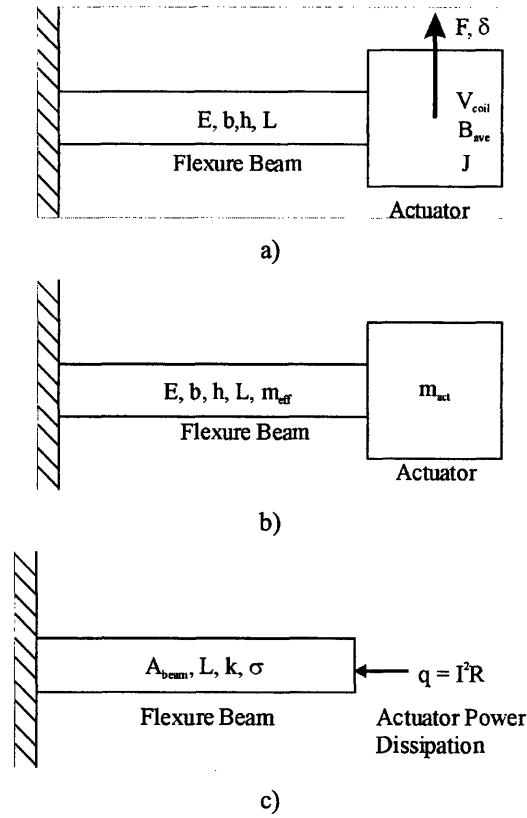


**Figure 2.11. First-order design models for a flexure-guided nanopositioner with suspended coil actuator: a) displacement due to linear beam-bending; b) dynamic mass-spring representation; c) coil power dissipation through the flexure bearing resulting in thermal growth.**

The models include: a) static deflection at the free end of the beam due to the actuator force; b) a dynamic mass-spring model of the actuator or stage mass and a lumped stiffness of the beam; and c) thermal growth along the length of the beam due to resistive power dissipation in the actuator coil. Referring to Figure 2.11a, the deflection of an end-loaded beam of rectangular cross-section is given by

$$\delta = \frac{4FL^3}{Eb^3h^3} \quad (2.12)$$

where  $b$  and  $h$  are the beam width and thickness,  $L$  is the length, and  $E$  is the elastic modulus. The actuator force in equation (2.9) may be combined with equation (2.12) to arrive at a relationship that predicts the beam deflection as a function of the beam and actuator coil parameters:

$$\delta = \frac{4JB_{ave}A_{coil}t_{coil}L^3}{Eb^3h^3} \quad (2.13)$$

Equation (2.13) is a first-order design equation for the static range-of-motion of a flexure-guided nanopositioner driven that is driven by moving-coil microactuators. The natural frequency of the model presented in Figure 2.11b may be approximated by a spring-mass system wherein the beam and actuator mass are lumped together. The resulting natural frequency is

$$f = \frac{1}{2\pi} \sqrt{\frac{Ebh^3}{4(m_{eff} + m_{act})L^3}} \quad (2.14)$$

where  $m_{eff}$  is the effective moving mass of the beam and  $m_{act}$  is the mass of the actuator. In most cases the beam mass may be neglected when compared to the actuator or stage mass. A similar first-order thermal analysis yields a relationship for the thermal growth along the length of the beam due to power dissipation from the actuator coil. The 1-D temperature distribution along a beam with constant input power at the free end as shown in Figure 2.11c is given by

$$T(x) - T_o = \frac{qx}{kA_{beam}} \quad (2.15)$$

where  $q$  is the input power of the actuator,  $k$  is the thermal conductivity of the beam,  $A_{beam}$  is the cross-sectional area of the beam, and  $T_o$  is the ambient temperature. Equation (2.15) is multiplied by the thermal coefficient of expansion of the beam,  $\alpha$ , and integrated from  $x = 0$  to  $x = L$  to arrive at the thermal deflection of the free end along the length of the beam:

$$\delta_t = \frac{\alpha L^2}{2kA_{beam}} q. \quad (2.16)$$

The power input is due to Joule heating of the actuator coil:

$$q = I^2 R = \rho_{res} L_{coil} A_{winding} J^2 \quad (2.17)$$

where  $\rho_{res}$  is the electrical resistivity of the coil windings,  $L_{coil}$  is the length of the unwound coil,  $A_{winding}$  is the cross-sectional area of the coil windings, and  $J$  is the current density in the coil. Equation (2.17) is substituted into equation (2.16) to obtain the equation for in-plane thermal growth of the beam due to power dissipation of the actuator coil:

$$\delta_t = \frac{\alpha L^2}{2kA_{beam}} (\rho_{res} L_{coil} A_{winding} J^2). \quad (2.18)$$

Equations (2.13), (2.14), and (2.18) serve as first-order design equations for the prototype nanopositioner. The equations capture the relationship of important design parameters to the

nanopositioner performance metrics. For instance, Equation (2.18) indicates that the thermal error is a quadratic function of the actuator current density, while the range-of-motion is linear with current density. This indicates that the actuator should be designed to operate with minimum input current so as to minimize the thermal error.

The first-order design equations may be used to estimate the sensitivity of the performance metrics to several design parameters. The sensitivities are presented in Table 2.11 in relation to the most important geometric parameters. Plus signs indicate a positive relationship, while minus signs indicate an inverse relationship. The number of plus or minus signs represents the degree-of-sensitivity to a change in the design parameter. For example, three plus signs indicate a cubed relationship, which would result in a 30 % change in performance for a 10 % change in the design parameter. The sensitivity matrix indicates that the characteristic beam length is the most sensitive parameter. A reduction in the length of the beam results in substantial improvements in resonant frequency and lateral thermal error, but it reduces the range-of-motion. Given an initial design, the sensitivity matrix may be used to help guide design parameter changes in order to arrive at a target performance.

**Table 2.11. First-order nanopositioner model parameter sensitivities.**

Parameter	$\delta$	f	$\delta$ (thermal)
L	+++	--	++
b	-	+	-
h	---	++	-
A (coil)	+	-	-
L (coil)	+	-	+

The first-order design equations may be used to develop scaling laws for the nanopositioner. The analysis assumes that the material properties do not scale with size, and that the current density is constant. Although maximum sustainable current density has been shown to scale as the inverse of the characteristic length [72], this analysis assumes the current density is constant with the length scaling. This results in a conservative scaling law for the range-of-motion, because current density improves at smaller scales. The scaling laws are derived by substituting a length factor  $L$  for each geometric parameter. Assuming constant current density, the scaling laws follow from the first-order design equations and are presented in Table 2.12.

**Table 2.12. Nanopositioner scaling laws.**

Performance Metric	Scaling Law
$\delta$	$L^2$
f	$L^{-1}$
$\delta$ (thermal)	$L^3$

The scaling laws indicate that the nanopositioner resonant frequency and thermal error benefit from scaling down in size, while the range-of-motion is reduced at smaller scales. The scaling laws indicate that the bandwidth and repeatability of coil-driven nanopositioners are improved by reducing the size, but at the expense of reduced range-of-motion. A meso-scale nanopositioner is a hybrid that possesses the large range-of-motion of macro-scale systems and the high-speed of micro-scale systems.

## **2.8 Design and Characterization of a Bench-level Prototype**

This section presents the design and measured performance of a centimeter-scale version of the nanopositioner. The bench-level prototype was designed and fabricated to create a physical model that could be used to characterize the planar six-axis electromagnetic nanopositioner concept. The design and results presented in this section have been published by the author [155]. The system models the meso-scale nanopositioner by using 1) a three-way symmetric planar flexure bearing with double-bent beams and 2) two-axis actuator composed of stacked planar spiral coils that are matched with arrays of alternating pole magnets.

The planar nanopositioner operates with a linear response over a range of nearly 8 micrometers in the x-, y- and z- directions. The nanopositioner has a first resonance at 120 Hz. Sensor-limited repeatability of better than 20nm has been demonstrated and the minimum step size has been measured at 10nm [155].

### **2.8.1 Design of the Bench-level Prototype**

The bench-level nanopositioner is shown in Figure 2.12a, while Figure 2.12b shows the actuator layers in cross section A-A.



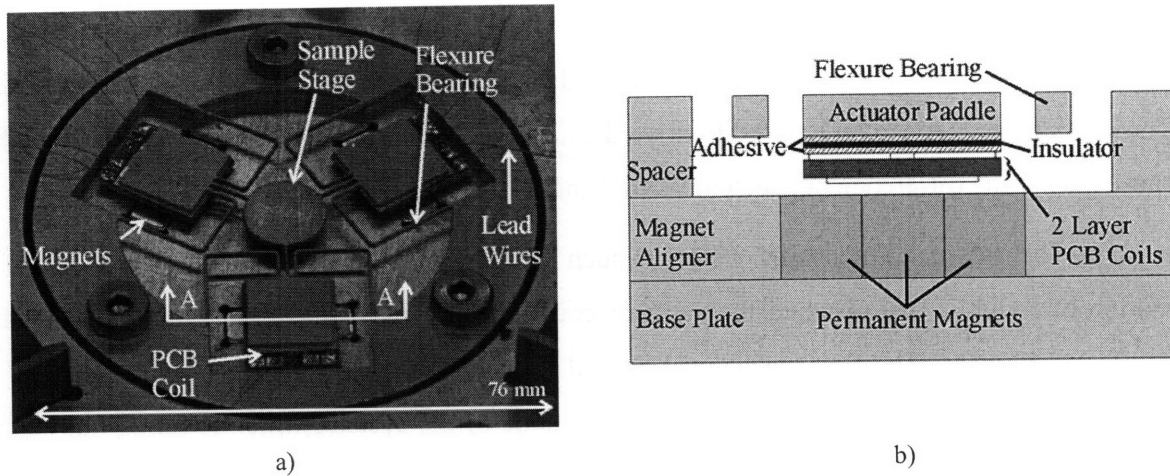


**Figure 2.12. a) Bench-level prototype nanopositioner. b) Cross-section A-A of the nanopositioner showing actuator components.**

The device operates in open-loop. It is comprised of a planar, spatially compliant 6061 aluminum HexFlex flexure mechanism [10], and three sets of the two-axes moving-coil actuators. The system has six independent actuator inputs and six outputs that include three translations and three rotations. The aluminum flexure bearings are 0.82mm thick and 0.64mm wide. The actuators consist of planar-coils that were patterned upon a printed circuit board (PCB) that was suspended above a set of three alternating-pole permanent magnets. An aluminum spacer is used to set the gap between the PCB coils and the permanent magnet structure. The PCB coils are bonded to the underside of the flexure mechanism's actuator paddles, and protected from shorting to the aluminum via a plastic insulator layer. Thirty-six gauge insulated lead wires were used to supply the moving coils with current while adding negligible stiffness to the system. The wires length was approximately 5 mm. The three-way symmetric design [10], and relatively small out-of-plane profile, help to minimize thermal errors in the stage position.

When powered, the actuators apply forces that deflect the flexure mechanism. Electromagnetic simulations were used to predict the force output of the actuators as a function of current. Assuming linearity, the set of input currents required to achieve a static output state,  $x$ , may be determined by using Equation (2.3). The actuator matrix,  $K_a$ , relates the command currents to actuator forces. The actuator matrix is premultiplied by the kinematic transformation matrix,  $T$ , that maps forces at the actuators to the stage. The preceding is then premultiplied by the stiffness matrix,  $K$ , is to relate the applied forces on the structure to the output displacement

of the center of the stage. In practice, this input-output mapping is measured, the errors between measured and predicted performance are mapped, and then a linear calibration matrix is created. The calibration matrix may be used to drive the nanopositioner without the systematic errors that cause part of the difference between measured and modeled behavior.

The flexure dimensions were set such that the force-limited system has a range of motion of roughly 10  $\mu\text{m}$  when the actuator coils are powered with the maximum sustainable current of 500mA. The first mechanical natural frequency of the system is roughly 125 Hz, as computed by FEA. Figure 2.13 shows the first mode of the system, which is tilting out-of-the-plane.

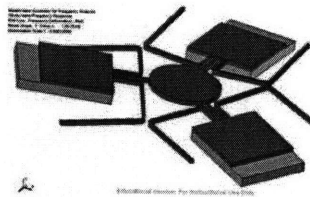


**Figure 2.13. First mode of the prototype nanopositioner at 125Hz as computed using FEA.**

## 2.8.2 Experimental Results

The prototype nanopositioner was calibrated and characterized in an experimental setup that used a set of six capacitance probes and target fixture that was attached to the central stage. Data was collected with a DSpace 16 bit real-time data acquisition system that operated at 1000Hz. Lion Precision capacitance probes were used to obtain displacement measurements from the multi-axis probe target. A custom-built 6-channel voltage-current amplifier was used to power the coils (Appendix C). Figure 2.14 shows the nanopositioner with target fitted to the sample stage where it is sensed by the six-probe fixture. In practical applications a smaller target/metrology system would be used. The target was as small as possible given the constraints of the minimum area that the capacitance probes require for sensing.

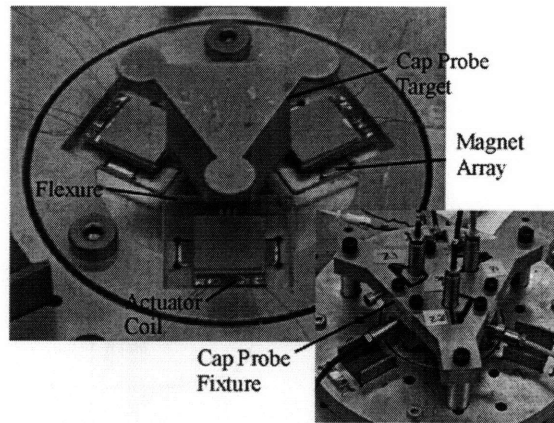


Figure 2.14. Bench-level nanopositioner with capacitance probes and measurement target.

The range-of-motion of the positioner is measured to be close to  $\pm 4$  microns in each of the  $x$ -,  $y$ -, and  $z$ -directions. The range is limited by the current-carrying capability of the PCB coils. Figure 2.15a and b show the input-output relationship of the system in the  $x$ - and  $z$ -direction.

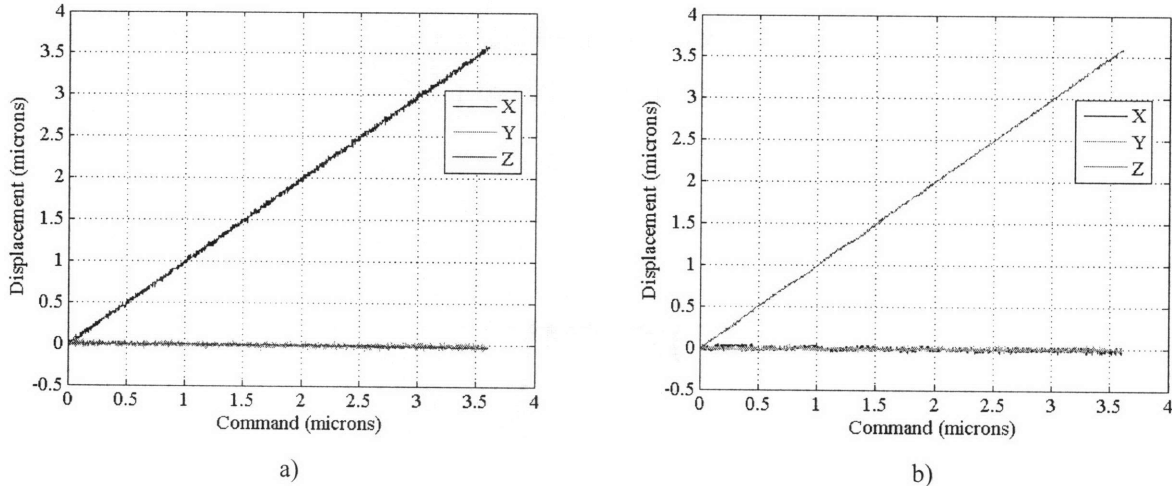
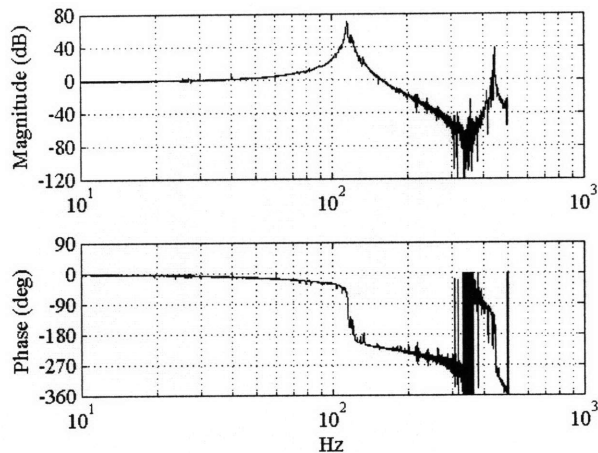


Figure 2.15. Measured vs. commanded displacement in the a)  $x$ -direction and b)  $z$ -direction.

The dynamics response of the system has been measured by referencing one capacitance probe off the sample stage without using the probe target. This was done because the target adds enough mass to the system so as to render any dynamic measurements far too inaccurate. Figure 2.16 shows the frequency response of the system in the out-of-plane,  $z$ -direction. The predicted out-of-plane first natural frequency of 125 Hz is 4% larger than the measured value of 120 Hz.



**Figure 2.16. Dynamic response in the z-direction without probe target.**

The in-plane repeatability and step response were measured with the capacitance probe target and 6-probe setup. The system was commanded to step in the  $x$ -direction by 600nm and then return after 3 seconds. The measured  $x$ -,  $y$ -, and  $z$ - motions are shown in Figure 2.17. The system is under-damped and “rings” for a few seconds in response to the step input. This vibration applies to all three axes as a result of the tilting mode harmonics. The figure indicates that the repeatability, excluding the vibration, is on the order of 20 nm.

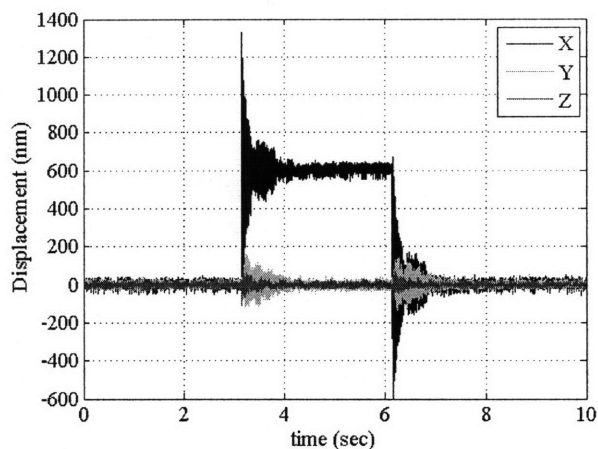


**Figure 2.17. Nanopositioner response to a 600nm step input in the x-direction with six-axis capacitance probe target.**

Out-of-plane repeatability and step response were also measured, but this was done without the capacitance probe target. In this case, a single probe measured displacement directly from the stage surface. Figure 2.18, Figure 2.19, and Figure 2.20 show the results of

commanded 10nm, 100nm, and 1000nm steps. Again, the under-damped system overshoots the target step height, but the oscillations damp below a significant level in less than 0.5 seconds. The oscillations could be removed faster in open-loop by using techniques such as input pre-filtering, or by adding visco-elastic elements. The data indicates that the repeatability of the system is approximately that of the noise floor of 20nm in all three cases.

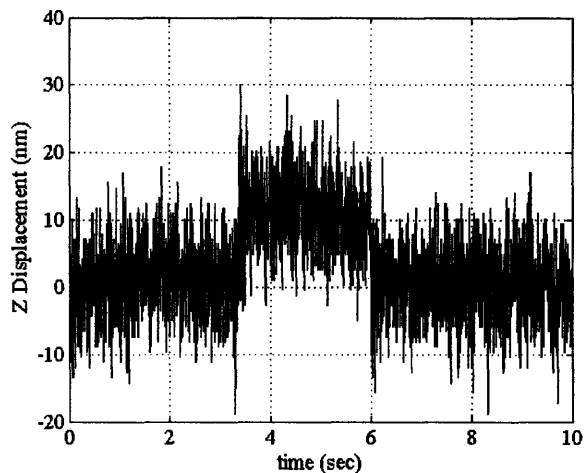


**Figure 2.18. Nanopositioner response to a 10nm step in the z-direction without the capacitance probe target.**

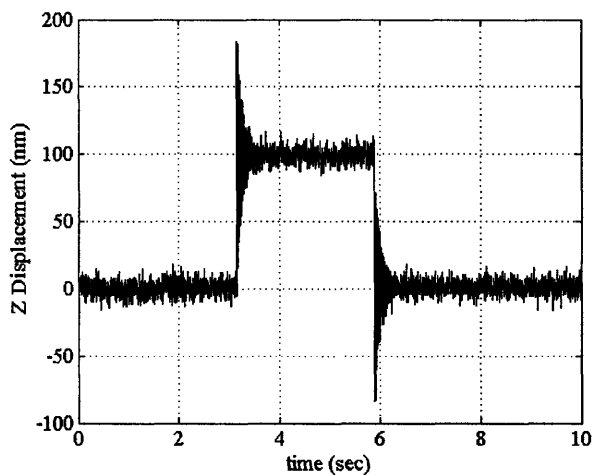


**Figure 2.19. Nanopositioner response to a 100nm step in the z-direction, without the capacitance probe target.**

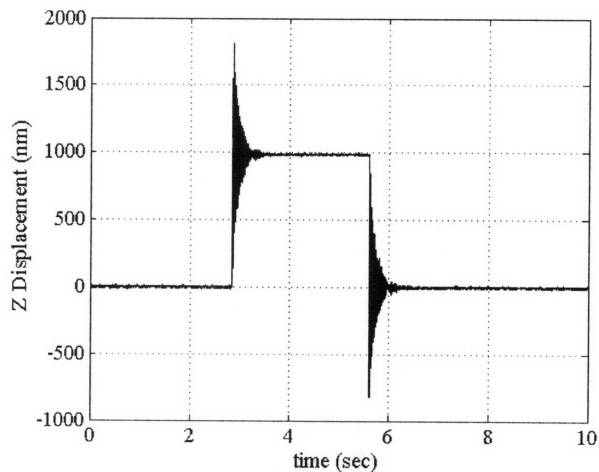


**Figure 2.20. Nanopositioner response to a 1000nm step in the z-direction, without the capacitance probe target.**

In order to demonstrate the three-dimensional motion capabilities of the nanopositioner, the system was commanded to traverse a 1  $\mu\text{m}$  spiral trajectory in open-loop over a time span of 10 seconds. The six-probe fixture and probe target were used to record the position of the stage during this test. The commanded and measured data are plotted in Figure 2.21.

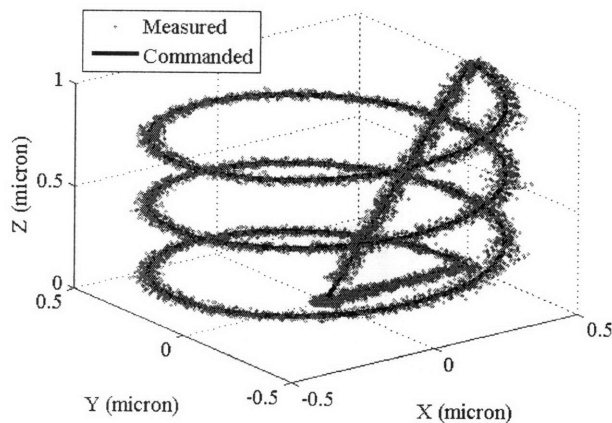


**Figure 2.21. Measured trajectory of the nanopositioner when commanded to follow a 3-loop spiral trajectory with diameter and total traversed height of 1000nm.**

The data indicates that the positioner follows the desired trajectory to an error that is within the noise of the measurement system. The results of the experiments presented in this section demonstrate the feasibility of the nanopositioner actuation concept. The data indicates that the combination of three sets of moving-coil actuators and the HexFlex mechanism may be

used to design nanopositioners that control six-axis motion in open-loop with precision on the order of 10s of nanometers.

## **2.9 Summary**

This chapter presented the functional requirements, constraints, conceptualization, and first-order concept design of a prototype nanopositioner that was driven by moving-coil microactuators. The planar flexure mechanism concept and flexure bearing topology were outlined in Sections 2.3 and 2.4, and the concept was used to guide derivation of the actuator's functional requirements. A two-axis, planar, moving-coil microactuator concept was designed so as to enable the nanopositioner to position the sample stage in 6 DOF. The concept was presented in Section 2.5. First-order equations were derived in Section 2.7 and used to a) relate the design parameters to performance metrics, b) enable system-level design, c) enable sensitivity analysis, and d) permit scaling analyses. A centimeter-scale prototype provided a geometrically similar model two-axis moving coil actuators and the HexFlex mechanism of the HSM nanopositioner. Section 2.8 presented experiments that were used to ascertain the nanopositioner concept's ability to perform six-axis motion. The prototype was measured to have 8 microns range-of-motion and repeatability of better than 20nm.

## MODELING AND ANALYSIS

---

This chapter presents physics-based models that will be used in Chapter 4 to design and optimize the HSM nanopositioner. The models are used to capture the physics in several domains: a) magnetoquasistatic permanent magnetic field modeling of the magnet arrays; b) Lorentz force models that predict the forces that act upon the coils; c) modeling of the actuator coils as electrical circuits; d) elastomechanic and kinematic modeling of the flexure mechanism; and e) thermo-mechanical model of the flexure bearing and actuator paddles.

### 3.1 Fourier Solution to the Permanent Magnet Fields

In this section the Fourier transform is used to model and simulate the three-dimensional magnetic field that is created by a finite, planar permanent magnet array that is Fourier-transformable and which exhibits vertical magnetization. The magnetic field model is used to generate a force model for the two-axis actuator concept. Model predictions are compared with analytical solutions for the three-pole alternating magnet array, and the measured values of a magnet array's flux density. The difference between measured and predicted values is less than 5%. The model and results presented in this section have been published by the author in [156].

#### 3.1.1 Introduction

Permanent magnet arrays are important to precision actuators such as linear motors that use Halbach arrays [16, 17, 157-159] and multi-axes magnetic levitation [21, 160-163] machines. These devices often consist of coils and a permanent magnet array. A generic example is shown in Figure 3.1a. A common characteristic of these devices is that the ratio of array length to magnet size is large enough that the fields which are far from the array ends



emulate those which are found in an infinite array. This assumption has enabled suitably accurate modeling of the array's magnetic field via infinite series solutions [17, 160].

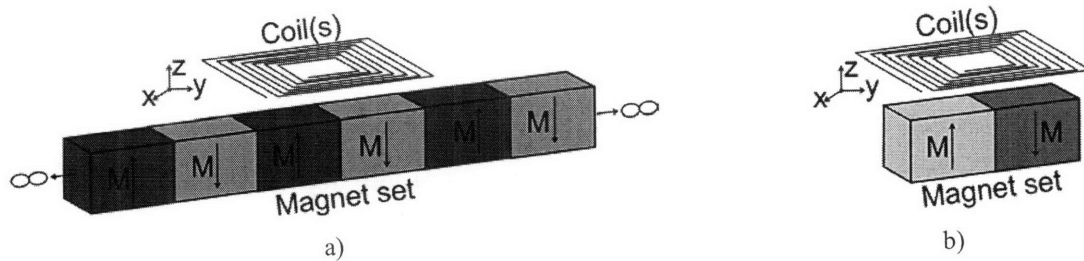


**Figure 3.1.** An actuator with a periodic array a) and an actuator with a non-periodic array b).

Some instruments, tools and equipment for nanomanufacturing and nano-scale research require meso-scale, i.e. millimeter-scale, precision machines to obtain viable bandwidth (kHz), resolution (nanometers), cost, and stability ( $\text{\AA}/\text{min}$ ) levels. It is difficult to create periodic magnet arrays for these machines because space constraints limit the size of the magnet arrays. For these reasons, designers often use non-periodic arrays such as the one shown in Figure 3.1b and Figure 3.2 [155]. Several small-scale devices that use non-periodic arrays include probe-based data storage devices [1, 3, 33] and optical switches [84, 86, 87, 164].

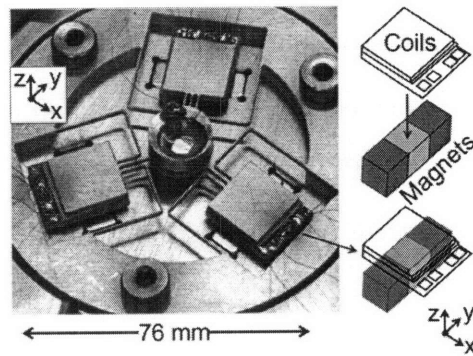


**Figure 3.2.** A meso-scale, six-axis nanopositioner.

The problem then reduces to accurately modeling the array's magnetic field characteristics given that classical infinite series approaches are not suitable. One important subset of problems involves the modeling of permanent magnet fields along planes, such as magnet pole surfaces or planar coils, for the purpose of computing actuator forces. This method has been used to compute the fields and forces that act upon planar moving coil actuators, and so it is of interest to the current design problem. For simple prismatic magnets, it may be possible to obtain a closed-form solution to the field characteristics from the superposition integral [165, 166], but this only covers a limited number of array geometries and the equations become

cumbersome for arrays of multiple magnets. In addition, the solution is unbounded along some of the magnet boundaries. In general, it is not possible to derive closed-form expressions for arbitrary in-plane arrangements of magnets. For these cases, one may numerically integrate the superposition integrals to obtain the magnetic field characteristics along a plane of interest. This becomes time consuming for systems with small gaps, where the field must be evaluated at, or close to, the pole surfaces. Examples include moving-magnet or moving-coil devices such as the microactuator that is proposed in this thesis. If this technique is applied to this type of magnet-coil device, the computation of the coil-field interactions within close proximity to the magnets will require fine discretization in order to ensure convergence when using standard quadrature algorithms. This is time and computationally intensive for design and optimization. Alternatively, it is possible to transform the problem in the Fourier domain. For geometries that cannot be solved in closed-form, the Fourier transform method makes use of computationally efficient Fast Fourier Transform (FFT) algorithms to evaluate the transform integrals and then quickly compute the field solutions. This method is advantageous for problems where the three-dimensional field is computed along a plane that is normal to the magnetization direction. For such problems, the advantages of using the Fourier transform method over the numerical approximation of the superposition integral include:

- a) FFT algorithms are more computationally more efficient than standard numerical integration methods. This will be demonstrated in Section 3.1.4;
- b) Convergence is independent of distance from the pole surfaces and this enables the consideration of small gaps without the burden of increased computation time;
- c) The resulting Fourier transform integral field equations provide insight into the field solutions.

Herein, a Fourier transform is used to model the fields for planar permanent magnet arrays that: 1) are Fourier-transformable; 2) are periodic or non-periodic; and 3) contain magnets that have vertical magnetization.

The method efficiently computes the fields along planes that are normal to the magnetization direction, which enables calculation of the A) surface stresses for moving magnet actuators and B) the field above the magnet for moving planar-coil actuators. The technique makes use of the principles of superposition and magnetic charge to create solutions that: a) are

expressed in the form of double Fourier integrals; b) are bounded everywhere; and c) may be used to create plots that provide insight into field changes with changes in design parameters.

### 3.1.2 Modeling

#### 3.1.2.A Model Setup and Boundary Conditions

Figure 3.3a shows a schematic of the model that consists of a general planar arrangement of permanent magnets with magnetization  $\mathbf{M}(x,y)$  that is oriented in the vertical direction. The magnitude and sign of this vector are free to vary in the  $x$  and  $y$  directions. Figure 3.3b shows three regions of interest – regions 1 and 3 exist in air and extend to “infinity” above and below the array.

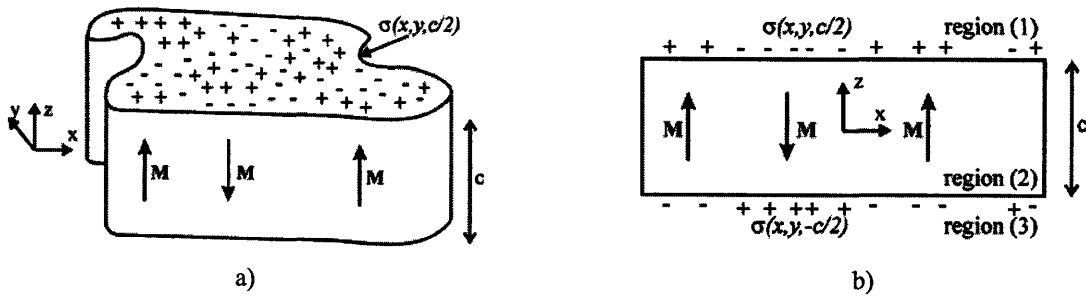


**Figure 3.3. Generalized in-plane magnet arrangement with equivalent surface magnetic charge distribution  $\sigma(x,y)$  at  $z = (1/2)c$  (a) and side view with detail of charge distribution on upper and lower surfaces (b).**

Region 2 encompasses the magnet volume, extends to infinity in the  $x$  and  $y$  directions, and is bounded by the planes that define the upper and lower surfaces of the magnets. Under the magnetoquasistatic (MQS) approximation [167] with zero current density, Maxwell’s Equations for the magnetic field intensity,  $\mathbf{H}$ , and flux density,  $\mathbf{B}$ , simplify to:

$$\nabla \times \mathbf{H} = 0 \quad (3.1)$$

$$\nabla \cdot \mathbf{B} = 0. \quad (3.2)$$

As a result, the magnetic field,  $\mathbf{H}$ , is irrotational and may be expressed as the gradient of the scalar magnetic potential  $\Psi$ :

$$\mathbf{H} = -\nabla \Psi. \quad (3.3)$$

From Equation (3.2), one may show that the magnetic potential satisfies Laplace’s equation:

$$\nabla^2 \Psi = 0. \quad (3.4)$$

Within the magnetized regions of the permanent magnets, the flux density is defined as:

$$\mathbf{B} = \mu_o (\mu_r \mathbf{H} + \mathbf{M}) \quad (3.5)$$

where  $\mathbf{M}$  is the magnetization of the permanent magnets. The vertical magnetization has no divergence and may be modeled as a surface charge density  $\sigma(x,y)$  on the magnet surfaces [142]:

$$\sigma = -\mathbf{n} \cdot \mu_o (\mathbf{M}_1 - \mathbf{M}_2). \quad (3.6)$$

The subscripts 1 and 2 correspond to adjacent regions, region 1 and region 2, at the top surface. In this model, the magnetization is a function of  $x$  and  $y$  and it is directed along the  $z$  direction. The charge density is located on the array's surfaces at  $z = \frac{1}{2} c$  and  $z = -\frac{1}{2} c$ . No charge density is located on the sides of the magnet array. The surface magnetic charge is:

$$\begin{aligned} \sigma(x, y, c/2) &= \mu_o M_z(x, y) \\ \sigma(x, y, -c/2) &= -\mu_o M_z(x, y) \end{aligned} \quad (3.7)$$

The boundary conditions for the problem are derived from the continuity conditions for the field,  $\mathbf{H}$ , and the potential,  $\Psi$ , at the charged surfaces [167]. As magnetic charge is present only on the planes that define the upper and lower surfaces of the magnets, the boundary conditions need only be considered on these surfaces. Continuity of the magnetic field,  $\mathbf{H}$ , across the charged surfaces yields the first boundary condition at  $z = \frac{1}{2} c$  and  $z = -\frac{1}{2} c$ :

$$\begin{aligned} \mathbf{n} \cdot \mu_o (\mathbf{H}_1 - \mathbf{H}_2) &= \sigma(x, y, c/2) \quad \text{at } z = +c/2 \\ \mathbf{n} \cdot \mu_o (\mathbf{H}_2 - \mathbf{H}_3) &= \sigma(x, y, -c/2) \quad \text{at } z = -c/2 \end{aligned} \quad (3.8)$$

The next boundary condition is set by continuity of the magnetic potential at the magnet surfaces [167]:

$$\begin{aligned} \Psi_1 &= \Psi_2 \quad \text{at } z = +c/2 \\ \Psi_2 &= \Psi_3 \quad \text{at } z = -c/2 \end{aligned} \quad (3.9)$$

For the final boundary condition, the potential must vanish at infinity, and so:

$$\lim_{|x,y,z| \rightarrow \infty} \Psi = 0. \quad (3.10)$$

The potential,  $\Psi$ , in Equation (3.4) may be solved in three dimensions as subject to Equations (3.8)–(3.10).

### 3.1.2.B Model Solution

The following sub-section provide a solution procedure for the magnetic potential and the fields. The solution to Equation (3.4), subject to Equations (3.8) - (3.10), is found via the classic technique of separation of variables

$$\Psi = X(x)Y(y)Z(z). \quad (3.11)$$

It is shown by Haus and Melcher [167] that the independent functions  $X$ ,  $Y$  and  $Z$  that solve Laplace's Equation (3.4) are of the form:

$$\begin{aligned} X &\sim e^{ik_x x} \\ Y &\sim e^{ik_y y} \\ Z &\sim e^{-k_{xy} z} \text{ or } \sinh(k_{xy} z) \end{aligned} \quad (3.12)$$

where  $k_x$ ,  $k_y$  and  $k_{xy}$  are separation constants related by:

$$k_{xy}^2 = k_x^2 + k_y^2. \quad (3.13)$$

The boundary condition in Equation (3.8) requires that the solution be an odd-symmetric function with respect to  $z$ , and the boundary condition in Equation (3.10) requires that the solution goes to zero as  $z$  goes to infinity. Therefore, homogeneous solutions that solve Equation (3.4) within each of the model regions are:

$$\Psi_{1h} = A(k_x, k_y) e^{-k_{xy} z} e^{i(k_x x + k_y y)} \quad \text{region 1} \quad (3.14)$$

$$\Psi_{2h} = C(k_x, k_y) \sinh(k_{xy} z) e^{i(k_x x + k_y y)} \quad \text{region 2} \quad (3.15)$$

$$\Psi_{3h} = -A(k_x, k_y) e^{k_{xy} z} e^{i(k_x x + k_y y)} \quad \text{region 3.} \quad (3.16)$$

The principle of superposition is employed to sum the possible homogeneous solutions over the continuous wave constants,  $k_x$  and  $k_y$ , in order to arrive at the general solutions for the potential:

$$\Psi_1(x, y, z) = \int_{-\infty}^{\infty} \int_{-\infty}^{\infty} A(k_x, k_y) e^{-k_{xy} z} e^{i(k_x x + k_y y)} dk_x dk_y \quad (3.17)$$

$$\Psi_2(x, y, z) = \int_{-\infty}^{\infty} \int_{-\infty}^{\infty} C(k_x, k_y) \sinh(k_{xy} z) e^{i(k_x x + k_y y)} dk_x dk_y \quad (3.18)$$

$$\Psi_3(x, y, z) = - \int_{-\infty}^{\infty} \int_{-\infty}^{\infty} A(k_x, k_y) e^{k_{xy} z} e^{i(k_x x + k_y y)} dk_x dk_y. \quad (3.19)$$

It should be noted that the solutions for the potential,  $\Psi$ , take the form of Fourier integrals over the continuous space that is defined by  $k_x$  and  $k_y$ . The constants  $A$  and  $C$  are functions of  $k_x$  and

$k_y$ , and they are independent of  $x$ ,  $y$  and  $z$ . It is necessary to solve for these constants in order to obtain the general solution for the potential. The boundary conditions from Equations (3.8) and (3.9) are used to obtain two simultaneous algebraic equations in  $A$  and  $C$ . The first equation is obtained from continuity of the magnetic potential at the upper surface of the magnet array. Equations (3.9), (3.17) and (3.18) are combined at  $z = \frac{1}{2} c$  to yield

$$\int_{-\infty}^{\infty} \int_{-\infty}^{\infty} \left[ A e^{-k_{xy} \frac{c}{2}} - C \sinh \left( k_{xy} \frac{c}{2} \right) \right] e^{i(k_x x + k_y y)} dk_x dk_y = 0 \quad (3.20)$$

which yields the non-trivial solution:

$$A e^{-k_{xy} \frac{c}{2}} - C \sinh \left( k_{xy} \frac{c}{2} \right) = 0. \quad (3.21)$$

The second equation for  $A$  and  $C$  comes from the continuity of the normal magnetic field in the  $z$  direction at the upper surface of the magnet array. The potentials in Equations (3.17) and (3.18) for regions 1 and 2 are then substituted into Equation (3.3) to obtain the  $z$  component of the fields  $H_{1z}$  and  $H_{2z}$  at  $z = \frac{1}{2} c$ :

$$H_{1z} (z = c/2) = \int_{-\infty}^{\infty} \int_{-\infty}^{\infty} k_{xy} A e^{-k_{xy} \frac{c}{2}} e^{i(k_x x + k_y y)} dk_x dk_y \quad (3.22)$$

$$H_{2z} (z = c/2) = - \int_{-\infty}^{\infty} \int_{-\infty}^{\infty} k_{xy} C \cosh \left( k_{xy} \frac{c}{2} \right) e^{i(k_x x + k_y y)} dk_x dk_y. \quad (3.23)$$

Next, the surface magnetic charge distribution  $\sigma$  at the upper surface of the magnet array is expressed as a double inverse Fourier transform over  $k_x$  and  $k_y$ :

$$\sigma(x, y, c/2) = \frac{1}{(2\pi)^2} \int_{-\infty}^{\infty} \int_{-\infty}^{\infty} \Theta(k_x, k_y) e^{i(k_x x + k_y y)} dk_x dk_y \quad (3.24)$$

where  $\Theta$  is the double Fourier transform of the surface magnetic charge distribution in the frequency domain. Equations (3.24), (3.22), and (3.23) are combined with Equation (3.8) at  $z = \frac{1}{2} c$  and then simplified to arrive at the second algebraic equation for  $A$  and  $C$ .

$$k_{xy} A e^{-k_{xy} \frac{c}{2}} + k_{xy} C \cosh \left( k_{xy} \frac{c}{2} \right) = \frac{1}{(2\pi)^2} \Theta. \quad (3.25)$$

The system of two simultaneous equations in  $A$  and  $C$  is:

$$\begin{aligned}
e^{-k_{xy}\frac{c}{2}}A - \sinh\left(k_{xy}\frac{c}{2}\right)C &= 0 \\
k_{xy}e^{-k_{xy}\frac{c}{2}}A + k_{xy}\cosh\left(k_{xy}\frac{c}{2}\right)C &= \frac{1}{(2\pi)^2}\Theta
\end{aligned} \tag{3.26}$$

which may be solved simultaneously to arrive at A and C:

$$\begin{aligned}
A &= \frac{1}{(2\pi)^2 k_{xy}} \sinh\left(k_{xy}\frac{c}{2}\right)\Theta \\
C &= \frac{1}{(2\pi)^2 k_{xy}} e^{-k_{xy}\frac{c}{2}}\Theta
\end{aligned} \tag{3.27}$$

The constants are expressed in terms of the Fourier Transform of the surface charge distribution, which may be determined for any in-plane magnet array so long as all magnets are of the same thickness  $c$  and have vertical magnetization. The general solution for the potential in the three regions in terms of the Fourier transform of the charge distribution is

$$\Psi_1 = \frac{1}{(2\pi)^2} \int_{-\infty}^{\infty} \int_{-\infty}^{\infty} \frac{\Theta(k_x, k_y)}{k_{xy}} \sinh\left(k_{xy}\frac{c}{2}\right) e^{-k_{xy}z} e^{i(k_x x + k_y y)} dk_x dk_y \tag{3.28}$$

$$\Psi_2 = \frac{1}{(2\pi)^2} \int_{-\infty}^{\infty} \int_{-\infty}^{\infty} \frac{\Theta(k_x, k_y)}{k_{xy}} e^{-k_{xy}\frac{c}{2}} \sinh(k_{xy}z) e^{i(k_x x + k_y y)} dk_x dk_y \tag{3.29}$$

$$\Psi_3 = \frac{-1}{(2\pi)^2} \int_{-\infty}^{\infty} \int_{-\infty}^{\infty} \frac{\Theta(k_x, k_y)}{k_{xy}} \sinh\left(k_{xy}\frac{c}{2}\right) e^{k_{xy}z} e^{i(k_x x + k_y y)} dk_x dk_y. \tag{3.30}$$

The magnetic field is found by substituting the potential into Equation (3.3). In region 1 above the magnets, the potential is differentiated to get the components of the magnetic field,  $H_1$ . The potential is a complex-valued function, and only the real part of each component is considered to find the field:

$$H_{1x} = \text{Re} \left[ \frac{-i}{(2\pi)^2} \int_{-\infty}^{\infty} \int_{-\infty}^{\infty} \Theta(k_x, k_y) \frac{k_x}{k_{xy}} \sinh\left(k_{xy}\frac{c}{2}\right) e^{-k_{xy}z} e^{i(k_x x + k_y y)} dk_x dk_y \right] \tag{3.31}$$

$$H_{1y} = \text{Re} \left[ \frac{-i}{(2\pi)^2} \int_{-\infty}^{\infty} \int_{-\infty}^{\infty} \Theta(k_x, k_y) \frac{k_y}{k_{xy}} \sinh\left(k_{xy}\frac{c}{2}\right) e^{-k_{xy}z} e^{i(k_x x + k_y y)} dk_x dk_y \right] \tag{3.32}$$

$$H_{1z} = \text{Re} \left[ \frac{1}{(2\pi)^2} \int_{-\infty}^{\infty} \int_{-\infty}^{\infty} \Theta(k_x, k_y) \sinh\left(k_{xy} \frac{c}{2}\right) e^{-k_{xy} z} e^{i(k_x x + k_y y)} dk_x dk_y \right]. \quad (3.33)$$

The same approach may be taken to find the field equations in regions 2 and 3. In practical applications, e.g. in micro-devices, the field within the magnets is not pertinent to the design problem and so this is generally not necessary to compute.

The preceding equations are calculated for a magnet array in air. In many applications, back iron is used beneath the magnet arrays. This may be easily modeled without loss of generality by assuming infinite permeability and by using the method of images as outlined in [167]. In this case, the solution effectively doubles the thickness of the magnets in the context of the simulation.

Equations (3.31) - (3.33) predict the magnetic field above a planar array of permanent magnets with vertical magnetization in air. The equations indicate that the fields are the double inverse Fourier Transform of the surface charge distribution that is multiplied by an exponential. For instance, the  $x$  component of the field is:

$$H_{1x} = \text{Re} \left[ -iF^{-2} \left( \Theta(k_x, k_y) \frac{k_x}{k_{xy}} \sinh\left(k_{xy} \frac{c}{2}\right) e^{-k_{xy} z} \right) \right] \quad (3.34)$$

where  $F^{-2}$  indicates the double inverse Fourier transform of the quantity in parenthesis. As long as the magnetic charge distribution is Fourier-transformable, the field may be calculated everywhere in three directions. It is typically difficult to directly calculate the integrals and therefore numerical solutions are useful. Several FFT algorithms have been created to quickly compute double Fourier transforms, and they may be used to conduct faster computation of the fields along horizontal planes, for instance at constant  $z$ , in comparison to calculation via the superposition integral.

### 3.1.2.C Model Limitations

The Fourier Transform field solution was created to enable efficient calculation of the fields that are a) due to permanent magnets and b) located along planes that are normal to the magnetization vector. The limitations of the model are listed below.



(a) The model assumes no current distributions throughout the solution region. Fields that are caused by current distributions must be solved independently and then added to the permanent magnet solution to arrive at the total field solution.

(b) The solution applies to magnet arrangements with vertical magnetization, as imposed by the boundary conditions. Geometries such as Halbach arrays with in-plane magnetization components cannot be accurately modeled using this approach.

(c) Vertical magnetization distributions in the  $x$ - $y$  plane must be Fourier-transformable.

(d) All magnets in the arrangement must have equivalent thickness and vertical position. This ensures that the magnetically-charged surfaces are at equal height, as required by the boundary conditions. If necessary, it is possible to solve the more general case by summing independent solutions for magnetic charges on different parallel planes.

(e) The solution does not apply to systems that include soft magnetic materials such as flux guides or permeable cores. The solution captures the effect of “infinitely extending” back-iron, as discussed in the previous sub-section.

(f) The FFT is computed once per field component and this yields field values that are along an  $x$ - $y$  plane. In cases where the field must be computed at multiple heights, for instance along a vertical plane, the FFT must be re-computed for each height value. In these cases, the Fourier method compares less favorably to numerical approximation of the superposition integral.

(g) The solution is bounded at the pole surfaces, but the resulting field may contain high frequencies. In order to obtain accurate results, the FFT may sometimes require a large range of frequencies and possibly increased computation time.

### 3.1.3 Three-Pole Actuator Magnet Array

The three-pole microactuator magnet array is used to illustrate the use of the field equations that were discussed in the preceding section. The array consists of three alternating-pole magnets. The magnet arrangement and parameters are shown in Figure 3.4. The uniform magnetization,  $\mathbf{M}$ , is along the  $z$  direction, and  $a$ ,  $b$  and  $c$  are the dimensions of the magnets. The

coordinate system is located at the centroid of the center magnet, such that the magnetic charge surfaces are located at  $z = \pm \frac{1}{2} c$  as in the preceding analysis.

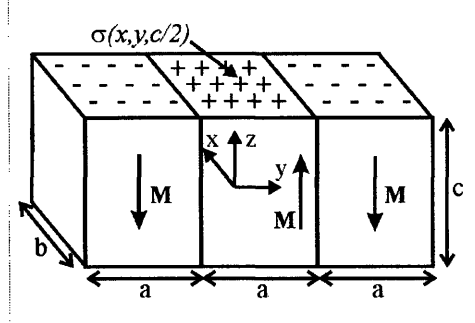


**Figure 3.4. Schematic representation of the example three-pole magnet arrangement.**

The arrangement of magnets in Figure 3.4 has an even surface charge distribution function  $\sigma(x, y, \frac{1}{2}c)$  that consists of three top-hat functions. The double Fourier transform of the distribution is:

$$\Theta(k_x, k_y) = \frac{4M}{k_x k_y} \sin \frac{1}{2} b k_y \left( 2 \sin \frac{1}{2} a k_x - \sin \frac{3}{2} a k_x \right). \quad (3.35)$$

The model in Figure 3.4 was used a) to predict the field characteristics in the following simulation studies and b) to compare predicted fields to measurements from an experiment. The model was also used to compute the Lorentz force acting on the planar-coil microactuator. This will be discussed in detail within section 3.2.

### 3.1.4 Numerical Analysis

The Fourier solution has been compared to the closed-form solution that is given by Akoun [165] and to numerical approximation of the superposition integral. The fields are compared at a height of  $z = c$  above the magnet mid-thickness. The normalized root-mean-square (RMS) percent error between the numerical approximations and the closed-form solution for each flux density component is computed as:

$$E_{x,y,z} = 100 \times \frac{1}{\max(B_{ref,x,y,z})} \sqrt{\frac{1}{N_x N_y} \sum_j^{N_y} \sum_i^{N_x} (B_{x,y,z}(i,j) - B_{ref,x,y,z}(i,j))^2}. \quad (3.36)$$

where  $\max(B_{ref,x,y,z})$  is the maximum flux density for each component;  $B_{x,y,z}$  is the field component that is computed from the Fourier or superposition integral methods;  $B_{ref,x,y,z}$  is the field component that is computed from the closed form solution; and  $N_x$  and  $N_y$  are the number of

points in the  $x$ - and  $y$ - directions. The RMS error is computed for variable discretizations in both the Fourier and superposition integral methods, and the resulting computation time is plotted on a log-log scale in Figure 3.5.

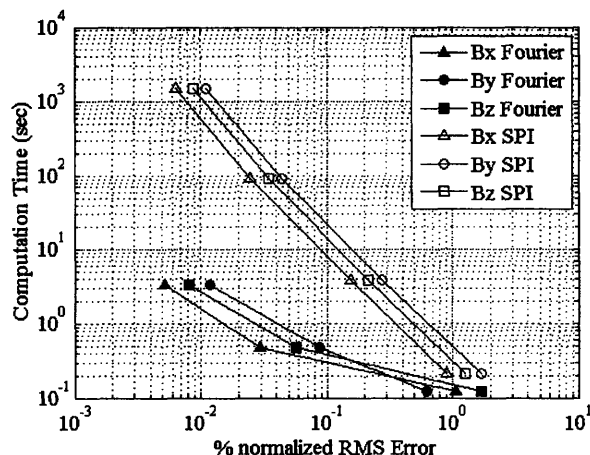


**Figure 3.5. Computation time vs. normalized RMS error for each component of the flux density at  $z = c/2$  above the example magnet surface as computed by the Fourier transform and superposition integral (SPI) methods**

The computation was executed in MATLAB using standard FFT routines on a 1.7 GHz Pentium processor with 1 Gb RAM operating Windows XP. The data shows that the Fourier method converges by an order-of-magnitude faster than the superposition integral method for errors that are less than 1%.

### 3.1.5 Comparison of Predicted and Measured Field Characteristics

An experiment was designed to provide the means to measure the magnetic flux density data in  $x$ - $y$ - $z$  directions upon a plane that was above a set of neodymium–iron–boron magnets. Figure 3.6 shows the setup.

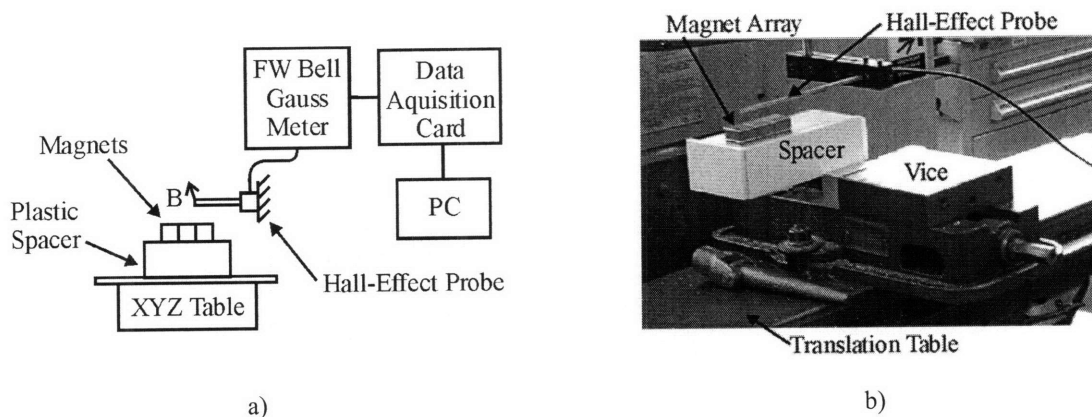


**Figure 3.6. Schematic of the Equipment used to acquire data (a) and corresponding experimental setup (b).**

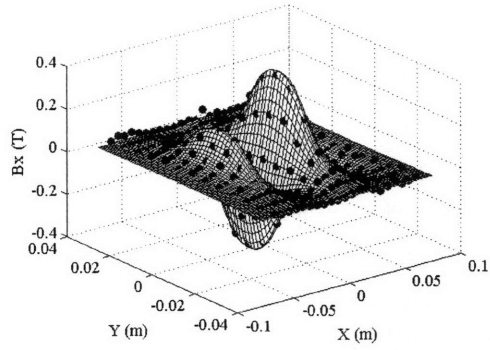
A set of the three permanent magnets were arranged according to Figure 3.4 and then mounted on a programmable  $x$ - $y$ - $z$  translation table with positional accuracy of 12.7 micrometers. The magnet array was mounted to the table with a 100 mm plastic spacer to minimize field interaction with the steel components of the translation table. A one-axis F. W. Bell Hall-effect probe (model HTG92-0608) was fixed above the magnet array and connected to an F. W. Bell Model 9550 Gauss meter. Total field measurement's linearity error was 2% of the reading. Data from the gauss meter was collected via a 12-bit National Instruments DAQCard-6024E PCMCIA card and a laptop PC running LabView. The system measurement noise floor was measured in regions of zero field to be 17.43 mT with a 95% confidence level.

Measurements of independent flux density components are made by orienting the probe and stepping through a preset grid of  $x$ - $y$  coordinates with step pitch  $p = 6.35$  mm. Measurements were taken at a fixed height,  $h = 5.08$  mm, above the magnet's upper surface. The location of the magnet array is registered to the probe before making measurements by locating the maximum and zero-values of the flux density. The flux density components were recorded at each  $x$ - $y$  coordinate, and the experiment was repeated for the field components,  $B_x$ ,  $B_y$  and  $B_z$ . Table 1 lists the geometric characteristics and the magnetic properties of the experiment. Nickel-plated N35-grade neodymium iron boron magnets were used in the experiment, and the catalog value for the remnance flux density was used in the calculations.

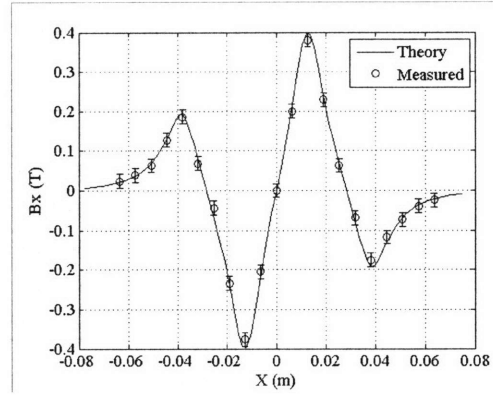
**Table 3.1. Dimensions and material properties of the experiment.**

Symbol	Description	Quantity	Units
a	Magnet width	25.4	mm
b	Magnet depth	25.4	mm
c	Magnet height	25.4	mm
h	Measurement height	5.08	mm
Br	Remnance	$1.23 \pm 0.01$	T
p	Measurement pitch	6.35	mm

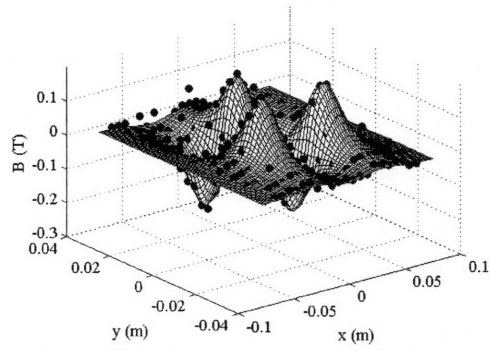
The predicted components are computed using a two-dimensional FFT algorithm. The  $m \times n$  point FFT is computed for  $m = n = 200$ , or 40,000 total points. The corresponding truncation limits for  $K_x$  and  $K_y$  are  $L = m\pi / 12a \approx 2.06\text{mm}^{-1}$ . Computation details are discussed in section 3.1.4. Discretization of the magnetic charge distribution required 1.5 sec, whereas calculation of all three field components along an  $m \times n$  plane required 0.15 sec. Figure 3.7a through Figure 3.7c compare the measured and predicted components of the flux density. The cross-sections of these plots, at fixed  $y$  values, are shown in Figure 3.7d-f in order to better illustrate the agreement between the measured and predicted values. The error bars represent the system noise floor of 17.4mT, or 4% of the maximum reading. The plots show that the predicted flux density values fall within the measurement error.



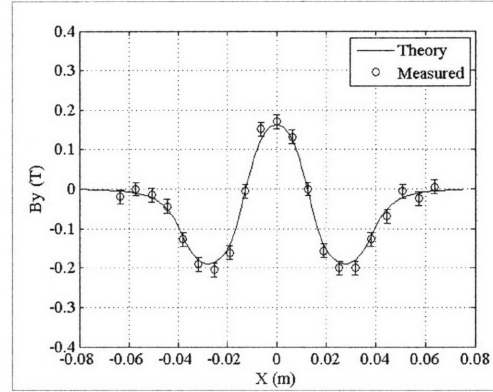
a)



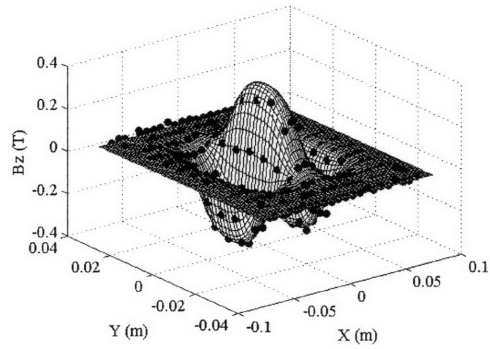
d)



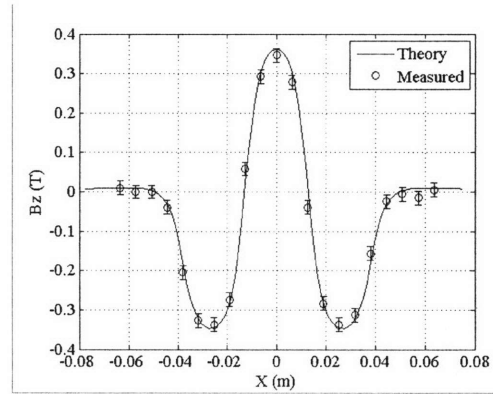
b)



e)



c)



f)

**Figure 3.7. Comparison of predicted (surface) vs. measured (points) values of the x (a), y (b), and z (c) components of the magnetic flux density. Cross-sections of the x surface at  $y = 0$  mm (d), y surface at  $y = 12.7$  mm (e) and z surface at  $y = 0$  mm (f).**

### 3.2 Lorentz Coil Force

The purpose of this section is to generate Lorentz force models that may be used to design and optimize the microactuator geometry. The Lorentz force that acts upon the actuator coil is caused by the interaction between the current in the coil windings and the external permanent magnetic field [168]. In a micro-coil actuator that uses millimeter-scale permanent magnets, the winding cross-section is typically tens-of-micrometers per side. This dimension is small when compared to the characteristic length over which the magnetic field changes, which is the same order of magnitude as the magnet dimensions. The coil current may therefore be modeled as a line current that acts at the center of the winding. This assumption breaks down when the field changes rapidly over the characteristic length of the winding cross-section ( $dB/dx \sim B_{\text{average}}/w_{\text{winding}}$ ). The coil windings are also fixed to a paddle so that windings cannot move with respect to one another. Therefore, the Lorentz forces that are caused by the fields from the current in one winding cannot do work upon another winding. As a result, the fields that are caused by the coil winding currents do not contribute to the Lorentz force. The Lorentz force is computed using the fields only from the permanent magnets. The total force acting on the coil is then computed by integrating the Lorentz force over the length of the coil:

$$\mathbf{F}_{\text{coil}} = \int_L i \mathbf{l}(\mathbf{r}) \times \mathbf{B}(\mathbf{r}) dl \quad (3.37)$$

In addition, the total moment about a reference point  $O$  is

$$\mathbf{M}_{\text{coil},o} = \int_L (\mathbf{r} - \mathbf{r}_o) \times i \mathbf{l}(\mathbf{r}) \times \mathbf{B}(\mathbf{r}) dl \quad (3.38)$$

In these equations,  $i$  represents the current flowing through the winding,  $\mathbf{r}$  is the position vector of the current,  $\mathbf{l}$  is the current direction,  $\mathbf{B}$  is the local magnetic field at the current increment,  $dl$  is the length increment, and  $\mathbf{r}_o$  is the position vector of the reference point. The parameter  $L$  represents the length of the coil. The  $x$ -,  $y$ -, and  $z$ - components of the forces and moments acting on the coil may be computed by using all three components of the local magnetic field.

The actuator architecture presented in section 2.5.4 uses three alternating pole magnets. The resulting fields were computed using the Fourier transform model and numerical method that was presented in section 3.1. The Lorentz force was computed using the field values from the Fourier model via numerical approximation of Equations (3.37) and (3.38) by the trapezoidal rule [169]. The algorithm first breaks the coil into straight segment legs and then discretizes

each segment. The local Lorentz force is computed for each discretization by taking the cross product of the permanent magnet flux density and the current vector. In this algorithm, the position of the segment does not coincide with the grid coordinates of the flux density. The flux density is therefore linearly interpolated at the segment coordinate. The algorithm computes the total force,  $F_s$ , that acts at the geometric center of the segment by summing the discretized forces over the length of the segment with the trapezoidal rule. By using a similar procedure, the total moment,  $M_s$ , about the center of the segment may be computed by summing the cross product of the discretized forces and the position vector from the center of the segment. After the force,  $F_s$ , and moment,  $M_s$ , are computed for each segment, the total force on the coils is then computed by summing the forces,  $F_s$ , of all coil segments. The total moment on the coil is then computed by summing a) the previously computed segment moments,  $M_s$ , and b) the moments that are caused by the segment forces,  $F_s$ , that act about the reference point  $O$ . This algorithm was implemented in MATLAB using 1000 discretizations per coil segment. The simulation requires less than 20 seconds of computation time when using standard quadrature routines on a 1.7 GHz Pentium processor with a Windows XP operating system with 1 Gb RAM.

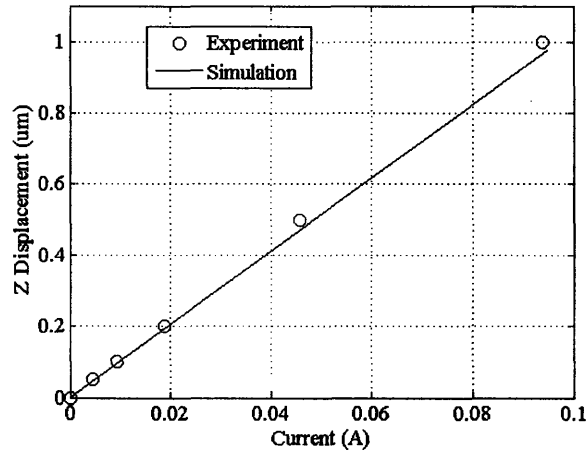
The accuracy of the Lorentz force model was ascertained by comparison of simulated and measured displacement of the bench-level nanopositioner that was presented in section 2.8. The predicted Lorentz coil force was applied to a linear-elastic CosmosWorks FEA model of the nanopositioner's HexFlex mechanism. In the simulation and experiment, the nanopositioner was driven in the out-of-plane z-direction by applying equivalent current to each of the out-of-plane actuator coils. The resulting stage displacement from simulation was then compared with measurements from the setup presented in 2.8.2. The geometric parameters that were used in simulation were measured from the experimental system. Table 3.2 shows the measured actuator coil parameters that were used in the force model.



**Table 3.2. Bench-level prototype coil actuator design parameters**

Symbol	Parameter	Value	Units
$A_{\text{coil}}$	Coil Footprint	156	$\text{mm}^2$
$I_{\text{max}}$	Maximum Current	500	mA
$A_{\text{winding}}$	Winding Cross-Sectional Area	10972	$\mu\text{m}^2$
$g$	Winding gap	254	$\mu\text{m}$
$N_x, N_z$	X, Z Actuator Coil Turns	5	Turns
$w_x, w_z$	X, Z Actuator Winding Width	2	mm
$d_x$	X Actuator Winding Spacing	1.2	mm
$d_z$	Z Actuator Winding Spacing	8.5	mm
$h_x$	X Actuator Height	3.73	mm
$h_z$	Z Actuator Height	5.23	mm
$a$	Cuboidal Magnet Dimension	6.35	mm

Figure 3.8 shows the measured and predicted out-of-plane displacement data versus the actuator current for the bench-level prototype. The error bars in the plot are  $\pm 20$  nm and they are therefore omitted. The data indicates that the predicted and measured displacements differ by less than 5%. This is suitable for initial engineering design and optimization efforts. The difference in experiment and prediction is attributed to the following measurement errors: a) estimated coil height error of 5% and b) and 3% variation in flexure beam width and thickness.

**Figure 3.8. Measured vs. predicted bench-level prototype displacement in the z-direction.**

### 3.3 Electrical Circuit Model

Each actuator coil may be modeled as a circuit that possess series inductance and resistance, as shown in Figure 3.9a. The stacked coils share a mutual inductance  $L_{xz}$  and a mutual capacitance  $C_m$ . The coil's self-capacitance is assumed to be negligible when compared

to the mutual capacitance. The self capacitance is small because of the relatively large gap between the coil windings, on the order of 10  $\mu\text{m}$ , and relatively small self-capacitance area of approximately 0.5  $\text{mm}^2$ .

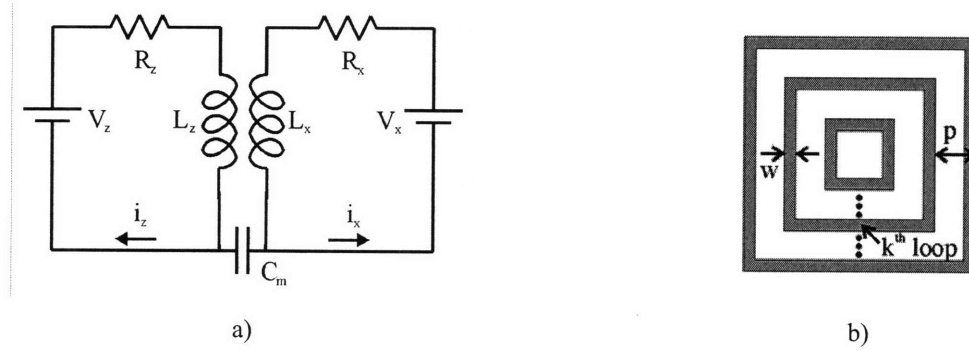


Figure 3.9. a) Electrical circuit model of an actuator coil. b) Planar-spiral coil model for approximating the inductance.

### 3.3.1 Coil Resistance

The coil resistance is modeled using the classic relation

$$R = \frac{\rho L_c}{w_w t_w} \quad (3.39)$$

where  $\rho$  is the resistivity of winding coil material,  $L_c$  is the length of the coil,  $w_w$  is the winding width, and  $t_w$  is the winding thickness. In this relation, the length of the coil is taken along the centerline of the windings and it is computed numerically for the actuator coils.

### 3.3.2 Self-Inductance

The self-inductance of the rectangular planar spiral coil may be calculated numerically by computing the total flux linkage through all concentric rectangular loops. Other numerical approaches have been developed to accurately compute the self inductances of circular planar coils [170]. The simplified model in Figure 3.9b may be used for the purpose of estimating the self-inductance and electrical time constant for one actuator coil. The  $z$ -component of the flux density along the planar coil is computed by numerical integration the Biot-Savart integral for fields due to line currents. The model assumes that the coils are in air so that the permeability is of free-space:  $\mu = \mu_o$ . The flux density within the  $k^{\text{th}}$  loop that is due to the current in the  $j^{\text{th}}$  loop is  $B_{kj}$ . The flux through the  $k^{\text{th}}$  loop that is due to the current in the  $j^{\text{th}}$  loop is  $\Phi_{kj}$ . The inductance is the sum of fluxes through all the loops divided by the current in the coil,  $i$ :

$$L = \frac{1}{i} \sum_{k=1}^N \sum_{j=1}^N \Phi_{kj} = \frac{1}{i} \sum_{k=1}^N \sum_{j=1}^N \int_{A_k} B_{kj} dA_k \quad (3.40)$$

where  $A_k$  is the area of the  $k^{\text{th}}$  loop. Equation (3.40) may be combined with Equation (3.39) to estimate the electrical roll-off frequency of a single-coil L-R circuit:

$$f = \frac{1}{2\pi} \frac{R}{L}. \quad (3.41)$$

### 3.3.3 Mutual Inductance

The mutual inductance of the stacked coil microactuator may be estimated using numerical methods [170]. In the proposed actuator, the stacked coils are separated by a thin dielectric, and therefore it is acceptable to approximate their height offset as zero. The mutual inductance may be estimated by calculating the field that is caused by one coil, then computing the flux of this field through the second coil. This computation has not yet been implemented for the stacked-coil actuator coil.

### 3.3.4 Mutual Capacitance

The mutual capacitance of the stacked actuator coils that are separated by a thin dielectric may be estimated by the parallel plate approximation:

$$C_m = \frac{\kappa \epsilon_0 A}{t} \quad (3.42)$$

where  $\kappa$  is the dielectric constant,  $A$  is the overlapping footprint area of the coils and  $t$  is the thickness of the dielectric insulator. In a planar spiral coil, some of the coil area is consumed by the gaps between windings. A coil winding packing factor may be used to more accurately model the overlapping conductor areas.

## 3.4 Kinematic and Dynamic Model

The purpose of this section is to generate a parametric mechanical model that predicts the static displacement and resonant frequency of the coil-driven nanopositioner. This model may then be used to design the flexure mechanism to meet the corresponding functional requirements. Figure 3.10 shows a schematic model of the double-sided bent-beam unit flexure, which is comprised of three beam elements in series with lengths  $L_1$ ,  $L_2$ , and  $L_3$ . The beams link the actuator paddle to ground. In the six-axis flexure, another beam element that is located between the bent-beam flexures links the actuator paddle and stage. Figure 3.10 also shows the cross-

section of the multi-layer flexure beams, which are comprised of two copper leads on a silicon beam. In the actual device, a thin dielectric separates the silicon and copper layers. This layer is omitted for clarity in the figure. The modeling approach begins by calculating the stiffness of the single-sided bent-beam flexure. The single-sided flexure stiffness is then combined with symmetry constraints to generate a stiffness model for the double bent-beam flexure. The unit double bent-beam stiffnesses values,  $k_x$ ,  $k_y$ , and  $k_z$ , are then used in six-DOF lumped-parameter mass-spring model of the nanopositioner flexure. This model of the six-axis flexure predicts the static displacement and resonant modal frequencies of the flexure mechanism.

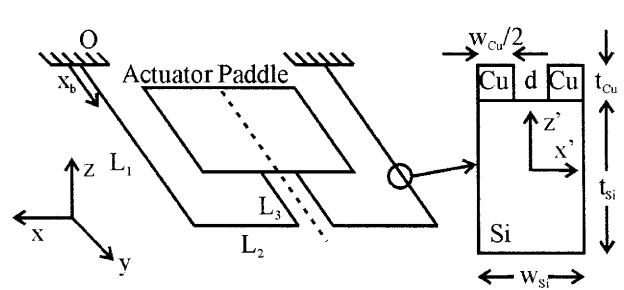


Figure 3.10. Schematic model of the double bent-beam flexure with cross-section of the multi-layer beam.

### 3.4.1 Model Setup and Boundary Conditions

The mechanical model uses small-deformation, linear elastic beam bending models [171]. This model assumes the following:

a) The ratio of beam length to beam thickness is larger than 10, therefore the deformation that is caused by shear will be less than 2% of those that are caused by bending and they are therefore neglected.

b) Lateral displacements of the beams are more than 1000 times less than the beam length and therefore a small angle approximation is suitable when predicting the angle of bent beams.

c) Axial stiffness is more than 1000 times greater than bending stiffness therefore compression deformations are not included.

d) The magnitude of compressive forces and lateral deflections that are required to induce buckling are at least 10 times larger than those that are experienced in this application.

The displacement  $u_i$  along the  $i^{th}$  beam that is caused by the bending moment  $M_b(x_i)$  along the beam is solved from:

$$\frac{d^2}{dx_i^2} u_i(x_i) = \frac{M_b(x_i)}{(EI)}. \quad (3.43)$$

The quantity  $(EI)$  represents the in-the-plane or out-of-the plane flexural rigidity of the beam about its neutral axis. In the case of out-of-plane forces, beam torsion must be considered. The twist angle  $\theta_i(x_i)$  along the  $i^{th}$  beam that is caused by the torsional moment is described by:

$$\theta_i(x_i) = \frac{M_t(x_i)x_i}{(KG)}. \quad (3.44)$$

In this equation, the quantity  $(KG)$  represents the torsional rigidity of the multi-layered beam about the neutral axis. The boundary conditions are specified at the point O in Figure 3.10, where the displacement and angle are constrained to be zero:

$$\begin{aligned} u_{x,1}(0) = u_{y,2}(0) = u_{z,3}(0) = 0 \\ \theta_{x,1}(0) = \theta_{y,2}(0) = \theta_{z,3}(0) = 0 \end{aligned} \quad (3.45)$$

### 3.4.2 Flexural Rigidity

The effective in-plane  $(EI)_z$  and out-of-plane  $(EI)_x$  flexural rigidity are computed with respect to the neutral axis of the cross-section  $x'-z'$  as shown in Figure 3.10. The out-of-plane rigidity of the multi-layer flexure beam about its neutral axis is derived using the method of Weinberg [136]. The dielectric layer that separates the silicon and copper less than 1% of the beam thickness and therefore it adds less than 1% to any beam's lateral stiffness. The dielectric's contributions to stiffness are therefore neglected. The flexural rigidity is computed only for the silicon-copper two-layer beam. The neutral axis of the two-layer beam as measured from the bottom of the stack is given by:

$$Z_n = \frac{t_{Si}E_{Si}A_{Si} + (2t_{Si} + t_{Cu})E_{Cu}A_{Cu}}{2(E_{Si}A_{Si} + E_{Cu}A_{Cu})} \quad (3.46)$$

where  $E$  and  $A$  are the modulus and cross-section area of the material layer, respectively. The out-of-plane bending rigidity about the  $x'$  neutral axis is:

$$(EI)_x = \frac{4(E_{Si}A_{Si} + E_{Cu}A_{Cu})(E_{Si}I_{x,Si} + E_{Cu}I_{x,Cu}) + (t_{Si} + t_{Cu})^2 E_{Si}E_{Cu}A_{Si}A_{Cu}}{4(E_{Si}A_{Si} + E_{Cu}A_{Cu})}. \quad (3.47)$$

In this expression,  $I$  is the area moment of inertia about the layer's neutral axis given by:

$$I_x = \frac{1}{12} wt^3 \quad (3.48)$$

where  $w$  and  $t$  are the width and thickness of the layer. The in-plane bending rigidity of the cross-section about its  $z'$  axis may be derived by treating the layers as side-by-side beams so that the bending rigidities may be added together. The two copper leads are treated as separate beams, and their moments about the neutral axis  $z'$  are determined by using the parallel axis theorem. This yields an expression for the in-plane flexural rigidity of the beam:

$$(EI)_z = E_{Si}I_{z,Si} + 2E_{Cu}I_{z,Cu} + \left(\frac{d}{2} + \frac{w_{Cu}}{4}\right)^2 A_{Cu}. \quad (3.49)$$

In this expression, the moment of inertia about the layer's neutral axis is given by:

$$I_z = \frac{1}{12} w^3 t \quad (3.50)$$

### 3.4.3 Torsional Rigidity

The solution to the torsional rigidity ( $KG$ ) of the composite cross-section in Equation (3.44) may not be derived in closed form. Instead, it is computed numerically by fitting Equation (3.44) to experimental or FEA data. In this approach, a known moment is applied to the end of a beam with the cross-section shown in Figure 3.10. The beam has known length, and the resulting angular displacement is measured at the free end. The rigidity is then determined by linear regression of the simulated moment and angular displacement. A linear-elastic simulation in COSMOSWorks was used to obtain the data for the linear fit.

### 3.4.4 Single-Sided Bent-Beam Unit Flexure

Figure 3.11 shows a schematic model of the actuator force,  $F$ , and moment,  $M$ , that act upon the single-sided unit flexure at point C, where the flexure connects to the actuator paddle.

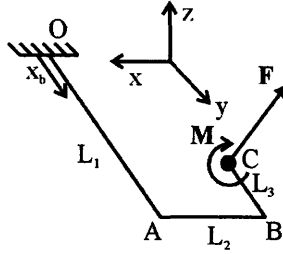


Figure 3.11. Schematic model of the single-sided bent-beam flexure.

The static displacement and static angle of rotation that is caused by the force and moment are derived via:

- a) application of a statics analysis to determine the forces on each beam element;
- b) solution of Equations (3.43) and (3.44) for the sequence of beams 1-3, starting with beam 1 and using the boundary conditions in Equation (3.45).

The displacement and angle of rotation at the end of the  $i^{\text{th}}$  beam ( $x_i = L_i$ ) is then used as the starting boundary condition for the next beam at  $x_{i+1} = 0$ . This procedure is repeated to arrive at the displacements and rotations at point C that are caused by each component of the force and moment. The resulting in-plane displacements and rotations at point C that are caused by the in-plane forces and moments that act upon the single-sided unit flexure are given by the following set of equations:

$$u_{x,Fx} = F_x \frac{1}{(EI)_z} \left( \frac{1}{3} L_1^3 + \frac{1}{3} L_3^3 + L_1 L_3^2 - L_1^2 L_3 + L_2 L_3^2 \right) \quad (3.51)$$

$$u_{x,Fy} = F_y \frac{1}{(EI)_z} \left( \frac{1}{2} L_1^2 L_2 - \frac{1}{2} L_2^2 L_3 - L_1 L_2 L_3 \right) \quad (3.52)$$

$$u_{x,Mz} = M_z \frac{1}{(EI)_z} \left( -\frac{1}{2} L_1^2 + \frac{1}{2} L_3^2 + L_3 (L_1 + L_2) \right) \quad (3.53)$$

$$u_{y,Fx} = F_x \frac{1}{(EI)_z} \left( \frac{1}{2} L_1^2 L_2 - \frac{1}{2} L_2^2 L_3 - L_1 L_2 L_3 \right) \quad (3.54)$$

$$u_{y,Fy} = F_y \frac{1}{(EI)_z} \left( \frac{1}{3} L_2^3 + L_1 L_2^2 \right) \quad (3.55)$$

$$u_{y,Mz} = M_z \frac{1}{(EI)_z} \left( -\frac{1}{2} L_2^2 - L_1 L_2 \right) \quad (3.56)$$

$$\theta_{z,Fx} = F_x \frac{1}{(EI)_z} \left( -\frac{1}{2}L_1^2 + \frac{1}{2}L_3^2 + L_3(L_1 + L_2) \right) \quad (3.57)$$

$$\theta_{z,Fy} = F_y \frac{1}{(EI)_z} \left( -\frac{1}{2}L_2^2 - L_1L_2 \right) \quad (3.58)$$

$$\theta_{z,Mz} = M_z \frac{1}{(EI)_z} (L_1 + L_2 + L_3). \quad (3.59)$$

The out-of-plane displacements and rotations at point C that are caused by the out-of-plane forces and in-plane moments that act upon the single-sided unit flexure are as follows:

$$u_{z,Fz} = F_z \left( \frac{1}{(EI)_x} \left( \frac{1}{3}L_1^3 + \frac{1}{3}L_2^3 + \frac{1}{3}L_3^3 + L_1L_3^2 - L_1^2L_3 \right) + \frac{1}{(KG)} (L_1L_2^2 + L_2L_3^2) \right) \quad (3.60)$$

$$u_{z,Mx} = M_x \left( \frac{1}{(EI)_x} \left( \frac{1}{2}L_1^2 - \frac{1}{2}L_3^2 - L_1L_3 \right) - \frac{1}{(KG)} L_2L_3 \right) \quad (3.61)$$

$$u_{z,My} = M_y \left( \frac{1}{2(EI)_x} L_2^2 + \frac{1}{(KG)} L_1L_2 \right) \quad (3.62)$$

$$\theta_{x,Fz} = F_z \left( \frac{1}{(EI)_x} \left( \frac{1}{2}L_1^2 - \frac{1}{2}L_3^2 - L_1L_3 \right) - \frac{1}{(KG)} L_2L_3 \right) \quad (3.63)$$

$$\theta_{x,Mx} = M_x \left( \frac{1}{(EI)_x} (L_1 + L_3) + \frac{1}{(KG)} L_2 \right) \quad (3.64)$$

$$\theta_{x,My} = 0 \quad (3.65)$$

$$\theta_{y,Fz} = F_z \left( \frac{1}{2(EI)_x} L_2^2 + \frac{1}{(KG)} L_1L_2 \right) \quad (3.66)$$

$$\theta_{y,Mx} = 0 \quad (3.67)$$

$$\theta_{y,My} = M_y \left( \frac{1}{(EI)_x} L_2 + \frac{1}{(KG)} (L_1 + L_3) \right). \quad (3.68)$$

Equations (3.51) through (3.68) provide a complete force-displacement model for the single-sided bent-beam flexure system that is shown in Figure 3.11.



### 3.4.5 Double Bent-Beam Flexure

The equations that were generated in the preceding section are combined with appropriate boundary conditions to yield stiffness relations for the double-bent beam flexure. Figure 3.12 shows a lumped parameter stiffness model for the double-bent beam flexure and the actuator paddle. The flexures connect to the actuator paddle at point  $C$  in the figure. The angular constraints are applied at point  $C$  where the flexure meets the actuator paddle in order to obtain expressions that predict pure translation. The displacement subject to the angular constraints is then expressed in terms of the applied force at point  $C$ . The stiffness for the single-sided flexure in each axis is then

$$k_{x,y,z,l} = \frac{F_{c,x,y,z}}{u_{c,x,y,z}}. \quad (3.69)$$

The double-sided flexure stiffness is then obtained by adding two single-sided bent beam flexures in parallel:

$$k_{x,y,z} = 2k_{x,y,z,l}. \quad (3.70)$$

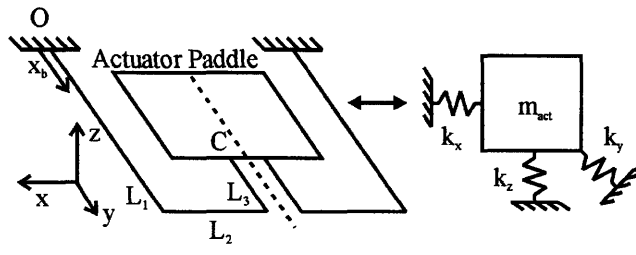


Figure 3.12. Lumped parameter stiffness model of the double-bent beam flexure.

The  $x$ -direction stiffness,  $k_{x,l}$ , of the single bent-beam flexure is derived by using the symmetry condition at point  $C$ :

$$\theta_z(C) = \theta_{z,F_x}(C) + \theta_{z,M_z}(C) = 0. \quad (3.71)$$

In this equation, the symmetry condition requires that a moment is applied to prevent rotation about the  $z$ -axis. This moment,  $M_z$ , is obtained from Equation (3.71) in terms of the input force  $F_x$ . The corresponding translation in  $x$  for a single-sided flexure is the sum of the displacement that is caused by the applied force and the displacement that is caused by the constraint moment:

$$u_x(C) = u_{z,F_x}(C) + u_{z,M_z}(C). \quad (3.72)$$

The stiffness in the x-direction is computed from Equations (3.69) and (3.70) by using the displacement and applied force from Equation (3.72):

$$k_x = 2(EI)_z \left( \begin{array}{c} \frac{1}{3}L_1^3 + \frac{1}{3}L_3^3 + L_1L_3^2 - L_1^2L_3 + L_2L_3^2 \\ -\frac{1}{L_1+L_2+L_3} \left( -\frac{1}{2}L_1^2 + \frac{1}{2}L_3^2 + L_3(L_1+L_2) \right)^2 \end{array} \right)^{-1}. \quad (3.73)$$

A similar procedure is used to determine the y-direction stiffness,  $k_y$ . In this case, the symmetry condition at point  $C$  consists of a rotational and translational constraint:

$$\theta_z(C) = \theta_{z,F_x}(C) + \theta_{z,F_y}(C) + \theta_{z,M_z}(C) = 0 \quad (3.74)$$

$$u_x(C) = u_{x,F_x}(C) + u_{x,F_y}(C) + u_{x,M_z}(C) = 0. \quad (3.75)$$

The constraining force,  $F_x$ , and moment,  $M_z$ , are solved in terms of  $F_y$  from the set of simultaneous Equations (3.74) and (3.75). The constraining force and moment are then used in the following expression for the translation that is caused by the y-directed force,  $F_y$ , and the constraining force and moment:

$$u_y(C) = u_{y,F_x}(C) + u_{y,F_y}(C) + u_{y,M_z}(C). \quad (3.76)$$

The total displacement that is given by Equation (3.76) is used to determine the stiffness in the y-direction:

$$k_y = 2(EI)_z \left( \begin{array}{c} \left( \frac{1}{3}L_2^3 + L_1L_2^2 \right) + \frac{F_x}{F_y} \left( \frac{1}{2}L_1^2L_2 - \frac{1}{2}L_2^2L_3 - L_1L_2L_3 \right) \\ + \frac{M_z}{F_y} \left( -\frac{1}{2}L_2^2 - L_1L_2 \right) \end{array} \right)^{-1}. \quad (3.77)$$

In this equation, the constraining force and moment are expressed in terms of  $F_y$ .

The stiffness,  $k_z$ , in the z-direction is determined by constraining the angle of rotation about  $y$  with moment  $M_y$  applied at point  $C$ :

$$\theta_y(C) = \theta_{y,F_z}(C) + \theta_{y,M_y}(C) = 0 \quad (3.78)$$

The constraining moment is obtained in terms of  $F_z$  by using Equation (3.78). The total displacement consists of the displacement that is caused by the applied force and constraint moment:

$$u_z(C) = u_{z,My}(C) + u_{z,Fz}(C) \quad (3.79)$$

The resulting stiffness in the z-direction is then:

$$k_z = 2 \left[ \frac{1}{(EI)_x} \left( \frac{1}{3}L_1^3 + \frac{1}{3}L_2^3 + \frac{1}{3}L_3^3 + L_1L_2^2 - L_1^2L_3 \right) + \frac{1}{(KG)} (L_1L_2^2 + L_2L_3^2) \right]^{-1} \cdot \frac{(KG)(EI)_x}{(L_1 + L_3)(EI)_x + L_2(KG)} \left( \frac{L_1L_2(EI)_x + L_2^2(KG)}{2(KG)(EI)_x} \right)^2 \quad (3.80)$$

The accuracy of the closed-form equations for translational stiffness characteristics were assessed by using a linear-elastic solid model FEA. The closed-form model values were computed in MATLAB and the FEA values were obtained from COSMOSWorks. Table 3.3 presents the model parameters used for the comparison to FEA. The model used for comparison does not include a copper layer in order to reduce the FEA simulation time. The accuracy of the model may be extended to the composite beam geometry as the cross-section properties of composite beams are readily modeled with good accuracy.

**Table 3.3. Parameters used to compare double bent-beam model to FEA.**

Symbol	Parameter	Value	Units
$t_{Si}$	Silicon Thickness	100	$\mu\text{m}$
$t_{Cu}$	Copper Thickness	0	$\mu\text{m}$
$w_{Si}$	Silicon Width	80	$\mu\text{m}$
$w_{Cu}$	Copper Width	0	$\mu\text{m}$
$L_1$	Length	4400	$\mu\text{m}$
$L_2$	Length	1537	$\mu\text{m}$
$L_3$	Length	1507	$\mu\text{m}$
$E_{Si}$	Modulus	165	GPa
$E_{Cu}$	Modulus	130	GPa

Table 3.4 shows the values of stiffness that were obtained from the closed-form model and FEA. The data indicates that the stiffness predicted by the closed-form model matches the FEA results with less than 1.7% error.

**Table 3.4. Comparison of unit flexure stiffness as predicted by the model and FEA.**

Stiffness	Units	Model	FEA	% Diff
$k_x$	N/m	101.9	100.7	1.1
$k_y$	N/m	532.9	526.3	1.2
$k_z$	N/m	92.2	93.7	1.7

The model for translation stiffness characteristics that were derived in this section are used in the following section to create a lumped-parameter, mass-spring model of the six-axis nanopositioner.

### 3.4.6 Six-Axis Nanopositioner Flexure

The stiffness model for double bent-beam flexure was used to derive lumped-parameter models for the static and dynamic behavior of the six-axis nanopositioner. These models use the Lagrangian formulation to derive the static displacement and resonant frequency for each axes of motion. The Lagrange method is outlined in [172]. In this analysis, the resonant frequency and static displacement are derived for each individual axis of motion. The analysis assumes the following:

1) Small angle approximations are suitable. A justification for this was provided in Section 3.4.1

2) The structural elements that connect the paddle to stage may be considered to be rigid within in-the-plane directions when compared to the double bent-beam unit flexure. This is reasonable because the ratio  $(w_s/L_s)/(w_b/L_b)$  of the beams and the structural elements is larger than 7.5X and therefore the stiffness ratios between them should be larger than 400X;

3) The effect of the beam elements' mass upon the model is negligible when compared to the effect of the paddle and stage masses. This is reasonable because the volume of beam elements is less than 8% of the combined paddle and stage volumes.

In the following sections, a capitalized axis name indicates the global nanopositioner reference frame as shown in Figure 2.2, while a lower-case name indicates the local actuator paddle frame as shown in Figure 3.12.

#### 3.4.6.A X-Axis Stiffness and Modal Frequency

Figure 3.12 shows a lumped-parameter mass-spring model for motion along the  $X$ -axis of the nanopositioner. The model only considers half of the nanopositioner flexure mechanism

because symmetry is assumed. The fixed angle is  $\theta_f = 30$  for the three-way symmetric flexure geometry.

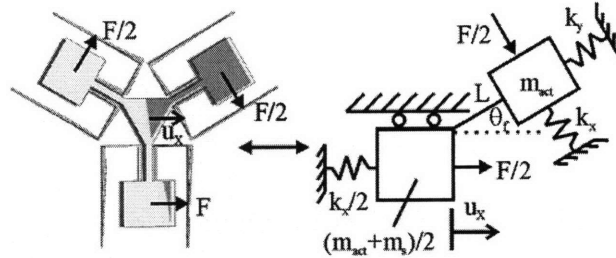


Figure 3.13. Lumped-parameter half model for X-axis translation.

The static displacement along the X-axis that is caused by the in-plane actuator force  $F$  is

$$u_x = F \frac{1}{(k_x + k_y)} \quad (3.81)$$

where  $k_x$  and  $k_y$  are the stiffness values of the double bent-beam unit flexure in the directions that are indicated by the subscripts. The natural frequency for this model is:

$$f_x = \frac{1}{2\pi} \sqrt{\frac{3(k_x + k_y)}{2(3m_{act} + m_s)}} \quad (3.82)$$

In this expression,  $m_{act}$  and  $m_s$  are the masses of actuator paddle and stage, respectively.

### 3.4.6.B Y-Axis Stiffness and Modal Frequency

Figure 3.14 shows a lumped-parameter mass-spring model for motion along the Y-axis of the nanopositioner. The model only considers half of the flexure mechanism because symmetry is assumed.

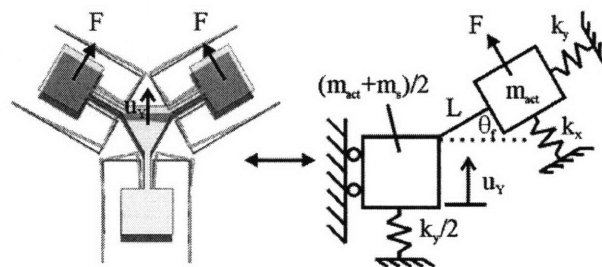


Figure 3.14. Lumped-parameter half model for Y-axis translation.

The static displacement along the Y-axis that is caused by the in-plane actuator force,  $F$ , is

$$u_y = F \frac{\sqrt{3}}{\sqrt{3k_x + 2k_y}}. \quad (3.83)$$

The natural frequency for the  $Y$ -axis motion model is

$$f_y = \frac{1}{2\pi} \sqrt{\frac{3(k_x + k_y)}{2(3m_{act} + m_s)}}. \quad (3.84)$$

### 3.4.6.C $\theta_z$ -Axis Stiffness and Modal Frequency

Figure 3.15 shows a lumped-parameter mass-spring model for rotation about the  $Z$ -axis of the nanopositioner. The model only considers one-third of the flexure mechanism and assumes rotation about a pinned joint at center of the stage. The moment stiffness,  $k_{\theta_z}$ , of the single-sided bent-beam unit flexure is included in the model to capture the rotation angle of the paddles.

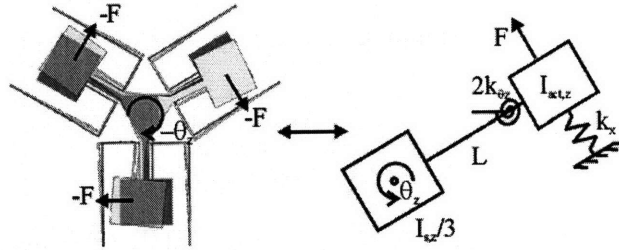


Figure 3.15. Lumped-parameter half model for  $\theta_z$  rotation.

The static rotation that is caused by the in-plane actuator force,  $F$ , is:

$$\theta_z = F \frac{L + L_p}{k_x L^2 + 2k_{\theta_z}} \quad (3.85)$$

where  $L$  is the distance from the center of the stage to the point of connection with the paddle. The length,  $L_p$ , is half the length of the paddle, and represents the distance from the point of application of  $F$  to the point where the paddle joins the paddle-stage link. The resonant frequency for this system is

$$f_{\theta z} = \frac{1}{2\pi} \sqrt{\frac{3(k_x L^2 + 2k_{\theta_z})}{m_{act} (L + L_p)^2 + I_{act,z} + I_{s,z}/3}}. \quad (3.86)$$

In this expression,  $I_{act,z}$  and  $I_{s,z}$  are the mass moment of inertia of the actuator paddle and stage, respectively. The mass moments are taken about a  $z$ -axis through their centroid.

### 3.4.6.D $\theta_x$ -Axis Stiffness and Modal Frequency

Figure 3.16 shows a lumped-parameter mass-spring model for rotation about the  $X$ -axis of the nanopositioner. The model lumps two of the paddles and unit flexures and assumes rotation about a pinned joint along the  $X$ -axis of the nanopositioner. The moment stiffness,  $k_{\theta_x}$ , of the single-sided bent-beam unit flexure is included in the model to capture the rotation angle of the paddles. The paddles are assumed to rotate only about the local paddle  $x$ -axis in order to simplify the model and the rotational stiffness,  $k_{\theta_y}$ , is thereby neglected.

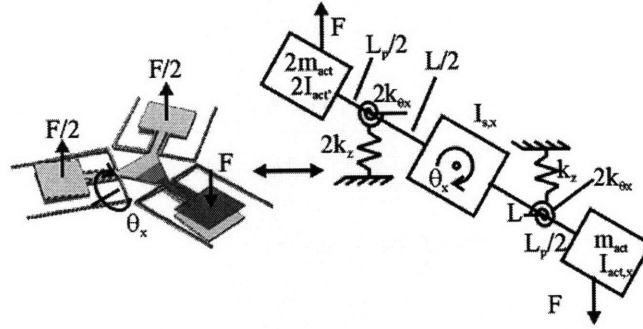


Figure 3.16. Lumped-parameter half model for  $\theta_x$  rotation.

The static rotation about the  $X$ -axis that is caused by the actuator force  $F$  is:

$$\theta_x = F \frac{3(L + L_p)}{3k_z L^2 + 8k_{\theta_x}}. \quad (3.87)$$

The resonant frequency of rotation about the  $X$ -axis is

$$f_{\theta_x} = \frac{1}{2\pi} \sqrt{\frac{\frac{3}{2}k_z L^2 + 4k_{\theta_y}}{\frac{3}{2}m_{act}(L + L_p)^2 + \sqrt{3}I_{act,y} + 2I_{act,x} + I_{s,x}}} \quad (3.88)$$

where the mass moments of inertia are taken about at  $x$ -axis at the centroid of the paddle and stage.

### 3.4.6.E $\theta_y$ -Axis Stiffness and Modal Frequency

Figure 3.17 shows a lumped-parameter mass-spring model for rotation about the  $Y$ -axis of the nanopositioner. The model assumes rotation about a pinned joint along the  $Y$ -axis of the nanopositioner. The moment stiffness values,  $k_{\theta_x}$  and  $k_{\theta_y}$ , of the single-sided bent-beam unit flexure are included in the model to capture the compound rotation of the paddles.

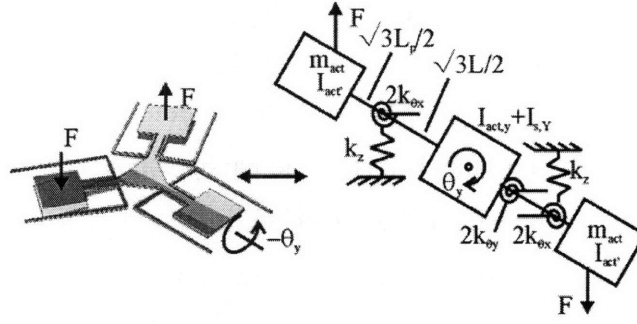


Figure 3.17. Lumped-parameter half model for  $\theta_y$  rotation.

The static rotation that is caused by the actuator force  $F$  is:

$$\theta_y = F \frac{\sqrt{3}(L + L_p)}{\frac{3}{2}k_z L^2 + 2k_{\theta y} + 4k_{\theta x}}. \quad (3.89)$$

The resonant frequency of rotation about the  $Y$ -axis is

$$f_{\theta y} = \frac{1}{2\pi} \sqrt{\frac{\frac{3}{2}k_z L^2 + 2k_{\theta y} + 4k_{\theta x}}{\frac{3}{2}m_{act}(L + L_p)^2 + \sqrt{3}I_{act,x} + 2I_{act,y} + I_{s,y}}}. \quad (3.90)$$

In this model, the mass moments of inertia are taken about the local  $x$ - and  $y$ -axes of the paddles and actuators.

### 3.4.6.F Z-Axis Stiffness and Modal Frequency

Figure 3.18 shows a lumped-parameter mass-spring model for translation along  $Z$ -axis of the nanopositioner.

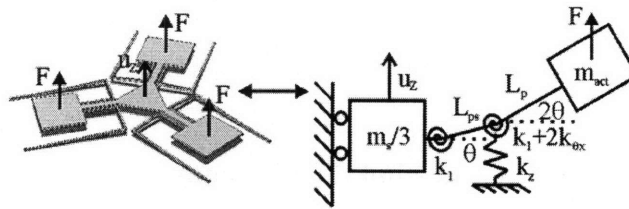


Figure 3.18. Lumped-parameter half model for  $Z$  translation.

The results of FEA simulation indicate that this axis of motion demonstrates two distinct resonant modes that include a rigid-body mode and a paddle flapping mode. As a result, the model includes the bending of the beams that connect the paddle to the stage. This bending is represented by torsional springs at both ends of the link beam. The moment stiffness,  $k_{\theta x}$ , of the



single-sided bent-beam flexure is also included in the model. The torsion spring stiffness of the link beam is:

$$k_1 = \frac{2EI}{L_{ps}} \quad (3.91)$$

where  $L_{ps}$  is the length of the connecting beam. Two modes are considered in this model and the following system of equations must be solved in order to obtain the resonant frequencies:

$$\begin{bmatrix} m_s/3 + m_{act} & Lm_{act} \\ Lm_{act} & L^2m_{act} + I_{act,x} \end{bmatrix} \begin{bmatrix} \ddot{u}_z \\ \ddot{\theta} \end{bmatrix} + \begin{bmatrix} k_z & k_z L_{ps} \\ k_z L_{ps} & k_z L_{ps}^2 + 2k_1 + 8k_{\theta x} \end{bmatrix} \begin{bmatrix} u_z \\ \theta \end{bmatrix} = F \begin{bmatrix} 1 \\ L \end{bmatrix}. \quad (3.92)$$

In this set of equations,  $L$  is defined as:

$$L = (L_{ps} + 2L_p). \quad (3.93)$$

In steady state, the equations may be solved explicitly for the stage displacement in the  $Z$ -direction:

$$u_z = F \frac{1}{k_z} \left( 1 - \frac{k_z L_p L_{ps}}{k_1 + 2k_{\theta x}} \right). \quad (3.94)$$

### 3.5 Thermomechanical Model

The integration of the moving coil actuator and the flexure presents two design problems: 1) heat generated by the coil is transferred through the flexure beam to ground; and 2) the multilayer beams bend as a result of the combination of the temperature gradient and the mismatch in coefficient of thermal expansion (CTE) for each layer. The bending may result in parasitic motion of the stage in out-of-plane directions. The steady-state thermomechanical models that are generated in this chapter will be used in Chapter 4 to design the multilayer flexure for passive compensation of the thermally-induced parasitic error motions.

#### 3.5.1 Model Setup and Boundary Conditions

Figure 3.19 shows a half-model schematic of the thermomechanical model for the double bent-beam flexure and actuator paddle. The dashed line indicates the axis of symmetry. The flexures beams are modeled as laminated copper and silicon layers. In this model, the power that is generated within the coil, and which flows into the paddle, is denoted by  $q$ . The volumetric power that is generated within the copper leads via Joule heating is  $\dot{q}$ .

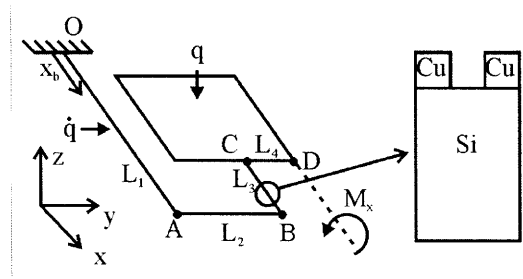


**Figure 3.19. Thermomechanical model schematic of the double bent-beam flexure and actuator paddle.**

The boundary conditions that are placed upon Equation (3.45) for the fixed end of the flexure will also apply to this model. The schematic shows a constraint moment,  $M_x$ , that acts along the axis of symmetry to prevent rotation about the  $x$ -axis. The angular symmetry constraint may be expressed as

$$\theta_{x,t}(D) + \theta_{x,m}(D) = 0 \quad (3.95)$$

where  $\theta_{x,t}$  is the angle of rotation that is caused by thermal bending and  $\theta_{x,m}$  is the rotation that is caused by the constraint moment. The  $z$ -axis displacement and the rotation about the  $x$ -axis that are induced by the constraint moment are:

$$u_{z,M_x}(D) = M_x \left( \frac{L_4^2}{2(EI)_{x,p}} + \frac{L_2^2 + L_2L_4}{2(EI)_x} + \frac{L_1L_2 + L_4(L_1 + L_3)}{(KG)} \right) \quad (3.96)$$

$$\theta_{x,M_x}(D) = M_x \left( \frac{L_4}{(EI)_{x,p}} + \frac{L_2}{(EI)_x} + \frac{L_1 + L_3}{(KG)} \right). \quad (3.97)$$

In order to determine the displacement and rotation, the angles and the displacements that are caused by thermally-induced bending must first be determined. Equation (3.95) may then be solved for the constraining moment as a function of the input parameters. The total displacement of the actuator paddle is the sum of the displacement that is caused by thermal bending and the constraint moment:

$$u_z(D) = u_{z,t}(D) + u_{z,m}(D). \quad (3.98)$$

The final boundary condition is the equivalence of the rotation angle about the  $y$ -axis at points C and D:

$$\theta_y(D) = \theta_y(C). \quad (3.99)$$

### 3.5.2 One-Dimensional Steady State Heat Conduction

The thermal model assumes one-dimensional heat conduction along the flexure beams that flows from the actuator paddle to ground. This assumption is justified via the inspection of the Biot number, which is a ratio of the thermal resistance of a mass that is related to conduction and convection [173]. If one assumes a silicon device with characteristic length  $L_c \approx 10$  mm, a convective heat transfer coefficient of  $h \approx 10$  W/m<sup>2</sup>-K, and thermal conductivity for silicon of  $k \approx 150$  W/m-K, the Biot number is

$$Bi = hL_c/k \approx 0.001 \ll 1 \quad (3.100)$$

This indicates that conduction is the dominant mode of heat transfer and therefore convection may be ignored.

It is also important to consider the temperature gradient across copper, dielectric, and silicon layers. Figure 3.20 shows a one-dimensional conduction model for the transverse temperature distribution across the multilayer flexure beams.

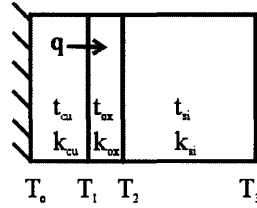


**Figure 3.20. One-dimensional heat conduction model for the transverse temperature distribution across the multilayer flexure beams.**

The heat  $q$  is generated by Ohmic losses in the copper coil leads:

$$\dot{q} = \frac{i^2 R}{A_x L} = \frac{i^2 \rho}{A_x^2} \quad (3.101)$$

where  $A_x$  is the cross section area of the conductor lead. This model uses silicon dioxide as the dielectric, as will be discussed in Chapter 4. The difference in temperature across the beam thickness is solved from Fourier's Law [173]:

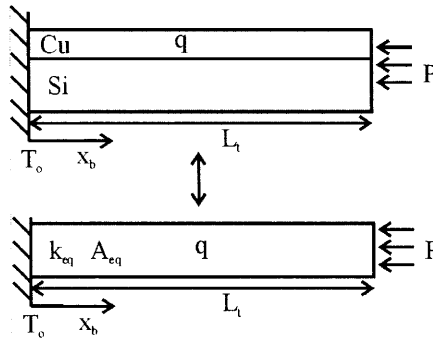
$$T_o - T_3 = \frac{2i^2 \rho_{Cu}}{A_x} \left( \frac{t_{ox}}{wk_{ox}} + \frac{t_{si}}{wk_{si}} + \frac{t_{cu}^2}{4k_{cu}A_x} \right) \quad (3.102)$$

Table 3.5 lists the material parameters that were to compute the transverse temperature difference in Equation (3.102).

**Table 3.5. Parameters used to compute the transverse temperature distribution across the multilayer beam**

Symbol	Parameter	Units	Copper	Silicon	Silicon Dioxide
t	Thickness	$\mu\text{m}$	30	100	1
k	Thermal Conductivity	W/m-K	400	157	1.4
$\rho$	Electrical Resistivity	$\Omega\text{-m}$	1.7E-08	-	-

The beam width is  $w = 80 \mu\text{m}$ , the cross sectional area of one lead is  $A_x = 900 \mu\text{m}^2$ , and the current in leads is  $i = 0.075 \text{ A}$ . The temperature difference across the beam is calculated to be:  $T_o - T_3 \approx 0.004K$ . This indicates that the temperature change across the beam is at least 1000X smaller than the expected temperature change along the beam. The gradients across the beam are therefore less important than those that are along the beam. The one-dimensional heat conduction model may therefore be used to predict the temperature distribution along the beam. A schematic of this steady-state model is shown in Figure 3.21.



**Figure 3.21. One-dimensional model of heat conduction along the flexure beams.**

In this model, the total length of the double bent-beam flexure is the sum of the individual beam lengths and the width of the right-angle corners between beams:

$$L_t = L_1 + L_2 + L_3 + 2w \quad (3.103)$$

The 1-D steady state heat conduction model uses an equivalent thermal conductivity and cross-section area for the multilayer beam since the transverse temperature variation may be neglected:

$$k_{eq} = \frac{k_{si}A_{si} + k_{cu}A_{cu}}{A_{si} + A_{cu}} \quad (3.104)$$

$$A_{eq} = A_{si} + A_{cu} \quad (3.105)$$

According to classical one-dimensional steady state heat transfer, the temperature distribution along the beams is

$$T(x_b) - T_o = A_i x_b^2 + B_i x_b \quad (3.106)$$

The coefficients are

$$A_i = \frac{-i^2 \rho_{Cu}}{2k_{eq} A_{Cu}^2} \quad (3.107)$$

$$B_i = \frac{i^2 \rho_{Cu} L_l}{k_{eq} A_{Cu}^2} + \frac{i^2 \rho_{Cu} L_{coil}}{k_{eq} A_{eq} A_{coil}} \quad (3.108)$$

In these equations,  $i$  is the current that flows through the coil and the leads,  $\rho_{Cu}$  is the electrical resistivity of the copper leads and the coil,  $L_{coil}$  is the length of the coil,  $A_{Cu}$  is the cross-section area of the leads on the flexure beams, and  $A_{coil}$  is the cross-section area of the coil windings. It should be noted that both terms are quadratic with respect to current.

Figure 3.22 shows a comparison of the temperature distribution that was computed from the model and from 3D FEA via CosmosWorks. The parameters that were used for the calculation are the same as those that were used to compute the transverse temperature change in equation (3.102). The current used here is  $i = 0.050$  A, and the power dissipated by the coil is assumed to be  $P = 5$  mW. The ground temperature is  $T_o = 298$  K. The total length of the bent-beam flexure used in this calculation is  $L_l = 8.1$  mm. The data in Figure 3.22 indicates that the model in Equation (3.106) matches the simulation to better than 1% error.

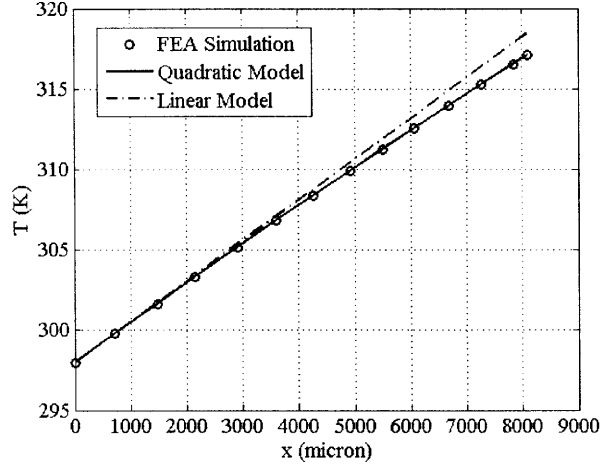


**Figure 3.22. Comparison of the steady-state temperature along the double-bent flexure beam as computed by FEA and the one-dimensional model.**

### 3.5.3 Thermomechanical Out-of-Plane Displacement

The temperature distribution that was derived in the previous section may be used to generate relations for the thermally-induced deflection of the actuator paddle at point D in Figure 3.19 due to thermally induced bending. In this method, a thermal flexural rigidity is defined and calculated according to the method that was derived by Weinberg [136]. The thermal flexural rigidity  $(EI)_t$  relates the curvature of the beam to the moment that is caused by the combination of CTE mismatch and temperature change. This rigidity value replaces the flexural rigidity that was used in section 3.4.2. In addition, the thermal rigidity  $(EI)_{tp}$  of the actuator paddle must be known in order to compute the curvature of the paddle between points C and D. As the thermal rigidity of the paddle depends on the paddle structure, and this is not readily modeled, the thermal rigidity value must be obtained via FEA simulation. The details will be discussed in Chapter 4. Given the temperature distribution along the beams and the thermal flexural rigidity, the displacement and rotation at point D may be computed via the beam bending method that was discussed in 3.4. This yields a set of equations for the thermally-induced motion of the half model in Figure 3.19:

$$u_{z,t}(D) = \frac{L_4^2}{2(EI)_{tp}} (A_t L_t^2 + B_t L_t) + L_4 \left( \frac{A_t}{(EI)_t} f_1 + \frac{B_t}{(EI)_t} f_2 \right) + \frac{A_t}{(EI)_t} f_3 + \frac{B_t}{(EI)_t} f_4 \quad (3.109)$$

$$\theta_{x,t}(D) = \frac{L_4}{(EI)_{tp}} (A_t L_t^2 + B_t L_t) + \frac{A_t}{(EI)_t} f_1 + \frac{B_t}{(EI)_t} f_2 \quad (3.110)$$

$$\theta_{y,t}(D) = \frac{A_t}{(EI)_t} f_5 + \frac{B_t}{(EI)_t} f_6 \quad (3.111)$$

$$f_1 = \frac{1}{3} L_2^3 + (L_1 + w) L_2^2 + (L_1 + w)^2 L_2 \quad (3.112)$$

$$f_2 = \frac{1}{2} L_2^2 + (L_1 + w) L_2 \quad (3.113)$$

$$f_3 = \frac{1}{12} (L_1^4 + L_2^4 + L_3^4) + \frac{1}{3} (L_1 + L_2 + 2w) L_3^3 + \frac{1}{3} (L_1 + w) L_2^3 \\ + \frac{1}{2} (L_1 + L_2 + 2w)^2 L_3^2 + \frac{1}{2} (L_1 + w)^2 L_2^2 - \frac{1}{3} L_1^3 L_3 \quad (3.114)$$

$$f_4 = \frac{1}{6} (L_1^3 + L_2^3 + L_3^3) + \frac{1}{2} (L_1 + L_2 + 2w)^2 L_3^2 + \frac{1}{2} (L_1 + w)^2 L_2^2 - \frac{1}{2} L_1^3 L_3 \quad (3.115)$$

$$f_5 = \frac{1}{3} L_3^3 - \frac{1}{3} L_1^3 + (L_1 + L_2 + 2w) L_3^2 + (L_1 + L_2 + 2w)^2 L_3 \quad (3.116)$$

$$f_6 = \frac{1}{2} L_3^2 - \frac{1}{2} L_1^2 + (L_1 + L_2 + 2w) L_3. \quad (3.117)$$

Equation (3.95) is solved for  $M_x$  in order to compute the total displacement:

$$M_x = -\theta_{x,t}(D) \left( \frac{L_4}{(EI)_{x,p}} + \frac{L_2}{(EI)_x} + \frac{L_1 + L_3}{(KG)} \right)^{-1}. \quad (3.118)$$

The total displacement that is caused by the thermal bending and the symmetry constraint moment is:

$$u_z(D) = u_{z,m}(D) + u_{z,t}(D) + u_k. \quad (3.119)$$

The term  $u_k$  represents the displacements that are caused by the kinematics of the beam rotation about its neutral axis. This term may be neglected for the mechanical model in section 3.4, but becomes important when using the thermal bending equations for optimization in Chapter 4. The total rotation  $\theta_y$  about the  $y$ -axis is only caused by thermal effects, and the value may be obtained from Equation (3.111).

### 3.6 Modeling Summary

This chapter presented physics-based models in multiple domains for prediction of the HSM nanopositioner performance metrics. A model of the magnetic field, which is based upon a new Fourier transform method, was generated in Section 3.1 and its accuracy was determined via

experiments. This model was then used to predict the Lorentz force that will act upon the actuator coil. The accuracy of the force model was ascertained by comparing the simulated and measured displacement of a bench-level prototype in Section 3.2. Lumped-parameter electrical circuit models were generated in Section 3.3 to estimate the power dissipation and electrical time constant of the coil actuators. A linear-elastic stiffness model of the single bent-beam flexure was also generated in Section 3.4. This model was then used to create a stiffness model for the double bent-beam flexure, and this was incorporated into a mass-spring model for each axis of motion of the nanopositioner. The accuracy of the stiffness model was ascertained via comparison with FEA simulation results. Finally, a one-dimensional thermomechanical model was derived in Section 3.5 and used to predict the displacement of the actuator paddles that are caused by thermally-induced bending of the multilayer flexure beams. The accuracy of the temperature distribution was determined via comparison with FEA simulation results. The models will be used in the next chapter to design the nanopositioner so that it meets the target functional requirements.



## DESIGN AND OPTIMIZATION

---

This chapter covers the design of the meso-scale prototype. The models that were developed in the previous chapter were used in concert with FEA to design the nanopositioner system so that it satisfies the functional requirements that were presented in Chapter 2. The design methods that are presented in this chapter enable optimization of the actuator coil and the double bent-beam flexure geometry. The actuator coils were tuned for maximum power efficiency, while the flexure mechanism's beam lengths were designed to minimize thermally-induced error motions. An iterative design loop combines physics-based models and FEA to design and optimize the nanopositioner. The magnet-coil alignment system is then discussed.

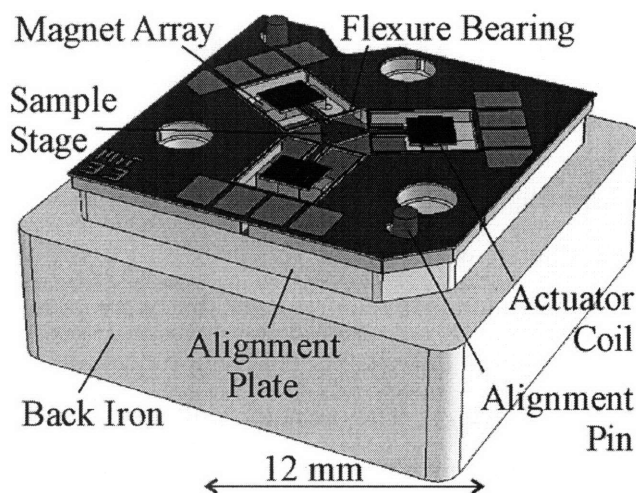
### 4.1 System-Level Design

Figure 4.1 shows a system layout of the HSM nanopositioner. The nanopositioner system consists of:

- 1) a microfabricated silicon chip wherein silicon flexure bearings, planar-spiral moving-coil microactuators, coil lead wires, and bond pads were integrated together;
- 2) three sets of alternating pole permanent magnets;
- 3) an alignment plate;
- 4) alignment pins; and
- 5) a back iron.

The silicon chip was preloaded against two alignment pins that were press fit into the alignment plate. Fasteners were used to preload the silicon chip, shim, and alignment plate to the back-iron. The fastener holes are visible in Figure 4.1. A shim was used to set the gap between

the permanent magnets and the bottom of the actuator paddle. The permanent magnets were mounted onto the back-iron and pressed against reference features in the alignment plate. The back-iron has high magnetic permeability and thereby acts to double the effective thickness of the magnets as explained in section 3.1.2.B. The design details of each subsystem will be presented later in this chapter.



**Figure 4.1. Solid model of the proposed nanopositioner system.**

Figure 4.2 shows assembled and exploded views of the two-axis moving-coil actuator and the double bent-beam unit flexure. The microfabricated actuator consists of four material layers:

- 1) a silicon paddle and flexure layer that contains trenches for the lower coil;
- 2) a lower copper coil;
- 3) an interlayer dielectric; and
- 4) an upper copper coil.

The use of silicon for the structural layer, and the use of copper for the coil conductor material, was justified in section 2.6

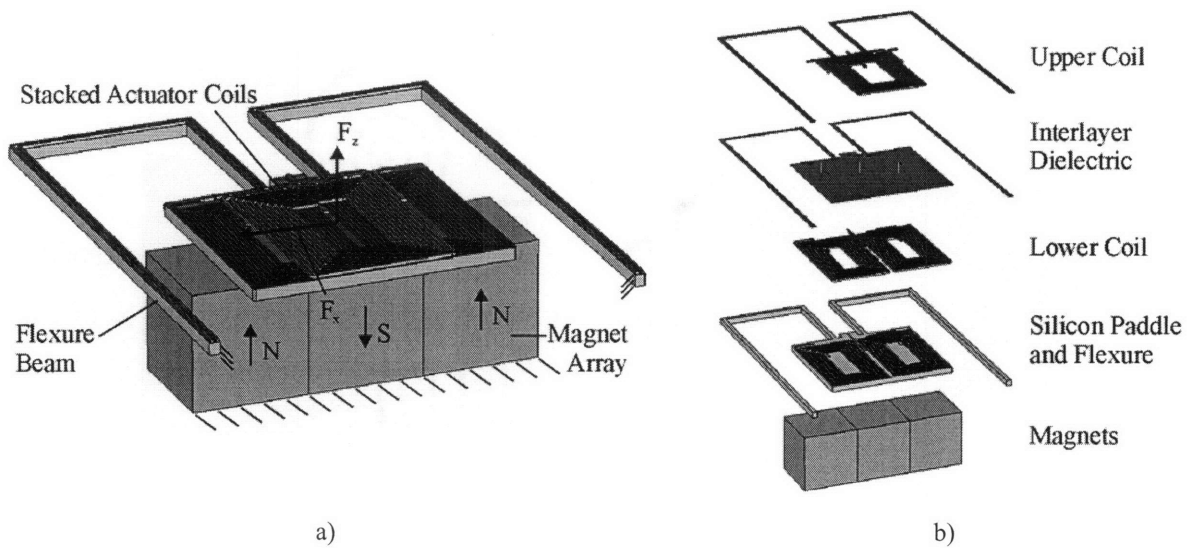


**Figure 4.2. Assembled a) and exploded view b) of the two-axis moving-coil microactuator and double bent-beam flexure.**

The upper copper coil layer contains the electrical leads that were used to power the coil. Each bent beam flexure has two leads to provide current to each of the actuator coils. The leads were electrically insulated from the silicon beams by the interlayer dielectric. The upper and lower coil layers also contain electrical jumpers. These jumpers were used with vias through the interlayer dielectric to route current to the coils. Figure 4.3 shows a cross-section view of the moving-coil microactuator along line A-A. The cross-section view shows a detail of the via structure through which a jumper in the upper coil layer makes contact to the lower coil. The design in Figure 4.2 and Figure 4.3 uses trenches in the silicon paddle as the mold for the buried lower coil layer.

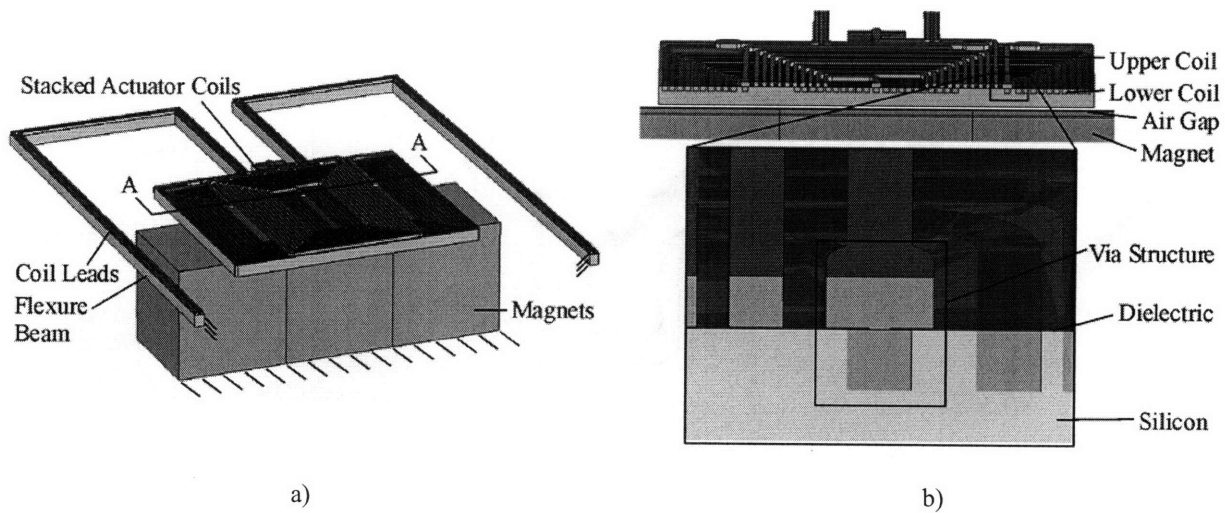


**Figure 4.3. Solid model a) and detailed cross-section view along A-A b) of the moving-coil microactuator.**

Previous work on thick micro-coil actuator coils has yielded coil structures that were built upon silicon and then encapsulated within a planarizing polymer such as SU-8 [150]. Jumpers and secondary coil layers were then fabricated on the planarized polymer surface. The encapsulated coils suffer from poor heat transfer because of the low thermal conductivity of the polymers. This leads to limited current density because the polymers have limited operating temperatures on the order of 100-150°C. This architecture was unacceptable for the HSM prototype nanopositioner, given that the design was actuator-limited. The design in Figure 4.3 uses coils that were buried within silicon so that the coils experience better heat dissipation than coils that would be encapsulated in SU-8 and stacked upon top of the paddle. Researchers have fabricated inductor coils that were buried in silicon but these coils were not encapsulated [175] and therefore their heat transfer characteristics are inferior to the design that was shown in Figure 4.3. Others have developed two-layer coils that contain lower coils that were buried in silicon, but separated from upper coils by a polymer dielectric [1, 33, 102]. This design is also subject to the temperature and processing limitations that are imposed by using polymer dielectrics. Section 5.1 discusses the performance and processing advantages of the various coil structures in more detail.

This research aimed to use unannealed silicon dioxide as a dielectric insulator that separates the upper and lower coil layers. Silicon dioxide possesses several structural and microfabrication advantages when compared to polymers dielectrics and silicon nitride. The processing advantages of silicon dioxide will be discussed in Chapter 5. Table 4.1 contrasts the

relevant material properties of silicon dioxide, polyimide, SU-8, and silicon nitride. The data was compiled from Madou [176], Senturia [177], and a respected material properties website [178].

**Table 4.1. Comparison of interlayer dielectric materials properties.**

Property	Units	PECVD Silicon Dioxide (unannealed)	PECVD Silicon Nitride	Polyimide	SU8
Young's Modulus	Gpa	85	160	2.5	4.02
Useful Strength	MPa	952	2400	231	34
Residual Stress on Silicon	MPa	-62.7	-600	35	16-19
Coefficient Thermal Expansion	ppm/K	0.7	2.3	16.0	50.0
Thermal Conductivity	W/m-K	1.1	16-33	0.12	0.2
Dielectric Constant	unitless	5	7	3.4	3
Max Operating Temp	C	300	>1000	520 (Cured)	200

The data in the table shows that unannealed silicon dioxide has a higher useful strength and a higher thermal conductivity than polyimide and SU-8. The silicon dioxide was therefore a better material from the viewpoint of flexure failure criteria and heat dissipation from the coils.

The following sections discuss the detailed design of the actuator and flexure geometry and the alignment system.

## 4.2 Actuator Design

There were four areas of concern to the design of the EM, stacked, moving-coil actuator:

(1) Force output and power optimization: The actuator coil geometry should be designed relative to the magnet set such that the coils output the maximum force and/or operate with maximum efficiency. A moving coil actuator dissipates power through the flexure elements which leads to thermally-induced deformation of the flexure. The efficiency, which is defined as the force per unit power dissipation, was maximized by tuning the actuator coil geometry.

(2) Parasitic loads: The actuator may be thought of as a six-pole system: three electrically controllable poles and three permanent magnetic poles. The lower double pole electrical coil produces a parasitic moment about the y-axis, whose magnitude depends upon the coil and magnet array design. The parasitic moment will lead to unwanted parasitic rotation of the coil platform and divert actuator power toward creating unwanted motions. Modeling and simulation

results show that it was possible to minimize this moment by optimizing the designs of the coils and magnet arrays.

(3) Linearity: The fields used in the actuator were not constant in magnitude or direction. Therefore, as the coils move, the forces on the coil will change. For the proposed design, the error as a percent of the desired force was less than 0.5% if the motion was a few percent or less of characteristic magnet dimensions. The models assume that the stroke was limited to a few percent of the magnet width. The design uses millimeter-scale magnets and therefore the model was suitable for tens-of-micrometers of stroke.

(4) Cross talk: Electrical cross-talk is known to be problematic at frequencies near the electrical coil resonance. The actuators may work independently below the excitation resonance of the coils. The resonance for similar coils is usually on the order of megahertz. The electrical resonances of the coils were several orders of magnitude above the kHz functional requirements.

The geometric parameters that describe the coils and magnets are shown in Figure 4.4. Current flow is represented by the variable  $i$  and the characteristic dimension for the cube magnet is  $a$ . The parameters  $w_x$  and  $w_z$  are the width of the  $y$ -directed working coil segments for the  $x$ - and  $z$ - actuators, respectively. The parameters  $d_x$  and  $d_z$  represent the spacing between these working segments.

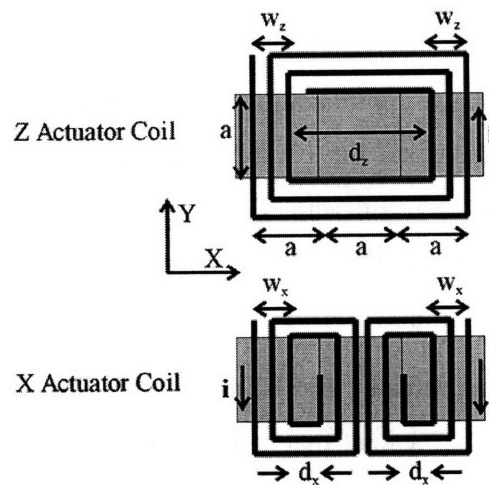
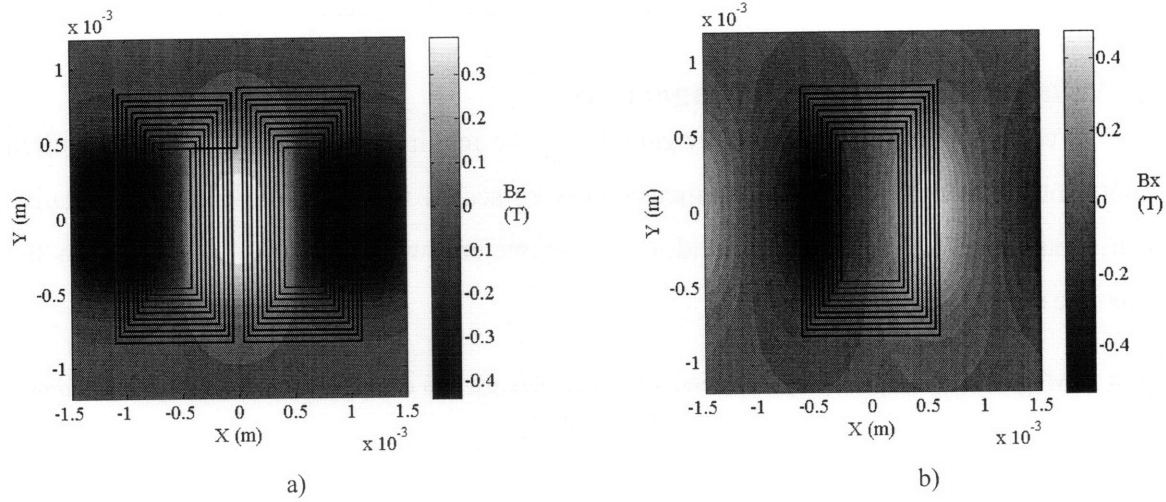


Figure 4.4. Actuator magnet and coil geometric parameters.

Equations (3.37) and (3.38) were used to compute the Lorentz force that acts upon the actuator coils. The Lorentz force calculations are based upon the permanent magnet field solution that was presented in section 3.1. The interaction of the coil and magnetic field may be

visualized by superimposing the stacked coil geometry over the magnet array's field lines. Figure 4.5 shows a plan view of the coil geometry of the in  $x$ - and  $z$ -actuators that are superimposed upon contour plots of the  $z$ - and  $x$ - components of the magnetic flux density.



**Figure 4.5.** X-actuator a) and Z-actuator b) coils superimposed upon the  $z$ -component a) and  $x$ -component of the simulated magnetic flux density that exists along the plane of the coils.

Table 4.2 provides the magnet geometry that was used to compute the flux density data in Figure 4.5.

**Table 4.2.** Magnet geometry that was used to compute the flux density contours for the example coil geometry.

Symbol	Parameter	Value	Units
$a$	Magnet width	1	mm
$c$	Magnet thickness	4	mm
$h$	Height above Magnets	150	$\mu\text{m}$
$B_r$	Remnance	1.25	T

The width of the winding segments was designed such that the ratio  $w_x/a = w_z/a = 0.33$  in order to make the optimization space tractable. The value of  $w_x/a = 0.33$  results in an  $x$ -actuator coil geometry that filled the magnetic field lobe as shown in Figure 4.5a. The same ratio was also used for the  $z$ -actuator coil. In this case, the working coil segments filled the magnetic field lobe as shown in Figure 4.5b.

#### 4.2.1 Coil Winding Cross-Section and Pitch

An increase in cross-section area of the coil reduces the resistance and this reduces the power consumption of the coil. In addition, a decrease in pitch leads to improved winding

packing density and force output. Practical microfabrication limits the winding thickness,  $t_{Cu}$ , to 30  $\mu\text{m}$ , the winding width,  $w_{Cu}$ , to 30  $\mu\text{m}$ , and the pitch,  $p$ , to approximately 40  $\mu\text{m}$ . These values were used to calculate the force and power dissipation of the coils in the following sections. Microfabrication constraints as will be discussed in more detail within Chapter 5.

## 4.2.2 Actuator Footprint and Magnet Size

The coil design process begins by calculating the required magnet size and the required coil footprint. The magnet and coil dimensions were scaled in size while fixing the relative geometric parameters. Table 4.3 provides the parameters and ratios that were used in the actuator size study.

**Table 4.3. Magnet and coil geometry characteristics that were used to compute force for variable actuator footprint.**

Symbol	Parameter	Value	Units
a	Magnet Width	variable	mm
c/a	Magnet Thickness	4	-
h/a	Height above Magnets	0.15	-
$w_{x,z}/a$	Winding Segment Width	0.33	-
$d_x/a$	X-Coil Segment Spacing	0.39	-
$d_z/a$	Z-Coil Segment Spacing	0.58	-
$B_r$	Remnance	1.25	T
p	Winding Pitch	40	$\mu\text{m}$
$A_w$	Winding Cross-Section Area	900	$\mu\text{m}^2$
i	Current	450	mA

The input current was set to half the typical maximum sustainable current density of typical microcoil cross-sections,  $J = 1000 \text{ A/mm}^2$  [72]. The values of coil height and winding geometry were chosen to reflect copper coil structures and air gaps that are feasible with respect to microfabrication. Figure 4.6 shows the calculated  $x$ - and  $z$ -actuator forces.



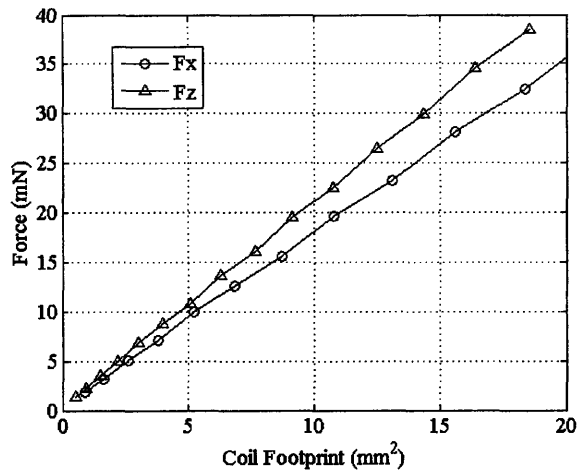


**Figure 4.6. Simulated force output of the  $x$ - and  $z$ -actuators versus coil footprint**

The simulated data shows that (1) the force scales linearly with coil footprint area and (2) a typical micro-coil with a footprint of a few square millimeters may output 5 - 10 mN in both axes. The nanopositioner functional requirements specify an actuator force of 10 mN. A footprint of a few square millimeters corresponds to a magnet width,  $a$ , equal to approximately 1 mm. Millimeter-sized permanent magnets are stock items that are readily purchased. The actuator was therefore designed to use 1.0 mm cube magnets that were arranged in alternating poles and stacked on back-iron. The magnets were stacked to a thickness of 2 mm and the use of back-iron causes an effective magnet thickness of  $c = 4.0$  mm.

### 4.2.3 Force and Power Optimization

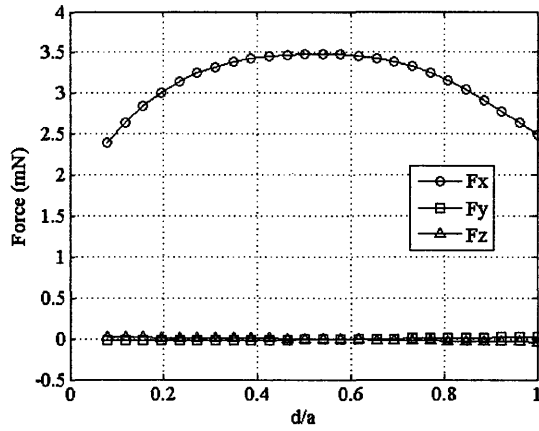
Several parametric studies were conducted in order to minimize the parasitic torque on the actuator and to optimize the force output. The most important parameters that affect the parasitic torque in the  $x$ -actuator, and force output, are the coil segment spacing,  $d_x$  and  $d_z$ , and the coil height above the magnets,  $h$ . The segment spacing has the effect of positioning the working coil segments with respect to the magnetic field lobes, thereby resulting in force and efficiency characteristics that are highly sensitive to these variables. Figure 4.5 illustrates the placement of the working coil segments with respect to the magnetic field lobes. The segment spacing was varied for the  $x$ - and  $z$ -actuator coils from a minimum of twice the pitch of the coils – 80  $\mu\text{m}$  – up to the characteristic magnet dimension,  $a$ . Table 4.4 lists the magnet and coil parameters that were used in the parametric study. The data was computed for a cuboidal

magnet dimension of  $a = 1.0$  mm, that reflects the size of magnets as designed for the microactuator. The input current was set to  $i/i_{max} = 0.25$ .

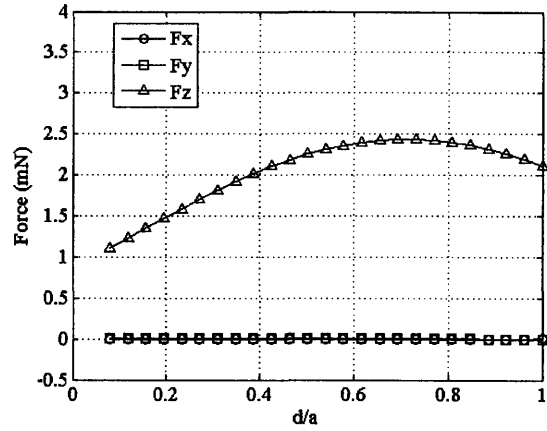
**Table 4.4. Magnet and coil geometry characteristics that were used to compute force and power for variable coil spacing  $d$**

Symbol	Parameter	Value	Units
$a$	Magnet Width	1	mm
$c/a$	Magnet Thickness	4	-
$h/a$	Height above Magnets	0.15	-
$w_{x,z}/a$	Winding Segment Width	0.33	-
$d_x/a, d_z/a$	X- and Z- Coil Segment Spacing	variable	-
$B_r$	Remnance	1.25	T
$p$	Winding Pitch	40	$\mu\text{m}$
$A_w$	Winding Cross-Section Area	900	$\mu\text{m}^2$
$i$	Current	225	mA

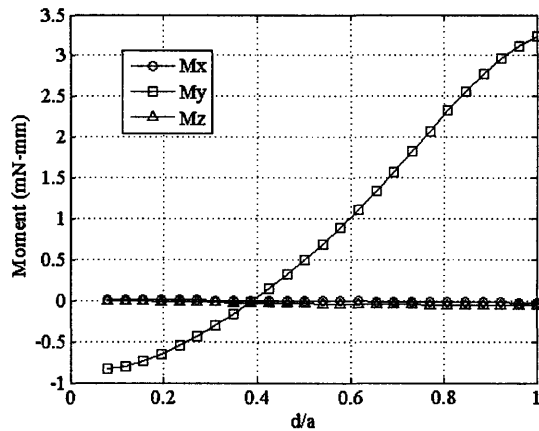
The resulting force and parasitic moment curves are plotted versus  $d/a$  in Figure 4.7 for the  $x$ - and  $z$ -actuators. The results of this parametric study have been published by the author [154].



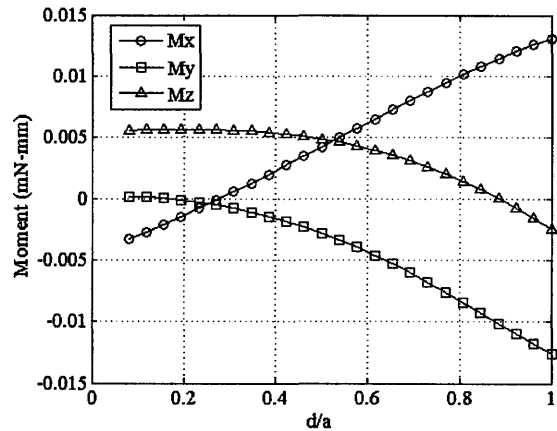
a)



b)



c)



d)

**Figure 4.7. Simulated actuator forces and moments versus coil segment spacing,  $d$ . The  $x$ -actuator forces and moments are presented in a) and c), while the  $z$ -actuator forces and moments are presented in b) and d).**

The data in Figure 4.7a and c shows that the  $x$ -actuator coil forces in the  $y$ - and  $z$ -direction are nearly zero, while the  $x$ -directed force has a broad maximum at approximately  $d_x/a \approx 0.5$ . More importantly, the aforementioned parasitic moment about the  $y$ -axis that is created by the  $x$ -actuator is minimized at  $d_x/a \approx 0.39$ . At this value, the  $x$ -actuator force is also near its maximum value. This result is important because the actuator may be designed as a pure force source with near-optimal  $x$ -directed force and parasitic moment that may be tuned to be near zero.

The  $z$ -actuator force data in Figure 4.7b and d shows the  $x$ - and  $y$ -axis forces are nearly zero, while the  $z$ -directed force has a maximum for  $d_z/a \approx 0.7$ . The parasitic moments that are

caused by the  $z$ -actuator are orders of magnitude less than the parasitic errors that are caused by  $x$ -actuator.

The maximization of efficiency is important in actuators that dissipate heat in precision machines. The moving coil actuators dissipate heat that may lead to unwanted, time-variable error motions. It was therefore desirable to maximize the actuator efficiency for a given level of force output. The force efficiency is defined as the ratio of actuator force to electrical power consumption:

$$E = \frac{F}{P} = \frac{k_a i}{i^2 R} = \frac{k_a}{iR}. \quad (4.1)$$

The force efficiency was calculated for variable segment spacing and the geometry that was presented in Table 4.4. The resulting force and parasitic moment curves are plotted versus the ratio  $d/a$  for the  $x$ - and  $z$ -actuators in Figure 4.8.

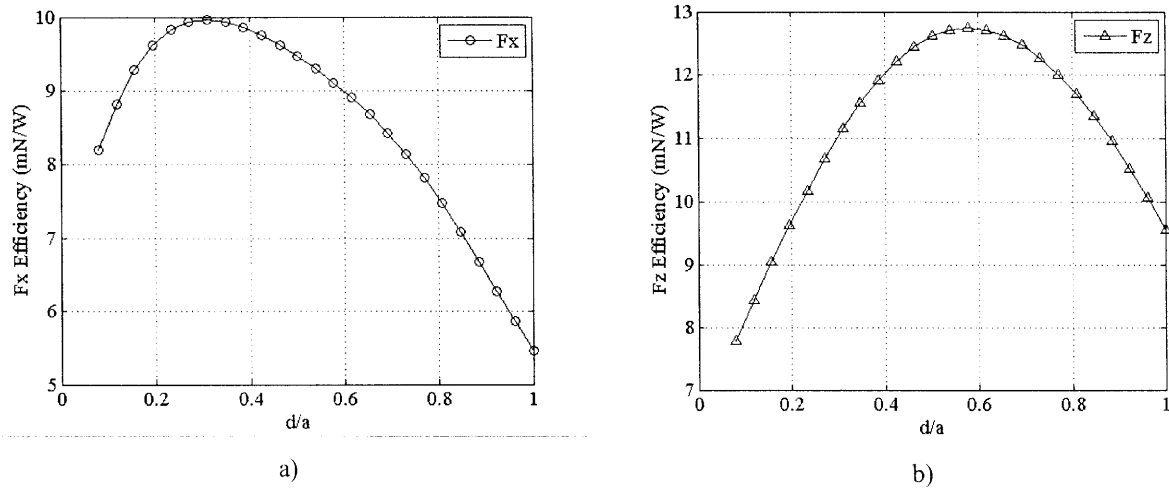


**Figure 4.8.** Simulated force efficiencies versus coil segment spacing,  $d$ , for the a)  $x$ - and b)  $z$ - actuators.

The data in Figure 4.8a shows that the  $x$ -actuator force efficiency has a maximum at  $d_x/a \approx 0.32$ . This is near the value for the minimum parasitic moment that occurs at  $d_x/a \approx 0.39$ . The data in Figure 4.8b shows that the  $z$ -actuator force efficiency was maximized at  $d_z/a \approx 0.58$ . The simulation results indicate that it was possible to design the coil segment spacing to optimize force efficiency or to minimize the parasitic moments. The result is important as it provides options for system optimization that may be guided by the requirements of the actuator system. The nanopositioner is capable of open-loop calibration that may be used to reduce systematic parasitic error motions, which includes those that are caused by parasitic actuator moments. The

actuator coil segment spacing was designed for optimal force efficiency, rather than parasitic moment reduction, so as to minimize the time-variable, thermally-induced error motions that occur during open-loop operation.

The actuator coil height also affects the force and moment that act upon the magnet-coil actuator. The actuator coil forces were calculated for values of the height ratio,  $h/a$ , that were varied from 0 to 1. Table 4.5 provides the magnet and coil parameters that were used in the parametric study.

**Table 4.5. Magnet and coil geometry that was used to compute force and power for variable coil height  $h$**

Symbol	Parameter	Value	Units
$a$	Magnet Width	1	mm
$c/a$	Magnet Thickness	4	-
$h/a$	Height above Magnets	Variable	-
$w_{x,z}/a$	Winding Segment Width	0.33	-
$d_x/a$	X- Coil Segment Spacing	0.32	-
$d_z/a$	Z- Coil Segment Spacing	0.58	-
$B_r$	Remnance	1.25	T
$p$	Winding Pitch	40	$\mu\text{m}$
$A_w$	Winding Cross-Section Area	900	$\mu\text{m}^2$
$i$	Current	225	mA

The force and parasitic moment curves are plotted in Figure 4.9 versus  $h/a$  for the  $x$ - and  $z$ -actuators.

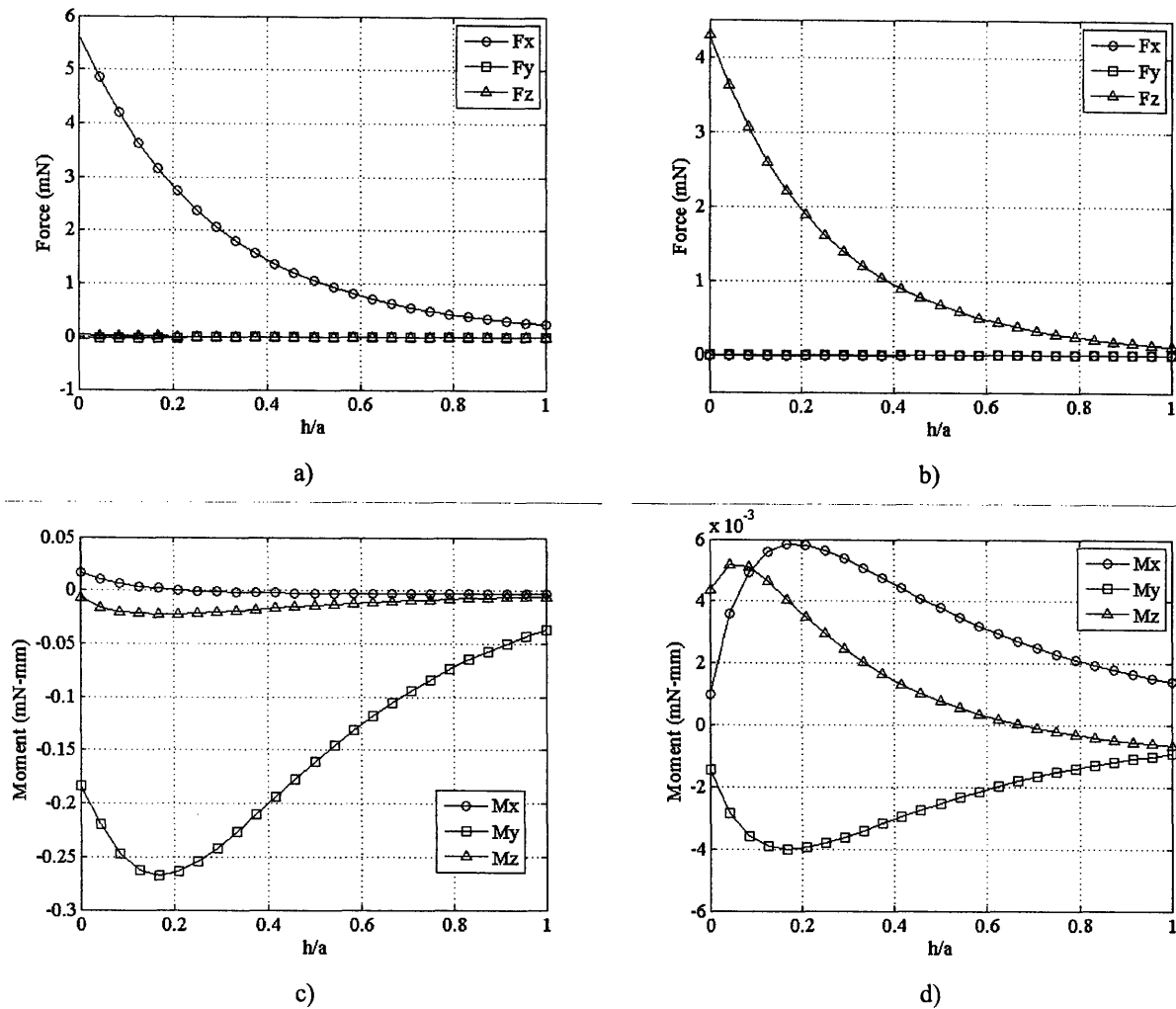


**Figure 4.9. Simulated actuator forces and moments versus coil height,  $h$ . The  $x$ - actuator forces and moments are shown in a) and c), while the  $z$ -actuator forces and moments are shown in b) and d).**

The data in Figure 4.9a and c shows that the  $x$ - and  $z$ - actuator output force varies inversely with the height, as expected. The force efficiency scales proportionally with force in this study because the coil length remains constant. It is important to investigate how the actuator forces change with small motions of the actuator paddles. The nominal height of the coils of the magnets must first be estimated. Practical fabrication and assembly limits the gap between the magnets and the actuator paddle to a minimum of approximately 25-50  $\mu\text{m}$ . A reasonable paddle thickness for a microfabricated silicon flexure is on the order of 100-200  $\mu\text{m}$ . The minimum practical coil height is then approximately 125-150  $\mu\text{m}$ . For this coil height above the magnets, the actuator force change is approximately linear for small actuator translations in

the vertical direction. Figure 4.10 shows the variation in  $x$ - and  $z$ - actuator force for small translations in the  $z$ -direction.

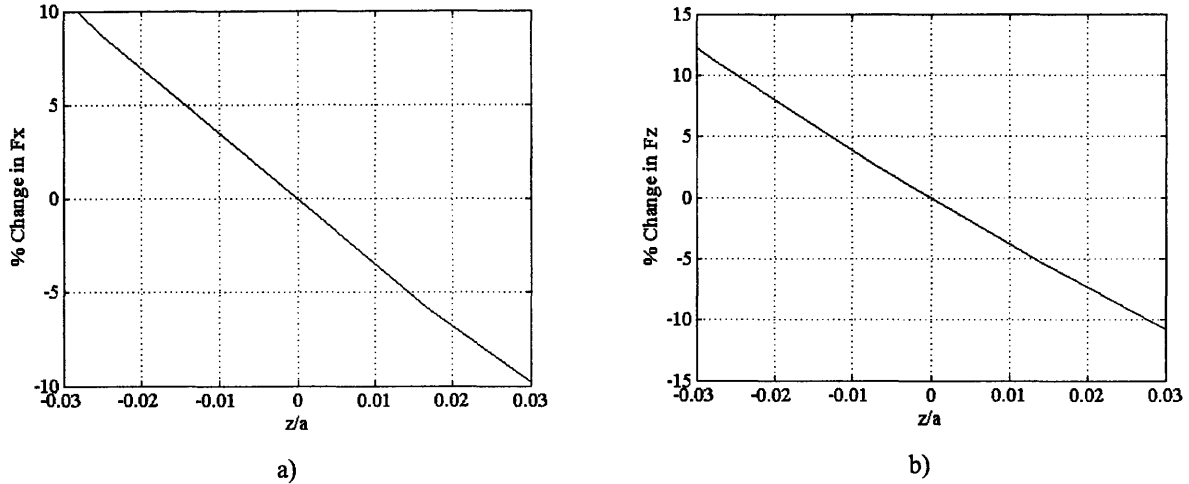


**Figure 4.10. Simulated actuator forces versus vertical coil position relative to  $h = 150 \mu\text{m}$ . The  $x$ - actuator  $x$ -directed force is shown in a) and the  $z$ -actuator  $z$ -directed force is shown in b).**

The data in Figure 4.10 shows that the actuator forces change by less than 10% for translations in the  $z$ -direction of less than  $25 \mu\text{m}$ . The change in force may be approximated as linear and the effect of the changes may be captured during open-loop operation by including the linear variation in the calibration calculations. This change in force output need not be considered during early design activities and hereafter the force was assumed constant.

Figure 4.11 shows the change in actuator force versus displacement in the lateral direction. The actuator geometry characteristics that were used in this study were shown in Table 4.5 with a fixed coil height,  $h = 150 \mu\text{m}$ .

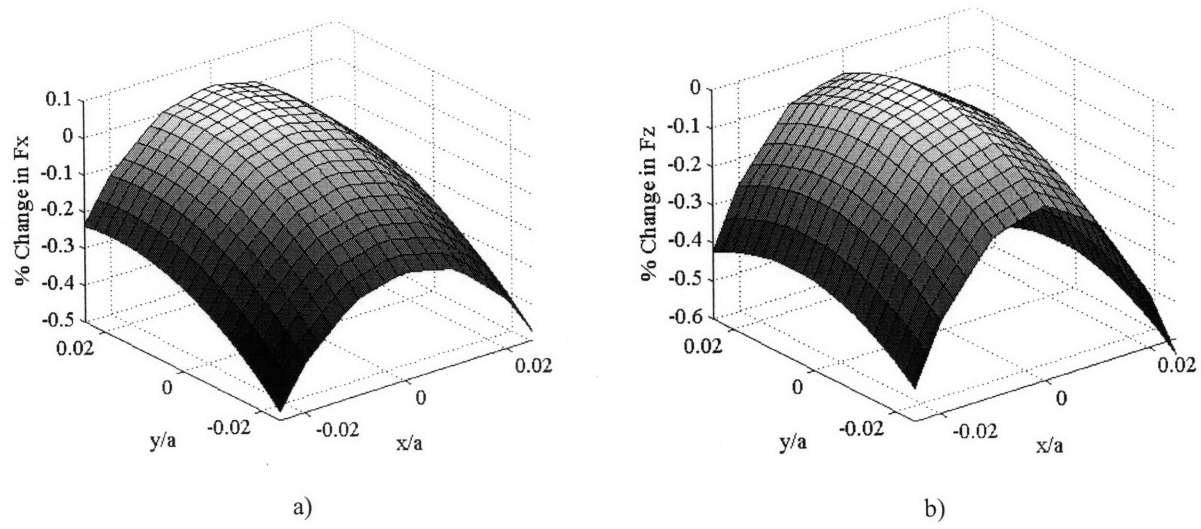


**Figure 4.11. Simulated actuator forces versus lateral position of the actuator coil. The  $x$ -actuator's,  $x$ -directed force is shown in a) and the  $z$ -actuator's  $z$ -directed force is shown in b).**

The data in Figure 4.11a and b shows that the actuator forces varies by less than 0.5% for translations in the  $x$ - and  $y$ -direction of less than 25  $\mu\text{m}$ . For the purposes of this thesis, this level of error motion was acceptable and so the actuator forces may be approximated as constant over the range-of-motion of the nanopositioner.

This section presented simulation studies that were used to investigate the actuator force output as a function of several geometric parameters. The results indicate that the actuator coil may be designed for either minimized parasitic moments or maximum force efficiency. The actuator coil geometry was selected to optimize force efficiency in order to minimize power dissipation. Simulation results also indicate that the forces exhibit a weak linear change with translations in the  $z$ -direction and the forces are nearly constant for translations in the  $x$  and  $y$ . Table 4.6 lists the coil geometry that was used to design the moving-coil actuator for the meso-scale nanopositioner.



**Table 4.6. Design geometry for the two-axis moving coil actuator.**

Symbol	Parameter	Value	Units
a	Magnet Width	1	mm
c/a	Magnet Thickness	4	-
h/a	Height above Magnets	0.15	-
$w_{x,z}/a$	Winding Segment Width	0.33	-
$d_x/a$	X- Coil Segment Spacing	0.32	-
$d_z/a$	Z- Coil Segment Spacing	0.58	-
p	Winding Pitch	40	$\mu\text{m}$
$A_w$	Winding Cross-Section Area	900	$\mu\text{m}^2$

#### 4.2.4 Electrical Circuit

The electrical circuit models presented in Section 3.3 were used to predict the resistance, self-inductance, and mutual capacitance of the coils. The coil length that was used in Equation (3.39) to calculate the resistance was obtained by summing the lengths of all segments in each coil. The inductance and  $L$ - $R$  roll-off frequency were estimated via Equations (3.40) and (3.41). Table 4.7 lists the model parameters that were used to compute the resistance, self-inductance, and electrical time constant of the microactuator coils.

**Table 4.7. Model parameters were used to compute the resistance, self-inductance, and electrical time constant.**

Symbol	Parameter	X Coil	Z Coil	Units
$L_c$	X-Coil Length	78.9	43.6	mm
$R_{\text{max}}$	Max Radius for Inductance	1	0.75	mm
N	Number turns for Inductance	10	10	-
$w_w$	Winding Width	30	25	$\mu\text{m}$
$t_w$	Winding Thickness	30	25	$\mu\text{m}$
$t_{\text{ox}}$	Dielectric Thickness	1	1	$\mu\text{m}$
p	Winding Pitch	40	40	$\mu\text{m}$
$\rho$	Resistivity of Copper ( $\times 10^{-6}$ )	1.7	1.7	$\Omega\text{-cm}$
R	Resistance	1.49	0.82	$\Omega$
L	Inductance	16	11	nH
$f_{LR}$	L-R Roll-off Frequency	60	86	MHz

The data in the table shows that the electrical roll-off frequency of the planar-spiral coils was in the megahertz range. This is well above the target mechanical resonance of 1 kHz. In general, the bandwidth of similar electromagnetic micro-actuators is limited by the mechanical system characteristics. The force computed by Equation (3.37) is valid for a coil that operates with

commanded current,  $i$ , at frequencies that are an order of magnitude lower than the electrical roll-off frequency.

Table 4.8 lists the model parameters that were used to compute the mutual capacitance between the stacked microactuator coils. In this calculation, the overlapping parallel plate capacitor area was estimated by using the footprint of the  $z$ -actuator coil and a packing factor that may be used to reflect the for the winding's packing density. The data in the table indicates that the mutual capacitance was on the order of picofarads, and therefore the electrical dynamics were not pertinent to the practical application of the microactuator.

**Table 4.8. Mutual capacitance model parameters.**

Symbol	Parameter	Value	Units
$t_{ox}$	Dielectric Thickness	1	$\mu\text{m}$
$\kappa$	Dielectric Constant	5	-
PF	Winding Packing factor	0.75	-
$A_{pp}$	Effective Capacitor Area	2.06	$\text{mm}^2$
$C_m$	Mutual Parasitic Capacitance	68	pF

The skin depth through which a sinusoidal current may penetrate the coil windings imposes an upper limit on the required cross-section. At a given excitation frequency,  $\omega$ , the current flowing through the winding will penetrate to a depth in the inductor that is given by [168]:

$$\delta = \sqrt{\frac{2\rho}{\omega\mu}} \quad (4.2)$$

Figure 4.12 shows the predicted skin depth as a function of the excitation frequency. The data indicates that the skin depth exceeds the coil cross-section width and thickness of  $30 \mu\text{m}$  for excitation frequencies that exceed 1MHz. This result indicates that the current will penetrate throughout the full cross-section of the coil windings for the anticipated operating frequencies of the coils. The skin depth sets an upper limit on the winding cross-section width and height such that the entire cross section may be utilized in conducting current.

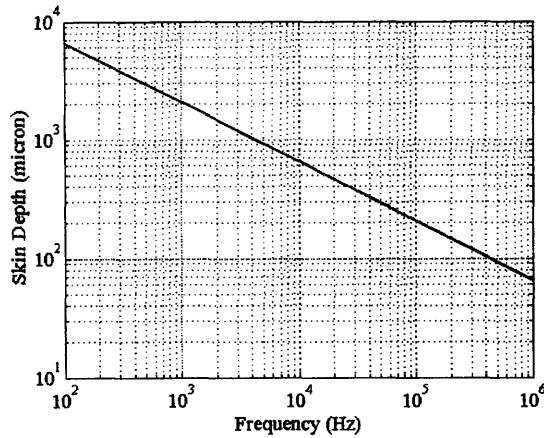


Figure 4.12. Skin depth for copper coil windings as a function of excitation frequency.

### 4.3 Double Bent-Beam Flexure Design Method

The thermomechanical double-bent beam model that was presented in section 3.5.3 may be employed to design the relative beam lengths for passive, steady-state thermally-induced error motion minimization in the  $z$ -direction. The model assumes that the conductive heat transfer from the actuator paddle to ground is driven by Joule heating within the multi-layer beams flexure beams.

#### 4.3.1 Nonlinear System of Equations

The out-of-plane actuator paddle translation displacement,  $u_z$ , and rotation displacement,  $\theta_x$ , are caused by thermally-induced bending of the multilayer beams. The magnitude of each may be obtained via Equations (3.119) and (3.111). The thermally-induced displacement and rotation of the paddle must be zero in order to minimize the error motion. These constraints are described by the following set of nonlinear equations for the double bent-beam flexure:

$$u_{z,t}(D) = f(L_1, L_2, L_3, L_4, (EI)_x, (KG), (EI)_l, (EI)_{x,p}, (EI)_{lp}, \rho_{Cu}, k_{eq}, A_{eq}, L_c, A_c) = 0 \quad (4.3)$$

$$\theta_{x,t}(D) = g(L_1, L_2, L_3, L_4, (EI)_l, (EI)_{lp}, \rho_{Cu}, k_{eq}, A_{eq}, L_c, A_c) = 0. \quad (4.4)$$

The equations indicate that the thermally-induced error motions scale in a nonlinear way with the lengths of the beam elements, cross-section of the beam and paddle, resistivity of copper, the thermal properties of the beam, and the actuator coil geometry. It is important to note that the input current multiplies each term in the nonlinear equations and therefore the magnitude of the

current drops out when the equations are set to zero. The equations may be solved irrespective of the input current. Assume that the following are specified:

- 1) material properties;
- 2) thermal properties;
- 3) cross-section mechanical properties; and
- 4) bent-beam lengths,  $L_1$  and  $L_4$ .

The equations then reduce to a set of two nonlinear equations in  $L_2$  and  $L_3$ :

$$u_{z,t}(D) = f(L_2, L_3) = 0 \quad (4.5)$$

$$\theta_{x,t}(D) = g(L_2, L_3) = 0 \quad (4.6)$$

The equations are solved simultaneously for  $L_2$  and  $L_3$  with the nonlinear Newton-Raphson method [169]. The solution results in a set of lengths,  $L_1$ ,  $L_2$ , and  $L_3$ , that enables the flexure to bend out-of-the-plane without imparting force to the remainder of the six-axis flexure. In this way, the double bent-beam flexure prevents steady-state error motion in the out-of-plane direction. The error motion is a result of the temperature distribution that was driven by power dissipation within the actuator coils. The solution is independent of the input current, and therefore provides passive prevention for any level of command current. The design method enables the optimal geometry to be set regardless of size, and then scaled with length  $L_1$  to a size that is suitable for a given application. As a result, the stiffness characteristics and the thermally-induced error prevention characteristics of the optimal double bent-beam flexure may be designed independently. This is the advantage of using the double bent-beam flexure in place of the single bent-beam. In the case of a single bent-beam flexure,  $L_1$  is zero and the solution is unique. There exists only one combination of lengths that may achieve passive prevention for a given set of material and cross-section properties.

The modeling and optimization of the beam dimensions requires the resistance of the power-dissipating coil as an input parameter. The model used in the method also assumes symmetry about the center of the paddle, which means that the leads on each side of the double bent-beam flexure dissipate equivalent power. The optimal beam geometry was therefore computed for the combined resistance of the x- and z-actuator coils and equivalent input current to each actuator.

The design method that was presented in this section will be used in section 4.4 to design the relative beam lengths for (i) thermally-induced error motion prevention and (ii) stiffness characteristics that enable the nanopositioner to satisfy its functional requirements.

### **4.3.2 Thermal “Rigidity” of the Actuator Paddle**

The solution method in the preceding section requires knowledge of the mechanical and thermal rigidity,  $(EI)_p$  and  $(EI)_{tp}$ , of the multi-layer actuator paddle as defined in Section 3.5.3. The stacked coil structure of the paddle precludes the use of closed form equations to model the paddle rigidities. These values are instead determined via FEA simulations. A COSMOSWorks FEA model was constructed using the mask layout to create the layers on the paddle. A known force and temperature were independently applied to the paddle structure, and the resulting curvature was then measured. The data was fit by linear regression to obtain the rigidity.

## **4.4 System-Level Performance Optimization**

The iterative design process uses the analytic and numerical models that were developed in Chapter 3, to converge upon a HexFlex-type flexure geometry that meets the functional requirements that were developed in Chapter 2. Figure 4.13 shows a block diagram of the iterative design process.

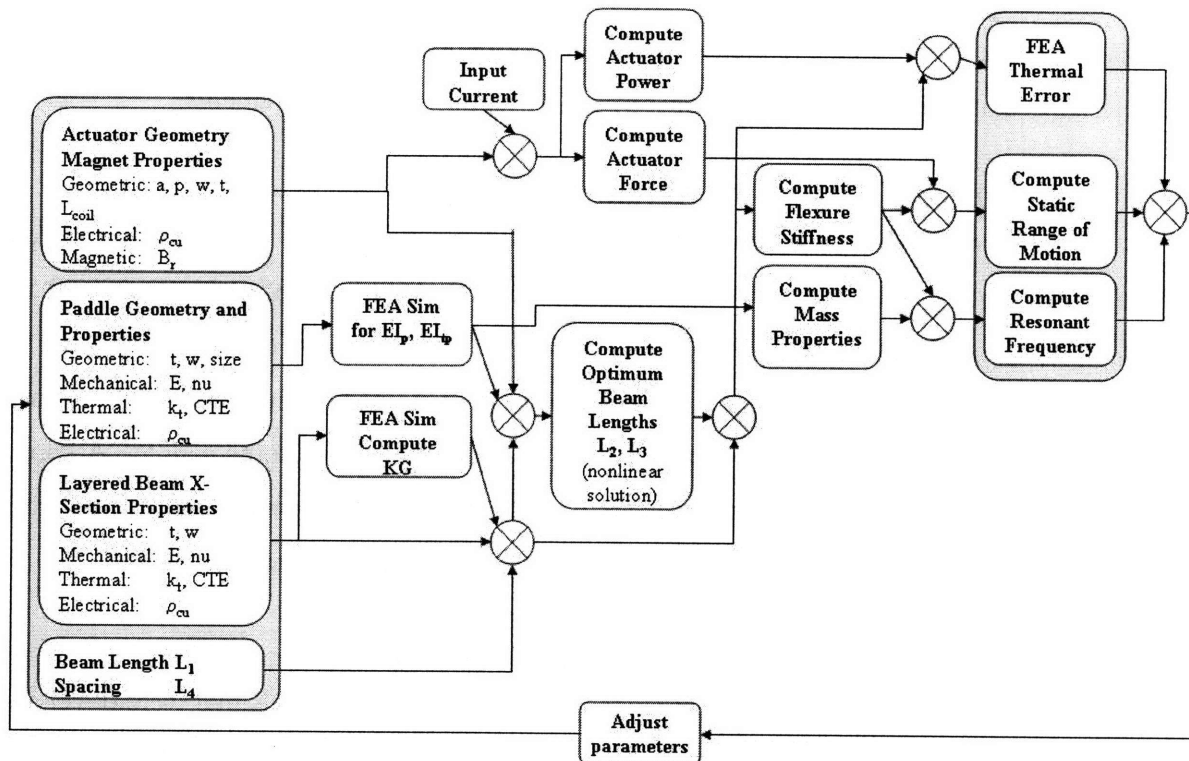
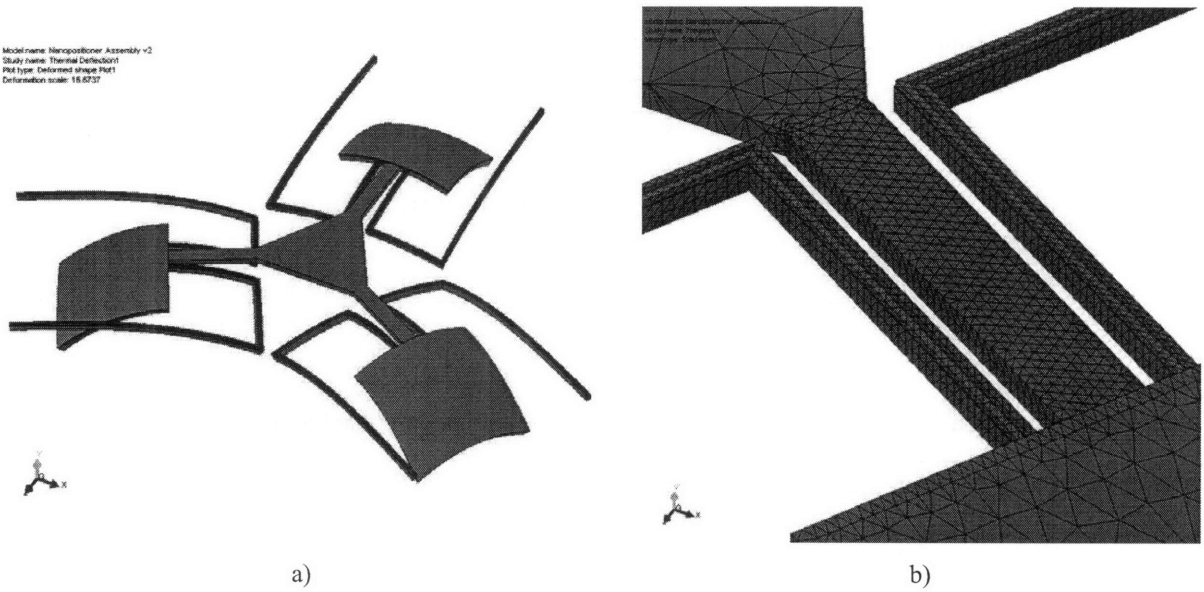


Figure 4.13. Iterative loop for the design of the nanopositioner.

The thermally-induced error motion, range of motion, and resonant frequency may be computed via FEA or the analytic models. At the time of the design, the mechanical displacement and resonant modal frequency models within section 3.4.6 were not complete. An FEA model of the structure was instead used to simulate the performance metrics. The forces that were calculated via the actuator force models were applied to an FEA model of the structure in order to predict the stage displacements. The FEA model was also used to compute the modal resonant frequencies and to predict the steady-state temperature, and subsequent thermally-induced error motion, that were caused by power dissipation within the paddles. The thermally-induced error motion was determined by applying the maximum power that was dissipated within the  $x$ -actuator to be dissipated within each of the two paddles. The stage error motion was then measured. The FEA model was composed of the silicon flexure and the copper leads that lie upon the flexure. The model does not include the silicon dioxide interlayer dielectric. It only simulates the coils as copper plates that lie upon the paddles. Figure 4.14a shows the exaggerated deformations of the nanopositioner that were caused by power dissipation in the coils. Figure 4.14b shows a close-up of the un-deformed mesh for reference.



**Figure 4.14. a) Exaggerated deformation of the nanopositioner FEA model that was caused by power dissipation in the coils; b) close-up view of the solid mesh used in the FEA model.**

The design process that was shown in Figure 4.13 was initialized by choosing practical values for the silicon thickness, silicon width, copper thickness, copper width, and beam length,  $L_1$ . Several iterations of the design process were manually completed in order to arrive at an optimal design. Table 4.9 provides the optimized geometry. Table 4.10 and Table 4.11 present the performance of the nanopositioner that was predicted via FEA simulations.

**Table 4.9. Flexure geometry of the optimized nanopositioner.**

Symbol	Parameter	Value	Units
$L_1$	Beam Length 1	4400	$\mu\text{m}$
$L_2$	Beam Length 2	1449	$\mu\text{m}$
$L_3$	Beam Length 3	1546	$\mu\text{m}$
$L_4$	Beam Separation	290	$\mu\text{m}$
$L_{ps}$	Paddle to Stage beam length	1626	$\mu\text{m}$
$w_s$	Stage Width	1970	$\mu\text{m}$
$w_p$	Paddle Width	2270	$\mu\text{m}$
$w_l$	Paddle Length	1965	$\mu\text{m}$
$t_{si}$	Flexure Thickness	100	$\mu\text{m}$
$w_{si}$	Flexure Width	80	$\mu\text{m}$
$t_{Cu}$	Copper Lead Thickness	25	$\mu\text{m}$
$w_{Cu}$	Copper Lead Width	25	$\mu\text{m}$
$g_{Cu}$	Spacing between Leads	20	$\mu\text{m}$

**Table 4.10. Predicted resonant modes of the optimized nanopositioner.**

Symbol	Mode	Value	Units
$f_{\theta z}$	$\theta_z$	972	Hz
$f_{\theta y}$	$\theta_y$	1013	Hz
$f_{\theta x}$	$\theta_x$	1014	Hz
$f_z$	Z	1058	Hz
$f_x$	X	1883	Hz

**Table 4.11. Predicted static motion, thermally-induced error motion, and maximum operating temperature.**

Symbol	Description	Value	Units
$\delta_y$	Static Displacement in Y	4.92	$\mu\text{m}$
$\delta_z$	Static Displacement in Z	6.02	$\mu\text{m}$
$i_x$	X Actuator Current	233	mA
$i_z$	Z Actuator Current	80	mA
$P_x$	X Actuator Power Dissipation	80.9	mW
$P_z$	Z Actuator Power Dissipation	5.3	mW
$\delta_{t,x}$	In-plane thermal error	100	nm
$\delta_{t,z}$	Out-of-plane thermal error	30	nm
$T_s$	Maximum Stage Temperature	147	$^{\circ}\text{C}$
$T_p$	Maximum Paddle Temperature	162	$^{\circ}\text{C}$

The nanopositioner's range-of-motion is twice the unidirectional static displacement that is shown in Table 4.11. The data in the preceding tables indicates that the models predict the nanopositioner will satisfy the functional requirements of 10  $\mu\text{m}$  range-of-motion and 1 kHz natural frequency. The simulations indicate that the thermally-induced error motion will be 30 nm out-of-plane and 100 nm in-plane. In theory, the out-of-plane thermally-induced error motion should be zero, but numerical error and the un-modeled kinematics result in a finite value of less than 30 nm. The un-modeled kinematics include the rotation of the corners that join the beam elements. The in-plane error motion of 100 nm was caused by the thermal gradient that occurs when two actuator paddles were powered to move the stage to its maximum range in the y-direction. The in-plane error motion may not be eliminated, but only minimized by reducing the power dissipation. The actuators may sustain greater currents than those that were listed in the table. The acceptable range-of-motion was thereby limited by the thermally-induced error motion that was induced by coil power dissipation. The thermally-induced error motion is a



quadratic function of input current, but it is a systematic error motion and therefore this error motion may be minimized in steady-state through nonlinear calibration.

The design for passive prevention minimizes the thermally-induced error motion that is experienced in steady state operation. Transient heating yields transient thermally-induced error motions that are not easily addressed by calibration. Figure 4.15 shows the simulated transient response of thermally-induced error motions that would result from an in-plane step command of  $5\ \mu\text{m}$  in the  $y$ -direction.

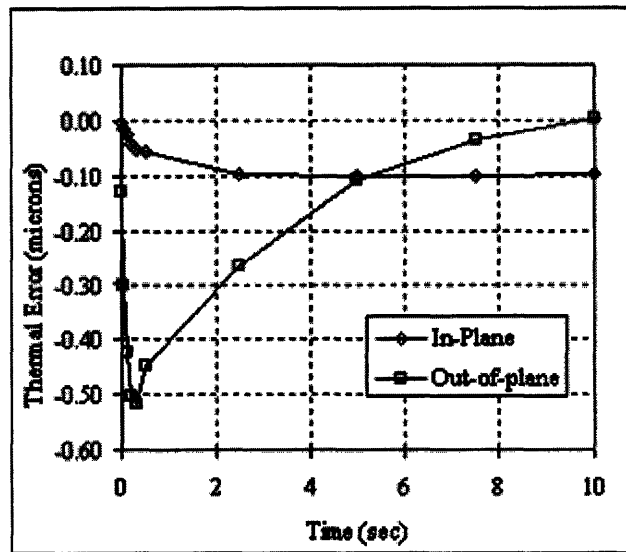
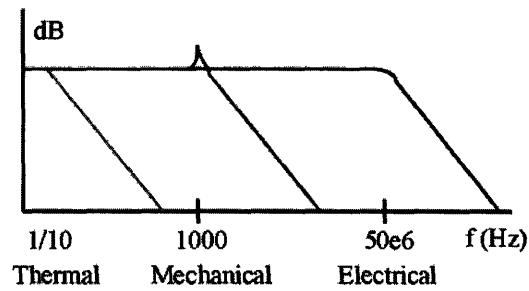


Figure 4.15. Simulated transient thermally-induced error motion of the nanopositioner.

The data in the figure shows that the system has a thermal time constant that was on the order of several seconds, that is it occurs with a characteristic frequency that was less than 1 Hz. Operation at frequencies that are above 10 Hz may attenuate the thermally-induced error motions that are exhibited by the system. The simulation result indicates that the nanopositioner may operate at frequencies that are below the mechanical resonance but above the thermally-induced dynamics in order to minimize thermally-induced error motions. Figure 4.16 shows a qualitative representation of the multi-domain dynamic response.



**Figure 4.16. Qualitative representation of the nanopositioner system dynamics in the thermal, mechanical, and electrical domains.**

The order-of-magnitude separations in roll off frequency indicates that it may be possible to combine motion command input signal with a high frequency modulation signal at 10-100 kHz to either preheat the device or actively control the thermally-induced error motions. The mechanical response characteristics are such that the system will attenuate actuator inputs if a high-frequency modulation signal is used as the RMS power input preheats the device to steady state.

## **4.5 Mask Design Geometry**

Figure 4.17 shows a plan view of the nanopositioner chip that has the characteristics which are listed in Table 4.6 and Table 4.9. More detail regarding the mask design/geometry may be found in Appendix A.

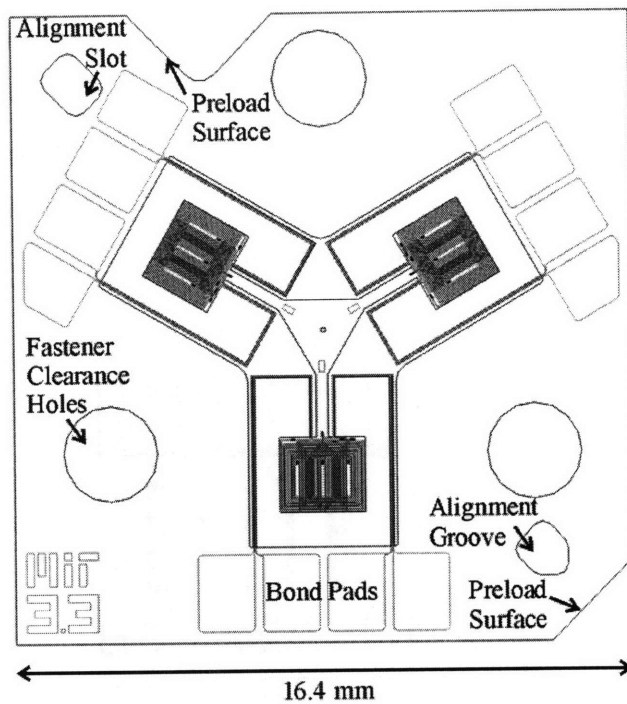


**Figure 4.17. Plan view of the front side of the nanopositioner chip.**

The microfabricated nanopositioner chip design includes the following:

- 1) actuator paddles that are comprised of stacked, copper actuator coils and jumpers that are separated by a layer of silicon dioxide;
- 2) vias through the silicon dioxide that are used to route current between the coil layers;
- 3) composite flexure beams that are comprised of silicon, silicon dioxide, and the copper leads;
- 4) a stage that contains metrology features;
- 5) electrical bond pads;
- 6) alignment features –a groove and slot;
- 7) fastener clearance holes; and
- 8) surfaces that are used to preload the chip against the alignment pins.

Other features that are not included in the figure are set based upon fabrication-specific requirements/constraints and will be discussed within Chapter 5.

Figure 4.18 shows the mask geometry for the stacked coil and jumper architecture. The jumpers and vias were configured to route current to, and from, the coils with two layers of copper. Eight vias and four jumpers were required to route the electrical current in this configuration. The jumper configuration imposes a limitation on the minimum coil segment spacing,  $d$ , so that the coil geometry has sufficient space for the vias.

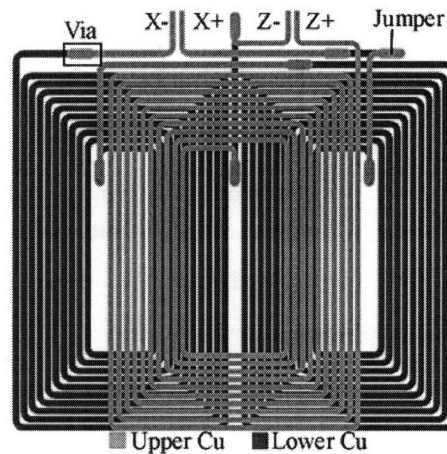


**Figure 4.18.** Mask geometry of the stacked actuator coils that shows the vias and jumper architecture that route current to the coils.

## 4.6 Package Design

The microfabricated nanopositioner chip must be aligned to three arrays of permanent magnets. A packaging architecture was created to align the magnets to the chip with an alignment plate that was fabricated by wire electro-discharge machining (EDM). The alignment plate also sets the height of the chip above the magnets. The magnetic gap was then adjusted with plastic shims. Figure 4.19 shows the assembly and an exploded view of the nanopositioner chip and with alignment package. Appendix B contains the part drawings for each component.

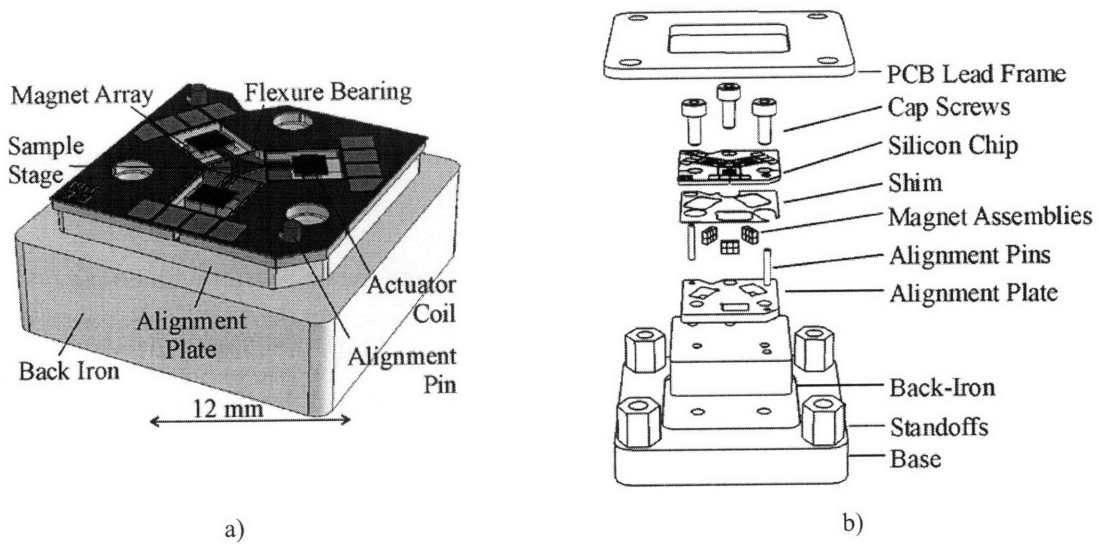


**Figure 4.19.** a) Solid model representation of the assembled nanopositioner chip and alignment package; b) exploded view of the complete nanopositioner assembly.

Fasteners were used to preload the silicon chip, the alignment plate, and the shim against the back-iron. The fasteners are omitted from Figure 4.19a for clarity. The exploded view in Figure 4.19b shows the printed circuit board (PCB) lead frame that was used to contact the bond pads on the chip. The lead frame components were assembled after alignment of the chip to the alignment plate. Figure 4.20 shows the method that was used to align the chip to the actuator magnets.

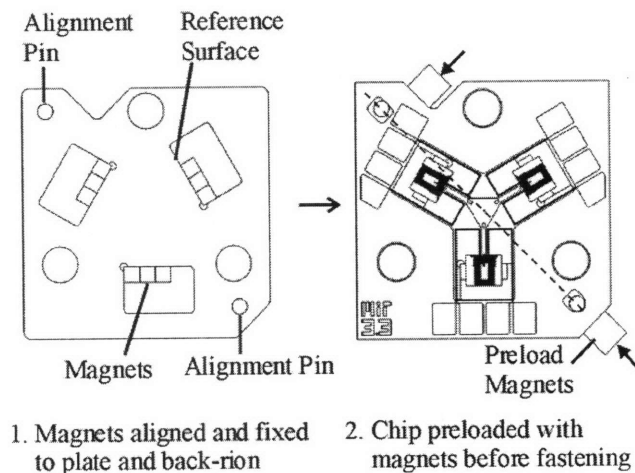


**Figure 4.20.** Schematic representation of the method that was used to align the chip to the actuator magnets.

The alignment method was conducted in several steps:

- 1) The alignment pins were press fit into the alignment plate and the plate was bonded to the back-iron with epoxy.
- 2) The magnet arrays were then assembled and installed into the cavities in the alignment plate.
- 3) The magnets were fixed to the alignment plate and the back-iron with epoxy.
- 4) The shim and nanopositioner chip were assembled on the alignment plate. Magnets were placed upon the back-iron and the chip was preloaded against the alignment pins.
- 5) Fasteners were installed to preload the chip, shim, and alignment plate against the back-iron. The preload magnets were removed after the application of these fasteners.
- 6) The aligned assembly was installed upon the base plate and the lead frame was connected to make electrical contact with the chip.

## 4.7 Summary

This chapter presented the physics-based methods that were used to design and optimize the nanopositioner so that it would satisfy functional requirements. Methods were developed to optimize the actuator coil geometry with respect to parasitic moment, force, and efficiency metrics in Section 4.2. The actuator coils were designed for maximum force efficiency in order to minimize thermally-induced error motions. A method was also developed in Section 4.3 to optimize the double bent-beam flexure geometry for passive, steady-state prevention of out-of-plane thermally-induced error motion. The actuator force models were then combined with an FEA stiffness model of the nanopositioner in an iterative loop to design the flexure and actuator geometry so that it would satisfy the functional requirements that were laid out in Table 2.1. The iterative design loop was presented in Section 4.4 The models indicate that the meso-scale nanopositioner will possess the following performance characteristics:

- a) a first mechanical resonance of 970 Hz;
- b) a range-of-motion in the  $x$ -direction of nearly 10  $\mu\text{m}$
- c) a range-of-motion in the  $z$ -direction of greater than 12  $\mu\text{m}$ ;
- d) thermally-induced error motion of approximately 100nm in-the-plane and 30nm out-of-the-plane;

e) maximum stage operating temperature of approximately 150°C.

In addition, the physical layout and mask geometry of the actuators, flexure, and packaging was presented in Section 4.5 and the magnet-coil alignment method was outlined in Section 4.6.

## MICROFABRICATION DEVELOPMENT

---

This chapter covers the development of the microfabrication process that was used to fabricate the nanopositioner. Microfabrication experiments were conducted in order to develop geometry-based design rules for the stacked coil actuator architecture. The dielectric strength of unannealed silicon dioxide layer was measured using a capacitor test structure. The microfabrication process was successful and yielded a functional meso-scale nanopositioners.

### 5.1 Introduction

The meso-scale nanopositioner design combines several features – silicon flexure elements, two layers of copper coils, and a dielectric that separates the coils. The fabrication process was composed of two primary fabrication modules:

- 1) the stacked planar-spiral coils; and
- 2) the silicon and copper flexure structure.

The coil and flexure modules were integrated together, rather than assembled, as part of the microfabrication process. The critical process module in this design was the stacked planar-spiral coil process.

Planar microcoil structures typically consist of a molded metal coil layer, electrical insulation, and a jumper layer. Coils have been fabricated by plating materials into various mold materials which include SU-8 [103, 174], polyimide [96, 179-181], photoresist [3, 75, 95, 103, 105, 119, 124, 125, 182, 183], and silicon [1, 33, 102, 175]. The advantages of SU-8 include vertical sidewalls, aspect-ratio that are greater than 10:1, thickness up to 100s of microns, and good planarization properties. SU-8 is difficult to remove and therefore it often remains as part of the structure. This is problematic for the proposed design because the thermal properties of



SU-8 limit power dissipation in microcoil devices [105, 125]. In addition, SU-8 contamination constraints and the material's thermal properties limit compatibility with processes such as deep reactive ion etching (DRIE). Polyimide molds may be removed by dry etching, but they are limited to make molds that are only tens-of-microns in thickness which is sufficient for the actuator design. Polyimide requires more processing steps than photoresist and dry-etching for removal, and thereby may reduce yield. Photoresist molds are commonly used because of their processing ease, good adhesion, and ease of removal. Photoresist molds may be fabricated up to 100 microns thick, with aspect-ratios of up to 6:1. Positive resist sidewall profiles have typical sidewall angles of 70 - 85° before post-baking. As compared to the aforementioned methods, DRIE silicon molds may be fabricated to 100s of microns, with aspect ratios that are larger than 20:1, and with excellent sidewall profile. The thermal conductivity of silicon is approximately 1000 times that of polymer-based materials. This is important because higher sustainable currents may be carried. A 1-D steady-state thermal conduction analysis will show that the maximum coil temperature may be reduced by a factor of two or greater by plating coils (a) into DRIE trenches rather than (b) on top of silicon and within a polymer mold. The improvement results from the increased coil-to-silicon contact area and reduced thermal resistance. Assume (i) an equivalent winding thickness and width for both cases, and (ii) that the backside of the chip was held at ambient, it may be shown that the ratio of steady-state coil temperature increase from ambient for cases (a) and (b) is:

$$\frac{\Delta T_{polymer}}{\Delta T_{silicon}} = 1 + \frac{2t_{Cu}}{w_{Cu}} \quad (5.1)$$

where  $t_{Cu}$  and  $w_{Cu}$  are the thickness and width of the coil winding. For square cross-sections, the temperature is reduced by a factor of three for coils that are plated in silicon versus polymer molds. The ability to reduce temperature would improve the efficiency and power density of many types of small-scale machines, for example micro-generators [102] and the actuators within this research. Other multi-axis actuator systems have employed a type of deep mold and flexure architecture [1, 33]. As opposed to bottom-up electroplating in polymer molds, deep silicon molds with high aspect ratios require damascene super-filling of copper for keyhole-free deposits [184].

The actuator design is comprised of planar spiral coils that require at least two metal layers, coil and jumper, that are separated by an interlayer dielectric insulator. The design consists of two molded coil layers with an integrated serpentine jumper. Combinations of mold structures have been used in previous work to design jumper system including SU-8 and photoresist [174, 185] and silicon and photoresist [102]. In all devices, single-coil and double-coil, polymers were used as the interlayer dielectric insulator and they were often used to encapsulate the coils for planarization. The common polymers include polyimide [82, 84, 88, 96, 124, 179], SU-8 [103, 105, 125, 174], BCB [119], and parylene [75]. These polymers exhibit poor thermal conductivity that are less than 0.2 W/m-K, and this limits the heat transfer away from the coils. The polymers also impose downstream processing limitations. For example, devices with SU-8 will contaminate deep reactive-ion etching, while polyimide is etched at rates that are similar to photoresist [186].

One may also consider silicon dioxide, which is compatible with standard processes. Silicon dioxide has an order-of-magnitude better thermal conductivity ( $\sim 1.1$  W/m-K) than the above-listed polymers and excellent mechanical and electrical properties as shown in Table 4.1. Un-annealed, plasma-enhanced CVD (PECVD) silicon dioxide was selected for use as the dielectric insulator. It is used in order to fabricate a high-current, thermally-efficient, double-layer copper coil structure for the meso-scale nanopositioner. The oxide insulates the silicon- and photoresist-molded copper coil layers. This material stack may be integrated with deep-etched silicon flexures in order to enable fabrication of the meso-scale nanopositioner. Several design and fabrication challenges must be addressed in order to realize the device. The challenges include:

- 1) electroplating coils with sufficient winding cross-section area;
- 2) thermally-induced stresses that were caused by CTE-mismatch during processing; and
- 3) un-annealed oxide electrical performance.

This chapter presents a process to create double-layered copper coils and silicon flexures by using a PECVD silicon dioxide layer between silicon- and photoresist-molded coils. The layers are connected using a serpentine jumper architecture. The double coil structure was released during a multi-step DRIE process that uses photoresist, silicon dioxide and the copper coils as the mask. The results of measurements are presented and then used to justify thermal-

mechanical limitations on the coil geometry's design space. The results of electrical breakdown experiments on the un-annealed oxide are also presented.

## 5.2 Process Overview

Figure 5.1 shows a cross-section of the proposed device that cuts through the actuator paddle and flexure beams. The nanopositioner chip consists of double copper coils that were separated by PECVD silicon dioxide and suspended over permanent magnets by silicon flexures. The device was fabricated with silicon-on-insulator (SOI) wafers in order to maintain tight control of the 100  $\mu\text{m}$  flexure thickness. The SOI handle also serves to set the height of the actuator paddles above the magnet array. Actuator coils were insulated from the silicon device layer with 2000  $\text{\AA}$  of wet thermal oxide. The PECVD silicon dioxide serves the following purposes:

- 1) electrical isolation between coils;
- 2) vias for current routing in the actuator; and
- 3) etch mask for DRIE of the silicon flexures and alignment features in the SOI device layer.

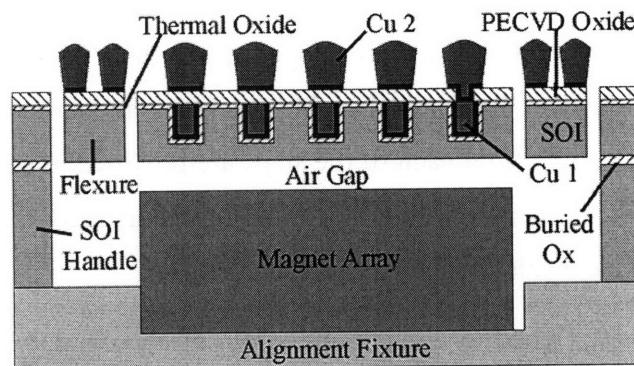


**Figure 5.1. Cross-section schematic of the meso-scale nanopositioner chip and magnet array**

Figure 5.2 shows the cross-section schematic process flow that was used to microfabricate the meso-scale nanopositioner. Detailed process steps are omitted for brevity.

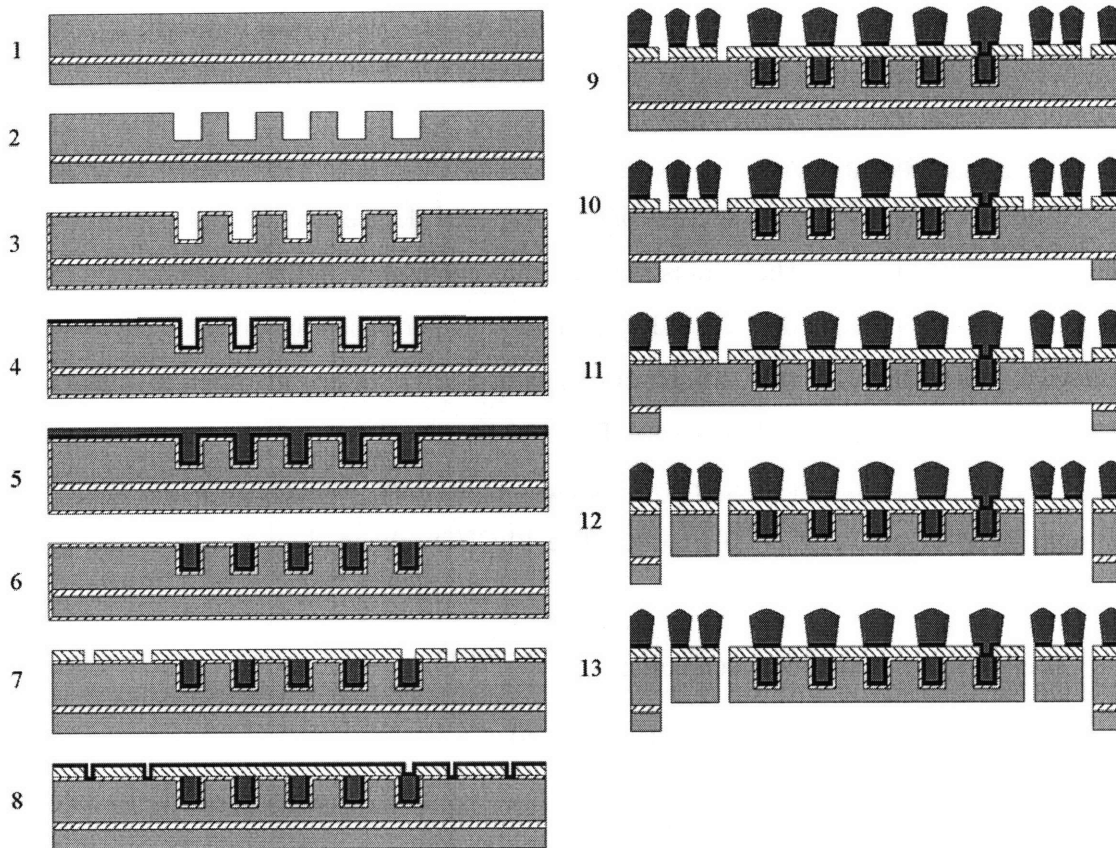


**Figure 5.2. Cross-section schematics of the microfabrication process that was used to realize the nanopositioner.**

The microfabrication process was developed in the MIT MTL and the MTL-approved process flow may be found in Appendix D. This includes all fabrication steps and machine settings. Images of the results from each of the steps are provided in subsequent sections. The process uses four masks and begins with a silicon-on-insulator wafer that has a 100  $\mu\text{m}$  device layer, 1  $\mu\text{m}$  silicon dioxide insulator, and 610  $\mu\text{m}$  handle layer.

Coil trenches were etched to a depth and width of approximately 30  $\mu\text{m}$  via the MTL-standard ‘OLE3’ recipe in step (2). DRIE silicon molds enable large coil winding cross-sections and dense winding packing. A 1  $\mu\text{m}$  OCG825 positive photoresist was used as the mask during this etch step. The photoresist was stripped after deep etching with oxygen plasma that was followed by a Piranha acid clean.

Wet thermal silicon dioxide was then grown to a thickness of 2000  $\text{\AA}$  in step (3) for the purpose of coil passivation. A 50 nm titanium and 500 nm copper electroplating seed layer was then sputtered by DC magnetron in step (4) without breaking vacuum. The wafers were cleaned

in Piranha immediately before sputtering. The wafers were then electroplated in step (5) by using a deep via trench plating chemistry and an aggressive agitation at Nexx Systems in Billerica, MA. The electroplating details were discussed in section 5.4.1. The plated overflow on the front side of the wafer was polished in step (6) by chemical-mechanical polishing (CMP) down to the thermal oxide, which acts as a polishing barrier. Typically 15-20% of the thermal oxide thickness was lost because of the combination of polishing and plating non-uniformity. Section 5.5 discusses copper CMP in more detail.

After CMP, the wafers were cleaned in dilute citric acid before oxide deposition in step (7). Although copper is known to diffuse into silicon dioxide, a barrier material was not deposited at this point in order to minimize the process complexity. Sections 5.6 and 5.7 discuss oxide design and provide justification for this decision. The PECVD oxide was deposited with a 13.56 MHz RF source at 300°C to a thickness of 1  $\mu\text{m}$  in step (7). The elevated processing temperature caused stress to build up in the copper-in-silicon structure as a consequence of the mismatch between the materials' coefficient of thermal expansion (CTE). The thermomechanical stress led to cracking and delamination of silicon and silicon dioxide in some cases where the geometry of the coils favored the defects. The delamination and cracking imposes design constraints on the coil geometry, as discussed in 5.6. After deposition, the oxide was patterned in step (7) by wet etching in buffered oxide etch (BOE) with a 2-3  $\mu\text{m}$  OCG825 positive photoresist mask. The thermal oxide on the backside of the wafer was stripped during this etch step. The oxide pattern consists of vias to the buried copper coil layer and halo patterns that help to etch the flexures, paddle, stage, and alignment features during DRIE. The vias were nested laterally within the buried copper in order to prevent BOE attack of the interfacial titanium and thermal oxide. Fabrication results indicate that the BOE does not attack the exposed copper in the vias. The resist was stripped in NMP at 65°C in order to minimize damage to the copper that was exposed in the vias.

A second electroplating seed layer of 20 nm Ti and 200 nm Cu was then deposited in step (8) by electron beam evaporation without breaking vacuum. AZ9260 photoresist was patterned in step (9) as an electroplating mold that possessed thickness of approximately 32  $\mu\text{m}$ . The photoresist was allowed to rehydrate for approximately 24 hours before exposure and development in AZ400K inorganic developer. The photoresist was not post-baked in order to

maintain a sidewall angle of nearly 85°. The resist surface was then made hydrophilic in preparation for electroplating by a short, low-power oxygen plasma ash. Copper was then DC-electroplated into the resist mold in a conventional copper-sulfate chemistry. See section 5.4.2 for a discussion of the photoresist and electroplating processes and limitations. The resist mold was stripped in acetone after electroplating. A two-step wet etch with ultrasonic agitation was then used in step (9) to etch the Ti/Cu seed with 100:1 H<sub>2</sub>O:HF and 50:1 H<sub>2</sub>O:HNO<sub>3</sub>, respectively. The dilute HF solution etched the underlying PECVD silicon dioxide by less than 10 nm. The HF also tended to undercut defects in the oxide that led to areas of visible discoloration. After seed etching, the copper coil structures were complete.

The wafer was then mounted upside-down on a mount wafer with thick photoresist and then etched from the backside with DRIE in step (10). Spray-coated positive photoresist protected the front side of the device wafer before mounting. The wafers were etched in DRIE for 1 hour intervals with the buried oxide as an etch stop. Thick AZ4620 photoresist was then used as the etch mask during this etch step. The top-layer of electroplated copper included the following features to help enable this step:

- 1) “dummy” copper features to promote thermal contact between the mount and device wafer; and
- 2) a seal ring around the device area to improve coater chuck vacuum for spinning resist onto the backside of the wafer.

After backside etching, but before dismounting, the buried oxide was etched in vapor HF for approximately 5 minutes in step (11). The wafers were then dismounted in acetone for approximately 24 hours. Residual resist and Teflon debris were cleaned with a low-power, pulsed oxygen plasma. The low-power pulsed oxygen plasma was not observed to damage or oxidize the exposed copper coils. Next, the wafers were mounted right-side-up on a mount wafer and the flexure and alignment features were through-etched via DRIE in step (12). Exposed copper and unannealed oxide served as the etch mask. The DRIE step did not damage the exposed copper but some oxidation was observed. The wafers were then dismounted upside-down in acetone and then cleaned with the low-power, pulsed oxygen plasma. Section 5.9 discusses the details of the flexure etch steps. After dismounting and oxygen cleaning, the dies remain linked together, and to the wafer, by tethers in the SOI device layer. Laser ablation was

used to cut the tethers and release the dies. Figure 5.3 shows an optical image of the completed nanositioner die after laser ablation of the tether links. The black spots on the perimeter of the die show the location of ablated tethers.

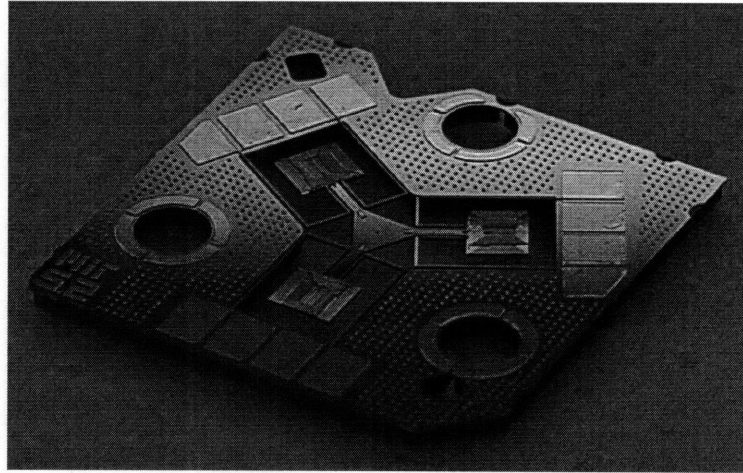


**Figure 5.3. Optical image of the completed nanositioner die.**

### **5.3 Mask Designs**

Several process-specific features were incorporated into the design of the mask in order to improve the yield of the process. Figure 5.4 shows mask layout designs for each layer. The following sections discuss the process specific features of these patterns. Mask 1 contains the pattern for the trenches that define the buried copper coils. Mask 2 serves as the etch mask for the silicon dioxide interlayer dielectric. The oxide was used as the etch mask for the final DRIE release etch. The oxide mask contains the via pattern and halo etch for the nanositioner structure, alignment features, and die tethers. Mask 3 consists of the photoresist mold patterns for the upper copper coil, leads, bond pads, and dummy features for promoting thermal contact during the backside etch. Mask 4 contains the pattern for the backside cavities and trenches.

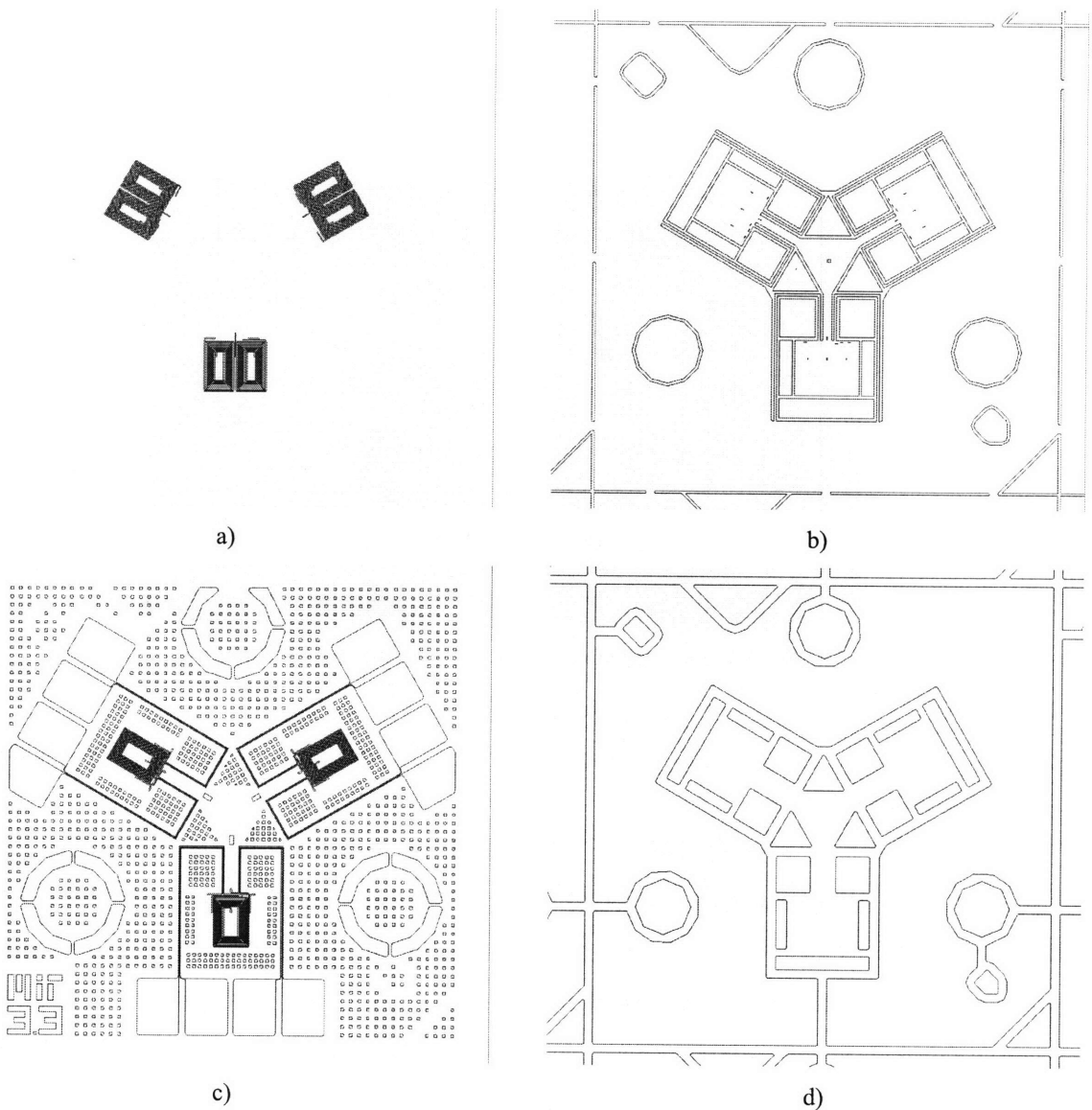


**Figure 5.4. Mask designs for the nanositioner process: a) mask 1, buried copper coil trenches; b) mask 2, silicon dioxide vias and DRIE mask; c) mask 3, photoresist mold for upper copper coil, leads, bond pads, and dummy features; and d) mask 4, backside cavity and trenches.**

## 5.4 Copper Electroplating

The fabrication process consists of two main copper electroplating steps:

a) top-down or “super-filling” into silicon mold followed by back-grinding the overflow;  
and

b) bottom-up filling into a photoresist trench followed by a mold and seed strip.



Each of these steps have been developed elsewhere [183, 184, 187, 188]. The following sections provide a brief overview of the processes and discuss some limitations as related to coil performance.

#### **5.4.1 Top-down filling in Silicon molds**

In this work, the mold depths and copper winding widths were chosen well within the limits of current copper super-filling capability. Although winding cross-section aspect ratio was no greater than 1:1 at a width of 30  $\mu\text{m}$  for the device, aspect ratios greater than 7:1 at depths up to 70  $\mu\text{m}$  have been achieved [189, 190]. Thermally-induced stresses in subsequent processing steps impose a limit on the maximum mold depth, as will be discussed in section 5.6. Mold width limitations were imposed by in-plane thermo-mechanical stresses during subsequent processing and by the thickness of the copper overflow. Copper CMP time increases in proportion to the overflow thickness for wide and deep coils. For the coils that were designed in this work, the copper overflow was between 20-30  $\mu\text{m}$  thick, and required approximately two hours of polishing time per wafer. A conservative aspect ratio of 1:1 and width 30  $\mu\text{m}$  was chosen for the buried coils in the microactuator. Aspect ratios that are greater than 1:1 require tighter control of the processing conditions and therefore as the ratio approaches 1:1, the yield is reduced. For a given trench depth, aspect ratios less than 1:1 lead to thicker copper overflow and increased polishing time. The width of the coils was designed to achieve a suitable trade-off between device performance and process yield. The coil resistance and power dissipation decrease as the coil cross-section increases, but the electroplating and CMP processes limit the yield as the cross-section increases.

Nexx Systems electroplated the buried coils in this work by using Enthone DVF 100 super-filling chemistry and pulse-reverse plating [191]. The DVF 100 copper sulfate chemistry employs additives for enabling deep plating in trenches that are 10s of  $\mu\text{m}$  wide and up to 100  $\mu\text{m}$  deep. The electroplating bath uses a proprietary agitation system to achieve high-velocity flow at the surface of the wafer and to enable bottom-up filling of deep trenches. Insufficient control of the processing conditions may lead to voids in the copper deposit as shown in optical image in Figure 5.5 and the SEM in Figure 5.6.

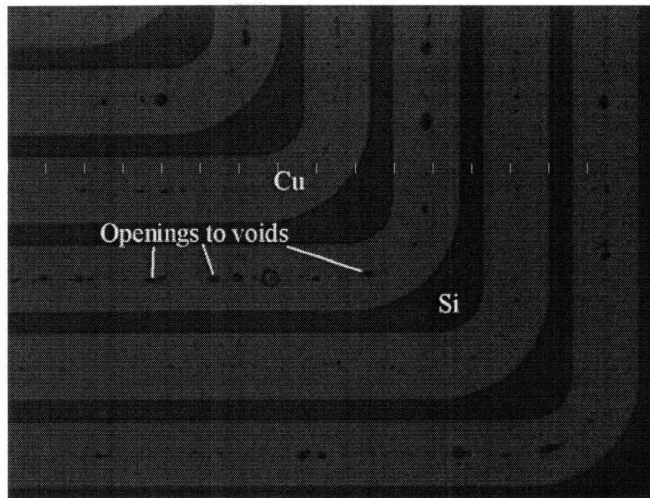


**Figure 5.5. Optical image a buried coil after CMP that shows voids in the copper deposits.**

The optical image was taken after CMP of the wafer. The image shows openings to voids within the copper windings. Figure 5.6 shows cross section SEM images of voids in the copper coils that come from different wafers. The wafers were processed in the same tool with similar process parameters, but with variable bath age.

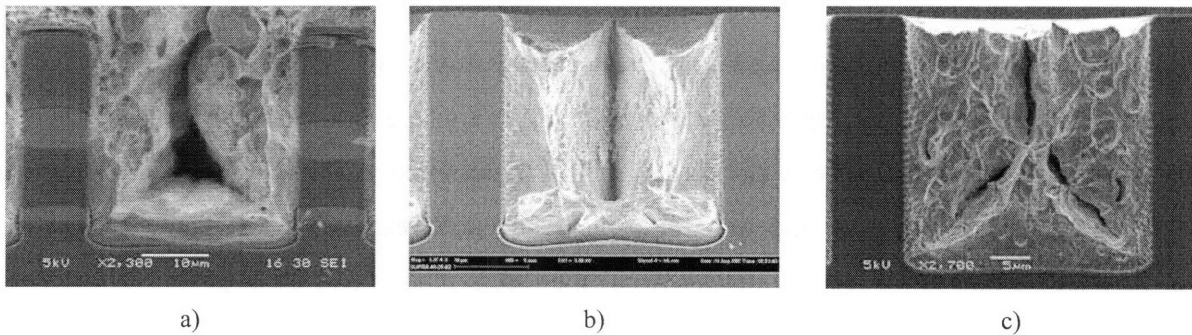


**Figure 5.6. SEM cross-section images of buried copper coils with void defects from different wafers. The cross-sections were created by cleaving the wafers and fracturing the copper in tension.**

The cross-sections were obtained by cleaving the wafers and fracturing the copper in tension. Cleaving was used instead of die-sawing or polishing so as to eliminate the possibility of plastic deformation of the copper that could obstruct voids. The SEM images illustrate the sensitivity of copper super-filling to process parameter control and contamination. The super-filling results change with bath chemistry ages as indicated in the figure. The copper super-filling process step was completed after the bath chemistry was replaced and conditioned by Nexx Systems. Appendix D provides the process parameters that were used to electroplate copper into the

trenches. Figure 5.7 shows an optical image of a void-free buried copper coil that was electroplated at Nexx by using the process conditions that are specified within Appendix D.

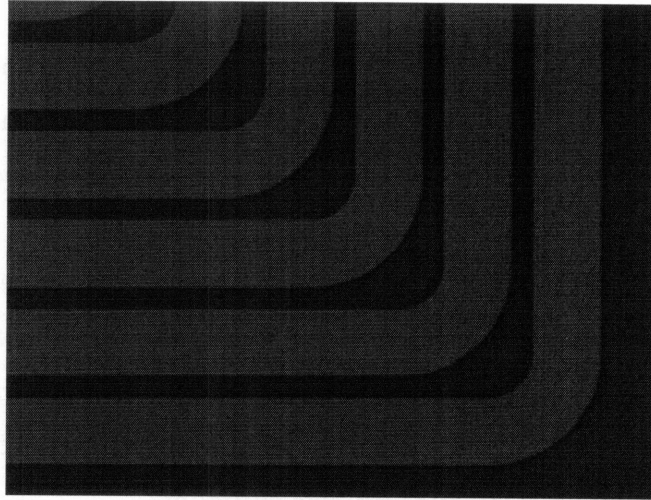


**Figure 5.7. Optical image a void-free buried coil after CMP.**

Figure 5.8 shows a cleaved cross section SEM image of void-free coil windings after partial CMP.

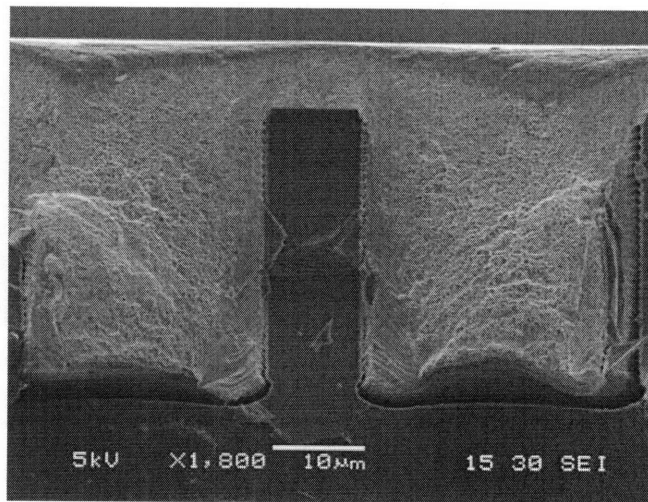


**Figure 5.8. SEM cross-section images of void-free buried copper coils after partial CMP.**

#### **5.4.2 Bottom-up filling in photoresist molds**

The upper copper coil layer was electroplated into a photoresist mold and electroplated from a seed layer that was at the bottom of the mold. A DC current was used in the process. An AZ9260 photoresist was spun twice at 1000 rpm and pre-baked at 95°C for 100 minutes in a convection oven. The resist was subsequently allowed to rehydrate for at least 24 hours and then

exposed and developed in AZ400K 1:4 inorganic developer. Postbaking the resist would cause the resist to flow and change the sidewall angle from nearly vertical to less than  $65^\circ$ . Postbaking was therefore eliminated in order to maintain vertical sidewalls and to enable thick resist and copper deposits. The photoresist surface was made hydrophilic with oxygen plasma so that surface tension would not inhibit the plating chemistry from entering the trenches. The low-power oxygen plasma was applied for less than 2 minutes and its use does not affect the resist sidewall profile. The wafers were pre-wet with water before placement in the bath chemistry. Copper was then DC-plated into the resist mold in a paddle-agitated electroplating bath using Enthone MicroFab SC copper sulfate electroplating formulation. The photoresist and seed metal were stripped after electroplating with acetone and then a two-step sequential acid etch was performed as previously discussed. Figure 5.9 shows SEM images of the copper lines that are  $25\ \mu\text{m}$  thick, an average of  $28\ \mu\text{m}$  wide, and separated by  $12\ \mu\text{m}$ .

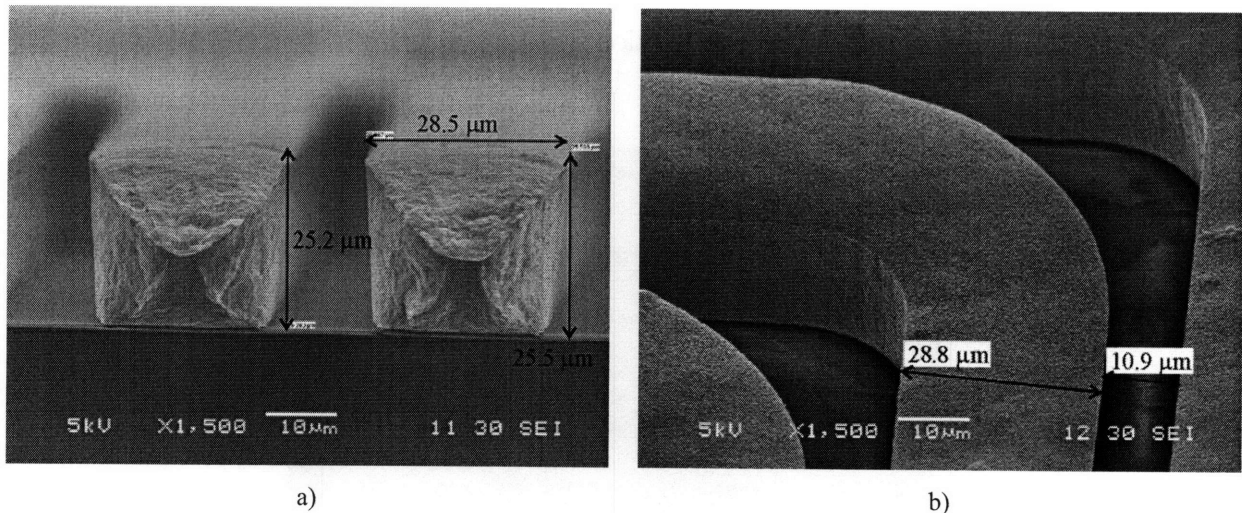


**Figure 5.9. SEM images of the a) cross-section of the resist-molded coil winding and b) coil corner before DRIE flexure etching.**

The AZ9260 resist adheres well to copper and is easily stripped in acetone, but the resist profile that may be achieved limits winding thickness and packing density. The resist aspect ratio, maximum thickness, and sidewall profile are strongly dependent upon the pre-bake and exposure recipes. The photoresist recipe was developed for vertical sidewalls through extensive recipe experiments that included variations in the pre-bake, rehydration, and exposure times. Appendix D provides the results of these experiments. Aspect ratios of 6:1 at a thickness of  $81\ \mu\text{m}$  have been reported elsewhere [183]. The subsequent metal seed etch step imposes a practical

limitation on aspect ratio and winding spacing. As the winding spacing decreases and thickness increases, the seed etchant diffusion time and required seed etch time increase. This leads to excessive erosion of the plated deposit, and this could lead to undercutting of the titanium adhesion layer. To date, coils with up to:

- 25  $\mu\text{m}$  thickness
- winding spacing of 15 $\mu\text{m}$ , and
- coil width of 25 $\mu\text{m}$

have been successfully fabricated. The final spacing and width of the coil windings was 12 $\mu\text{m}$  and 28 $\mu\text{m}$ , respectively, after resist processing and seed etching. The coil geometry was shown in Figure 5.9.

## 5.5 Copper CMP

Chemical-mechanical planarization was used to polish the overflow copper in step (6) of Figure 5.2. The copper was polished down to the underlying thermal oxide, which acts as a polish stop. CMP performance depends upon several process variables, including total down force pressure, differential backpressure, table velocity, head velocity, sweep velocity, slurry type and slurry concentration, pad type and condition, and wafer pattern, material stack and structure, wafer bow, and wafer edge profile. The CMP process experiments yielded a set of optimum process settings that minimized wafer slip-out within reasonable polishing time. The process resulted in what was deemed acceptable dishing and erosion of the copper and silicon features. Appendix D provides the CMP process settings and measured polishing rates. Figure 5.7 shows an example of the polished copper coils in silicon. The polishing non-uniformity and non-uniform copper deposit required over-polishing in some regions of the wafers in order to clear out a sufficient number of dies. Over-polishing resulted in dishing of the copper features and erosion of the silicon dioxide on the silicon features. Typically 15-20% of the thermal oxide thickness was lost because of over-polishing during this step. The dishing and erosion were minimized by terminating the CMP process before the wafer was fully polished. Copper dishing was measured with a Dektak profilometer to be less than 500 nm, and this was acceptable for further processing on the wafer surface. Dishing greater than approximately 1  $\mu\text{m}$  could result in surface topography that a) causes excessive stress in the 1  $\mu\text{m}$  PECVD silicon dioxide, and b)

prevents uniform coating of the thin photoresist used in subsequent steps to pattern the PECVD silicon dioxide.

## 5.6 Silicon Dioxide Thermomechanical Stress Experiments

Differential thermal expansion is an important consideration for copper-in-silicon structures. The CTE of copper,  $1.6 \times 10^{-5} \text{ 1/}^\circ\text{K}$ , is approximately 6 times that of silicon's CTE,  $2.6 \times 10^{-6} \text{ 1/}^\circ\text{K}$ . As a result, significant thermally-induced stresses may develop at elevated temperatures in copper-in-silicon coil structures. This was an important consideration for the proposed process, because the process includes PECVD oxide deposition at  $300^\circ\text{C}$  after filling and planarizing the buried coils. There are two modes of failure during this step:

- 1) cracking of the silicon near the copper structures and
- 2) delamination of the deposited oxide in areas of copper lines.

Failure of the silicon spacers along the silicon crystal planes has been observed after oxide deposition, as shown in Figure 5.10.

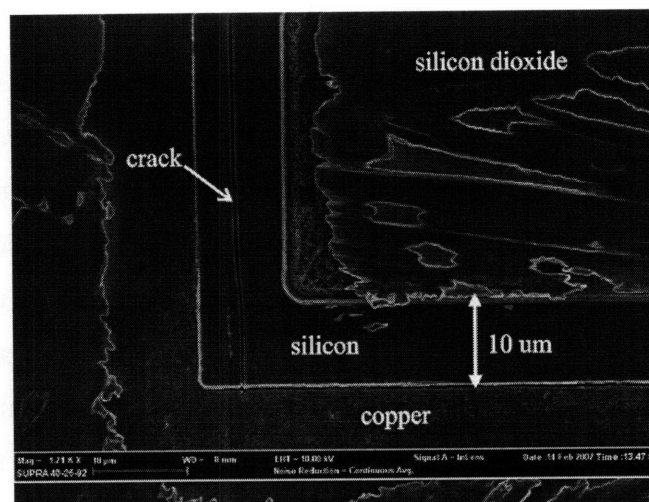


**Figure 5.10. SEM image of cracked silicon isolators after deposition and patterning of PECVD oxide. Wet-etched oxide is visible around the perimeter of the silicon isolator**

The sample was etched with BOE and then coated with 20 nm titanium and 200 nm copper before imaging within the SEM. The crack in the silicon extended into the oxide and was attacked by the BOE etch. The oxide etch exposed the underlying structures. In this case, the elevated oxide deposition temperature resulted in mechanical stresses that were sufficient to propagate cracks along the silicon spacers. The cracks terminate in the ductile copper, as shown

in the figure. Stress concentrations near the coil corners may exceed the critical stress that must be reached in order to cause crack initiation and growth along the silicon spacers. Observations indicate that it was possible to eliminate cracking during oxide deposition by rounding the inside corners such that the copper lines have constant cross-section around the corner. Figure 5.11 shows an example of a crack-free copper coil in silicon with rounded corners and 1  $\mu\text{m}$  of PECVD oxide.

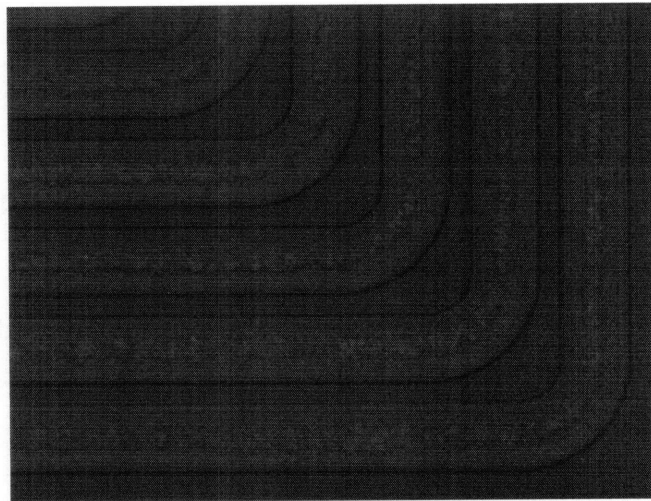


Figure 5.11. Optical image of a crack-free copper coil embedded in silicon with 1  $\mu\text{m}$  of PECVD oxide.

The second failure mode that was observed after oxide deposition involves delamination of the deposited oxide from the underlying copper structures. This defect may be seen in Figure 5.12.

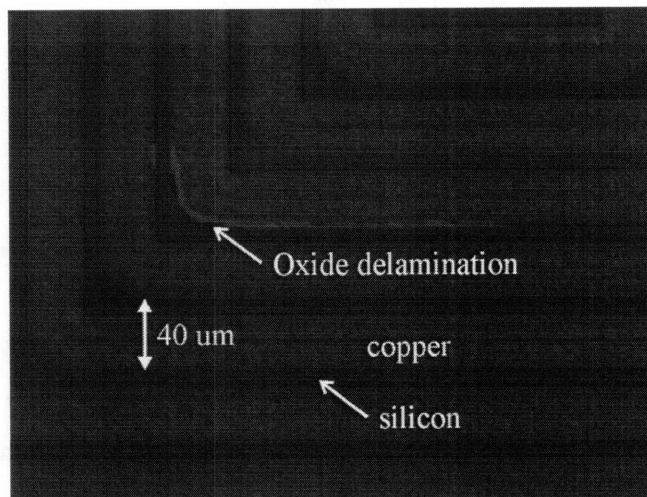


Figure 5.12. Delaminations in silicon dioxide after etching of the seed layer for upper copper coil layer.

The delaminations are visible as opaquely discolored areas and they likely result from:

- 1) expansion and contraction of the copper during and after oxide deposition, and
- 2) cracking at the copper-silicon interface that is followed by capillary-driven, acid etch undercutting during the downstream electroplating seed metal etch in step (9).

The delamination failures were observed to occur along the copper-silicon interface, including corners and straight regions. CMP-induced dishing likely enhances the oxide stress at the interface by creating a step in the copper-silicon surface that creates an area of stress concentration. In addition, the out-of-plane, thermally-induced strain at the wafer surface increases with the depth of the plated copper windings. Deep, high-aspect ratio copper lines will cause high stresses to build up in the oxide upon cooling after deposition. This leads to a higher probability of oxide delamination and therefore this imposes a practical limit on the depth and aspect ratio of the copper trenches.

Several variations in lateral coil geometry were fabricated in order to investigate how lateral coil geometry affects the probability of oxide delaminations. Figure 5.13 shows the lateral and cross-sectional geometry of the buried copper coil architecture.

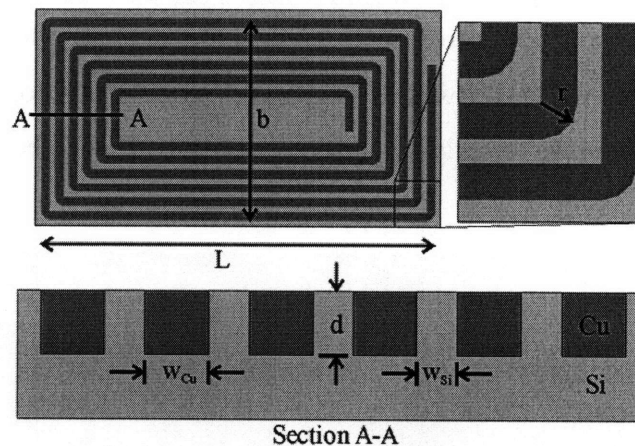


**Figure 5.13. In-plane and cross-sectional buried copper coil geometric parameters. Thermal oxide and Ti/Cu seed are not shown for clarity.**

The primary variables include the width of the copper windings,  $w_{cu}$ , and the width of the silicon spacers,  $w_{si}$ . Table 5.1 presents the experiment parameters. The coil trench depth was constant at  $d = 30 \mu\text{m}$ . Coil length and width were set to  $L = 2.14 \text{ mm}$  and  $b = 1.08 \text{ mm}$ , with variable pitch and number of turns.



**Table 5.1. Experimental parameters for the oxide delamination study.**

Design	Cu width (um)	Si width (um)	Ratio C/S	Pitch (um)	Number Inspected
1	14.0	6.0	2.3	20.0	27
2	14.0	16.0	0.9	30.0	37
3	14.0	26.0	0.5	40.0	37
4	34.0	6.0	5.7	40.0	26
5	34.0	16.0	2.1	50.0	28
6	34.0	26.0	1.3	60.0	37
7	49.0	6.0	8.2	55.0	37
8	48.0	17.0	2.8	65.0	48
9	48.0	27.0	1.8	75.0	47

The wafers contained over 30 replicates of each geometry combination that were randomly distributed across the wafer. The corners were rounded such that  $r \sim w_{cu}$ , thereby resulting in the elimination of silicon spacer cracking in all inspected devices. After oxide deposition, the wafers were seeded and electroplated with copper test structures. The seed layer was then wet etched to reveal the oxide and buried coils. The wafers were subsequently inspected with an optical microscope for delamination defects. A coil was deemed to have a defect if a delamination of the oxide was found. It should be noted that not all delamination defects were visible because less than 10% of the buried coils were blocked by the electroplated copper layer. Figure 5.14 plots the number of coils with oxide defects for each geometry combination as a percentage of inspected devices.

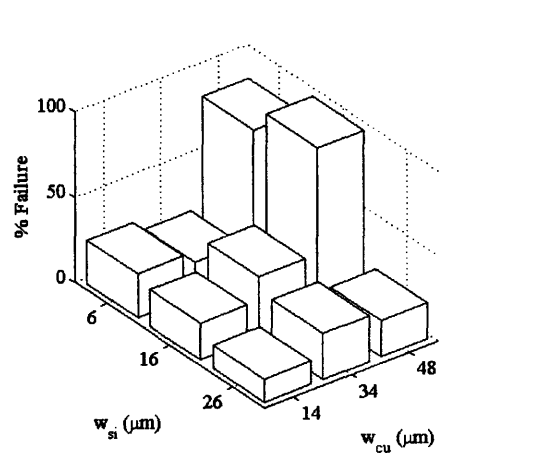


**Figure 5.14. Mechanical defect rate of the silicon dioxide versus copper and silicon line widths. The defect rate was measured after completion of the double coil process.**

The data indicates a baseline defect rate of approximately 20%, which means an 80% process yield, across all devices. This was a result of defects in the oxide and stress concentrations at the copper-silicon interface that were caused by CMP-induced dishing. The data also indicates that wide copper coils with considerably smaller silicon spacers (designs 7 and 8) exhibit more than 85% of the oxide delamination defects. This was most likely due to the thermally-induced strains that are associated with wide coil windings. The results from this experiment indicate that it was possible to design coil geometries that minimize the probability of oxide delamination. The coils designed for the nanopositioner have a copper width of 30  $\mu\text{m}$  and a silicon width of 10  $\mu\text{m}$ . This combination exhibits a defect probability that is similar to the baseline.

## **5.7 Silicon Dioxide Electrical Design and Experiments**

The proposed process includes deposition of PECVD silicon dioxide as the interlayer dielectric. This oxide was not annealed at elevated temperature to avoid melting the copper and to prevent the formation of thermally-induced stresses that would develop in the copper structures. An un-annealed PECVD oxide dielectric exhibits the following problems:

- 1) potential outgassing of hydrogen, absorption of water, and pinholes [192];
- 2) diffusion of copper into oxide without a diffusion barrier at elevated temperatures [193, 194];
- 3) reduced electrical breakdown field when compared to annealed PECVD oxide or thermal oxide.

These problems may all lead to shorting through the oxide layers that would cause device failure. The oxide has been designed to be 1  $\mu\text{m}$  thick in order to overcome defects, copper diffusion, and breakdown field. A sufficiently thick oxide layer will prevent pinholes from forming through the oxide during deposition, or during subsequent steps in vacuum where hydrogen outgassing is a concern.

The absence of a capping barrier metal between the polished copper and deposited oxide introduces the possibility of copper diffusion into the silicon dioxide. Integration of a barrier metal cap, such as tantalum or titanium, adds complexity to the process and therefore this feature omitted. Simulation results of the solid-state diffusion of copper into the silicon dioxide were

used to justify this decision. Fick's diffusion equations were solved for the copper-silicon dioxide system in 1-D that was normal to the film plane. An infinite-slab copper source [192] was assumed. The diffusion coefficients that were used in this analysis were obtained via experiment for the copper-silicon system [193]. Figure 5.15 shows the resulting copper concentration versus depth into the silicon dioxide, for different times, and at the deposition temperature of 300°C. The typical deposition time for 1 μm of PECVD oxide was less than 0.3 hour. This would result in copper diffusion through less than 0.2 μm oxide. As a result, the oxide thickness was designed to be 1 μm in order to prevent copper diffusion across the dielectric and possible shorting. This design would be adequate for devices that operate at, or below, 300°C for less than 10 hours. The device could operate at temperatures that are well below 300°C for extended periods of time.

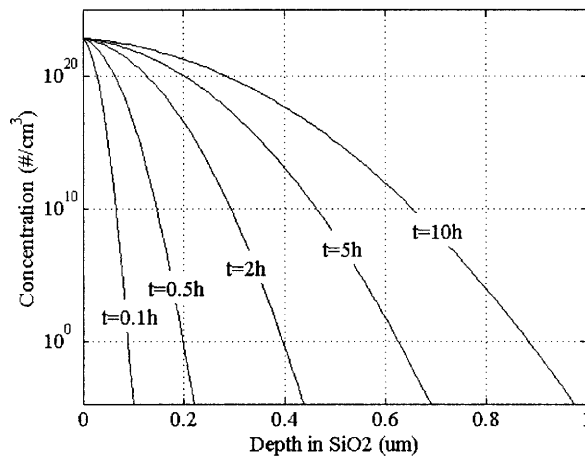


**Figure 5.15. Simulated copper concentration vs. depth in silicon dioxide for various times at T = 300°C. A 1 μm PECVD silicon dioxide was deposited in approximately 0.3 hours at 300°C.**

The second design consideration is related to the breakdown strength of PECVD oxide. In a planar copper inductor coil, the maximum voltage across the dielectric is typically less than 10 V. This would be seen between two electroplated coils, or between a planar coil and its jumper. Neglecting end effects, the electric field across the dielectric is:

$$E = \frac{V}{t} \quad (5.2)$$

where  $V$  is the voltage and  $t$  is the dielectric thickness. In the design of planar spiral coils with 10 V across 1 μm oxide, the maximum expected field is roughly 0.1 MV/cm. It is widely known that un-annealed PECVD silicon dioxide has reduced breakdown strength when compared to

thermal oxide or annealed PECVD oxide. Unfortunately no breakdown histograms were found in the literature. Consequently, the field strength for 1  $\mu\text{m}$  thick un-annealed PECVD oxide was determined via experiment. Figure 5.16 shows a cross section of the electrical test capacitor structure that was used in the study. The capacitor structure consists of a thermally oxidized silicon substrate with un-annealed PECVD silicon dioxide that was sandwiched between two layers of evaporated metal. This sandwich structure forms 1 mm x 1 mm oxide capacitors with upper and lower contacts. The lower contact was accessed through vias in the oxide. After thermal oxidation of the substrate wafer, a bottom electrode that consists of 20 nm titanium and 200 nm copper, was sputtered and patterned via wet etch. One micrometer of oxide was then deposited and patterned with a wet etch. This was followed by a second deposition and then by wet-etch patterning of the sputtered 20 nm titanium and 600 nm copper.

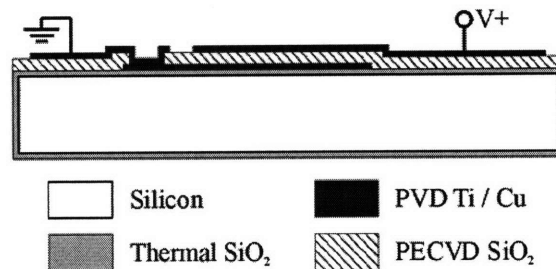


**Figure 5.16. Cross-section schematic of the capacitor test structure that was used to measure the electrical breakdown strength of unannealed silicon dioxide.**

The devices were then tested with an HP wafer probe station and Tektronix Type 576 Curve Tracer that used 300  $\mu\text{sec}$  pulse steps. The voltage was ramped by 50 V increments and held for approximately 10 seconds at each voltage. The breakdown field was defined as the field at which a few nano-amps of current begin to flow. This field value was less than the field at which catastrophic physical breakdown occurs. Figure 5.17 shows the measured breakdown field histogram for 15 test capacitors.

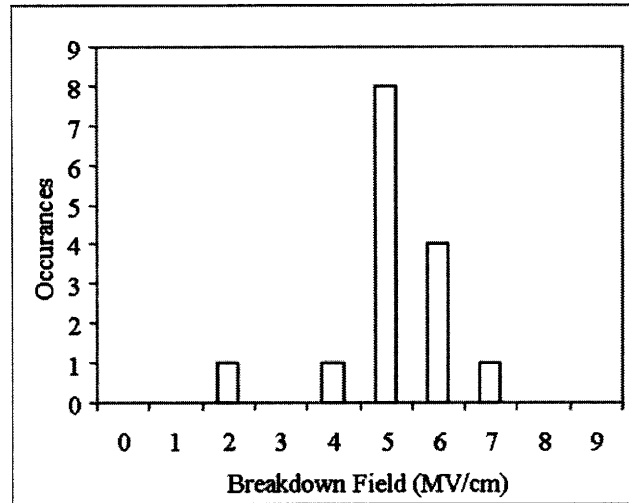


**Figure 5.17.** Measured electrical breakdown field for 1 mm<sup>2</sup> un-annealed PECVD silicon dioxide capacitors. The mean breakdown field was 4.56 MV/cm. This was roughly a factor of three less than the reported 12 MV/cm breakdown strength of thermal silicon dioxide [192]. The field strength was an order of magnitude greater than the maximum expected field of 0.1MV/cm for spiral coil dielectric. A layer of 1 μm thick, un-annealed PECVD silicon dioxide was therefore deemed sufficient for electrical insulation between the planar spiral copper coils or between a coil and its jumper.

## 5.8 Nested Via Structure

The via structures were etched through the silicon dioxide to the underlying copper in step (7) of the nanopositioner process. The vias were designed to match the 900 μm<sup>2</sup> cross-section area of the buried coils so that the current density flowing through the via is similar to the current density in the windings. The vias were nested within the width of the buried coils to eliminate the possibility of the BOE attacking the copper-silicon interface of the buried coils. Figure 5.18a shows an optical image of the nested vias after wet etching. After etching the oxide, the titanium-copper seed layer was evaporated onto the wafer in preparation for the second electroplating step. The seed metal must make electrical contact to the underlying copper so that the vias are electroplated. SEM images indicate that a gap of tens-of-nanometers separates the underlying copper from the edge of the etched oxide in the via. Figure 5.18b shows the evaporated metal seed layer bridges this gap in several places along the interface.

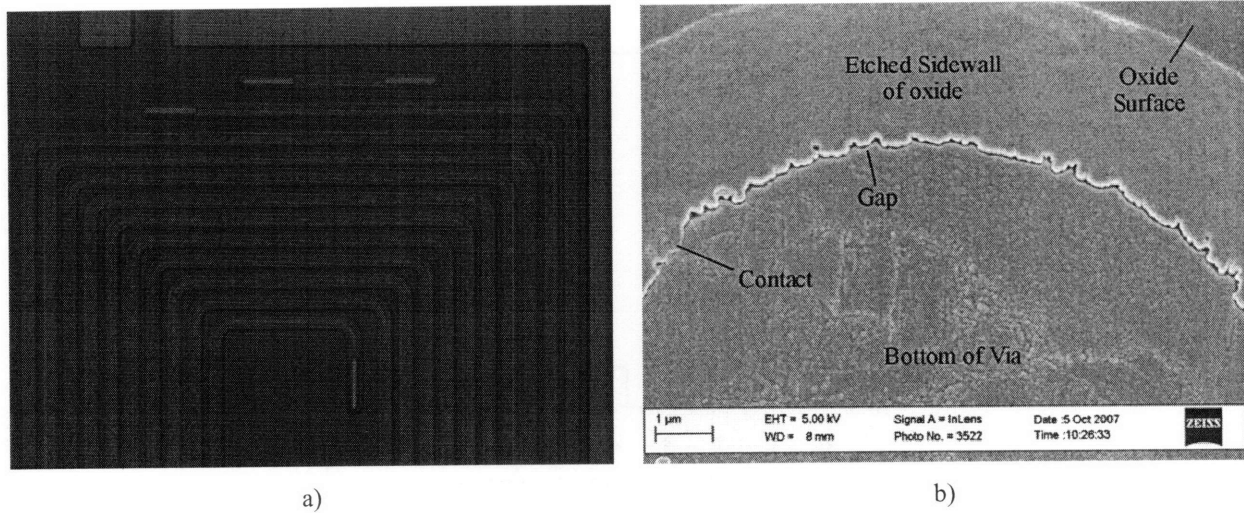


Figure 5.18. a) Optical image of nested vias etched through the oxide to the underlying copper coils. b) Inclined SEM image of a via after seed layer deposition.

## 5.9 Deep Reactive-Ion Etching

Several features were incorporated into the masks for DRIE of the back side cavity and the front side trenches. The features aid in the release of the device in steps (10) through (12). The back side etch required that the wafer was mounted upside-down with contact made through the copper structures on the front side of the wafer. “Dummy” features were designed into the photoresist plating mold (mask 3) in order to increase the mounted contact area so as to improve the heat transfer through the mount during the DRIE backside etch. The use of “dummy” features improves etch uniformity across the wafer to better than 15% over the total etch depth of the 610  $\mu\text{m}$  etch. The backside etch pattern (mask 4) included “halos” around all cutout features in order to reduce the total etched area to less than 20% of the wafer area and to improve the uniformity and etch rate. The backside pattern also included trenches that linked all cavities and enabled outgassing through the mount wafer target during the downstream, front side DRIE. If not vented properly, the air that is trapped within the cavity during mounting would cause a pressure difference in the vacuum chamber and this could lead to failure of the membranes.

The mask pattern for the front side DRIE (mask 2) included 100  $\mu\text{m}$  halos around all features in order to minimize the etched area and to maximize uniformity. The upper coil layer was exposed to the etch reactants during this step, but no damage or sputtering of the copper was observed. Some of the copper coils oxidized during the DRIE. After etching, the device wafer was dismounted in acetone by placing it upside-down in a horizontal cassette. The cutout pieces

drifted to the bottom of the tank upon release by acetone. This was accomplished without damaging the flexure structures. Tethers in the SOI device layer linked all the dies to the wafer and prevented the dies from separating in the acetone bath. The dies were separated by laser ablation after cleaning the wafer in oxygen plasma. Figure 5.19 shows SEM images of the copper leads upon the 100  $\mu\text{m}$ -thick flexure and at the edge of the actuator paddle.

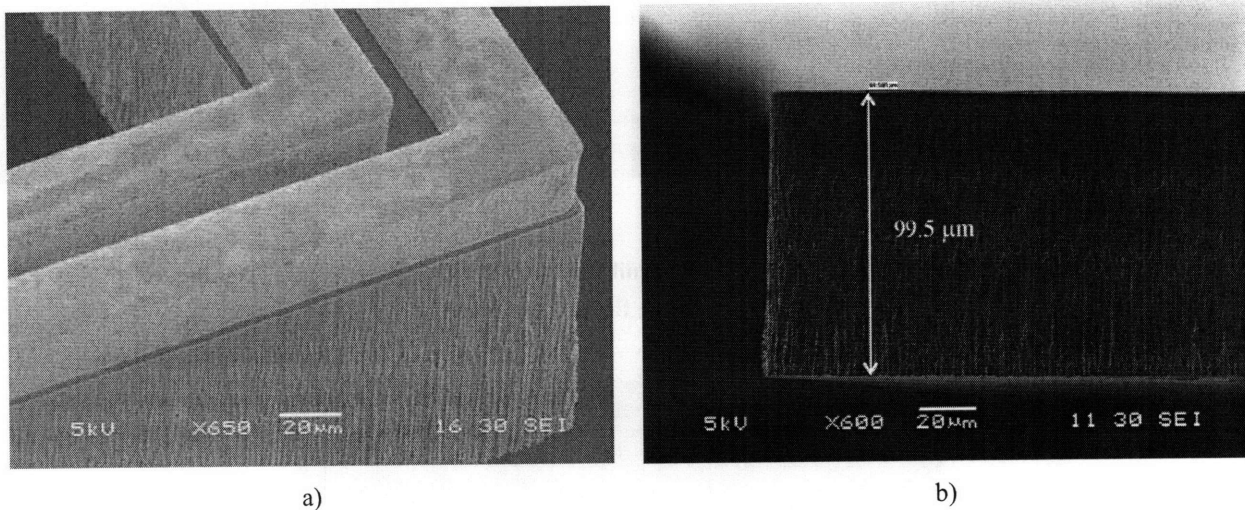


Figure 5.19. SEM images of the a) composite flexure beam and b) edge of the actuator paddle

## 5.10 Oxygen Plasma cleaning with Exposed Copper

A low power, pulsed oxygen plasma was used to clean the wafer of resist and Teflon debris after dismounting the wafer in steps (10) and (12). The oxygen plasma was applied at 5 minute intervals, and at a power level of 300 W, until the Teflon and photoresist debris was removed. The oxygen plasma was not observed to further oxidize the copper coils when pulsed at 5 minute intervals. Oxidation was observed at the same power for intervals of 15 minutes or greater.

## 5.11 Integrated Fabrication Results

Figure 5.20 shows an optical image of the stacked coils before and after DRIE, dismounting, and cleaning of the wafer. Some oxidation of the copper coils was observed, but this does not affect the electrical performance of the device. Figure 5.21 shows an SEM image of a released actuator paddle after completion of the fabrication process. The outline of the buried coils is visible under the silicon dioxide.

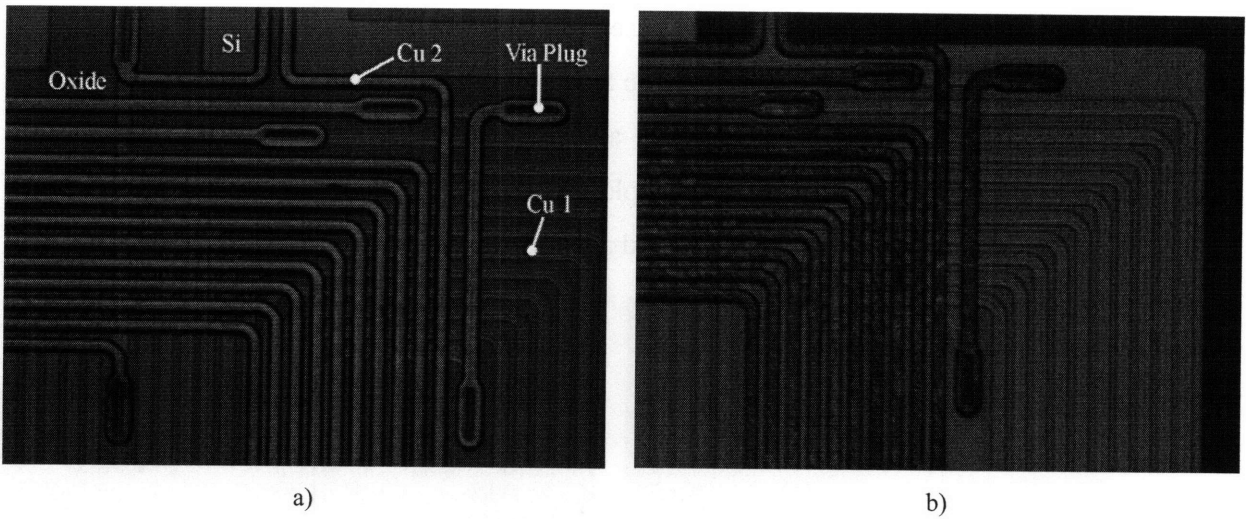


**Figure 5.20.** Optical images of the stacked double coil structure a) before and b) after etching, release, and cleaning of the flexure structure.

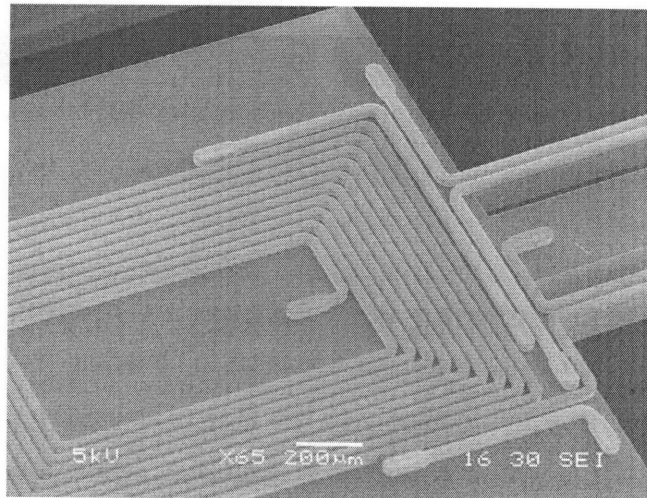


**Figure 5.21.** SEM image of a stacked-coil actuator paddle after completion of the fabrication process. The outline of the buried copper coils is visible under the oxide.

## 5.12 Summary

A new microfabrication process was presented in this chapter. The process was used to integrate the stacked copper coils and a silicon flexure. Section 5.6 and 5.7 presented process experiments that were used to determine the bounds upon the design space for successful microfabrication of the coils and the unannealed silicon dioxide dielectric that separates them. The process yielded functioning meso-scale nanopositioners that were experimentally characterized. The characterization will be discussed in the next chapter.



## EXPERIMENTAL RESULTS

---

This chapter covers the experimental characterization of the mechanical and electrical performance of the meso-scale nanopositioner. The chapter also discusses electrical measurements of a test coil that was embedded within silicon. The electrical measurements include voltage-current response, self-inductance, and mutual capacitance. Mechanical performance measurements include in-plane and out-of-plane dynamic response, un-calibrated quasistatic input-output response, calibrated input-output response, out-of-plane step response, and quasistatic in-plane repeatability.

### 6.1 Assembled Meso-Scale Nanopositioner

Figure 6.1 shows an image of the assembled meso-scale nanopositioner.

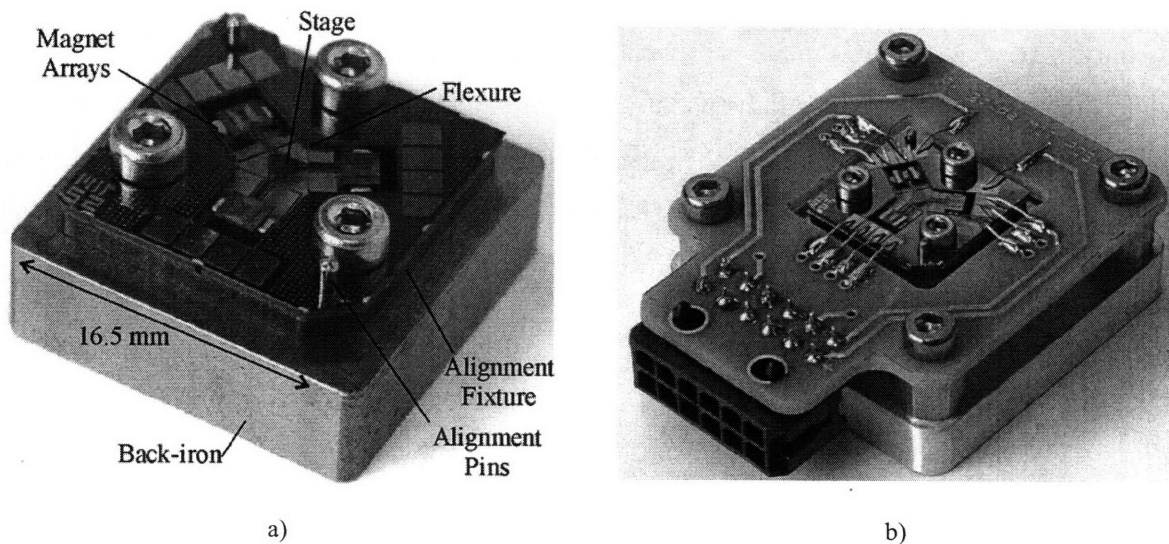
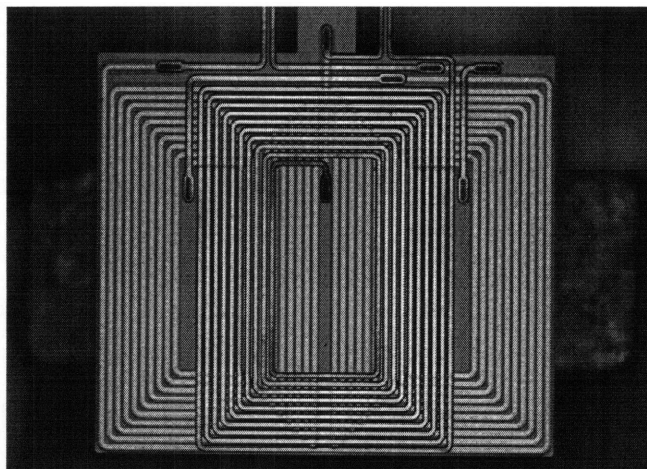


Figure 6.1. Image of the assembled meso-scale nanopositioner: a) silicon chip that was mounted on the magnet fixture; b) chip and magnet fixture that was assembled to the PCB electrical lead frame.

The system was assembled according to the sequence that was presented in Section 4.6. Figure 6.2 shows an optical microscope image of an actuator paddle on the assembled nanopositioner. The magnet array is visible beneath the actuator paddle.



**Figure 6.2. Optical image of a completed actuator paddle from an assembled nanopositioner. The magnets are visible under the paddle.**

Magnetic debris that accumulated below the magnets, and assembly errors, resulted in variations in the height and lateral position of magnets with respect to the coils. The magnet heights and the corresponding air gap were measured before and after assembly with an optical microscope that used an interferometric objective lens and height readout. The measurement error was less than 2  $\mu\text{m}$ . The height of each magnet in each array was measured before assembly. After assembly, the air gap was measured to the highest point on each of the side magnets that were visible beneath the paddle. The air gap above the center magnet was inferred from the relative measured height of the magnets. The magnetic gap was then calculated to the center of each actuator coil's thickness. Table 6.1 lists values for the measured air gap and estimated magnetic gap.

**Table 6.1. Measured magnetic gaps for each actuator coil in the meso-scale nanopositioner.**

Parameter	Units	Actuator	Actuator	Actuator
		A	B	C
Measured Mean Air Gap	$\mu\text{m}$	80	97	60
Magnetic Plating	$\mu\text{m}$	20	20	20
X Actuator Height in Paddle	$\mu\text{m}$	85	85	85
Z Actuator Height in Paddle	$\mu\text{m}$	113	113	113
X Actuator Magnetic Gap	$\mu\text{m}$	185	202	165
Z Actuator Magnetic Gap	$\mu\text{m}$	213	230	193

The data given in the table is a conservative estimate because the magnet pole surfaces are not flat and the heights were measured to the peaks in the pole surface. The predicted actuator output force and displacement are computed by using the estimated magnetic gap for comparison to measurements. These experiments provided the perspective on the difficulty of obtaining accurate alignment of the coils and the magnet arrays. The variation will be shown to have a large effect upon the performance of the nanopositioner. Robust design methods or improved assembly techniques will be required to mitigate these effects.

## 6.2 Electrical Experiments

This section presents electrical measurements that characterize the nanopositioner actuator coils and silicon-embedded test coil. The test coil was a single-layer coil that was buried in silicon. Two vias, leads and bond pads were located within the upper copper layer. The test coil has identical geometry to one-half of the *x*-actuator coil.

### 6.2.1 Resistance and Sustainable Current

The resistance between the *x*- and *z*-coils on each of the three nanopositioner actuator paddles was measured to be greater than 10 M $\Omega$  (open-loop) with a digital multimeter. It may therefore be concluded that the two coils are electrically isolated for practical purposes. The series resistances of the coils and leads were measured using a four-point probe setup. A digital multimeter measured the voltage drop across the bond pads and a power supply was used to control the current flowing through the coil and leads. The coils were allowed to stabilize for 15-20 seconds before reading the voltage. The voltage measurement error was 2mV and the current measurement error was 5mA. The bulk temperature change of the coils was inferred from the nonlinearity in the I-V response because of the temperature dependence of resistivity of copper.

The coil is assumed to be at uniform temperature. The temperature of the coil is proportional to the square of the current and the resistivity of the copper as shown in Equation (3.106). The resistivity varies with temperature as

$$\rho = \rho_o (1 + \alpha_e \Delta T) \quad (6.1)$$

where  $\alpha_e$  is the temperature coefficient of resistivity for copper and  $\rho_o$  is the resistivity at room temperature. The temperature coefficient of resistivity for copper is  $0.0068 \text{ }^\circ\text{C}^{-1}$  [195]. The temperature-varying resistivity may be used to solve for the voltage,  $V$ , and the coil temperature,  $T$ , in terms of the resistance at room temperature,  $R_o$ , and the temperature constant,  $C$ , and the input current,  $I$ :

$$V = IR_o + \alpha_e CR_o \frac{I^3}{1 - \alpha_e CI^2} \quad (6.2)$$

$$\Delta T = C \frac{I^2}{1 - \alpha_e CI^2} \quad (6.3)$$

The measured  $I$ - $V$  data was fit to Equation (6.2) to obtain estimates for the temperature constant,  $C$ , and the resistivity at room temperature,  $R_o$ . The fit parameters were then used in Equation (6.3) to estimate the coil temperature. Figure 6.3 and Figure 6.4 show the static current-voltage characteristics and the estimated coil temperature for the  $x$ - and  $z$ -actuator coils.

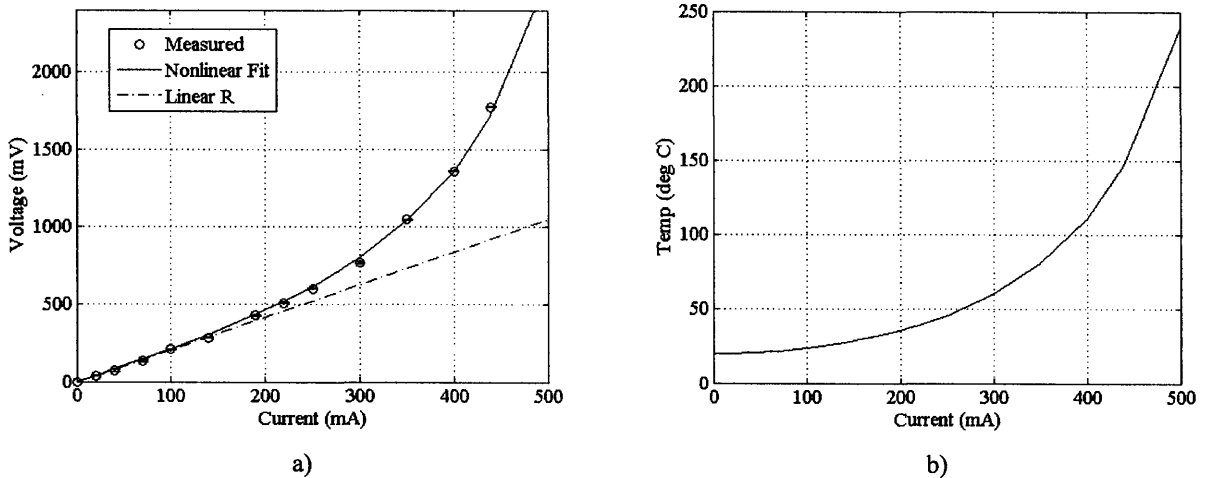


**Figure 6.3. a) Measured static I-V characteristics for a suspended x-actuator coil and b) calculated average static coil temperature versus input current.**

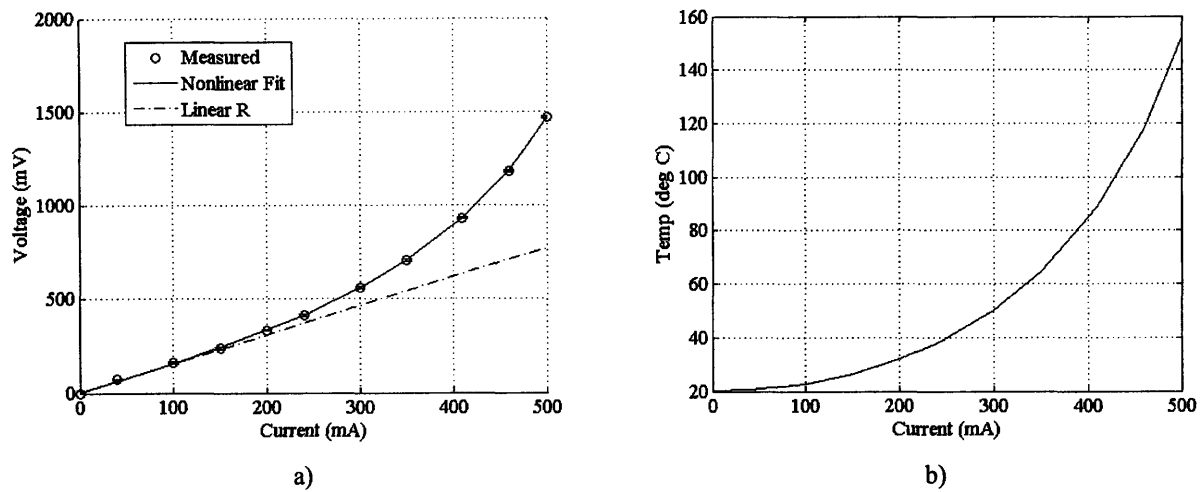


**Figure 6.4. a) Measured static I-V characteristics for a suspended z-actuator coil and b) calculated average coil temperature versus input current.**

The data in the figures shows that the temperature of the suspended actuator coils begins to increase above 200 mA of input current. At currents below 200mA, the temperature was near room temperature. The temperature data indicates that the *x*-actuator coil can sustain 500mA current before the coil temperature reaches 300°C. The coil windings on the paddle began to oxidize at this current input. The estimated temperature data imposes a limit on the sustainable actuator current in order to minimize damage that is due to thermally-induced stresses in the coil structure. A conservative limit for the sustainable current in the *x*-actuator coil was 430 mA so that the coil temperature does not exceed 150°C, which is half of the maximum fabrication temperature. The *z*-actuator coil may sustain 460 mA before the coil temperature exceeds 150°C.

The buried test coil had the capacity to sustain much higher currents because it was in intimate contact with the surrounding silicon chip. Figure 6.5 shows the static current-voltage characteristics and estimated coil temperature for the test coil.

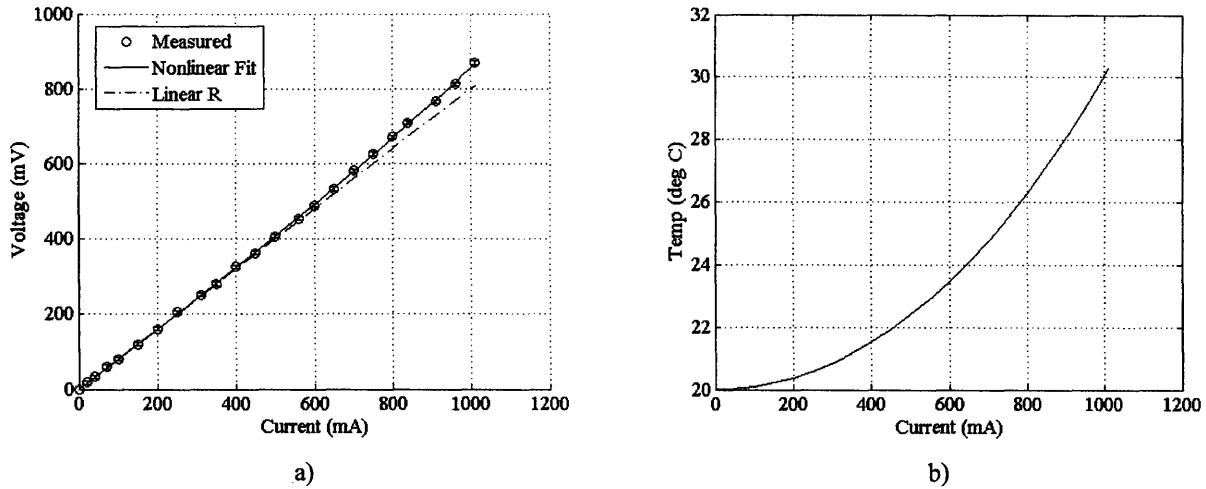


**Figure 6.5. a) Measured static I-V characteristics for a test coil and b) average coil temperature calculated from the change in resistivity of the copper coil windings.**

The data in the figure indicates that the test coil may sustain over 1 A of current at a current density of  $1122 \text{ A/mm}^2$  that leads to a temperature rise of less than  $10^\circ\text{C}$ . The test coils sustain greater current than the actuator coil because of the intimate contact of the coil and surrounding bulk silicon chip. The temperature of the coil exhibits noticeable increases for currents above 600 mA. The results indicate that micro-coils that are buried in a silicon chip may sustain at least four times more current than the suspended coils with ten times less temperature rise. This result indicates that a moving-magnet actuator design may sustain at least four times the current and output more than four times more force than a moving coil actuator while exhibiting at least three times less temperature rise. A moving coil actuator may thereby be more suited for positioning applications where the increased mass of a moving magnet actuator is traded for reduced operating temperatures and increased range.

Table 6.2 presents the measured and predicted resistance of the copper actuator and test coils. The predicted actuator coil resistance includes the resistance of the leads along the flexure beams. The predicted resistance does not include the jumper and via resistance.

**Table 6.2. Comparison of measured and predicted coil resistance.**

Coil	Parameter	Units	Predicted	Measured	% Error
X Actuator	$R_x$	$\Omega$	1.85	2.10	12.09
Z Actuator	$R_z$	$\Omega$	1.46	1.55	5.68
Test	$R_c$	$\Omega$	0.75	0.80	6.99

The error in the table is attributed to the following:

- 1) un-modeled jumper and via resistance;
- 2) variation in the resistivity of the plated copper from the literature value that was used for prediction; and
- 3) variations in the thickness of the copper deposits.

### 6.2.2 Self-Inductance

The self-inductances of the actuator and test coils were measured using two probes and an HP4192A impedance analyzer. The measurement error was estimated to be less than 10 nH. The parasitic inductance of the shorted test leads was first measured at each frequency and then subtracted from the measured inductance of the coils. Figure 6.6 and Figure 6.7 show the measured self-inductances of the *x*- and *z*-actuator and test coils versus measurement excitation frequency.

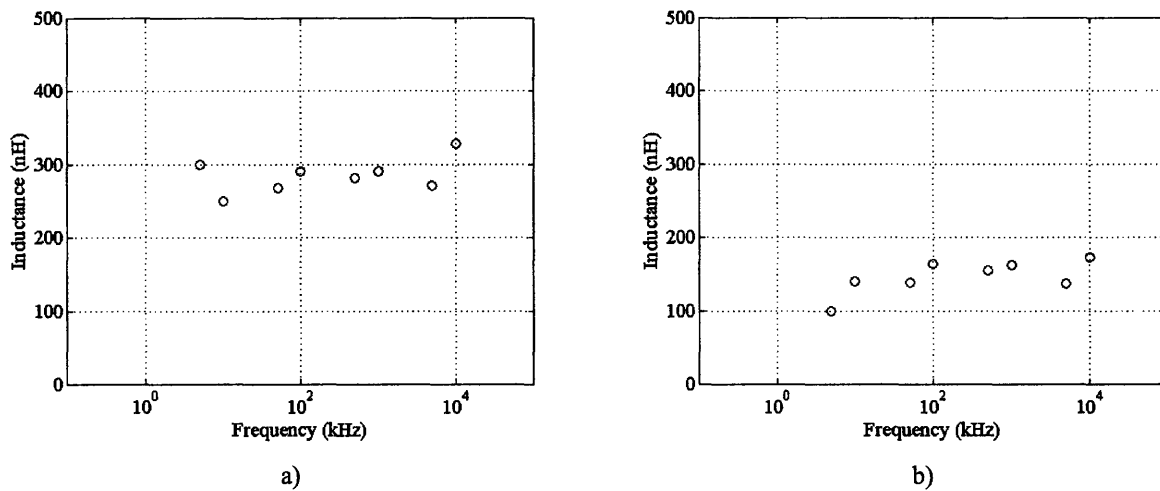


Figure 6.6. Measured self-inductance of the a) *x*-actuator and b) *z*-actuator coils.

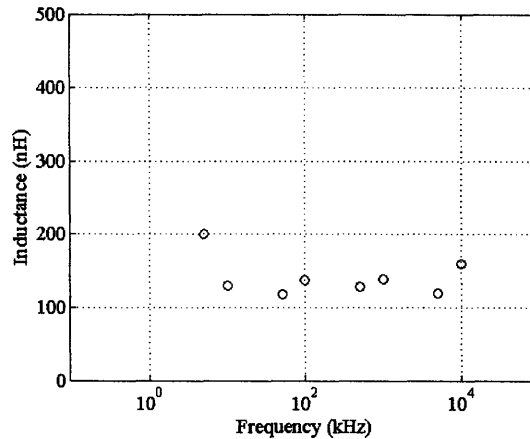


Figure 6.7. Measured self-inductance of the test coil.

The data in the figures indicate that the inductance of the  $x$ - and  $z$ -actuator and test coils was approximately constant for the range of measured frequencies. The measured resistance and inductance were used to compute the  $L$ - $R$  electrical roll-off frequency of the coils. Table 6.3 compares the measured and predicted inductance and electrical roll-off frequency.

Table 6.3. Comparison of the measured and predicted inductance and  $L$ - $R$  frequency

Coil	Measured Inductance	Predicted Inductance	Units	Measured L-R Freq	Predicted L-R Freq	Units
X Actuator	285	193	nH	7	9.58	MHz
Z Actuator	153	116	nH	10	12.56	MHz
Test	141	-	nH	6	-	MHz

The predicted inductance and roll-off frequency differs from the measured values by less than 30%. The error may be attributed to the subtraction of the measured parasitic inductance from the measured total inductance. The parasitic inductance was measured to be approximately 1.5  $\mu$ H, which is large when compared to the coil inductance of 150 – 300 nH. The coils have electrical roll-off frequencies that are three orders of magnitude greater than the predicted mechanical frequency ( $\sim 1000$  Hz) of the nanopositioner system. As a result, the electrical dynamics of the actuator coils may be ignored during mechanical motion experiments. The high electrical bandwidth of the actuators (10 MHz) opens the possibility of using modulation signals on the order of MHz so that the actuators operate in a thermal steady-state. The mechanical response to a modulation signal in the MHz range would be attenuated by the mechanical dynamics of the system.



The mutual inductance of the  $x$ - and  $z$ -actuator coils were measured by driving a sinusoidal current to one of the coils with a current controller (Appendix C) and measuring the voltage output by the other coil with a digital oscilloscope. Signals were measured with probes that contacted the coil pads. The input coil was driven with 50 mA at excitation frequencies that were up to 100 kHz. The measurement noise on the oscilloscope was 20 mV peak-peak. An output signal was not detected on the oscilloscope and indicates that the output voltage was less than the noise threshold of the oscilloscope. The result indicates that the mutual inductance of the coils was less than 300 nH.

### 6.2.3 Mutual Capacitance

The mutual capacitance between the  $x$ - and  $z$ -actuator coils was measured by using an HP4192A impedance analyzer and two probes. The parasitic capacitance of the open test leads was first measured at each frequency and then subtracted from the measured capacitance of the coils. Figure 6.8 shows the measured mutual capacitance of the  $x$ - and  $z$ -actuator coils versus the measurement excitation frequency.

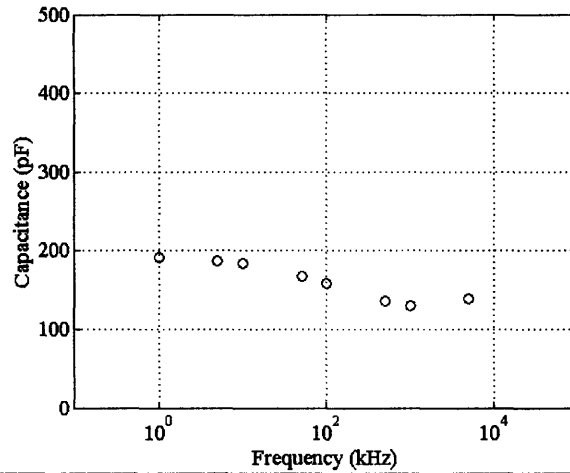


Figure 6.8. Measured mutual capacitance between the  $x$ - and  $z$ - actuator coils

The data in the figure indicates that the mutual capacitance has a value of 190 pF at 1 kHz and 130 pF at 50 MHz. The predicted mutual capacitance was 68 pF and is on the same order of magnitude as the measured value. The resulting  $L$ - $C$  frequency for coupling between the coils was greater than 30 MHz. The electrical coupling between the coils was negligible for actuation excitation frequencies that are an order of magnitude below the  $L$ - $C$  frequency.

## 6.3 Mechanical Measurements

The mechanical performance of the meso-scale nanopositioner system was characterized by using a  $\mu$ Mech MEMS Motion Analyzer (MMA) system and a Polytec MSA-400 laser vibrometer. The systems will be discussed in more detail in the following sections. The MMA system was used to collect the following measurements:

- 1) quasistatic, open-loop input-output response of nanopositioner in the in- and out-of-the plane directions;
- 2) frequency response in-the-plane; and
- 3) open-loop repeatability in-the-plane.

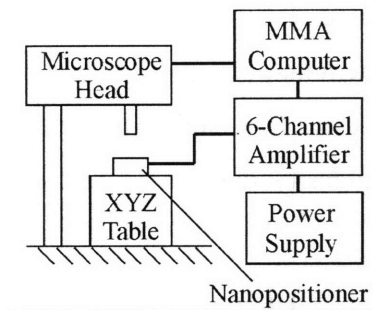
The laser vibrometer was used to measure the out-of-plane frequency response and open-loop, out-of-plane step response of the nanopositioner.

A closed-loop analog current controller was designed and built to drive the current in the actuator coils in response to a command voltage. The design of the current controller is presented in Appendix C. The six-channel current controller delivers up to 500 mA per channel with a measured steady-state inverting gain of  $-49.5$  mA/V and a bandwidth of 300 kHz. The amplifier was powered by a laboratory power supply.

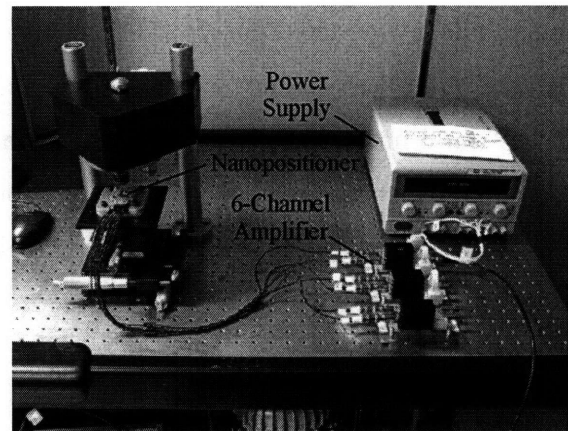
### 6.3.1 Experiments using the MEMS Motion Analyzer

#### 6.3.1.A Experimental Setup

The in-plane response and out-of-plane static response of the nanopositioner was measured with a  $\mu$ Mech MEMS Motion Analyzer (MMA) system ([www.umech.com](http://www.umech.com)). Figure 6.9 shows a schematic diagram and image of the experiment setup.



a)



b)

**Figure 6.9. a) Schematic diagram and b) image of the MMA experiment setup.**

The MMA system synchronizes an oscillating device input signal and a stroboscopic light source while it captures images of the device motion at various phases of the input signal. The in-plane motion was obtained by correlating the acquired images. A 5x objective was used in the experiments presented in this work. The in-plane motion resolution of the system when using the 5x objective was 40 nm. The device under test must have metrology features such that device motion results in changes in the intensity distribution of the regions of interest. An ideal feature should have a sharp change in intensity in both the  $x$ - and  $y$ -directions. Examples include etched holes or corners. The system uses an error minimization algorithm to fit  $x$ - and  $y$ - motion of the target. The algorithm leads to errors when non-circular features undergo rotational motion. The rotation error is not quantified and it depends upon the shape of the target and the angle of rotation. The ideal metrology feature is a set of circular features that are etched in the surface of the device. The relative motion of each feature may be measured to calculate the in-plane rotation of the device.

The MMA system cannot measure in-plane and out-of-plane motion simultaneously. The system uses a stroboscopic laser interferometer to overlay a set of fringes upon the surface of the device in order to measure out-of-plane motion. The fringe intensity changes at each pixel as the device moves out-of-plane. The MMA creates an intensity phase map at each command input level by changing the distance of the reference leg of the interferometer. The system creates an eight-point intensity phase map that requires eight images per input level. The phase map was measured for each phase and the amplitude of the input signal. Algorithms correlate the fringe intensity phase maps to extract the out-of-plane motion. A static input-output response with 5

amplitude levels, and 8 phases in the input signal, requires 320 images. The out-of-plane motion resolution of the system was quoted to be 0.5 nm but a more realistic estimate given the current setup was 5 nm. The maximum displacement that the system may measure was limited by phase correlation to be less than  $\lambda/4$ , or 164 nm for the laser in use. Translations that are greater than the limiting value will yield phase wrapping of the intensity data and therefore unreliable displacement measurements.

The MMA system computes the response to an oscillating input signal by fitting the motion amplitude data. The system outputs positive amplitude data so that the measurements presented in the following sections represent half of the range of motion of the system.

Figure 6.10 shows an optical image of the nanopositioner target for in-plane and out-of-plane measurements that were obtained with the MMA system. The geometric center of the nanopositioner stage was located at the upper-left corner of the etched target hole.

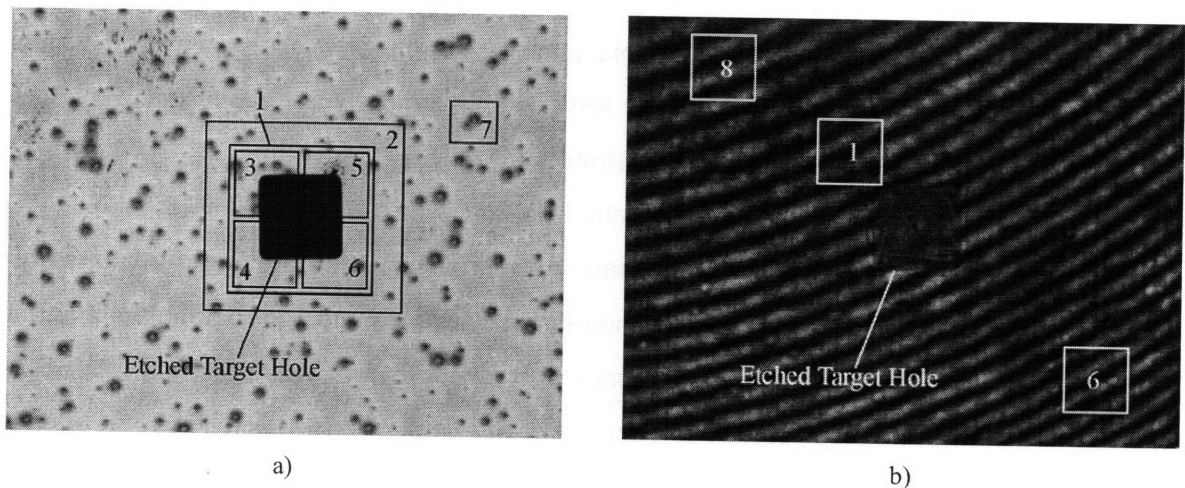


**Figure 6.10. Optical image of the MMA target showing the regions of interest used for calculation of: a) in-plane translations and rotation; and b) out-of-plane translations and rotation.**

The fringes captured during out-of-plane measurements are shown in Figure 6.10b. The figures show the regions of interest (ROI) used to compute displacements and rotations. The in-plane translations were measured from ROI3, ROI4, and ROI5 while the in-plane rotation was computed by comparing the relative motion of ROI3 and ROI7 in Figure 6.10a. The out-of-plane translation was measured for ROI 1 and the rotations were then computed from the relative motions of the ROI6 and ROI8 that are shown in Figure 6.10b.

The bias rotation of the target and nanopositioner relative to the MMA was subtracted from the data in order to compute the translations relative to the nanopositioner reference frame.

The MMA outputs four independent and synchronized command signals and thereby could not be used to measure motion that was generated by simultaneous operation of all six actuators coils. The MMA accepts a signal that could be used to synchronize external actuation signals with the strobe signal. In this way, a multi-channel digital control system such as DSpace may drive the nanopositioner.

### 6.3.1.B Pre-Calibrated Input Command Signals

Table 6.4 shows the idealized, relative input signals that were used to command the nanopositioner to translate and rotate about the  $X$ ,  $Y$ , and  $Z$  axes before calibration. Figure 2.2 shows the layout of the input signals that are provided in the table.

**Table 6.4. Relative command inputs for motion along each axis of the nanopositioner prior to calibration.**

Desired Motion	$i_1$	$i_2$	$i_3$	$i_4$	$i_5$	$i_6$
X	1	-1/2	-1/2	0	0	0
Y	0	-1	-1	0	0	0
$\theta_z$	1	1	1	0	0	0
$\theta_x$	0	0	0	-1	1/2	1/2
$\theta_y$	0	0	0	0	1	-1
Z	0	0	0	1	1	1

### 6.3.1.C In-Plane Frequency Response

The in-plane frequency response of the nanopositioner system was measured with the MMA system prior to calibration. The  $x$ -actuator input signals were setup according to Table 6.4 to drive the stage in the  $x$ -,  $y$ - and  $\theta_z$ - directions. An input amplitude of 50 mA was applied to the actuator coils at frequencies ranging from 1 Hz to 10 kHz. Figure 6.11 and Figure 6.12 shows the measured frequency response in the  $x$ -,  $y$ - and  $\theta_z$ - directions.

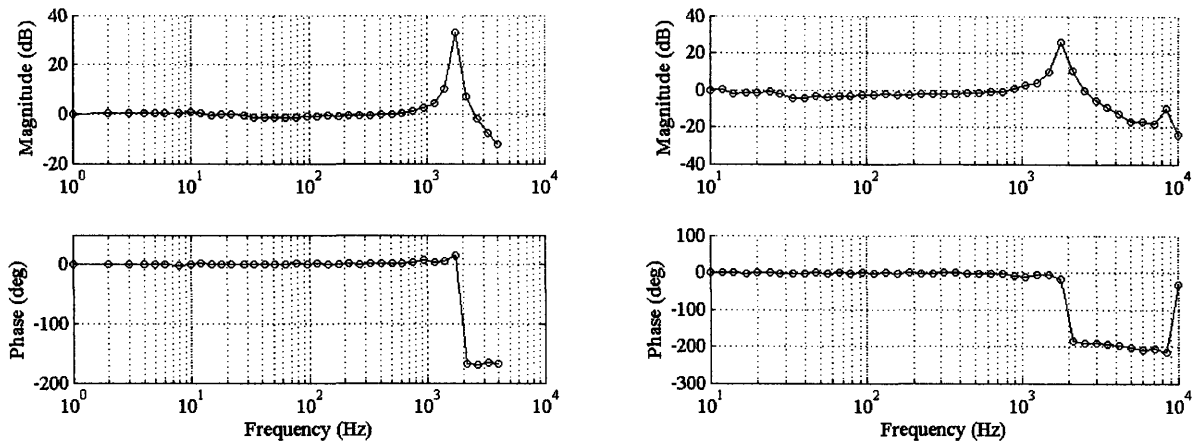


Figure 6.11. Measured frequency response of the nanopositioner for pre-calibrated actuation in the a) x- and b) y-directions.

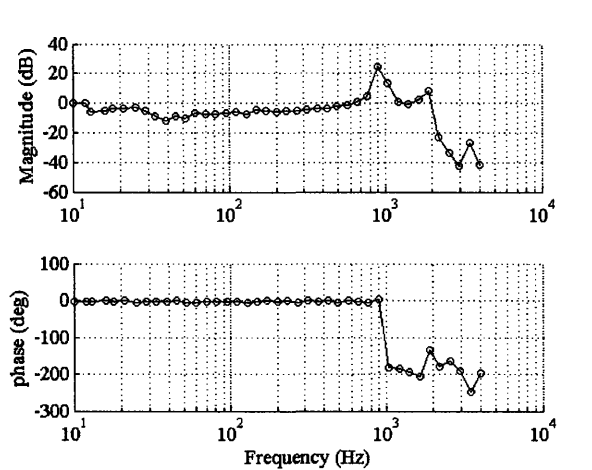


Figure 6.12. Measured frequency response of the nanopositioner for pre-calibrated actuation in the  $\theta_z$  direction.

The data in Figure 6.11 shows under-damped resonant peaks at 1780 and 1746 Hz for motion in the  $x$ - and  $y$ -directions, respectively. The data in Figure 6.12 shows an under-damped first resonant peak at 900 Hz. Table 6.5 compares the predicted and measured in-plane resonant modes.

Table 6.5. Comparison of predicted and measured in-plane resonant modes.

Symbol	Mode	Predicted	Measured	% Error	Units
$f_{\theta_z}$	$\theta_z$	972	900	8.0	Hz
$f_y$	X	1883	1746	7.8	Hz
$f_x$	Y	1883	1780	5.8	Hz

The error between the predicted and measured values was speculated to be attributed to the following sources:

1) lateral over-etching of the silicon flexure beams; and

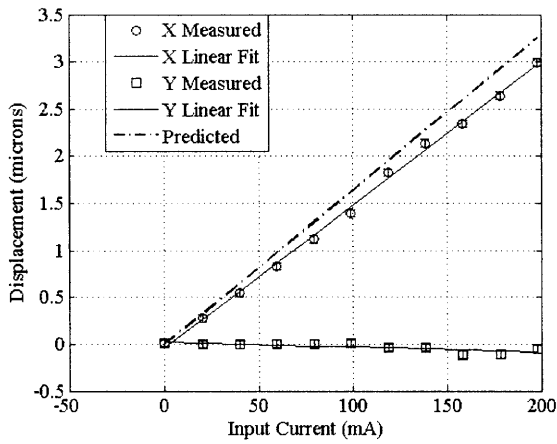
2) differences in the material properties from the literature values that were used in the calculations.

The predicted resonant frequencies are computed by using the nominal mask design geometry. Lateral over-etch of the flexure beams was estimated at 2  $\mu\text{m}$ , or 2.5% of the width of the flexure beams. The reduction in beam width results in a 7.5% reduction of the in-plane stiffness when compared to the nominal case. Estimated material property variation on the order of 2% may also contribute to the error.

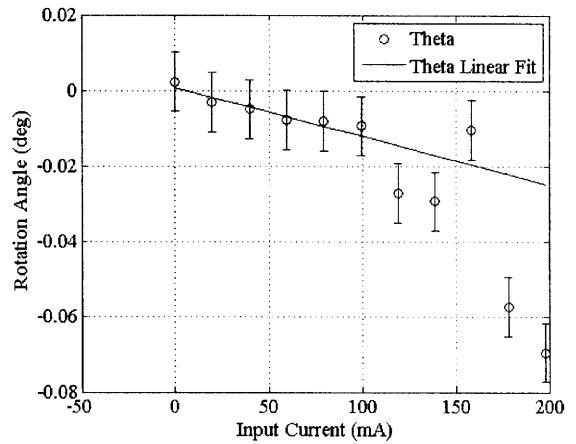
The high quality factor of the resonant peaks in the measured frequency responses indicates that the system is highly underdamped. In practice, the nanopositioner would “ring” in response to in-plane step inputs and thereby exhibit long settling time. The settling time limits the achievable system speed in step-and-hold applications such as nanomanufacturing. Underdamped oscillations in the step response may be minimized with integrated sensing and closed-loop feedback. Feed-forward input-shaping may be used in open-loop to improve response time, but requires *a priori* knowledge of the system dynamics.

#### **6.3.1.D Quasistatic In-Plane Motion**

The nanopositioner was commanded to translate and rotate about the  $x$ ,  $y$ , and  $z$  axes prior to input calibration. The resulting quasistatic in-plane motion was measured with the MMA. Measurements were made at an excitation frequency of 10 Hz. The pre-calibrated, quasistatic input-output response was compared to the predicted response for translation along the  $x$ ,  $y$ , and  $z$  axes and rotation about the  $z$  axis. The in-plane translation and rotation for each commanded motion were plotted versus the maximum current input to the actuator coils. Figure 6.13, Figure 6.14, and Figure 6.15 show the in-plane quasistatic response of the meso-scale nanopositioner to in-plane actuation commands in  $x$ -,  $y$ -, and  $\theta_z$  directions. The predicted motion was also plotted for comparison. The first six data points were used to fit the  $\theta_z$  rotational data. Measurement error bars are plotted in each figure.

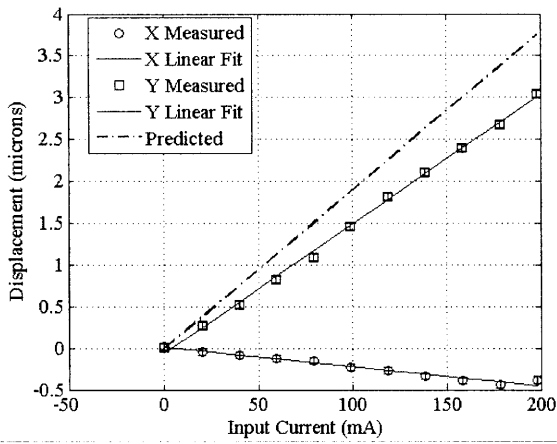


a)

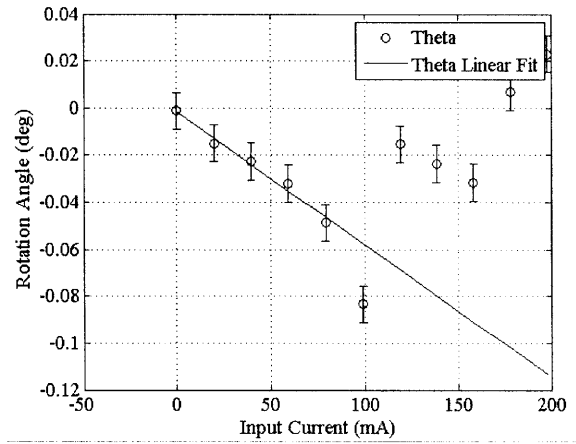


b)

Figure 6.13. Pre-calibrated, in-plane quasistatic response versus input current for commanded motion in the x-direction: a) measured and predicted x-motion and parasitic y-motion; b) measured  $\theta_z$  parasitic motion.



a)



b)

Figure 6.14. Pre-calibrated, in-plane quasistatic response versus input current for commanded motion in the y-direction: a) measured and predicted y-motion and parasitic x-motion; b) measured  $\theta_z$  parasitic motion.



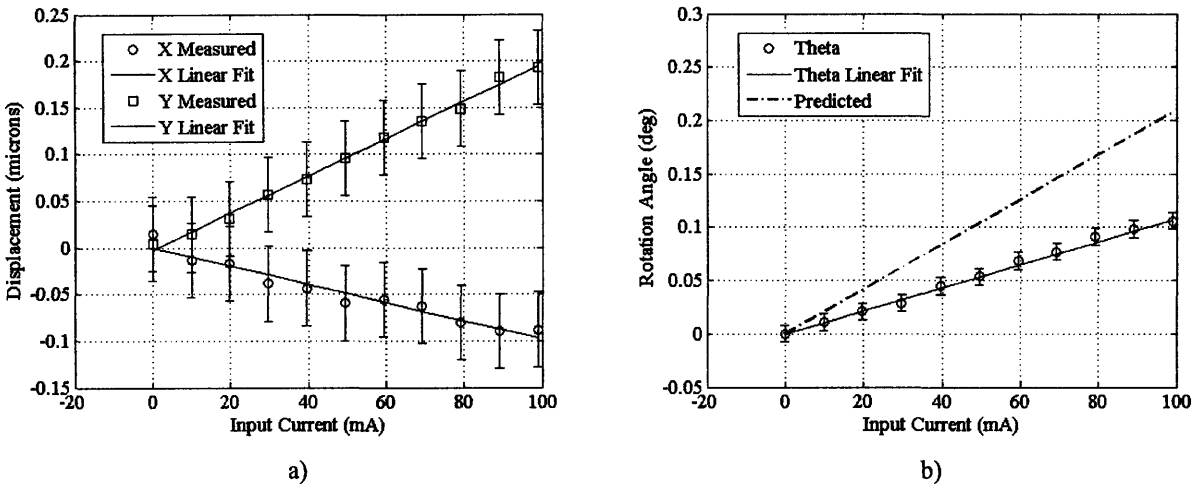


**Figure 6.15. Pre-calibrated, in-plane quasistatic response versus input current for commanded motion in the  $\theta_z$ -direction: a) measured parasitic x- and y-motion; b) measured and predicted  $\theta_z$  motion.**

The data in the figures indicates that the commanded translations and rotations are linear functions of the input current. The data also shows linear parasitic motion for the most part. The parasitic motion was caused by the following:

- 1) variable force output from differences in the magnetic gap between actuators;
- 2) parasitic forces that are applied by the actuators sources;
- 3) misalignment of the coils and magnets.

The outlying data points in the rotation data for commanded translations in the  $x$ - and  $y$ -directions are measurement artifacts of the target. The translations that were measured for commanded rotation about the  $z$ -axis in Figure 6.15 are partially caused by the measurement artifacts from rotation of the target. The error between predicted and measured motion was less than 8% for translation along the  $x$ -axis, less than 23% for translation along the  $y$ -axis, and less than 95% for rotations about the  $z$ -axis. Variations in the height and lateral alignment of the coils relative to the magnets result in variation in force output between the coils and therefore parasitic motion. Rotational motion about the  $z$ -axis exacerbates the result and leads to the computed error of 95% because the idealized predictive model assumes that each actuator outputs equivalent force. These results and the measurements of the actuator air gap indicate that the alignment and assembly of the magnets and the chip have important implications on the actuator performance. Variations in the magnetic gap result in variations in force and the

possibility of enhanced parasitic forces and moments. Precise assembly of the magnets and control of the magnetic gap with appropriate shims may help to improve the distribution of the gap heights between the actuators and within the magnet arrays. Improvements in the assembly precision may thereby improve the following: a) the force output of the actuators; b) the uniformity of the force output between actuators; and c) minimize the parasitic errors due to gap height variation. In addition, the parasitic moments due to the actuators were not used to predict the system motion during the design phase. The variable force output and parasitic forces result in parasitic motions as indicated by the data. The parasitic motions are linear and may therefore be minimized by open-loop calibration as demonstrated in the next section.

Figure 6.16, Figure 6.17, and Figure 6.18 show the in-plane, parasitic motion of the meso-scale nanopositioner as a result of out-of-plane quasistatic actuation commands in the  $z$ ,  $\theta_x$ , and  $\theta_y$  directions. The first six data points were used to fit the  $\theta_z$  rotational data. Measurement error bars are plotted for the data in each figure.

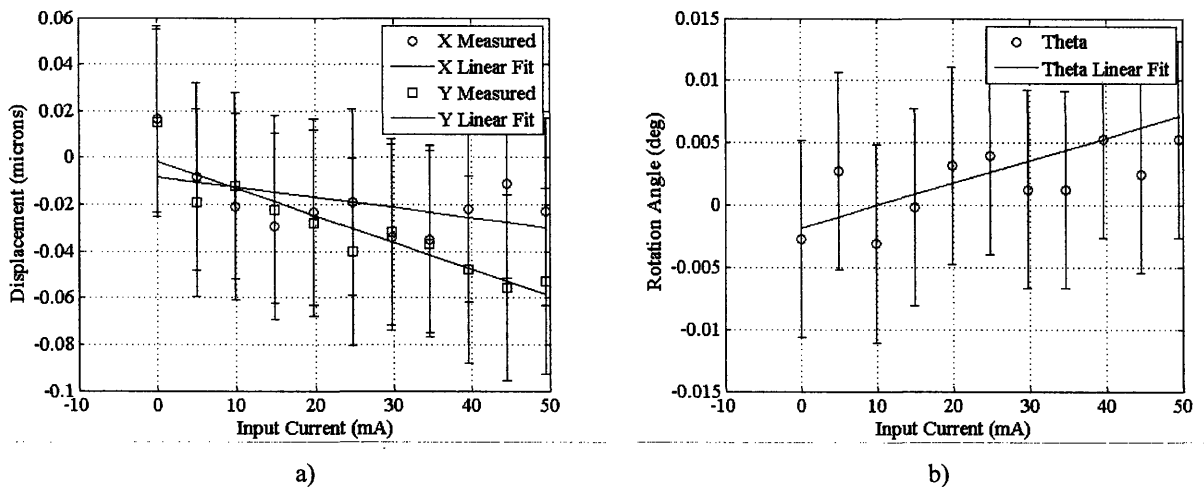
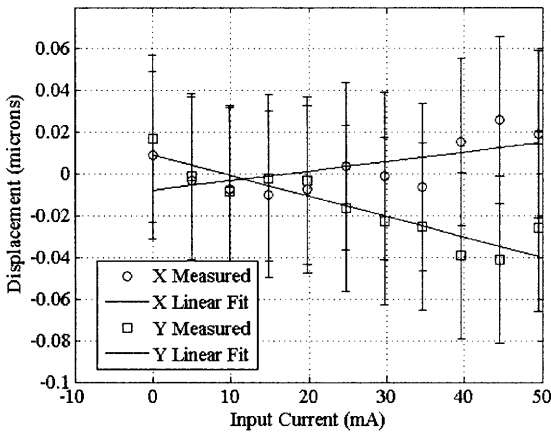
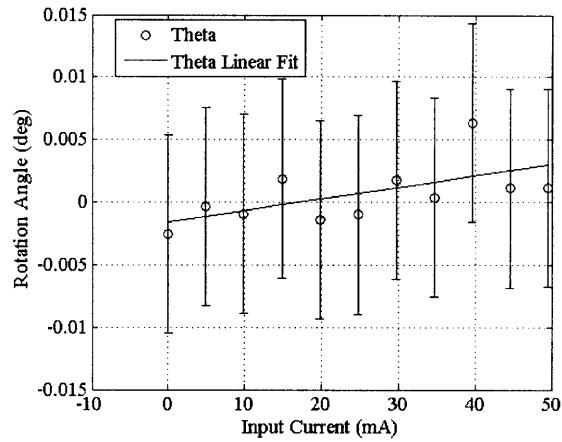


**Figure 6.16. Pre-calibrated in-plane static response versus input current for commanded motion in the  $z$ -direction: a) measured parasitic  $x$ - and  $y$ -motion; b) measured and predicted  $\theta_z$  motion.**

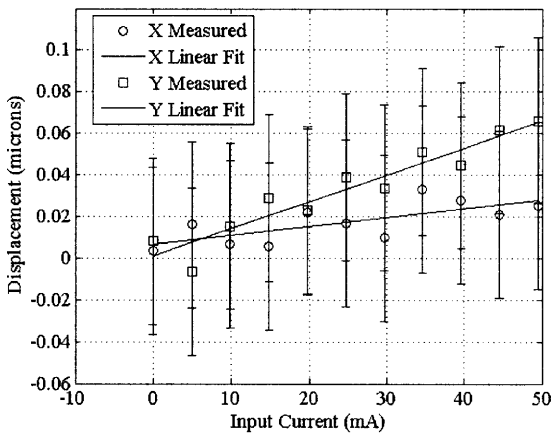


a)

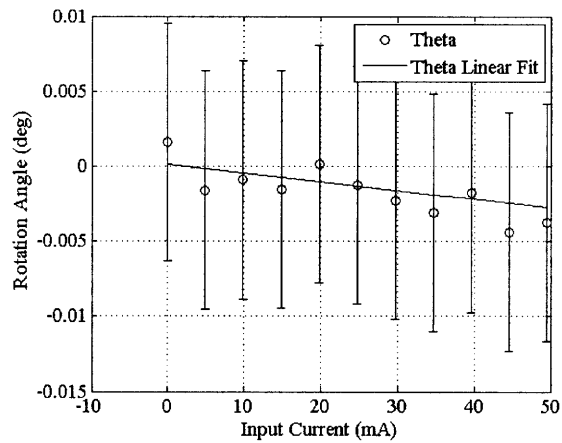


b)

**Figure 6.17. Pre-calibrated, in-plane static response versus input current for commanded motion in the  $\theta_x$ -direction: a) measured parasitic x- and y-motion; b) measured parasitic  $\theta_z$  motion.**



a)



b)

**Figure 6.18. Pre-calibrated, in-plane static response versus input current for commanded motion in the  $\theta_y$ -direction: a) measured parasitic x- and y-motion; b) measured parasitic  $\theta_z$  motion.**

The data in the figures indicates that the resulting parasitic translations are less than 60 nm and the parasitic rotation about the z-axis was less than the measurement noise of the MMA system. The results show that the z-actuators generate minimal in-plane forces and parasitic in-plane motions as predicted by the actuator models. The results in this section show that the nanopositioner actuators demonstrate nominally orthogonal actuator force outputs and validate the design concept. The measured parasitic motions are linear and therefore may be minimized by open-loop calibration in six axes. The current measurement capabilities of the MMA limit calibration to three actuators that act in-plane or out-of-plane but not six actuators

simultaneously. Six-axis calibration requires a metrology system with the capability of simultaneous measurement of in- and out-of-plane motion. Metrology systems that enable measurement of meso- and micro-scale device motions simultaneously in six-axis present several challenges and have yet to be realized.

### 6.3.1.E Calibration procedure

The nanopositioner calibration matrix relates actuator inputs to motion outputs per the following relation:

$$\begin{bmatrix} \Delta x \\ \Delta y \\ \Delta \theta_z \\ \Delta \theta_x \\ \Delta \theta_y \\ \Delta z \end{bmatrix} = \begin{bmatrix} C_{11} & \dots & C_{13} & C_{14} & \dots & C_{16} \\ \vdots & \ddots & \vdots & \vdots & \ddots & \vdots \\ C_{31} & \dots & C_{33} & C_{34} & \dots & C_{36} \\ C_{41} & \dots & C_{43} & C_{44} & \dots & C_{46} \\ \vdots & \ddots & \vdots & \vdots & \ddots & \vdots \\ C_{61} & \dots & C_{63} & C_{64} & \dots & C_{66} \end{bmatrix} \begin{bmatrix} i_1 \\ i_2 \\ i_3 \\ i_4 \\ i_5 \\ i_6 \end{bmatrix} = \begin{bmatrix} C_{i-i} & C_{i-o} \\ C_{o-i} & C_{o-o} \end{bmatrix} \begin{bmatrix} i_1 \\ i_2 \\ i_3 \\ i_4 \\ i_5 \\ i_6 \end{bmatrix} \quad (6.4)$$

The matrix was segmented to four sub-matrices that relate the following:

- 1) in-plane actuation to in-plane motion,
- 2) in-plane actuation to out-of-plane motion,
- 3) out-of-plane actuation to in-plane motion; and
- 4) out-of-plane actuation to out-of-plane motion.

The 6 x 6 calibration matrix has 36 unknowns that require a total of 36 input-output experiments. The MMA system outputs four channels and thereby limits the calibration to in-plane motion that was caused by in-plane actuation and out-of-plane motion that was caused by out-of-plane actuation. The cross terms may be determined from experiment but they are not used for calibrated motion experiments because of the limited number of actuation channels.

The calibration constants were computed by solving sets of linear equations that relate input actuation to output motion. The relative inputs listed in Table 6.4 were applied for actuation in the  $x$ -,  $y$ -, and  $\theta_z$ -directions and the resulting in-plane motion was measured. The system of nine equations was solved for the nine unknown calibration constants. The measured calibration matrix was inverted to compute the required actuator inputs that relate in-plane actuation current to in-plane motion is:

$$\begin{bmatrix} \Delta x \\ \Delta y \\ \Delta \theta_z \end{bmatrix} = \begin{bmatrix} 9.8005 & -4.2330 & -6.5472 \\ 0.3061 & -6.8919 & 8.5796 \\ 0.0075 & 0.0053 & 0.0076 \end{bmatrix} \begin{bmatrix} i_1 \\ i_2 \\ i_3 \end{bmatrix} \quad (6.5)$$

The first two rows of the calibration matrix have units of  $\mu\text{m} / \text{A}$  and the third row has units of  $\text{radian} / \text{A}$ . When compared to the actuation matrix in Equation (2.5), the elements of measured calibration matrix in Equation (6.5) demonstrate the parasitic motions of the nanopositioner. The parasitic motions are linear. The nanopositioner design generates a set of linearly independent forces that may be combined in open-loop to minimize the parasitic error motions, as will be demonstrated in the next section.

### 6.3.1.F Calibrated Quasistatic In-Plane Motion

The calibration matrix from the previous section was used to determine the actuation inputs that were required to generate near parasitic-free in-plane motion. Figure 6.19, Figure 6.20, and Figure 6.21 show the calibrated quasistatic response of the meso-scale nanopositioner to in-plane actuation commands in  $x$ -,  $y$ -, and  $\theta_z$  directions. The data is plotted versus the maximum actuation command input current. The current was limited so that the temperature of actuator paddles remained below  $150^\circ\text{C}$  as estimated from Figure 6.3.

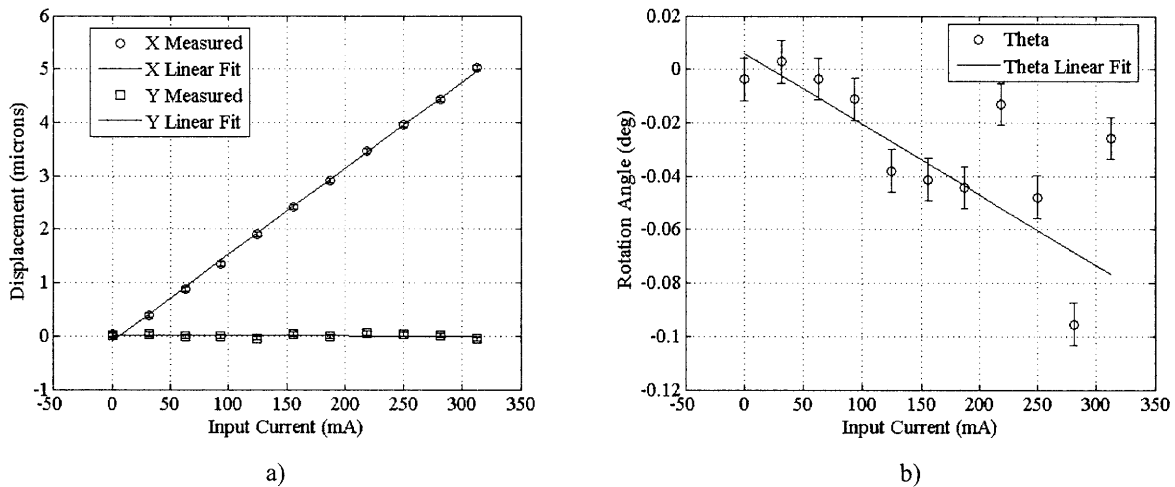
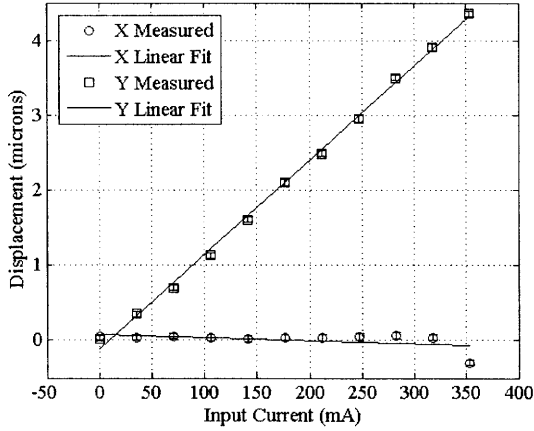
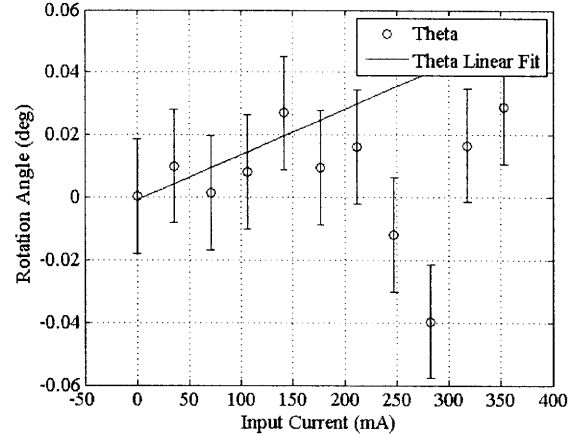


**Figure 6.19. Calibrated, in-plane static response versus input current for desired motion in the x-direction: a) measured x-motion and parasitic y-motion; b)  $\theta_z$  parasitic motion.**

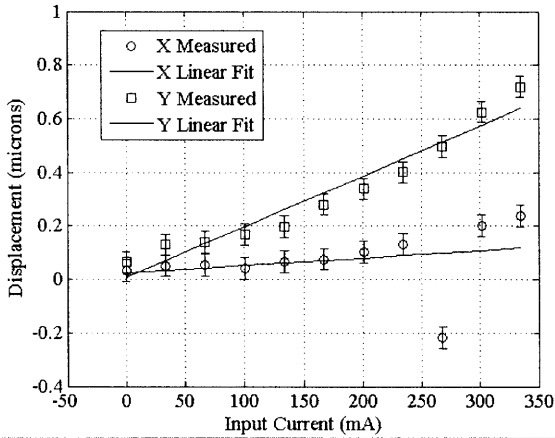


a)

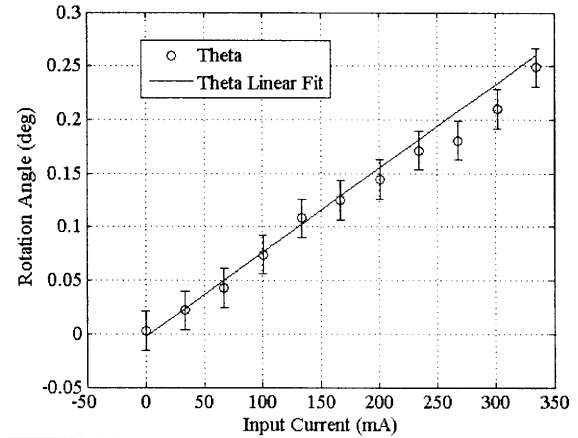


b)

**Figure 6.20. Calibrated, in-plane static response versus input current for desired motion in the  $y$ -direction:**  
**a) measured  $y$ -motion and parasitic  $x$ -motion; b)  $\theta_z$  parasitic motion.**



a)



b)

**Figure 6.21. Calibrated, in-plane static response versus input current for desired motion in the  $\theta_z$ -direction:**  
**a) measured parasitic  $x$ - and  $y$ -motion; b) measured  $\theta_z$  motion.**

The scattering within the parasitic rotation data in Figure 6.20b and Figure 6.21b was a measurement artifact of the target that was used to compute the rotation. The outlying data point in Figure 6.20a and the parasitic translation in Figure 6.21a are also measurement artifacts of the target. The data in the figures indicates that the nanopositioner was capable of unidirectional translations in the  $x$ - and  $y$ - directions of  $5\ \mu\text{m}$  and  $4.5\ \mu\text{m}$ , respectively. Less than  $50\ \text{nm}$  of parasitic translation was recorded during these commanded translations. The parasitic rotation was measured to be less than  $0.02^\circ$  for translations of less than  $2\ \mu\text{m}$ . Measurement artifacts

skew the parasitic rotation data for translations greater than 2  $\mu\text{m}$ . The nanopositioner was also capable of rotations about the  $z$ -axis of  $0.25^\circ$ .

The data shows that the nanopositioner exhibits an in-plane range-of-motion that meets the functional requirements developed in Chapter 1 and 2. The actuator current that was required to achieve this range was larger than the designed input current by 50%. This is attributed to the measured actuator air gap that varied between 20 – 120  $\mu\text{m}$  between actuator paddles. In addition, the static current-voltage response in Section 6.2.1 suggests that the nanopositioner may have a range of 15  $\mu\text{m}$  if actuated to the current limit of 450 mA. Improved assembly actuator gap height control may yield a smaller mean gap height and a narrower distribution of gaps which could improve the force and range-of-motion by up to 30%. This may result in one the following: a) 60% reduction in power consumption and temperature rise for equivalent range-of-motion; or b) 30% increase in range of motion for equivalent power and temperature rise.

The data in this section also demonstrates that the parasitic motions that are due to parasitic moments and forces may be minimized during open-loop operation by linear calibration. The resolution to which the parasitic motions may be minimized is limited by the measurement capabilities of the metrology system. Measurement errors that are due to the square target feature may be eliminated by using a more suitable target such as a set of three round features that are etched in the stage. A set of round target features may eliminate the error due to rotation of the target and may thereby result in improvements in the linearity of the measured data. In addition, measurement errors also result from the intensity variation that is due to motion of the circular discolorations in the stage surface as seen in Figure 6.10. These discolorations are fabrication artifacts and add nonlinearities to the motion data as they move in and out of the regions of interest. The problem may be minimized by evaporating metal upon the sample stage. The limitations of an optical-based system suggest that an alternative measurement system, such as capacitive sensing, may be more suitable for measuring six-axis motion of the meso-scale nanopositioner.

#### **6.3.1.G Quasistatic Out-of-Plane Motion**

The out-of-plane translation and rotations of the nanopositioner were measured for calibrated in-plane actuation and pre-calibrated out-of-plane actuation. Figure 6.22 and Figure

6.23 show the out-of-plane quasistatic input-output response to calibrated in-plane actuation commands in for  $x$  and  $y$  displacements. The translation and rotation data was fit to the first three data points.

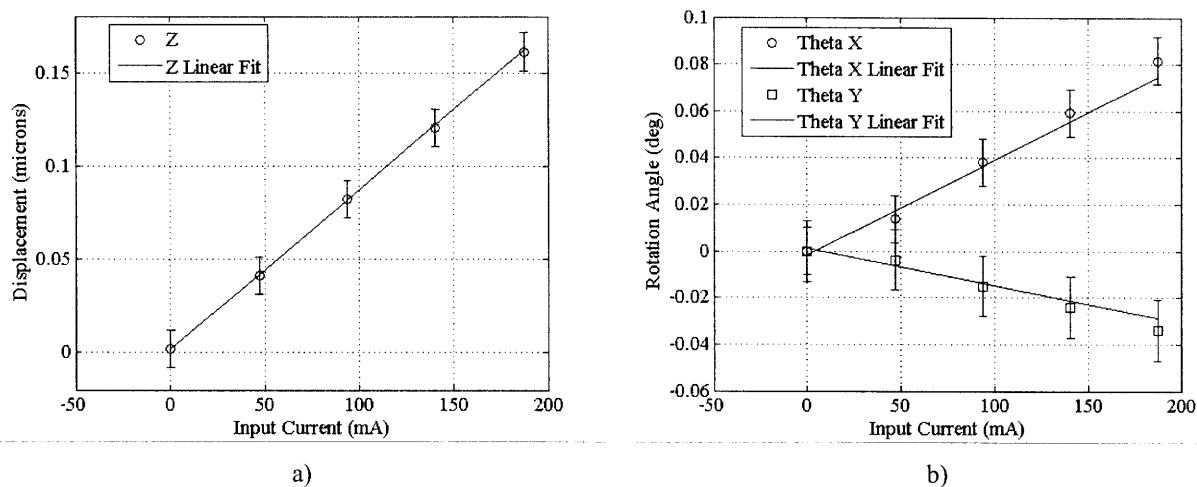


**Figure 6.22. Out-of-plane static response versus input current for calibrated motion in the  $x$ -direction: a) measured parasitic motion in the  $z$ -direction; b) measured parasitic motion in the  $\theta_x$ - and  $\theta_y$ -direction.**

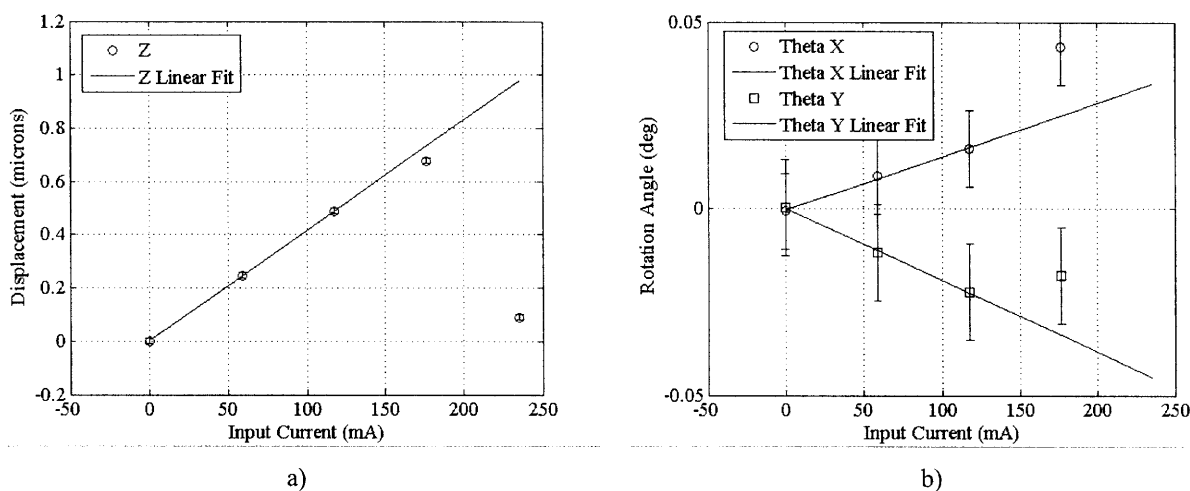


**Figure 6.23. Out-of-plane static response versus input current for calibrated motion in the  $y$ -direction: a) measured parasitic motion in the  $z$ -direction; b) measured parasitic motion in the  $\theta_x$ - and  $\theta_y$ -direction.**

The data in Figure 6.22 shows that the nanopositioner stage translates by more than 150 nm in the  $z$ -direction and rotates by more than  $0.08^\circ$  for  $x$ -axis actuation commands that are less than 200 mA. Figure 6.23 shows the stage translates by more than 600 nm in the  $z$ -direction for  $y$ -



axis actuation commands less than 200 mA. The outlier in the data was caused by phase wrapping of the data and this indicates that a displacement of more than 164 nanometers occurred. The parasitic motion was caused by the parasitic forces and moments that act upon the actuator paddles and may also result from the thermally-induced error that was caused by the bending of the flexure beams. Further experiments are required in order to determine if the error motions were caused by thermomechanical bending of the flexure beams. The thermally-induced error may be measured by removing the nanopositioner chip from the magnet fixture and repeating the experiment. The parasitic error motions are linear for actuator inputs up to 125 mA in the case of commanded motion in the  $y$ -direction and thereby may be minimized in open-loop by six-axis calibration.

Figure 6.24, Figure 6.25, and Figure 6.26 show the out-of-plane quasistatic response of the meso-scale nanopositioner to pre-calibrated, out-of-plane actuation commands in the  $z$ -,  $\theta_x$ , and  $\theta_y$  directions. The translation and rotation data was fit to the first three data points. The predicted translation in the  $z$ -direction was also plotted in Figure 6.26 for comparison to the measured data.

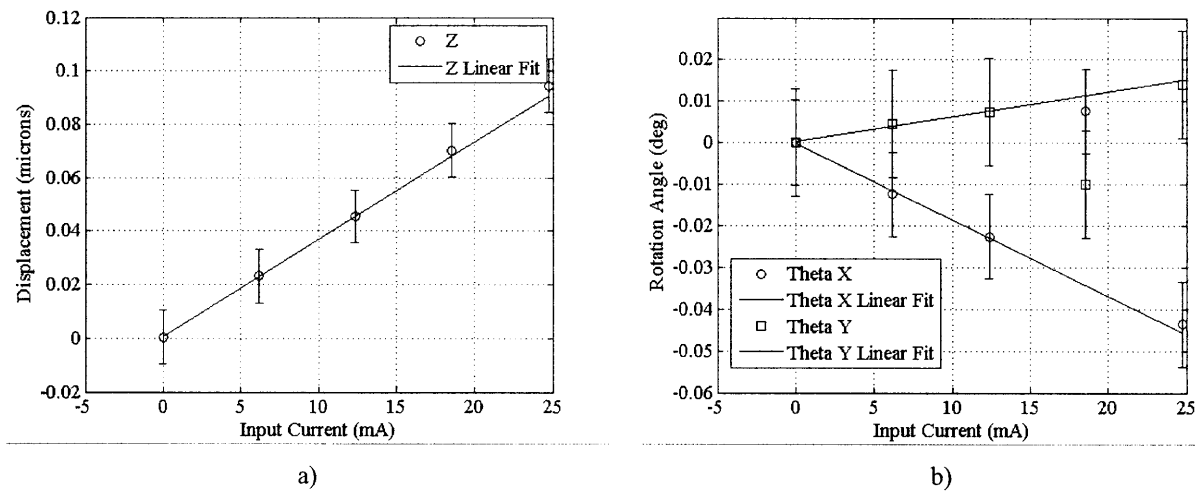


**Figure 6.24. Out-of-plane static response versus input current for commanded motion in the  $\theta_x$ - direction: a) measured parasitic motion in the  $z$ -direction; b) measured motion in the  $\theta_x$ -direction and parasitic motion in the  $\theta_y$ -direction.**

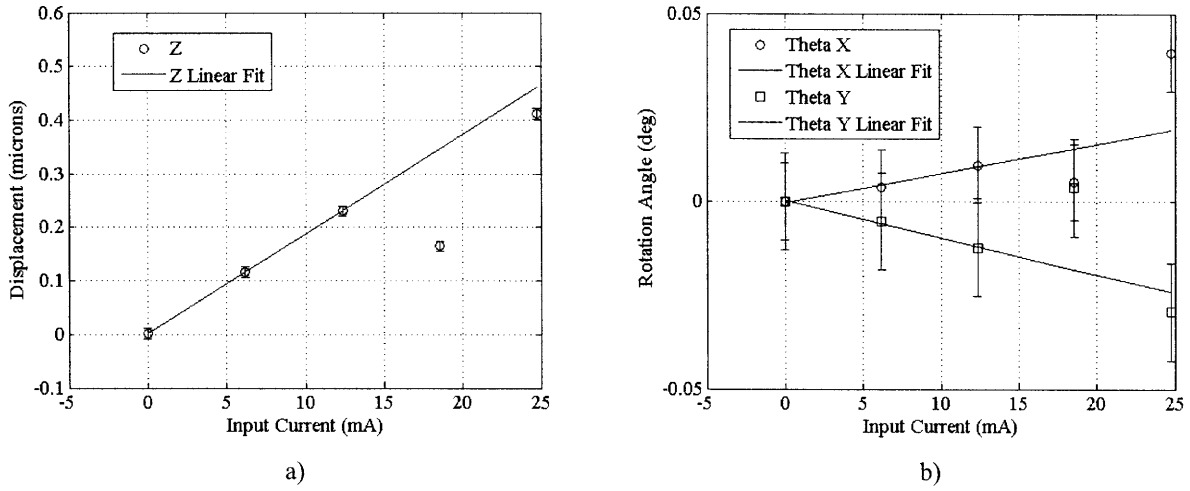


**Figure 6.25. Out-of-plane static response versus input current for commanded motion in the  $\theta_y$ -direction: a) measured parasitic motion in the z-direction; b) measured motion in the  $\theta_y$ -direction and parasitic motion in the  $\theta_x$ -direction.**

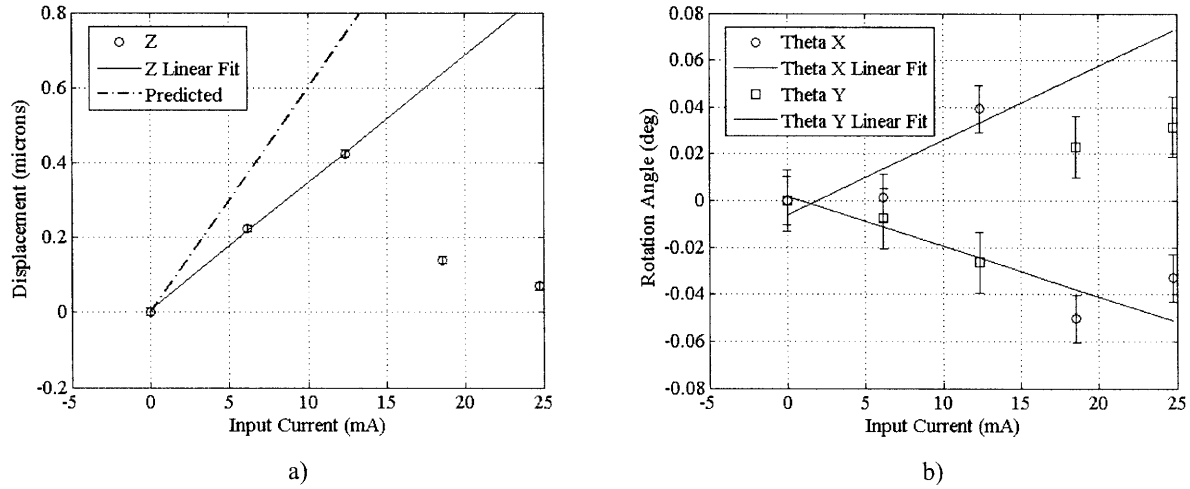


**Figure 6.26. Out-of-plane static response versus input current for commanded motion in the z-direction: a) measured motion in the z-direction; b) measured parasitic motion in the  $\theta_x$ - and  $\theta_y$ -direction.**

The scatter in z-translations was caused by phase wrapping of the intensity data. This indicates a displacement greater than 164 nm occurred. The data indicates that the nanopositioner exhibits parasitic motion in the z-direction that was likely caused by the thermally-induced error that was driven by bending of the flexure beams. The measured data for in-plane and out-of-plane actuation indicates that the passive thermal error prevention concept does not prevent thermally-induced error at the 10 Hz excitation frequency that was used in these experiments. The poor performance of the compensation scheme was likely the result of the thermally-induced transient

error which has a time constant on the order of the excitation signal. The out-of-plane motion should be measured statically and the system should be allowed to reach thermal equilibrium in order to measure the performance of the passive thermal error prevention. A laser interferometer could be used to measure the out-of-plane motion in steady state.

### 6.3.1.H Calibrated Quasistatic Out-of-Plane Motion

The nanopositioner was calibrated for motion in the out-of-plane direction by using the data that was presented in the previous section. Figure 6.27 shows the calibrated, quasistatic input-output response to out-of-plane actuation commands in the z-direction.

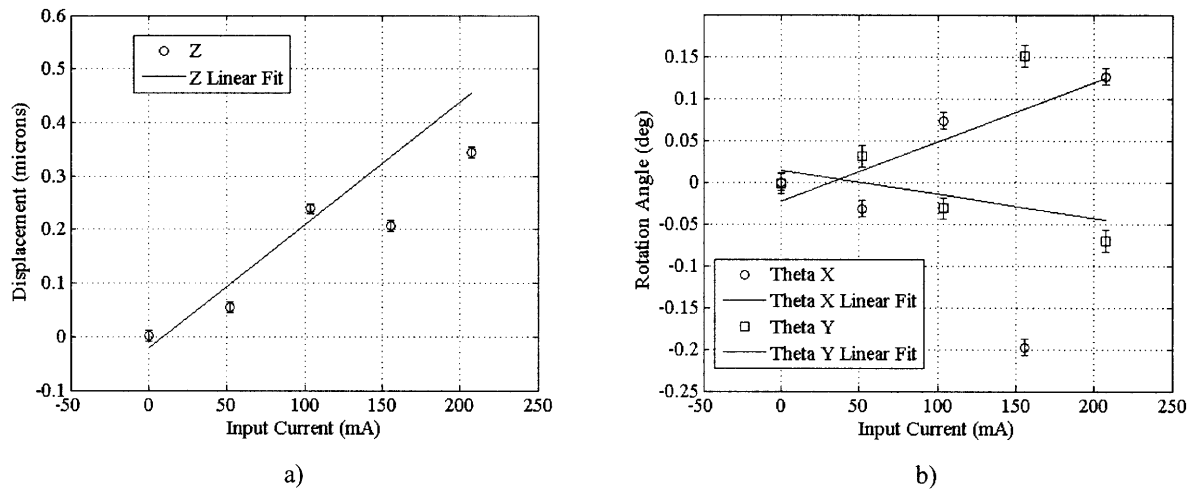


Figure 6.27. Calibrated, out-of-plane static response versus input current for commanded motion in the z-direction: a) measured motion in the z-direction; b) measured parasitic motion in the  $\theta_x$ - and  $\theta_y$ -directions.

The data in the figure shows marked deviations from linear behavior and increased parasitic rotational error when compared to the pre-calibrated data in the previous section. The results lead to the hypothesis that the out-of-plane motion that was presented in the previous section was not driven by out-of-plane actuation effects, but rather by thermally-induced errors. The motions that are caused by thermally-induced errors may be masking the actuator output and this yielded a skewed calibration matrix that reflected the thermal characteristics rather than the error sources that are associated with actuator motion. The motion in these experiments was measured at an excitation frequency of 10 Hz and may have resulted from unsettled thermal transients error motions. As discussed in the previous section, the out-of-plane motion experiments should be repeated such that the system is allowed to reach thermal steady state before measuring the

motion. A square wave with period of greater than 20 seconds may be appropriate excitation signal in order to allow settling of the thermal transients.

The thermal error motions may also be caused by excessive thermally-induced bending of the flexure beams in steady-state. The flexure design for thermal error motion prevention may induce larger-than-expected out-of-plane error motions because of its sensitivity to the parameters values used in design. The variations between design parameters and fabricated results that affect the thermal error motions include: a) material properties of the flexures and actuator paddles; b) cross-sectional geometry; and c) the actuator coils and lead resistances. The variation between the design parameter values and the fabricated properties may lead to errors in the optimum beam lengths in regards to the fabricated device. The sub-optimal geometry in the fabricated device may thereby result in substantive out-of-plane error motions. A possible solution is to run a batch of test wafers to measure the material properties and then use the measured values to design the optimal beam lengths. This solution is appropriate in the case that wafer-to-wafer and batch-to-batch material property variations are minimized. In summary, tight control and knowledge of the material properties of the fabricated device is required in order to design the flexure for thermal error motion prevention in open-loop. In the long term, closed-loop feedback control may be implemented in order to compensate for the thermal error motions. Several challenges must be addressed in order to integrate six-axis sensing in a meso-scale nanopositioner, as will be discussed in Section 7.2.3

#### **6.3.1.1 In-Plane Repeatability**

The in-plane repeatability of the nanopositioner was estimated by comparing multiple measurements of the calibrated, quasistatic response in the  $x$ - and  $y$ -directions. Figure 6.28 shows the results of three different  $y$ -actuation experiments and two different  $x$ -actuation experiments versus maximum input current. The measurement error is 40 nm. The error bars are smaller than the data markers and are therefore omitted.

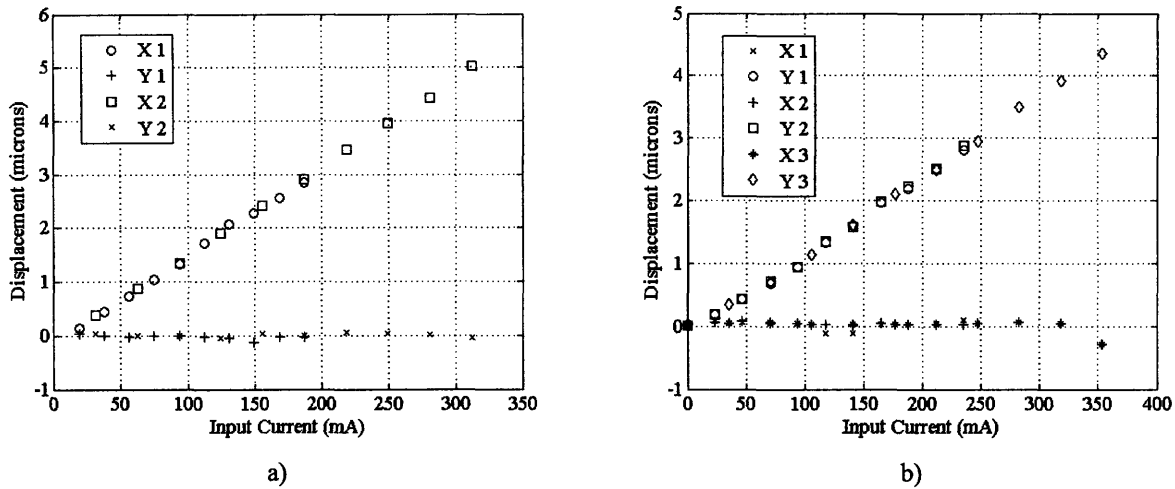


**Figure 6.28. Calibrated static in-plane response versus input current for multiple trials of commanded motion: a) commanded motion in the x-direction; b) commanded motion in the y-direction.**

The data in the figure shows that the repeated motion of the nanopositioner share similar slopes. The fitted slopes were measured to differ by less than 2% for motion in the  $x$ -direction and by less than 3% for motion in the  $y$ -direction. This is a first attempt at measuring the repeatability of the nanopositioner. Measurements of the response to repeated command inputs are required to capture a statistical distribution and quantify the in-plane repeatability.

### 6.3.2 Experiments using the Polytec MSA-400

A Polytec MSA-400 laser vibrometer was used to measure the pre-calibrated, out-of-plane dynamics of the meso-scale nanopositioner. The laser vibrometer determines the out-of-plane velocity of a sample by measuring the Doppler shift of the returned laser light. The system has a resolution of less than  $1 \mu\text{m} / \text{sec}$ , a maximum velocity of  $10 \text{ m/s}$ , and a maximum excitation frequency of  $1.5 \text{ MHz}$ . The system can output one synchronized excitation signal. This signal was used with the current-controller to drive one  $z$ -actuator for the frequency response experiments. The excitation signal was used to command three  $z$ -actuators for measurement of the out-of-plane step response. The measurements were taken at the geometric center of the nanopositioner stage. The measurement setup was similar to that of the MMA experiments that was shown in Figure 6.9.

#### 6.3.2.A Out-of-Plane Frequency Response

The out-of-plane frequency response was measured by exciting the nanopositioner with a sinusoidal current input of variable frequency and fixed amplitude of  $25 \text{ mA}$ . The excitation

frequency varied from 10 Hz to 20 kHz. The Polytec MSA-400 outputs the magnitude and phase of the displacement by transforming the measured velocity to displacement in the frequency domain. Figure 6.29 shows the measured frequency response for one out-of-plane actuator input.

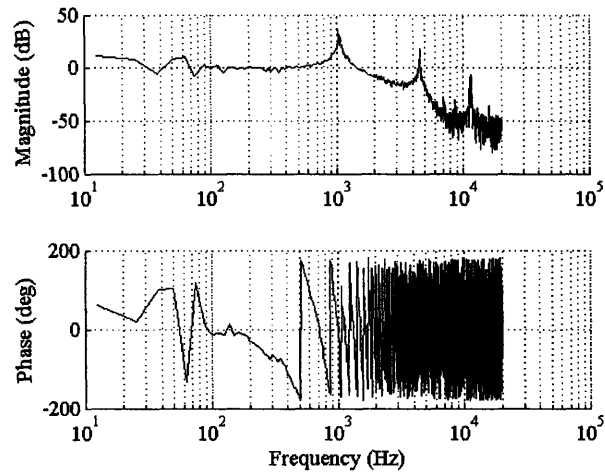


**Figure 6.29. Measured out-of-plane frequency response of the nanopositioner for input into one  $z$ -actuator.**

The data in the figure shows two under-damped resonant peaks at 1038 Hz and 1063 Hz. These values correspond to the tilting and translational modes of the system. The discontinuities in phase may result from two possible sources: a) numerical errors that are caused by computation errors within the Polytec tool; and b) phase errors associated with returned light that reflects from the oxide surface and underlying silicon. The latter problem may be eliminated by evaporating metal on the stage. The  $\theta_x$  and  $\theta_y$  tilting modes are assumed to occur at equivalent frequencies as predicted by the simulation model. Table 6.6 contrasts the predicted and measured out-of-plane resonant modes.

**Table 6.6. Comparison of predicted and measured out-of-plane resonant modes.**

Symbol	Mode	Predicted	Measured	% Error	Units
$f_{\theta_y}$	$\theta_y$	1013	1038	2.4	Hz
$f_{\theta_x}$	$\theta_x$	1014	1038	2.3	Hz
$f_z$	Z	1058	1063	0.5	Hz

The data in the table indicates that the model predicts the resonant modes with less than 3% error, which was sufficient for the purpose of designing the system.

### 6.3.2.B Out-of-Plane Step Response

The pre-calibrated out-of-plane step response was measured by exciting the out-of-plane actuator coils with a square wave signal. The square wave oscillated between  $\pm 50$  mA. The measured velocity data was integrated using the trapezoidal rule to obtain displacement. The resulting bias slope of the displacement was then subtracted from the data to obtain the displacement relative to the initial measured position. Figure 6.30a and b show the out-of-plane response to a square wave with period of 1 second and 10 seconds, respectively. The command signal was input to one z-actuator in Figure 6.30a and three actuators in Figure 6.30b.

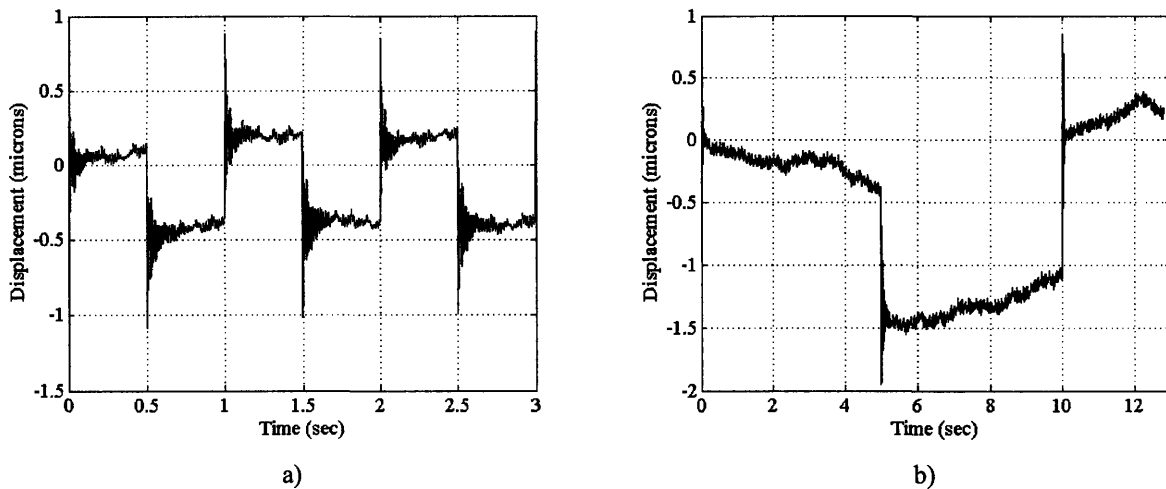


**Figure 6.30.** Measured out-of-plane response for a pre-calibrated, square wave input signal to the z-actuator coils: a) one z-actuator excited by a signal with 1 sec period; and b) three z-actuators excited by a signal with 10 sec period.

The data in the figure shows that the nanopositioner moves out-of-plane by more than  $1 \mu\text{m}$  for an input step of 100 mA to each of the out-of-plane actuators. The nanopositioner may therefore move up to  $3 \mu\text{m}$  for sustainable current inputs up to 300 mA. The drift in the data within Figure 6.30b was attributed to the thermally-induced transient error. The transient thermal error motions result from transient heating and bending of the multi-layer flexure beams as predicted by the design models in Section 4.4. A possible open-loop design solution is to decouple the silicon beams from the copper leads in order to eliminate the thermally-induced bending. A second design solution is to design the flexures so that the copper leads are located on the neutral axis of the beam cross section, thereby minimizing the thermal bending. These design solutions pose several fabrication challenges that must be addressed in order to realize the structure. Closed-loop feedback control may provide an alternative method to minimize the thermal

transients. Section 7.2.3 discusses some of the challenges that must be overcome in order to integrate six-axis sensing in a meso-scale nanopositioner.

In this experiment, the actuators dissipate power throughout the duration of the measurement because the square wave varies between  $\pm 50$  mA. The experiment should be repeated for an input signal that oscillates between zero and the step amplitude with a period of at least 20 seconds. The experiment should be repeated with the nanopositioner removed from the magnet fixture in order to characterize the transient thermally-induced error that was caused by the bending of the flexure beams. An interferometer may be used to measure position as opposed to integrating the velocity data from the vibrometer as in the experiments presented in this section.

## 6.4 Summary

Experimental characterization of the mechanical and electrical performance of the meso-scale nanopositioner was presented. The error between predicted and measured resistance of the actuator coils was less than 12%. Sustainable current experiments were presented in Section 6.2.1. The actuator coils sustained a measured current of 500 mA, but the operating current was kept under 400 mA so that the estimated coil temperature does not exceed 150°C. Test coils that were buried in silicon were shown to sustain greater than 1 A at density of 1122 A/mm<sup>2</sup> and at an estimated temperature rise of less than 10°C. This result indicates that a moving coil actuator with fixed coils may be more suited for positioning applications where bandwidth is traded for reduced operating temperatures and increased range.

The self inductance of the coils was measured in Section 6.2.2 to be on the order of magnitude of the predicted values. The electrical roll-off frequency of the coils was estimated to be near 10 MHz so that electrical dynamics may be ignored at the operating frequencies of the nanopositioner.

The measured mechanical resonance frequencies were presented in Section 6.3.1.C and differed from the predicted values by less than 8%. The error was related to lateral over-etching of the flexure beams. The predicted and measured quasistatic in-plane response of the system in Section 6.3.1.D differed by up to 95%. The error was attributed to variations in the magnetic gap between the actuator paddles. These results and the measurements of the actuator air gap



indicate that the alignment and assembly of the magnets and the chip have important implications on the actuator performance.

The nanopositioner was calibrated for in-plane motion and was measured to have a range of motion of  $\pm 5 \mu\text{m} \times \pm 4.5 \mu\text{m}$  in the  $x$ - and  $y$ -directions; and a rotational range of  $\pm 0.25^\circ$  about the  $z$ -axis, as shown in 6.3.1.F. The parasitic translation and rotation was measured to be less than 50 nm and  $0.02^\circ$ , respectively. The in-plane repeatability was estimated to be better than 100 nm. The results indicate that the nanopositioner is capable of minimizing the linear in-plane parasitic motions in open loop by way of a simple calibration procedure.

Quasistatic out-of-plane displacement experiments with the MMA system that were presented in Sections 6.3.1.G and 6.3.1.H indicated that the thermally-induced error may mask the actuated motion. The measured data for in-plane and out-of-plane actuation indicates that the passive thermal error prevention concept does not prevent thermally-induced error at the 10 Hz excitation frequency. The poor performance of the compensation scheme was likely the result of the thermally-induced transient error which has a time constant on the order of the excitation signal.

Section 6.3.2 presented results from laser vibrometer experiments. The data indicated that the nanopositioner has the capability to step in the  $z$ -direction by more than  $1 \mu\text{m}$ , that the thermally-induced error of the system exceeds 400 nm and has a time constant that was larger than 5 seconds. The thermal error motions result from the multi-layer design of the flexure beams and may be minimized by redesigning the beams and leads or by implementing closed-loop feedback control. Further experiments are necessary to fully quantify the out-of-plane motion of the nanopositioner in open-loop.

The results in this chapter suggest that alternative measurement techniques may be more suitable than optical measurement systems used in this work for measuring six-axis, nanometer-level motions of meso-scale nanopositioner. Errors that are due to image-processing artifacts of the target may be minimized by implementing a non-optical technique such as capacitive sensing as discussed in Section 7.2.3.

## CONCLUSIONS AND FUTURE WORK

---

### 7.1 Summary and Conclusions

The purpose of this thesis is to generate the design and fabrication knowledge that is required to engineer high-speed, six-axis, meso-scale nanositioners that are driven by electromagnetic actuators. When compared to macro-scale nanositioners, meso-scale nanositioners enable a combination of greater bandwidth, improved thermal stability, portability, and capacity for massively parallel operation. Meso-scale nanositioners are envisioned to impact emerging applications in data storage and nanomanufacturing, which will benefit from low-cost, portable, multi-axis nanositioners that can position samples with nanometer-level precision at bandwidth of 100s Hz and over a working envelope greater than  $10 \times 10 \times 10 \mu\text{m}^3$ . This thesis forms the foundation of design and fabrication knowledge required to engineer meso-scale systems to meet these needs.

A set of functional requirements for open-loop operation were developed for the nanositioner in Sections 1.1.1 and 1.1.2 in order to satisfy the performance needs of the target applications. The functional requirements included:

- 1) work volume of  $10 \times 10 \times 10$  micrometers<sup>3</sup>;
- 2) first mode resonant frequency of 1 kHz; and
- 3) repeatability better than 10 nm.

A review of the prior art in Sections 1.2 revealed that previous meso-scale systems failed to meet the functional requirements and that a departure from conventional design techniques may enable enhanced performance.

This work proposed new concepts, design rules, and performance models for flexure bearings and electromagnetic actuators as presented in Section 2.3-2.6. The design combines a planar silicon flexure mechanism and moving-coil microactuators that employ millimeter-scale permanent magnets and stacked, planar-spiral micro-coils. The moving-coil actuator outperforms previous coil designs as it enables orthogonal and linear force capability in two-axis while minimizing parasitic forces. The 6-axis actuation concept was demonstrated with a centimeter-scale, prototype nanopositioner.

The meso-scale nanopositioner system performance was modeled in the structural, thermal, electrical, and magnetic domains with analytical and finite-element techniques in Chapter 3. A new method was created to model the three-dimensional magnetic fields that are due to finite permanent magnet arrays. The solution uses the Fourier Transform method to solve for the fields along planes that are above magnet arrays and that have vertical magnetization, as presented in 3.1. The magnetic field model agreed with experimental measurements for a prototype magnet array with less than 4% error. The magnetic field model was then used in Section 4.2 to simulate and optimize the force that acts upon the moving-coil microactuators. A kinematic and dynamic model lumped-parameter model of the flexure was derived in Section 3.4 but has not yet been implemented. The coil force model was combined with a finite-element simulation of the flexure mechanism to predict the static displacement and dynamic response of the nanopositioner. The models were used in Sections 4.3 and 4.4 to optimize the actuator coil and flexure geometry in order to achieve the desired motions, stiffness, and operating temperature, and to reduce thermal errors.

Chapter 5 presented a new microfabrication process and design-for-manufacturing rules that were generated to create integrated, multilayer actuator coils and silicon flexure bearings via low-temperature microfabrication process steps. The process combines electroplating for the copper coils, plasma deposition of an un-annealed silicon dioxide interlayer dielectric, and deep reactive-ion etching for the silicon flexures and alignment features. Several fabrication challenges were addressed in order to successfully realize the process. Electroplating of void-free deposits in the silicon molds was the most critical challenge in the process. Deep-via plating chemistry, aggressive agitation, and conservative coil cross-section designs were used to eliminate voids in the buried copper. The resulting copper-in-silicon coil structure exhibited thermal stresses during deposition of the oxide that then resulted in delamination of the oxide

and cracking of the silicon. Microfabrication experiments were used to formulate coil geometry design rules in Section 5.6 that minimized the delamination and cracking of the materials that comprise the coil structure. The previously-unreported breakdown strength of un-annealed PECVD silicon dioxide was measured with capacitor test structures and shown to be acceptable in Section 5.7, but a factor of three times less than that of thermal silicon dioxide.

The results of this research were used to design and fabricate a meso-scale nanopositioner system that satisfied the functional requirements for emerging applications. The predicted electrical and mechanical performance of the system was compared with experiments in Chapter 6. The predicted resistance and inductance of the actuator coils were also compared to measurements in Section 6.2. The suspended actuator coils demonstrated sustainable currents up to 400 mA at an estimated operating temperature of 150°C. This result imposes limitations on the sustainable current of the actuators in order to limit the thermally-induced stresses that may damage the coil structures. A test coil buried in silicon with similar winding geometry as the actuator coils was measured to sustain currents that were greater than 1 A at a density of 1122 A/mm<sup>2</sup> with a estimated temperature rise of less than 10°C. The result indicates that a moving coil actuator with fixed coils may be more suited for positioning applications where bandwidth is traded for reduced operating temperatures and increased range.

The electrical roll-off frequency of the coils was estimated from resistance and inductance measurements to be near 10 MHz so that electrical dynamics may be ignored at the operating frequencies of the nanopositioner.

The predicted mechanical performance was compared with motion experiments that were conducted on a micro-motion analyzer and laser vibrometer as presented in Sections 6.3.1 and 6.3.2, respectively. The nanopositioner was measured to have a first mode resonant frequency at 900 Hz. The measured in-plane mechanical resonance frequencies differed from the predicted values by less than 8%. The error is due to lateral over-etching of the flexure beams, but is acceptable for the purposes of design. The underdamped resonant peaks indicate that the nanopositioner will “ring” in response to step inputs and its response time is thereby limited by settling of the oscillations. Closed-loop feed back or feed-forward input filtering may be applied to minimize the underdamped oscillations and improve response time.

The predicted and measured quasi-static in-plane motion response of the system differed by less than 8% for translation along the  $x$ -axis, less than 23% for translation along the  $y$ -axis, and less than 95% for rotations about the  $z$ -axis. The error is attributed to variations in the magnetic gap between the actuator paddles. These results and the measurements of the actuator air gap indicate that the alignment and assembly of the magnets and the chip have important implications on the actuator performance. Improvements in the assembly precision may thereby improve the following: a) the force output of the actuators; b) the uniformity of the force output between actuators; and c) minimize the parasitic errors due to gap height variation.

The nanopositioner was calibrated for in-plane motion and it was shown to have a range of motion of  $\pm 5 \mu\text{m} \times \pm 4.5 \mu\text{m}$  in the  $x$ - and  $y$ -directions and a rotational range of  $\pm 0.25^\circ$  about the  $z$ -axis. The parasitic translation and rotation was measured to be less than 50 nm and  $0.02^\circ$ , respectively. The results indicate that the nanopositioner is capable of minimizing the linear in-plane parasitic motions via open loop calibration. The in-plane repeatability was estimated to be better than 100 nm. The results in Chapter 6 suggest that alternative measurement techniques may be more suitable than optical measurement systems used in this work for measuring six-axis, nanometer-level motions of meso-scale nanopositioner. Errors that are due to image-processing artifacts of the target may be minimized by implementing a non-optical technique such as capacitive sensing as discussed in Section 7.2.3.

Quasi-static out-of-plane motion experiments with the MMA system indicated that the thermal parasitic error may mask the actuated motion. The measured data for in-plane and out-of-plane actuation indicates that the passive thermal error prevention concept does not prevent thermally-induced error at the 10 Hz excitation frequency. The poor performance of the compensation scheme was likely the result of the thermally-induced transient error which has a time constant on the order of the excitation signal. In addition, the method that was used to design the beam geometry for passive thermal error prevention is sensitive to the design parameters. Variations in fabricated material and cross-section properties may thereby lead to sub-optimal beam geometry that then result in substantive steady-state thermal error motions. Passive, steady-state minimization of the thermal error motions may be improved by using measured values for the cross-section and material parameters. The steady-state thermal errors may also be minimized by employing closed-loop feedback control or by redesigning the beam

and leads in order to eliminate thermal bending during open-loop operation. For instance, the copper and silicon layer may be separated or the copper leads may be integrated in the flexure along the neutral axis.

Results from laser vibrometer experiments indicate that the nanopositioner has the capability to step in the z-direction by more than 1  $\mu\text{m}$ . The transient thermal error of the system exceeds 400 nm and has a time constant that is greater than 5 seconds. The thermal error motions result from the multi-layer design of the flexure beams and may be minimized by redesigning the beams and leads or by implementing closed-loop feedback control. Further experiments are necessary to fully quantify the out-of-plane motion of the nanopositioner.

Table 7.1 shows a summary comparison of the measured performance of the meso-scale nanopositioner and the functional requirements as derived for the nanomanufacturing and data storage applications.

**Table 7.1. Summary comparison of the functional requirements and measured performance of the meso-scale nanopositioner.**

Parameter	Units	FR	Measured
X Translation Range	$\mu\text{m}$	10	10
Y Translation Range	$\mu\text{m}$	10	9.5
Z Translation Range	$\mu\text{m}$	10	2
Z Rotation Range	deg	3	0.5
Natural Frequency	Hz	1000	900
Precision	nm	10	TBD

## 7.2 Future Work

### 7.2.1 Near-Term Motion Experiments

The aim of this research was to design a prototype and characterize its dynamic response, static range, and repeatability. The full characterization of the meso-scale nanopositioner was beyond the scope of this research. Additional experiments are being planned in order to acquire data for the next phase of research on this project:

1) Out-of-plane thermal parasitic motion. The out-of-plane thermal parasitic motion may be characterized by removing the nanopositioner chip from the magnet fixture. Test chips were fabricated with one actuator paddle that was suspended by a unit flexure. The flexures on

one of the test chips were designed to minimize the thermal error while the other chip was intentionally designed with a non-compensating beam geometry. The passive thermal prevention geometry may be evaluated by comparing measurements from these two designs. A laser vibrometer or interferometer should be used to measure the transient and steady-state out-of-plane motion of the stage as power is supplied to the actuator coils. The laser should have the capability to measure position at three points in order to determine tip and tilt motions

2) Six-axis calibration. The system should be calibrated for six-axis motion and the in-plane and out-of-plane static responses need to be measured with inputs supplied to all actuator coils. The MMA may be used to run the experiment so long as an external data acquisition system controls the six actuator inputs. The digital control system may be synchronized to the strobe signal through the sync input on the MMA. The excitation frequency for the experiments should be chosen per the results of Experiment 1).

3) In-plane repeatability. The repeatability of the calibrated system for in-plane motions was estimated from three experiment trials. A thorough, in-plane repeatability experiment should measure the response to repeated in-plane step inputs. The in-plane repeatability may be measured with the MMA or a similar system.

4) Out-of-plane step response and stability. A laser interferometer should be used to measure the calibrated, out-of-plane step response and corresponding stability in order to measure the transient and steady-state behavior. The out-of-plane range-of-motion may also be measured with the interferometer. In addition, an interferometer may be used to measure the transient and steady-state out-of-plane response that result from the in-plane actuation inputs.

5) Out-of-plane repeatability. A laser interferometer should be used to measure the response to a repeating, calibrated, out-of-plane step input.

6) Thermal measurements. An infrared camera, or other temperature sensing instrument, should be used to measure the temperature of the stage and paddles during operation of the actuators in steady state. This data should then be contrasted with the estimated temperature rise that was calculated from the change in resistivity of the copper in the actuator coils.

## 7.2.2 Thermal Error Compensation

It may be possible to minimize the transient out-of-plane thermal error by conditioning the command signals with a high-frequency sinusoidal carrier signal. The nanopositioner will attenuate the mechanical response of a carrier signal that has a frequency that is well above the mechanical resonance. A carrier signal at 10-50kHz is sufficient for the prototype nanopositioner. The carrier signal would supply RMS power to the coils that could help to reduce the transient thermal error.

The transient thermal error could also be compensated by supplying a feed-forward actuation input to the coils that cancels the effect of the thermal transients. The thermal transients would be measured as discussed in the previous section, and the input signal to the out-of-plane actuators could then be designed to oppose the thermal transients. The steady state thermal error varies with the square of the input current and therefore it may be minimized in steady-state by way of a quadratic calibration matrix.

## 7.2.3 Capacitive Sensing

Capacitive sensing may be used to detect the motion of the sample stage in six-axis by using a combination of parallel electrodes that are fabricated to the backside of the stage and a set that are fixed to mechanical ground. Figure 7.1 shows a concept of the six-axis capacitive sensor arrangement.

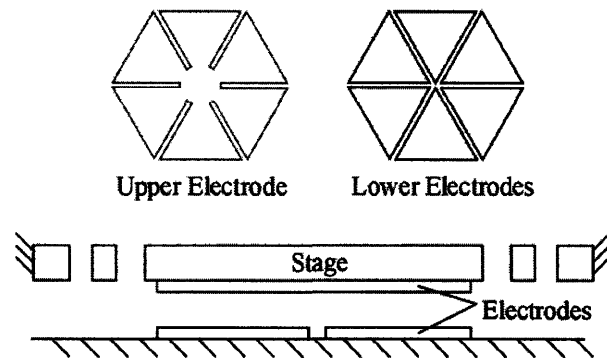


Figure 7.1. Six-axis capacitive sensing concept.

As the stage moves in six axes, the capacitance between the electrodes will change. The capacitance of a parallel plate electrode at a gap height of 10  $\mu\text{m}$  and with electrode area of approximately 1  $\text{mm}^2$  is approximately 1 pF. It may be possible to detect this magnitude of change in capacitance with a detection circuit such as the one discussed in [177]. Some of the



challenges associated with capacitive sensing in six-axis include: a) design of the electrodes to yield detectable changes in capacitance; b) sufficient signal-to-noise ratio; c) design of detection circuits to amplify the small changes in capacitance; d) integration of an electrode layer on the nanopositioner; e) assembly and alignment of a chip with the grounded sensing electrodes.

### 7.2.4 Integration into a Nanomanufacturing System

A variant of this nanopositioner will be fitted with a probe tip for integration into a high-speed, probe-based nanomanufacturing system. Integration of the tip onto the delicate flexure system presents several design challenges including:

- 1) assembly or microfabrication of a probe-tip onto the sample stage and
- 2) routing of electrical leads to the probe-tip along the flexure beams.

Figure 7.2 shows illustrations of how the meso-scale nanopositioner may be integrated into a bench-top nanomanufacturing system for operation on meso-scale and macro-scale substrates.

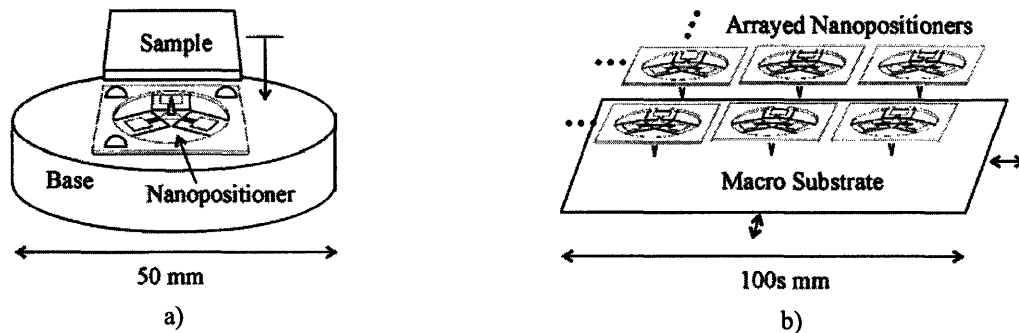


**Figure 7.2.** a) Schematic illustration of a bench-top, probe-based nanomanufacturing and metrology system; b) schematic illustration of arrayed nanomanufacturing on macro-scale substrates.

# REFERENCES

---

- [1] H. Rothuizen, U. Drechsler, G. Genolet, W. Haberle, M. Lutwyche, R. Stutz, R. Widmer, and P. Vettiger, "Fabrication of a micromachined magnetic X/Y/Z scanner for parallel scanning probe applications," *Microelectronic Engineering*, vol. 53, pp. 509-512, 2000.
- [2] K. Stoev, F. Liu, X. Shi, H. C. Tong, Y. Chen, C. Chien, Z. W. Dong, M. Gibbons, S. Funada, P. Prabhu, H. Nguyen, D. Wachenschwanz, L. Mei, M. Schultz, S. Malhotra, B. Lal, J. Kimmal, M. Russak, A. Talalai, and A. Varlahanov, "Demonstration and characterization of greater than 60 Gb/in/sup 2/ recording systems," *Eighth Joint Magnetism and Magnetic Materials Intermag Conference, 7-11 Jan. 2001*, vol. 37, pp. 1264-7, 2001.
- [3] H. Rothuizen, M. Despont, U. Drechsler, G. Genolet, W. Haberle, M. Lutwyche, R. Stutz, and P. Vettiger, "Compact copper/epoxy-based electromagnetic scanner for scanning probe applications," presented at 15th IEEE International Conference on Micro Electro Mechanical Systems MEMS 2002, Jan 20-24 2002, Las Vegas, NV, 2002.
- [4] Y. Sun, D. Piyabongkarn, A. Sezen, B. J. Nelson, and R. Rajamani, "A high-aspect-ratio two-axis electrostatic microactuator with extended travel range," *Sensors and Actuators A: Physical*, vol. 102, pp. 49-60, 2002.
- [5] E. Eleftheriou, T. Antonakopoulos, G. K. Binnig, G. Cherubini, M. Despont, A. Dholakia, U. Durig, M. A. Lantz, H. Pozidis, H. E. Rothuizen, and P. Vettiger, "Millipede - a MEMS-based scanning-probe data-storage system," *IEEE Transactions on Magnetics*, vol. 39, pp. 938-45, 2003.
- [6] A. Pantazi, M. A. Lantz, G. Cherubini, H. Pozidis, and E. Eleftheriou, "A servomechanism for a micro-electromechanical-system-based scanning-probe data storage device," *Nanotechnology*, vol. 15, pp. 612-621, 2004.
- [7] H. Pozidis, W. Haberle, D. Wiesmann, U. Drechsler, M. Despont, T. R. Albrecht, and E. Eleftheriou, "Demonstration of thermomechanical recording at 641 Gbit/in/sup 2/," *IEEE Transactions on Magnetics*, vol. 40, pp. 2531-6, 2004.
- [8] A. P. Malshe, K. Virwani, K. P. Rajurkar, and D. Deshpande, "Investigation of nanoscale electro machining (nano-EM) in dielectric oil," presented at 55th CIRP General Assembly, Antalya, Turkey, 2005.
- [9] A. A. Tseng and A. Notargiacomo, "Nanofabrication by scanning probe microscope lithography: a review," *Journal of Vacuum Science Technology B*, vol. 23, pp. 877-894, 2005.
- [10] M. L. Culpepper and G. Anderson, "Design of a low-cost nano-manipulator which utilizes a monolithic, spatial compliant mechanism," *Precision Engineering*, vol. 28, pp. 469-482, 2004.
- [11] P. Vettiger, M. Despont, U. Drechsler, U. Durig, W. Haberle, M. I. Lutwyche, H. E. Rothuizen, R. Stutz, R. Widmer, and G. K. Binnig, "'Millipede' - more than one thousand tips for future AFM data storage," *IBM Journal of Research and Development*, vol. 44, pp. 323-340, 2000.
- [12] M. Despont, J. Brugger, U. Drechsler, U. Durig, W. Haberle, M. Lutwyche, H. Rothuizen, R. Stutz, R. Widmer, G. Binnig, H. Rohrer, and P. Vettiger, "VLSI-NEMS

- chip for parallel AFM data storage," *12th IEEE International Workshop on Micro Electro Mechanical Systems (MEMS-99), Jan 17-Jan 21 1999*, vol. 80, pp. 100-107, 2000.
- [13] M. I. Lutwyche, M. Despont, U. Drechsler, U. Durig, W. Haberle, H. Rothuizen, R. Stutz, R. Widmer, G. K. Binnig, and P. Vettiger, "Highly parallel data storage system based on scanning probe arrays," *Applied Physics Letters*, vol. 77, pp. 3299-3301, 2000.
- [14] K. Salaita, Y. Wang, J. Fragala, R. A. Vega, C. Liu, and C. A. Mirkin, "Massively Parallel Dip-Pen Nanolithography with 55 000-Pen Two-Dimensional Arrays," *Angewandte Chemie*, pp. 7220-7223, 2006.
- [15] J. Guan and L. J. Lee, "Generating highly ordered DNA nanostrand arrays," *Proceedings of the National Academy of Sciences*, vol. 102, pp. 18321-18325, 2005.
- [16] D. L. Trumper, M. E. Williams, and T. H. Nguyen, "Magnet arrays for synchronous machines," presented at Proceedings of the 28th IEEE Industry Applications Conference. Part 1 (of 3), Oct 3-8 1993, Toronto, Ont, Can, 1993.
- [17] D. L. Trumper, W.-j. Kim, and M. E. Williams, "Design and analysis framework for linear permanent-magnet machines," *IEEE Transactions on Industry Applications*, vol. 32, pp. 371-379, 1996.
- [18] W.-j. Kim, "Six-axis nano-positioning with planar magnetic levitation," presented at Proceedings of the 2001 1st IEEE Conference on Nanotechnology. IEEE-NANO 2001, 28-30 Oct. 2001, Maui, HI, USA, 2001.
- [19] K.-S. Chen, D. L. Trumper, and S. T. Smith, "Design and control for an electromagnetically driven X-Y-&theta; stage," *Precision Engineering*, vol. 26, pp. 355-369, 2002.
- [20] K. S. Jung and Y. S. Baek, "Contact-free moving-magnet type of micropositioner with optimized specification," *IEEE Transactions on Magnetics*, vol. 38, pp. 1539-1548, 2002.
- [21] I. J. C. Compter, "Electro-dynamic planar motor," *Precision Engineering*, vol. 28, pp. 171-180, 2004.
- [22] S. Verma, W.-j. Kim, and J. Gu, "Six-axis nanopositioning device with precision magnetic levitation technology," *IEEE/ASME Transactions on Mechatronics*, vol. 9, pp. 384-91, 2004.
- [23] S.-Q. Lee and D.-G. Gweon, "New 3-DOF Z-tilts micropositioning system using electromagnetic actuators and air bearings," *Precision Engineering*, vol. 24, pp. 24-31, 2000.
- [24] W. Gao, S. Dejima, H. Yanai, K. Katakura, S. Kiyono, and Y. Tomita, "A surface motor-driven planar motion stage integrated with an XY-theta-Z surface encoder for precision positioning," *Precision Engineering*, vol. 28, pp. 329-337, 2004.
- [25] W. Wang and T. He, "A high precision micropositioner with five degrees of freedom based on an electromagnetic driving principle," *Review of Scientific Instruments*, vol. 67, pp. 312-17, 1996.
- [26] C.-W. Lee and S.-W. Kim, "An ultraprecision stage for alignment of wafers in advanced microlithography," *Precision Engineering*, vol. 21, pp. 113-122, 1997.
- [27] S.-S. Ku, U. Pinoson, S. Cetinkunt, and S. Nakajima, "Design, fabrication, and real-time neural network control of a three-degrees-of-freedom nanopositioner," *Mechatronics, IEEE/ASME Transactions on*, vol. 5, pp. 273-280, 2000.
- [28] C.-H. Kim, H.-M. Jeong, J.-U. Jeon, and Y.-K. Kim, "Silicon micro XY-stage with a large area shuttle and no-etching holes for SPM-based data storage," *Journal of Microelectromechanical Systems*, vol. 12, pp. 470-8, 2003.

- [29] P.-F. Indermuhle, V. P. Jaecklin, J. Brugger, C. Linder, N. F. De Rooij, and M. Binggeli, "AFM imaging with an xy-micropositioner with integrated tip," *Sensors and Actuators A: Physical*, vol. 47, pp. 562-565, 1995.
- [30] S. Hoen, Q. Bai, J. A. Harley, D. A. Horsley, F. Matta, T. Verhoeven, J. Williams, and K. R. Williams, "A high-performance dipole surface drive for large travel and force," presented at IEEE International Solid-State Sensors and Actuators Conference, 8-12 June 2003, Boston, MA, USA, 2003.
- [31] M. Agarwal, D. T. Dutton, J. A. Theil, Q. Bai, E. Par, and S. Hoen, "Characterization of a Dipole Surface Drive Actuator With Large Travel and Force," *Microelectromechanical Systems, Journal of*, vol. 15, pp. 1726-1734, 2006.
- [32] L. Fan, M. C. Wu, K. D. Choquette, and M. H. Crawford, "Self-assembled microactuated XYZ stages for optical scanning and alignment," presented at Solid State Sensors and Actuators, 1997. TRANSDUCERS '97 Chicago., 1997 International Conference on, 1997.
- [33] J.-j. Choi, H. Park, K. Y. Kim, and J. U. Jeon, "Electromagnetic Micro x-y Stage for Probe-Based Data Storage," *Journal of Semiconductor Technology and Science*, vol. 1, pp. 84-93, 2001.
- [34] M. A. Lantz, H. E. Rothuizen, U. Drechsler, W. Haberle, and M. Despont, "A vibration resistant nanopositioner for mobile parallel-probe storage applications," *Journal of Microelectromechanical Systems*, vol. 16, pp. 130-139, 2007.
- [35] S.-C. Chen and M. L. Culpepper, "Design of a six-axis micro-scale nanopositioner - uHexFlex," *Precision Engineering*, vol. 30, pp. 314-324, 2006.
- [36] J. E. Huber, N. A. Fleck, and M. F. Ashby, "The Selection of Mechanical Actuators based on Performance Indices," *Proceedings of the Royal Society of London: Mathematical, Physical, and Engineering Sciences*, vol. 453, pp. 2185-2205, 1997.
- [37] M. Zupan, M. F. Ashby, and N. A. Fleck, "Actuator classification and selection - the development of a database," *Advanced Engineering Materials*, vol. 4, pp. 933-40, 2002.
- [38] D. J. Bell, T. J. Lu, N. A. Fleck, and S. M. Spearing, "MEMS actuators and sensors: observations on their performance and selection for purpose," *Journal of Micromechanics and Microengineering*, vol. 15, pp. S153, 2005.
- [39] W. C. Tang, T. C. H. Nguyen, and R. T. Howe, "Laterally driven polysilicon resonant microstructures," presented at Proceedings of IEEE Micro Electro Mechanical Systems (MEMS '89), Salt Lake City, 1989.
- [40] J. J. Sniegowski and E. J. Garcia, "Surface-Micromachined Gear Trains Driven by an On-Chip Electrostatic Microengine," *Electron Device Letters*, vol. 17, pp. 366-368, 1996.
- [41] T. Hirano, L.-S. Fan, T. Semba, W. Y. Lee, J. Hong, S. Pattanaik, P. Webb, W.-H. Juan, and S. Chan, "Micro-actuator for tera-storage," presented at Proceedings of the 1999 12th IEEE International Conference on Micro Electro Mechanical Systems, MEMS, Jan 17-21 1999, Orlando, FL, USA, 1999.
- [42] M. S. Rodgers, S. Kota, J. Hetrick, Z. Li, B. D. Jensen, T. W. Krygowski, S. L. Miller, S. M. Barnes, and M. S. Burg, "A New Class of High Force, Low-Voltage, Compliant Actuation Systems," presented at Proceedings of the Solid State Sensor and Actuator Workshop, Hilton Head, NC, 2000.
- [43] J. D. Berger, Y. Zhang, J. D. Grade, H. Lee, S. Hrinya, and H. Jerman, "Widely tunable external cavity diode laser based on a MEMS electrostatic rotary actuator," presented at

- OFC 2001. Optical Fiber Communication Conference and Exhibition. Technical Digest, 17-22 March 2001, Anaheim, CA, USA, 2001.
- [44] W. C. Lee, Y.-H. Jin, and Y.-H. Cho, "Nonlinearly modulated digital microactuators for nano-precision digital motion generation," presented at Technical Digest. MEMS 2002 IEEE International Conference. Fifteenth IEEE International Conference on Micro Electro Mechanical Systems, 20-24 Jan. 2002, Las Vegas, NV, USA, 2002.
- [45] D. M. Tanner, J. A. Walraven, S. S. Mani, and S. E. Swanson, "Pin-joint design effect on the reliability of a polysilicon microengine," presented at 2002 IEEE International Reliability Physics Symposium Proceedings. 40th Annual, 7-11 April 2002, Dallas, TX, USA, 2002.
- [46] J. D. Grade, H. Jerman, and T. W. Kenny, "Design of Large Deflection Electrostatic Actuators," *Journal of Microelectromechanical Systems*, vol. 12, pp. 335-343, 2003.
- [47] H. Xie, Y. Pan, and G. K. Fedder, "A CMOS-MEMS Mirror With Curled-Hinge Comb Drives," *Journal of Microelectromechanical Systems*, vol. 12, pp. 450-457, 2003.
- [48] J. Branebjerg and P. Gravesen, "A new electrostatic actuator providing improved stroke length and force," presented at Micro Electro Mechanical Systems, 1992, MEMS '92, Proceedings. 'An Investigation of Micro Structures, Sensors, Actuators, Machines and Robot'. IEEE, 1992.
- [49] T. Imamura, T. Koshikawa, and M. Katayama, "Transverse mode electrostatic microactuator for MEMS-based HDD slider," presented at Proceedings of the 1995 9th Annual International Workshop on Micro Electro Mechanical Systems, Feb 11-15 1996, San Diego, CA, USA, 1996.
- [50] H. Toshiyoshi and H. Fujita, "Electrostatic Micro Torsion Mirrors for an Optical Switch Matrix," *Journal of Microelectromechanical Systems*, vol. 5, pp. 231-237, 1996.
- [51] D. A. Horsley, M. B. Cohn, A. Singh, R. Horowitz, and A. P. Pisano, "Design and fabrication of an angular microactuator for magnetic disk drives," *Microelectromechanical Systems, Journal of*, vol. 7, pp. 141-148, 1998.
- [52] E. S. Hung and S. D. Senturia, "Extending the travel range of analog-tuned electrostatic actuators," *Journal of Microelectromechanical Systems*, vol. 8, pp. 497-505, 1999.
- [53] J.-E. Wong, J. H. Lang, and M. A. Schmidt, "An electrostatically-actuated MEMS switch for power applications," presented at Micro Electro Mechanical Systems, 2000. MEMS 2000. The Thirteenth Annual International Conference on, 2000.
- [54] F. Chen, H. Xie, and G. K. Fedder, "A MEMS-Based Monolithic Electrostatic Microactuator for Ultra-Low Magnetic Disk Head Fly Height Control," *Journal of Microelectromechanical Systems*, vol. 37, pp. 1915-1918, 2001.
- [55] M. Hoffmann, D. Nusse, and E. Voges, "Electrostatic parallel-plate actuators with large deflections for use in optical moving-fibre switches," presented at 11th Micromechanics Europe Workshop, 1-3 Oct. 2000, Uppsala, Sweden, 2001.
- [56] H. Toshiyoshi, W. Piyawattanametha, C.-T. Chan, and M. C. Wu, "Linearization of electrostatically actuated surface micromachined 2-D optical scanner," *Microelectromechanical Systems, Journal of*, vol. 10, pp. 205-214, 2001.
- [57] H.-S. Lee, C. H. Leung, J. Shi, and S.-C. Chang, "Electrostatically actuated copper-blade microrelays," *Sensors and Actuators A: Physical*, vol. 100, pp. 105-113, 2002.
- [58] H. Toshiyoshi, M. Mita, and H. Fujita, "A MEMS piggyback actuator for hard-disk drives," *Microelectromechanical Systems, Journal of*, vol. 11, pp. 648-654, 2002.

- [59] E. R. Deutsch, J. P. Bardhan, S. D. Senturia, G. B. Hocker, D. W. Youngner, M. B. Sinclair, and M. A. Butler, "A Large-Travel Vertical Planar Actuator with Improved Stability," presented at Transducers '03 -12th International Conference on Solid State Sensors, Actuators, Microsystems, Boston, MA, 2003.
- [60] D. S. Greywall, P. A. Busch, F. Pardo, D. W. Carr, G. Bogart, and H. T. Soh, "Crystalline Silicon Tilting Mirrors for Optical Cross-Connect Switches," *Journal of Microelectromechanical Systems*, vol. 12, pp. 708-712, 2003.
- [61] M. V. Shutov, D. L. Howard, E. E. Sandoz, R. L. Smith, and S. D. Collins, "Electrostatic Actuators with Long Range Translation," presented at Transducers '03 -12th International Conference on Solid State Sensors, Actuators, Microsystems, Boston, MA, 2003.
- [62] C. S. B. Lee, S. Han, and N. C. MacDonald, "Single crystal silicon (SCS) XY-stage fabricated by DRIE and IR alignment," presented at Micro Electro Mechanical Systems, 2000. MEMS 2000. The Thirteenth Annual International Conference on, 2000.
- [63] D. Hah, C.-A. Choi, C.-K. Kim, and C.-H. Jun, "A self-aligned vertical comb-drive actuator on an SOI wafer for a 2D scanning micromirror," *Journal of Micromechanics and Microengineering*, vol. 14, pp. 1148-56, 2004.
- [64] D. Hah, S. T.-Y. Huang, J.-C. Tsai, H. Toshiyoshi, and M. C. Wu, "Low-voltage, large-scan angle MEMS analog micromirror arrays with hidden vertical comb-drive actuators," *Journal of Microelectromechanical Systems*, vol. 13, pp. 279-89, 2004.
- [65] R. Yeh, S. Hollar, and K. S. J. Pister, "Single mask, large force, and large displacement electrostatic linear inchworm motors," *Journal of Microelectromechanical Systems*, vol. 11, pp. 330-336, 2002.
- [66] R. Legtenberg, J. Gilbert, S. D. Senturia, and M. Elwenspoek, "Electrostatic curved electrode actuators," *Microelectromechanical Systems, Journal of*, vol. 6, pp. 257-265, 1997.
- [67] J. Li, M. P. Brenner, J. H. Lang, A. H. Slocum, and R. Struempfer, "DRIE-fabricated curved-electrode zipping actuators with low pull-in voltage," presented at Transducers '03 - IEEE International Solid-State Sensors and Actuators Conference, 8-12 June 2003, Boston, MA, USA, 2003.
- [68] J. Li, M. P. Brenner, T. Christen, M. S. Kotilainen, J. H. Lang, and A. H. Slocum, "Deep-reactive ion-etched compliant starting zone electrostatic zipping actuators," *Microelectromechanical Systems, Journal of*, vol. 14, pp. 1283-1297, 2005.
- [69] M. Baltzer, T. Kraus, and E. Obermeier, "A linear stepping actuator in surface micromachining technology for low voltages and large displacements," presented at Solid State Sensors and Actuators, 1997. TRANSDUCERS '97 Chicago., 1997 International Conference on, 1997.
- [70] B. Wagner, M. Kreutzer, and W. Benecke, "Electromagnetic microactuators with multiple degrees of freedom," presented at TRANSDUCERS '91. 1991 International Conference on Solid-State Sensors and Actuators. Digest of Technical Papers (Cat. No.91CH2817-5), 24-27 June 1991, San Francisco, CA, USA, 1991.
- [71] B. Wagner and W. Benecke, "Microfabricated actuator with moving permanent magnet," presented at Proceedings of the 1991 IEEE Micro Electro Mechanical Systems - MEMS '91, Jan 30-Feb 2 1991, Nara, Jpn, 1991.
- [72] O. Cugat, J. Delamare, and G. Reyne, "Magnetic Micro-Actuators and Systems (MAGMAS)," *IEEE Transactions on Magnetics*, vol. 39, pp. 3607-3612, 2003.

- [73] D. Niarchos, "Magnetic MEMS: key issues and some applications," *Sensors and Actuators A: Physical*, vol. 109, pp. 166-173, 2003.
- [74] D.-W. Lee, T. Ono, and M. Esashi, "High-speed imaging by electro-magnetically actuated probe with dual spring," *Journal of Microelectromechanical Systems*, vol. 9, pp. 419-24, 2000.
- [75] K. H. Kim, H. J. Yoon, O. C. Jeong, and S. S. Yang, "Fabrication and test of a micro electromagnetic actuator," *Sensors and Actuators A: Physical*, vol. 117, pp. 8-16, 2005.
- [76] J. W. Judy and R. S. Muller, "Magnetically actuated, addressable microstructures," *Journal of Microelectromechanical Systems*, vol. 6, pp. 249-56, 1997.
- [77] L. O. S. Ferreira and S. Moehlecke, "Silicon micromechanical galvanometric scanner," *Sensors and Actuators, A: Physical*, vol. 73, pp. 252-260, 1999.
- [78] N. Asada, M. Takeuchi, V. Vaganov, N. Belov, S. i. t. Hout, and I. Sluchak, "Silicon micro-optical scanner," *Sensors and Actuators A: Physical*, vol. 83, pp. 284-290, 2000.
- [79] J. S. Han, J. S. Ko, Y. T. Kim, and B. M. Kwak, "Parametric study and optimization of a micro-optical switch with a laterally driven electromagnetic microactuator," *Journal of Micromechanics and Microengineering*, vol. 12, pp. 939-47, 2002.
- [80] J. S. Ko, M. L. Lee, D.-S. Lee, C. A. Choi, and Y. T. Kim, "Development and application of a laterally driven electromagnetic microactuator," *Applied Physics Letters*, vol. 81, pp. 547-9, 2002.
- [81] H. J. Cho and C. H. Ahn, "Magnetically-driven bi-directional optical microscanner," *Journal of Micromechanics and Microengineering*, vol. 13, pp. 383-389, 2003.
- [82] H. Miyajima, N. Asaoka, T. Isokawa, M. Ogata, Y. Aoki, M. Imai, O. Fujimori, M. Katashiro, and K. Matsumoto, "A MEMS Electromagnetic Optical Scanner for a Commercial Confocal Laser Scanning Microscope," *Journal of Microelectromechanical Systems*, vol. 12, pp. 243-251, 2003.
- [83] S.-H. Ahn and Y.-K. Kim, "Silicon scanning mirror of two DOF with compensation current routing," *Journal of Micromechanics and Microengineering*, vol. 14, pp. 1455-1461, 2004.
- [84] J. J. Bernstein, W. P. Taylor, J. D. Brazzle, C. J. Corcoran, G. Kirkos, J. E. Odhner, A. Pareek, M. Waelti, and M. Zai, "Electromagnetically actuated mirror arrays for use in 3-D optical switching applications," *Journal of Microelectromechanical Systems*, vol. 13, pp. 526-535, 2004.
- [85] J. S. Han, J. S. Ko, and J. G. Korvink, "Structural optimization of a large-displacement electromagnetic Lorentz force microactuator for optical switching applications," *Journal of Micromechanics and Microengineering*, vol. 14, pp. 1585-1596, 2004.
- [86] W. P. Taylor, J. D. Brazzle, A. B. Osenar, C. J. Corcoran, I. H. Jafri, D. Keating, G. Kirkos, M. Lockwood, A. Pareek, and J. J. Bernstein, "A high fill factor linear mirror array for a wavelength selective switch," *Journal of Micromechanics and Microengineering*, vol. 14, pp. 147-152, 2004.
- [87] D. A. Horsley, W. O. Davis, K. J. Hogan, M. R. Hart, E. C. Ying, M. Chaparala, B. Behin, M. J. Daneman, and M.-H. Kiang, "Optical and mechanical performance of a novel magnetically actuated MEMS-based optical switch," *Journal of Microelectromechanical Systems*, vol. 14, pp. 274-284, 2005.
- [88] Z. Huang and J. Shen, "Latching micromagnetic optical switch," *Microelectromechanical Systems, Journal of*, vol. 15, pp. 16-23, 2006.

- [89] L. C. M. Oliveira, P. R. Barbaroto, L. O. S. Ferreira, and I. Doi, "A novel Si micromachined moving-coil induction actuated mm-sized resonant scanner," *Journal of Micromechanics and Microengineering*, vol. 16, pp. 165-72, 2006.
- [90] A. D. Yalcinkaya, H. Urey, D. Brown, T. Montague, and R. Sprague, "Two-axis electromagnetic microscanner for high resolution displays," *Microelectromechanical Systems, Journal of*, vol. 15, pp. 786-794, 2006.
- [91] A. D. Yalcinkaya, H. Urey, and S. Holmstrom, "NiFe Plated Biaxial MEMS Scanner for 2-D Imaging," *Photonics Technology Letters, IEEE*, vol. 19, pp. 330-332, 2007.
- [92] B. Rogge, J. Schulz, J. Mohr, A. Thommes, and W. Menz, "Fully batch fabricated magnetic microactuators using a two layer LIGA process," presented at Proceedings of the International Solid-State Sensors and Actuators Conference - TRANSDUCERS '95, 25-29 June 1995, Stockholm, Sweden, 1995.
- [93] H. Ren and E. Gerhard, "Design and fabrication of a current-pulse-excited bistable magnetic microactuator," *Sensors and Actuators, A: Physical*, vol. 58, pp. 259-264, 1997.
- [94] J. A. Wright, Y.-C. Tai, and S.-C. Chang, "A large-force, fully-integrated MEMS magnetic actuator," presented at Proceedings of International Solid State Sensors and Actuators Conference (Transducers '97), 16-19 June 1997, Chicago, IL, USA, 1997.
- [95] E. Fullin, J. Gobet, H. A. C. Tilmans, and J. Bergqvist, "A new basic technology for magnetic micro-actuators," presented at Proceedings IEEE Eleventh Annual International Workshop on Micro Electro Mechanical Systems An Investigation of Micro Structures, Sensors, Actuators, Machines and Systems, 25-29 Jan. 1998, Heidelberg, Germany, 1998.
- [96] W. P. Taylor, O. Brand, and M. G. Allen, "Fully integrated magnetically actuated micromachined relays," *Journal of Microelectromechanical Systems*, vol. 7, pp. 181-91, 1998.
- [97] H. A. C. Tilmans, E. Fullin, H. Ziad, M. D. J. Van de Peer, J. Kesters, E. Van Geffen, J. Bergqvist, M. Pantus, E. Beyne, K. Baert, and F. Naso, "Fully-packaged electromagnetic microrelay," presented at Proceedings of the 1999 12th IEEE International Conference on Micro Electro Mechanical Systems, MEMS, Jan 17-21 1999, Orlando, FL, USA, 1999.
- [98] J. A. Wright and Y.-C. Tai, "Magnetostatic MEMS relays for the miniaturization of brushless DC motor controllers," presented at Proceedings of 12th International Workshop on Micro Electro Mechanical Systems - MEMS, 17-21 Jan. 1999, Orlando, FL, USA, 1999.
- [99] G. D. Gray, Jr. and P. A. Kohl, "Magnetically bistable actuator: Part 1. Ultra-low switching energy and modeling," *Sensors and Actuators A: Physical*, vol. 119, pp. 489-501, 2005.
- [100] G. D. Gray, Jr., E. M. Prophet, L. Zhu, and P. A. Kohl, "Magnetically bistable actuator: Part 2. Fabrication and performance," *Sensors and Actuators, A: Physical*, vol. 119, pp. 502-511, 2005.
- [101] H. Koser, F. Cros, M. G. Allen, and J. H. Lang, "A high torque density MEMS magnetic induction machine," presented at Proceedings of 11th International Conference on Solid State Sensors and Actuators Transducers '01/Eurosensors XV, 10-14 June 2001, Munich, Germany, 2001.
- [102] N. Achotte, P. A. Gilles, O. Cugat, J. Delamare, P. Gaud, and C. Dieppedale, "Planar brushless magnetic micromotors," *Microelectromechanical Systems, Journal of*, vol. 15, pp. 1001-1014, 2006.



- [103] D. P. Arnold, S. Das, F. Cros, I. Zana, M. G. Allen, and J. H. Lang, "Magnetic induction machines integrated into bulk-micromachined silicon," *Microelectromechanical Systems, Journal of*, vol. 15, pp. 406-414, 2006.
- [104] D. P. Arnold, S. Das, J. W. Park, I. Zana, J. H. Lang, and M. G. Allen, "Microfabricated High-Speed Axial-Flux Multiwatt Permanent-Magnet Generators: Part II: Design, Fabrication, and Testing," *Microelectromechanical Systems, Journal of*, vol. 15, pp. 1351-1363, 2006.
- [105] F. Cros, H. Koser, M. G. Allen, and J. H. Lang, "Magnetic induction micromachine-part II: fabrication and testing," *Microelectromechanical Systems, Journal of*, vol. 15, pp. 427-439, 2006.
- [106] S. Das, D. P. Arnold, I. Zana, J. W. Park, M. G. Allen, and J. H. L. Lang, "Microfabricated High-Speed Axial-Flux Multiwatt Permanent-Magnet Generators: Part I: Modeling," *Microelectromechanical Systems, Journal of*, vol. 15, pp. 1330-1350, 2006.
- [107] H. Koser and J. H. Lang, "Magnetic induction micromachine-part I: Design and analysis," *Microelectromechanical Systems, Journal of*, vol. 15, pp. 415-426, 2006.
- [108] H. J. Cho and C. H. Ahn, "Microscale resin-bonded permanent magnets for magnetic micro-electro-mechanical systems applications," *Journal of Applied Physics*, vol. 93, pp. 8674-6, 2003.
- [109] S. Guan and B. J. Nelson, "Magnetic composite electrodeposition of micro-array magnets for MEMS actuators," presented at 17th IEEE International Conference on Micro Electro Mechanical Systems. Maastricht MEMS 2004 Technical Digest, 25-29 Jan. 2004, Maastricht, Netherlands, 2004.
- [110] B. Pawlowski and J. Topfer, "Permanent magnetic NdFeB thick films," *Journal of Materials Science*, vol. 39, pp. 1321-1324, 2004.
- [111] Y. Sverdlov, Y. Rosenberg, Y. I. Rozenberg, R. Zmood, R. Erlich, S. Natan, and Y. Shacham-Diamand, "The electrodeposition of cobalt-nickel-iron high aspect ratio thick film structures for magnetic MEMS applications," presented at European Workshop on Materials for Advanced Metallization 2004, 7-10 March 2004, Brussels, Belgium, 2004.
- [112] M. Bedenbecker, R. Bandorf, H. Luethje, G. Braeuer, and H. H. Gatzel, "Development and fabrication of magnetic thin films," *Microsystem Technologies*, vol. 12, pp. 655-658, 2006.
- [113] M. Bedenbecker and H. H. Gatzel, "Electroplated CoFe thin films for electromagnetic microactuators," in *50th Annual Conference on Magnetism and Magnetic Materials*, vol. 99, 8 ed. San Jose, California (USA): AIP, 2006, pp. 08M308-3.
- [114] Y. I. Rozenberg, Y. Rosenberg, V. Krylov, G. Belitsky, and Y. Shacham-Diamand, "Resin-bonded permanent magnetic films with out-of-plane magnetization for MEMS applications," *Journal of Magnetism and Magnetic Materials*, vol. 305, pp. 357-360, 2006.
- [115] H. Guckel, T. Earles, J. Klein, J. D. Zook, and T. Ohnstein, "Electromagnetic linear actuators with inductive position sensing," presented at International Solid-State Sensors and Actuators Conference - TRANSDUCERS '95, 25-29 June 1995, Stockholm, Sweden, 1996.
- [116] K. Fischer and H. Guckel, "Long throw linear magnetic actuators stackable to one millimeter of structural height," *Microsystem Technologies*, vol. 4, pp. 180-3, 1998.

- [117] D. J. Sadler, T. M. Liakopoulos, and C. H. Ahn, "Universal electromagnetic microactuator using magnetic interconnection concepts," *Journal of Microelectromechanical Systems*, vol. 9, pp. 460-468, 2000.
- [118] H. J. Cho and C. H. Ahn, "A bidirectional magnetic microactuator using electroplated permanent magnet arrays," *Journal of Microelectromechanical Systems*, vol. 11, pp. 78-84, 2002.
- [119] J. Rehder, P. Rombach, and O. Hansen, "Magnetic flux generator for balanced membrane loudspeaker," *Proceedings of 11th International Conference on Solid State Sensors and Actuators Transducers '01/Euroensors XV, 10-14 June 2001*, vol. A97-98, pp. 61-7, 2002.
- [120] H. Lehr, W. Ehrfeld, M. Schmidt, E. Kallenbach, and H. A. Tuan, "Application of the LIGA technique for the development of microactuators based on electromagnetic principles," *Journal of Micromechanics and Microengineering*, vol. 2, pp. 229-33, 1992.
- [121] M. Fohse, T. Kohlmeier, and H. H. Gatzen, "Thin film technologies to fabricate a linear microactuator," *Proceedings of 3rd European Conference on Magnetic Sensors and Actuators. EMSA 2000, 19-21 July 2000*, vol. A91, pp. 145-9, 2001.
- [122] M. Feldmann and S. Bttgenbach, "Linear Variable Reluctance (VR) Micro Motors With Compensated Attraction Force: Concept, Simulation, Fabrication and Test," *Magnetics, IEEE Transactions on*, vol. 43, pp. 2567-2569, 2007.
- [123] H. Miyajima, N. Asaoka, M. Arima, Y. Minamoto, K. Murakami, K. Tokuda, and K. Matsumoto, "A durable, shock-resistant electromagnetic optical scanner with polyimide-based hinges," *Journal of Microelectromechanical Systems*, vol. 10, pp. 418-424, 2001.
- [124] M. V. Shutov, E. E. Sandoz, D. L. Howard, T. C. Hsia, R. L. Smith, and S. D. Collins, "A microfabricated electromagnetic linear synchronous motor," *Sensors and Actuators, A: Physical*, vol. 121, pp. 566-575, 2005.
- [125] M. Fohse, J. Edler, H.-D. Stolting, and H. H. Gatzen, "A batch fabricated linear synchronous motor," presented at 2003 ASME International Mechanical Engineering Congress, Nov 15-21 2003, Washington, DC, United States, 2003.
- [126] W.-H. Chu, M. Mehregany, and R. L. Mullen, "Analysis of tip deflection and force of a bimetallic cantilever microactuator," *Journal of Micromechanics and Microengineering*, vol. 3, pp. 4, 1993.
- [127] J. H. Comtois and V. M. Bright, "Applications for surface-micromachined polysilicon thermal actuators and arrays," *Sensors and Actuators A: Physical*, vol. 58, pp. 19-25, 1997.
- [128] J.-S. Park, L. L. Chu, A. D. Oliver, and Y. B. Gianchandani, "Bent-Beam Electrothermal Actuators—Part II: Linear and Rotary Microengines," *Journal of Microelectromechanical Systems*, vol. 10, pp. 255-262, 2001.
- [129] L. Que, J.-S. Park, and Y. B. Gianchandani, "Bent-Beam Electrothermal Actuators—Part I: Single Beam and Cascaded Devices," *Journal of Microelectromechanical Systems*, vol. 10, pp. 247-254, 2001.
- [130] D. Yan, A. Khajepour, and R. Mansour, "Design and modeling of a MEMS bidirectional vertical thermal actuator," *Journal of Micromechanics and Microengineering*, vol. 14, pp. 841-850, 2004.
- [131] J. Qui, J. H. Lang, A. H. Slocum, and R. Strumpler, "A high-current electrothermal bistable MEMS relay," presented at Micro Electro Mechanical Systems, 2003. MEMS-03 Kyoto. IEEE The Sixteenth Annual International Conference on, 2003.

- [132] A. Jain and H. Xie, "A single-crystal silicon micromirror for large bi-directional 2D scanning applications," *Sensors and Actuators A: Physical*, vol. 130-131, pp. 454-460, 2006.
- [133] P. Muralt, "Ferroelectric thin films for micro-sensors and actuators: a review," *Journal of Micromechanics and Microengineering*, vol. 10, pp. 136, 2000.
- [134] P. Luginbuhl, G.-A. Racine, P. Lerch, B. Romanowicz, K. G. Brooks, N. F. de Rooij, P. Renaud, and N. Setter, "Piezoelectric cantilever beams actuated by PZT sol-gel thin film," presented at International Solid-State Sensors and Actuators Conference - TRANSDUCERS '95, 25-29 June 1995, Stockholm, Sweden, 1996.
- [135] D. L. DeVoe and A. P. Pisano, "Modeling and Optimal Design of Piezoelectric Cantilever Microactuators," *Journal of Microelectromechanical Systems*, vol. 6, pp. 266-270, 1997.
- [136] M. S. Weinberg, "Working Equations for Piezoelectric Actuators and Sensors," *Journal of Microelectromechanical Systems*, vol. 8, pp. 529-533, 1999.
- [137] J. Ahn, S. Jun, D. Kim, G. Y. Yeom, J. B. Yoo, J. Lee, and T. Sands, "Fabrication of piezoelectrically driven micro-cantilever using Pb(Zr, Ti)O<sub>3</sub> films," presented at Proceedings of the 2000 12th IEEE International Symposium on Applications of Ferroelectrics, 2000.
- [138] W. P. Robbins, D. L. Polla, T. Tamagawa, D. E. Glumac, and W. Tjhen, "Design of Linear-Motion Microactuators using Piezoelectric Thin Films," *Journal of Micromechanics and Microengineering*, vol. 1, pp. 247-252, 1991.
- [139] M.-A. Dubois and P. Muralt, "PZT Thin Film Actuated Elastic Fin Micromotor," *IEEE Transactions on Ultrasonics, Ferroelectrics, and Frequency Control*, vol. 45, 1998.
- [140] Y. Yee, H.-J. Nam, S.-H. Lee, J. U. Bu, and J.-W. Lee, "PZT actuated micromirror for fine-tracking mechanism of high-density optical data storage," *Sensors and Actuators A (Physical)*, vol. A89, pp. 166-73, 2001.
- [141] J. Tsaour, L. Zhang, R. Maeda, and S. Matsumoto, "2D Micro Scanner Actuated by Sol-gel Derived Double Layered PZT," presented at Proceedings of the 15th IEEE International Conference on MEMS, 2002.
- [142] C. W. Wong, Y. Jeon, G. Barbastathis, and S.-G. Kim, "Analog tunable gratings driven by thin-film piezoelectric microelectromechanical actuators," *Applied Optics*, vol. 42, pp. 621-626, 2003.
- [143] N. J. Conway and S.-G. Kim, "Large-Strain, Piezoelectric, In-Plane Micro-Actuator," presented at Proceedings of the 17th International Conference on MEMS, Amsterdam, 2004.
- [144] A. Feustel, O. Krusemark, and J. Muller, "Numerical simulation and optimization of planar electromagnetic actuators," *Sensors and Actuators A: Physical*, vol. 70, pp. 276-282, 1998.
- [145] A. Kruusing, "Actuators with permanent magnets having variable in space orientation of magnetization," *Sensors and Actuators A: Physical*, vol. 101, pp. 168-174, 2002.
- [146] M. Lutwyche, U. Dreschler, W. Haberle, H. Rothuizen, R. Widmer, P. Vettiger, and J. Thaysen, "Planar micromagnetic x/y/z scanner with five degrees of freedom," presented at Proceedings of the 194th Meeting of the Electrochemical Society, Boston, 1998.
- [147] S. T. Smith and X. Liu, "A profilometer for surface proximity probe applications," *Nanotechnology*, pp. 37, 1992.

- [148] J. W. Ryu, D.-G. Gweon, and K. S. Moon, "Optimal design of a flexure hinge based XY[phi] wafer stage," *Precision Engineering*, vol. 21, pp. 18-28, 1997.
- [149] B. J. Choi, S. V. Sreenivasan, S. Johnson, M. Colburn, and C. G. Wilson, "Design of orientation stages for step and flash imprint lithography," *Precision Engineering*, vol. 25, pp. 192-199, 2001.
- [150] P. Gao and S.-M. Swei, "A six-degree-of-freedom micro-manipulator based on piezoelectric translators," *Nanotechnology*, pp. 447, 1999.
- [151] J. E. McInroy and J. C. Hamann, "Design and control of flexure jointed hexapods," *IEEE Transactions on Robotics and Automation*, vol. 16, pp. 372-81, 2000.
- [152] B. Jokiel, B. L. Benavides, L. F. Bieg, and J. J. Allen, "Planar and spatial three-degree-of-freedom micro-stages in silicon MEMS," presented at 2001 Annual Meeting of the American Society for Precision Engineering, Crystal City, VA, 2001.
- [153] K. Halbach, "Design of permanent multipole magnets with oriented rare earth cobalt material," *Nuclear Instruments and Methods*, vol. 169, pp. 1-10, 1980.
- [154] D. Golda and M. L. Culpepper, "Two-axis electromagnetic moving-coil micro-actuator," presented at 2006 ASME International Mechanical Engineering Conference and Exposition, Chicago, Illinois, 2006.
- [155] D. Golda and M. L. Culpepper, "A scalable six-axis electromagnetically-driven nanopositioner for nanomanufacturing," presented at 21st Annual Meeting of the American Society of Precision Engineers, Monterey, CA, 2006.
- [156] D. Golda and M. L. Culpepper, "Modeling 3D magnetic fields for precision magnetic actuators that use non-periodic magnet arrays," *Precision Engineering*, accepted for publication August 2007.
- [157] S.-M. Jang and S.-H. Lee, "Comparison of two types of PM linear synchronous servo and miniature motor with air-cored film coil," *IEEE Transactions on Magnetics*, vol. 38, pp. 3264-6, 2002.
- [158] Z. Q. Zhu and D. Howe, "Halbach permanent magnet machines and applications: a review," *IEE Proceedings-Electric Power Applications*, vol. 148, pp. 299-308, 2001.
- [159] M. G. Lee and D.-G. Gweon, "Optimal design of a double-sided linear motor with a multi-segmented trapezoidal magnet array for a high precision positioning system," *Journal of Magnetism and Magnetic Materials*, vol. 281, pp. 336-346, 2004.
- [160] J. Cao, Y. Zhu, J. Wang, W. Yin, and G. Duan, "Analysis and comparison of two-dimensional permanent-magnet arrays for planar motor," *IEEE Transactions on Magnetics*, vol. 40, pp. 3490-4, 2004.
- [161] J. Cao, Y. Zhu, J. Wang, W. Yin, and G. Duan, "A novel synchronous permanent magnet planar motor and its model for control applications," *IEEE Transactions on Magnetics*, vol. 41, pp. 2156-63, 2005.
- [162] M. A. da Silveira, A. F. F. Filho, and R. P. Homrich, "Evaluation of the normal force of a planar actuator," *Magnetics, IEEE Transactions on*, vol. 41, pp. 4006-4008, 2005.
- [163] H.-S. Cho, C.-H. Im, and H.-K. Jung, "Magnetic field analysis of 2-D permanent magnet array for planar motor," *Magnetics, IEEE Transactions on*, vol. 37, pp. 3762-3766, 2001.
- [164] W. P. Taylor, J. J. Bernstein, J. D. Brazzle, and C. J. Corcoran, "Magnet arrays for use in a 3-D MEMS mirror array for optical switching," *IEEE Transactions on Magnetics*, vol. 39, pp. 3286-3288, 2003.
- [165] G. Akoun and J.-P. Yonnet, "3D analytical calculation of the forces exerted between two cuboidal magnets," *IEEE Transactions on Magnetics*, vol. MAG-20, pp. 1962-4, 1984.

- [166] J. C. Compter, E. A. Lomonova, and J. Makarovic, "Direct 3-D method for performance prediction of a linear moving coil actuator with various topologies," *IEE Proceedings: Science, Measurement and Technology*, vol. 150, pp. 183-191, 2003.
- [167] H. A. Haus and J. R. Melcher, *Electromagnetic Fields and Energy*. Englewood Cliffs, NJ: Prentice-Hall, 1989.
- [168] M. Zahn, *Electromagnetic Field Theory: A Problem Solving Approach*, 3 ed: Wiley and Sons, 2003.
- [169] W. H. Press, S. A. Teukolsky, W. T. Vetterling, and B. P. Flannery, *Numerical Recipes in C*, 2nd ed. New York: Cambridge University Press, 1992.
- [170] W. G. Hurley and M. C. Duffy, "Calculation of self and mutual impedances in planar magnetic structures," *IEEE Transactions on Magnetics*, vol. 31, pp. 2416-2422, 1995.
- [171] J. M. Gere and S. P. Timoshenko, *Mechanics of Materials*, 4th ed. Boston: PWS Publishing Company, 1997.
- [172] S. H. Crandall, D. C. Karnopp, J. E. F. Kurtz, and D. C. Pridmore-Brown, *Dyanmics of Mechanical and Electromechanical Systems*: Krieger, 1982.
- [173] F. P. Incropera and D. P. DeWitt, *Introduction to Heat Transfer*, 3rd ed. New York: John Wiley and Sons, 1996.
- [174] Y.-K. Yoon and M. G. Allen, "Embedded conductor technology for micromachined RF elements," *Journal of Micromechanics and Microengineering*, vol. 15, pp. 1317, 2005.
- [175] T. Pan, A. Baldi, E. Davies-Venn, R. F. Drayton, and B. Ziaie, "Fabrication and modeling of silicon-embedded high-Q inductors," *Journal of Micromechanics and Microengineering*, vol. 15, pp. 849-54, 2005.
- [176] M. J. Madou, *Fundamentals of Microfabrication: The Science of Miniaturization*, 2nd ed. New York: CRC Press, 2002.
- [177] S. D. Senturia, *Microsystem Design*, 3 ed: Kluwer, 2001.
- [178] "6.777 MEMS Material Properties Webpage - <http://web.mit.edu/6.777/www/matprops/matprops.htm>."
- [179] C. H. Ahn and M. G. Allen, "A fully integrated surface micromachined magnetic microactuator with a multilevel meander magnetic core," *Journal of Microelectromechanical Systems*, vol. 2, pp. 15-22, 1993.
- [180] C. H. Ahn and M. G. Allen, "A planar micromachined spiral inductor for integrated magnetic microactuator applications," *Journal of Micromechanics and Microengineering*, vol. 3, pp. 37-44, 1993.
- [181] C. H. Ahn and M. G. Allen, "A new toroidal-meander type integrated inductor with a multilevel meander magnetic core," *IEEE Transactions on Magnetics*, vol. 30, pp. 73-79, 1994.
- [182] M. Rais-Zadeh and F. Ayazi, "Characterization of high-Q spiral inductors on thick insulator-on-silicon," *Journal of Micromechanics and Microengineering*, vol. 15, pp. 2105-12, 2005.
- [183] M. Brunet, T. O'Donnell, J. O'Brien, P. McCloskey, and S. C. O. Mathuna, "Thick photoresist development for fabrication of high aspect ratio magnetic coils," *Journal of Micromechanics and Microengineering*, vol. 12, pp. 444-449, 2002.
- [184] P. C. Andricacos, C. Uzoh, J. O. Dukovic, J. Horkans, and H. Deligianni, "Damascene copper electroplating for chip interconnections," *IBM Journal of Research and Development*, vol. 42, pp. 567-574, 1998.

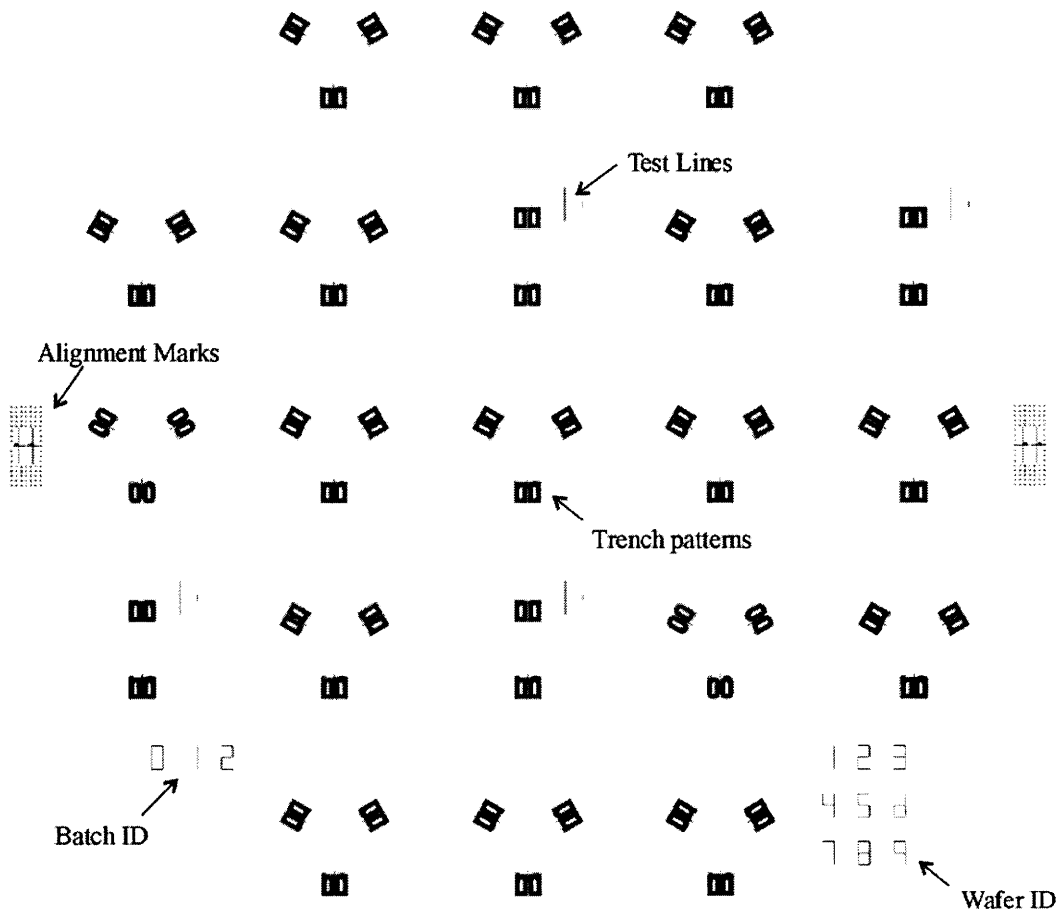
- [185] J. Phinney, J. H. Lang, and D. J. Perreault, "Multi-resonant microfabricated inductors and transformers," presented at Power Electronics Specialists Conference, 2004. PESC 04. 2004 IEEE 35th Annual, 2004.
- [186] K. R. Williams, K. Gupta, and M. Wasilik, "Etch rates for micromachining processing- Part II," *Microelectromechanical Systems, Journal of*, vol. 12, pp. 761-778, 2003.
- [187] J.-M. Quemper, E. Dufour-Gergam, N. g. Frantz-Rodriguez, J.-P. Gilles, J.-P. Grandchamp, and A. Bosseboeuf, "Effects of direct and pulse current on copper electrodeposition through photoresist molds," *Journal of Micromechanics and Microengineering*, vol. 10, pp. 116, 2000.
- [188] B. Q. Wu, Z. Liu, A. Keigler, and J. Harrell, "Diffusion Boundary Layer Studies in an Industrial Wafer Plating Cell," *Journal of The Electrochemical Society*, vol. 152, pp. C272-C276, 2005.
- [189] K. Kondo, T. Yonezawa, D. Mikami, T. Okubo, Y. Taguchi, K. Takahashi, and D. P. Barkey, "High-Aspect-Ratio Copper-Via-Filling for Three-Dimensional Chip Stacking," *Journal of The Electrochemical Society*, vol. 152, pp. H173-H177, 2005.
- [190] J.-J. Sun, K. Kondo, T. Okamura, S. Oh, M. Tomisaka, H. Yonemura, M. Hoshino, and K. Takahashi, "High-Aspect-Ratio Copper Via Filling Used for Three-Dimensional Chip Stacking," *Journal of The Electrochemical Society*, vol. 150, pp. G355-G358, 2003.
- [191] A. C. West, C.-C. Cheng, and B. C. Baker, "Pulse reverse copper electrodeposition in high aspect ratio trenches and vias," *Journal of the Electrochemical Society*, vol. 145, pp. 3070-4, 1998.
- [192] S. A. Campbell, *The Science and Engineering of Microelectronic Fabrication*, 2nd ed. New York: Oxford University Press, 2004.
- [193] K.-S. Kim, Y.-C. Joo, K.-B. Kim, and J.-Y. Kwon, "Extraction of Cu diffusivities in dielectric materials by numerical calculation and capacitance-voltage measurement," *Journal of Applied Physics*, vol. 100, pp. 063517-6, 2006.
- [194] J. D. McBrayer, R. M. Swanson, and T. W. Sigmon, "Diffusion of Metals in Silicon Dioxide," *Journal of The Electrochemical Society*, vol. 133, pp. 1242-1246, 1986.
- [195] J. P. Schaffer, A. Saxena, S. D. Antolovich, T. H. S. Jr., and S. B. Warner, *The Science and Design of Engineering Materials*, 2nd ed. Boston: McGraw-Hill, 1999.

# A

## PHOTOMASKS

### A.1 Mask 1 – Trenches for Buried Copper Coils

Dark field 5" mask (data clear). Minimum feature size is 30  $\mu\text{m}$ .

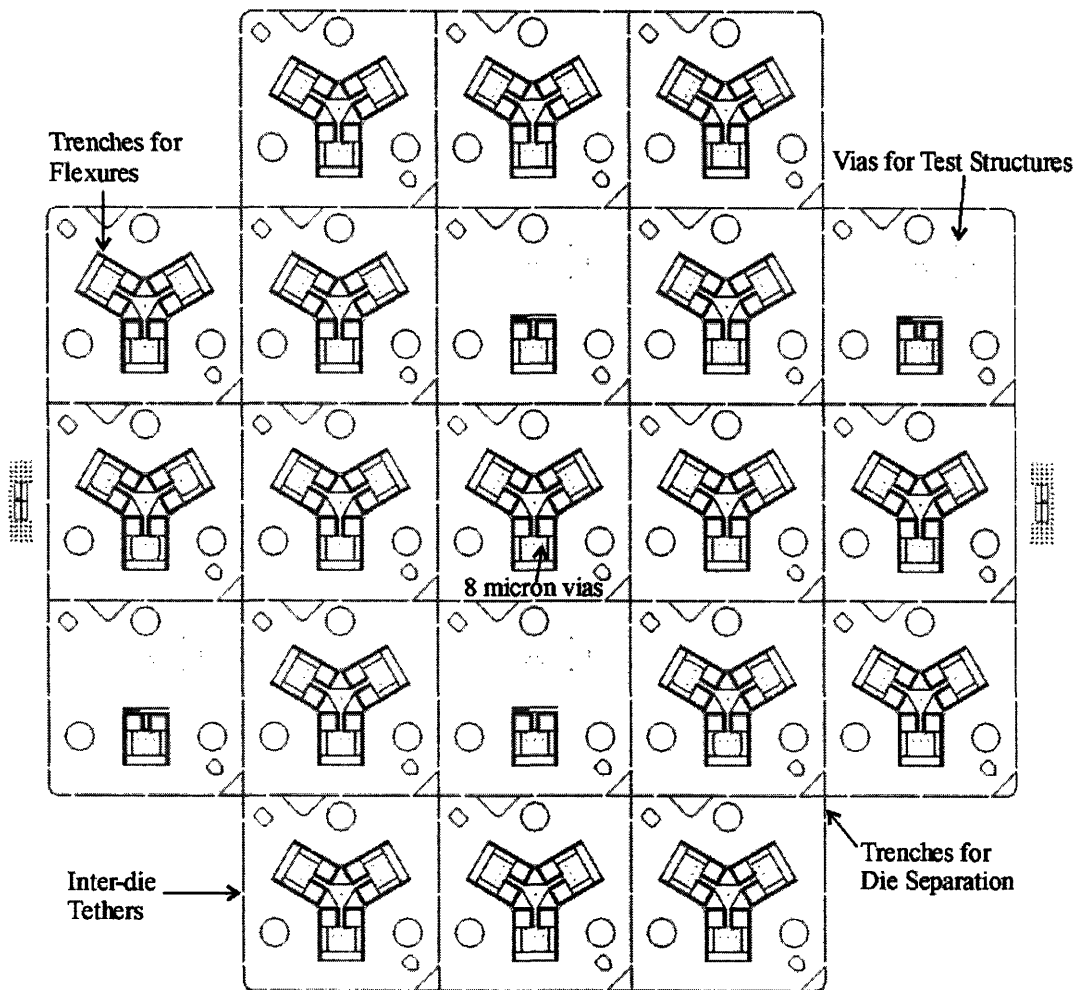


All patterns on this mask have 30  $\mu\text{m}$  line widths. The coil winding spacing is 10  $\mu\text{m}$  (40  $\mu\text{m}$  winding pitch).

Masks 1 – 3 were produced at Advanced Reproductions in North Andover Massachusetts with 0.5  $\mu\text{m}$  resolution. Mask 4 was produced at the MTL using the Heidelberg laser exposure system with approximately 1  $\mu\text{m}$  resolution.

## A.2 Mask 2 – Interlayer Silicon Dioxide

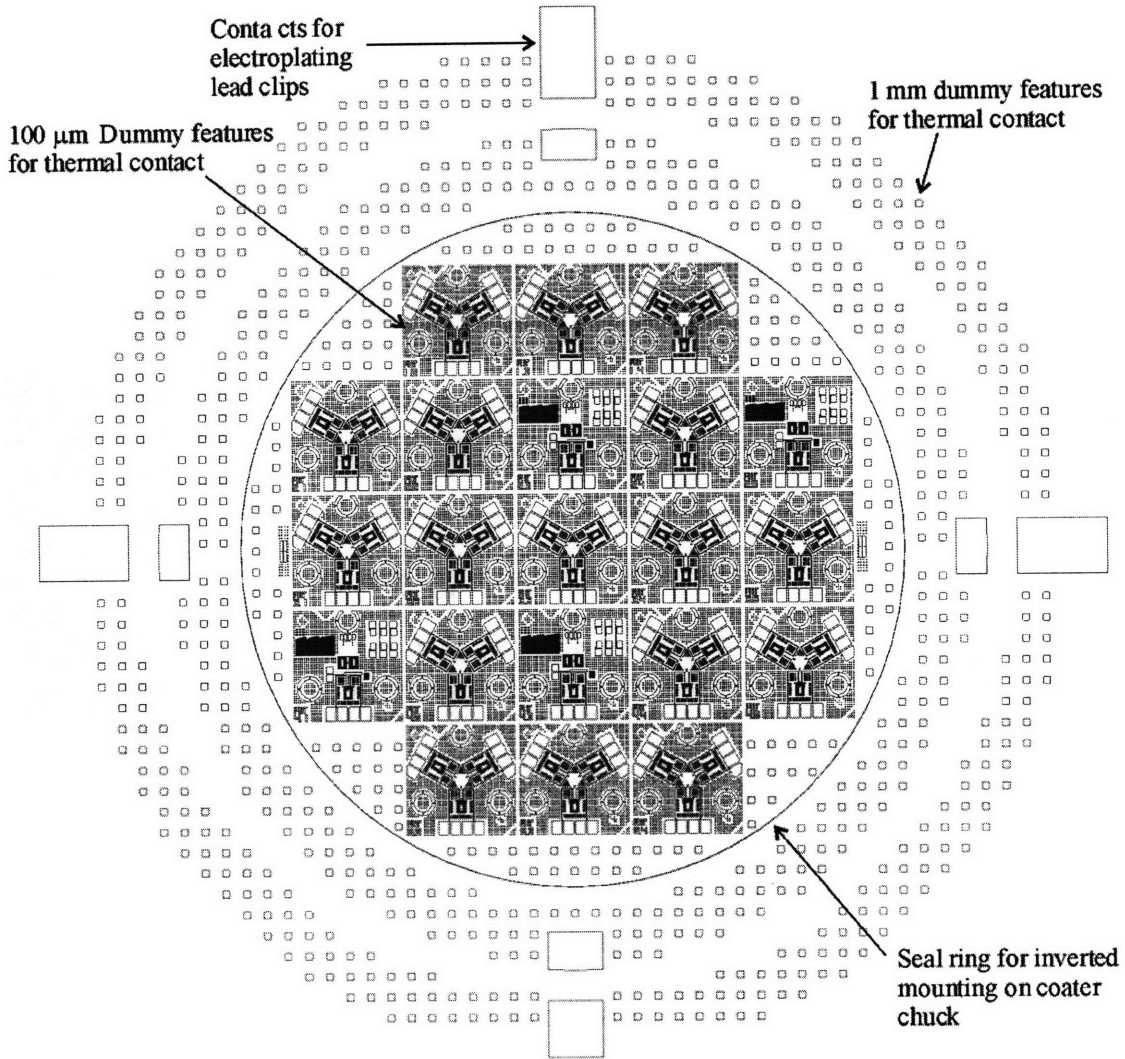
Dark field 5" mask (clear data). Minimum feature size is 8  $\mu\text{m}$  for the oxide vias. All other features on this mask have 100  $\mu\text{m}$  line widths. The tethers are 300  $\mu\text{m}$  long and removed by laser ablation in the last step of the process.





### A.3 Mask 3 – Photoresist Mold for Upper Copper Coils

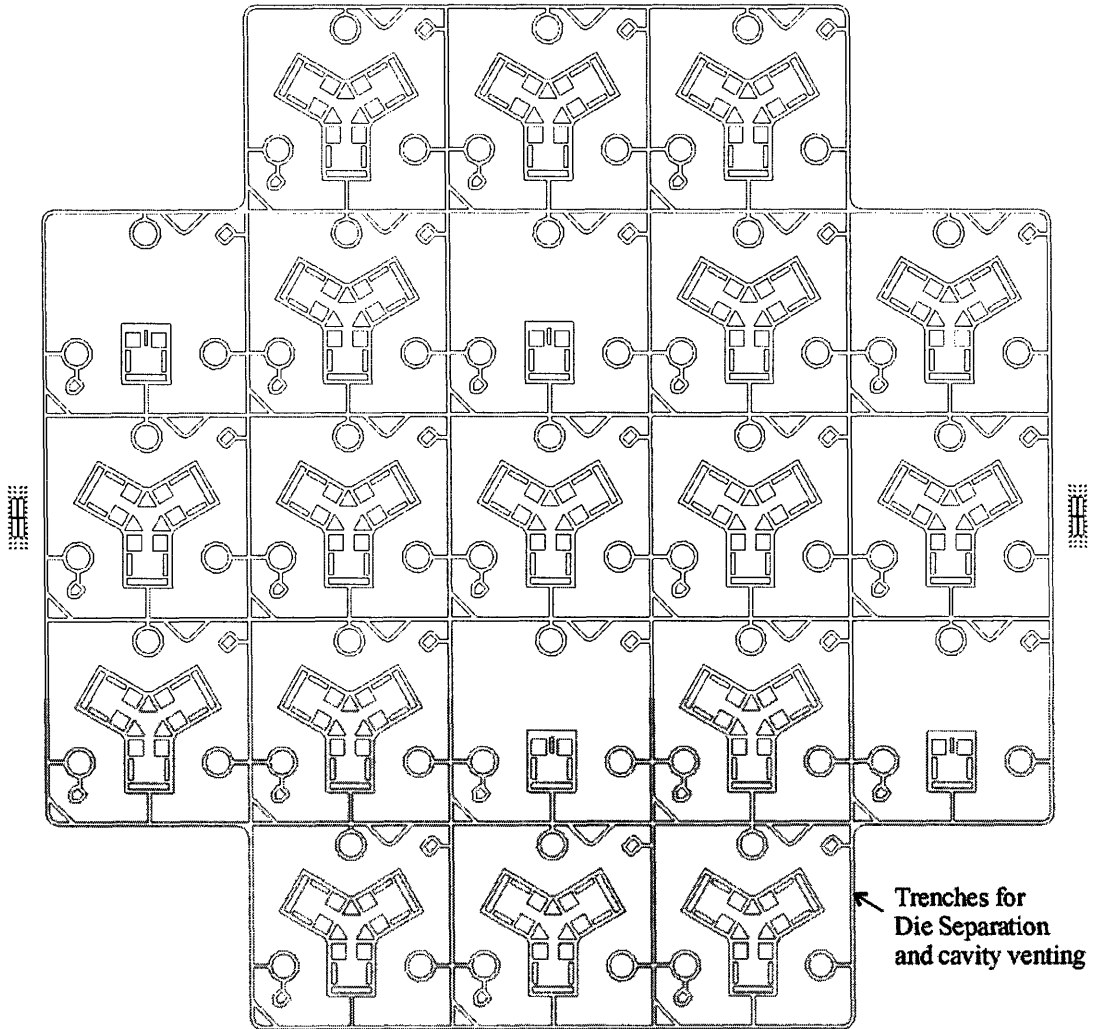
Dark field 7" mask (clear data). Minimum feature size is 10  $\mu\text{m}$  at the alignment marks. This layer defines the photoresist mold that is used for electroplating the upper copper coils. The coil mold widths are 25  $\mu\text{m}$ , and the winding spacing is 15  $\mu\text{m}$  (40  $\mu\text{m}$  pitch).



### A.4 Mask 4 – Backside Silicon Cavities

Dark field 5" mask (clear data). Minimum feature size is 30  $\mu\text{m}$  at the alignment marks. The trench widths in this mask are 300  $\mu\text{m}$  except for the alignment marks. All cavities and

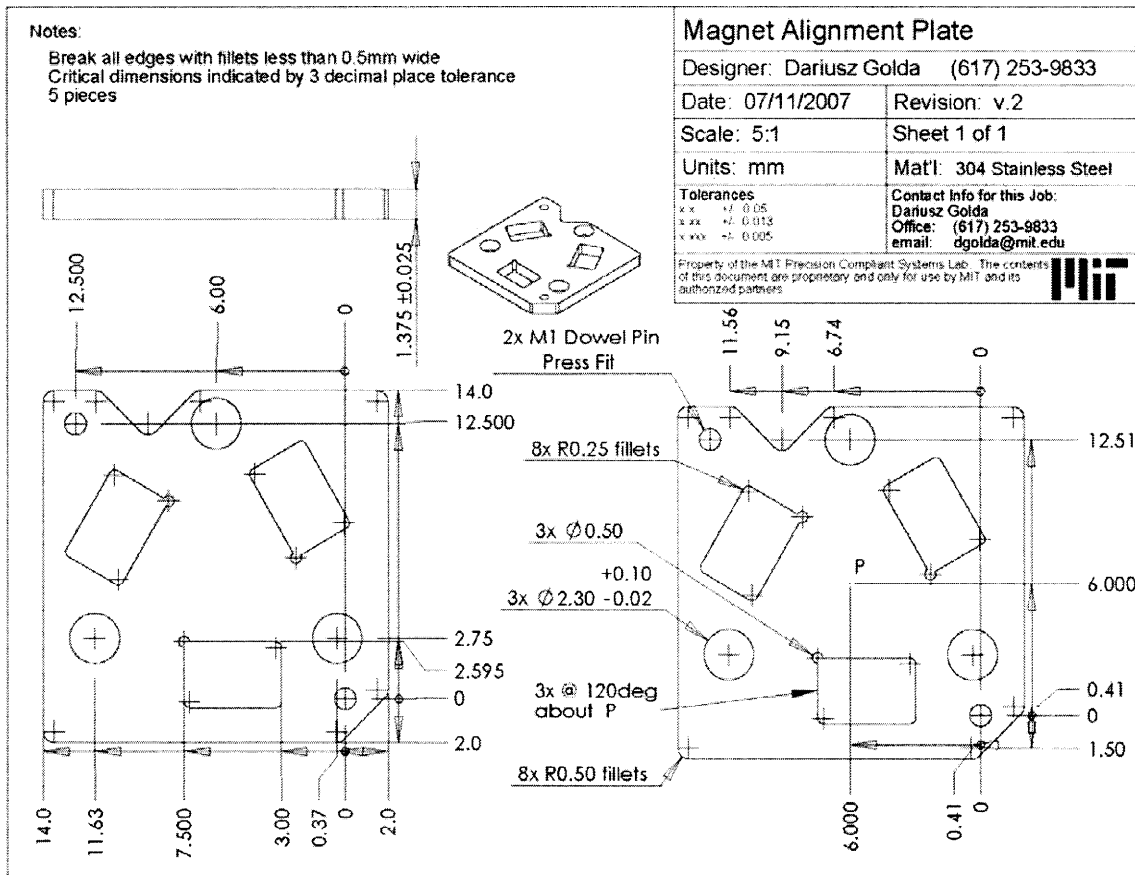
trenches are connected to ensure that the cavities are vented during the final front-side DRIE etch step which requires wafer mounting.



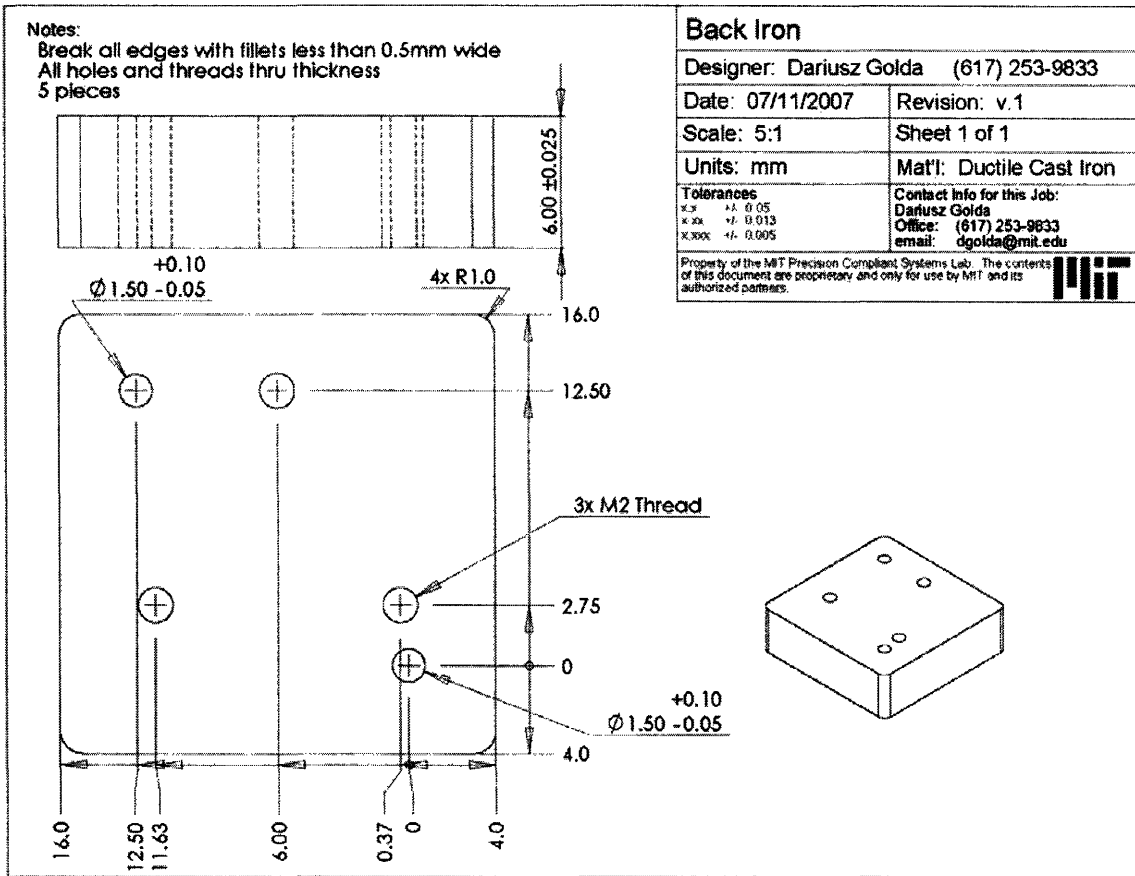
# B

## PART DRAWINGS

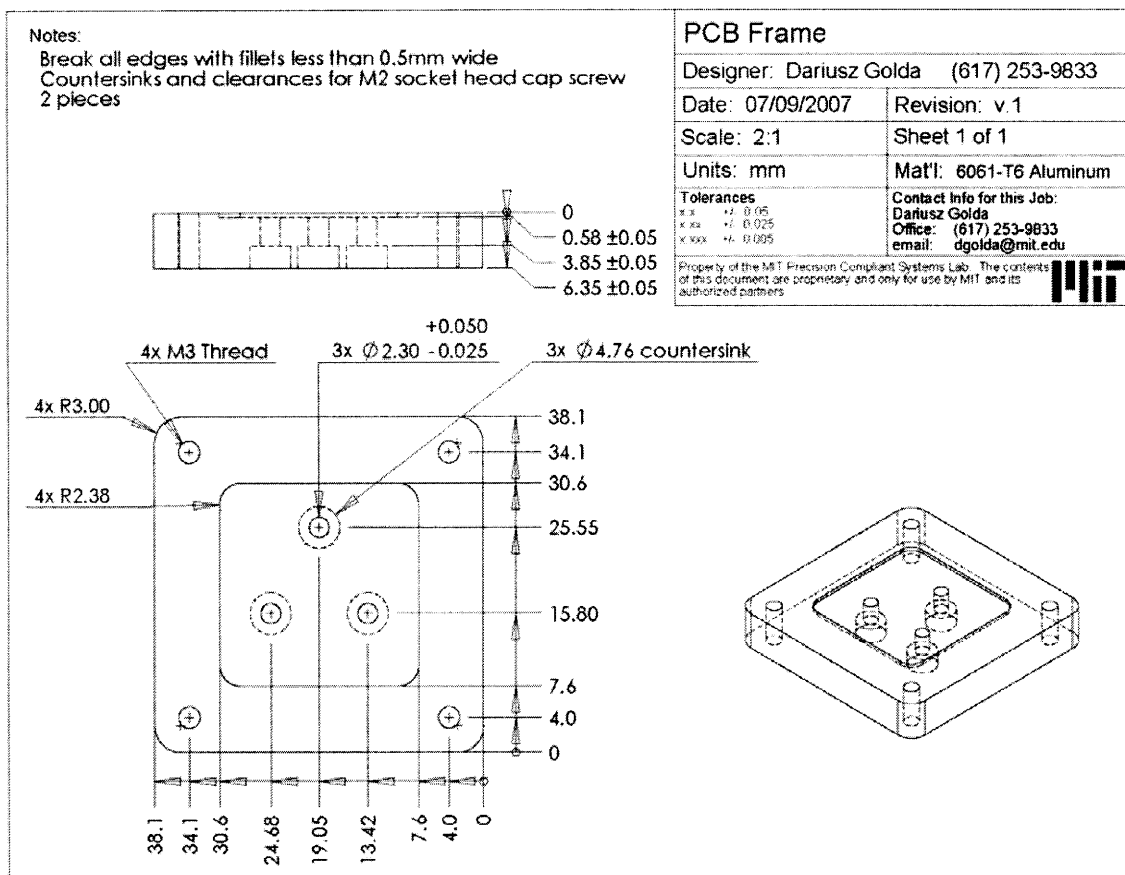
### B.1 Alignment Plate



## B.2 Back Iron

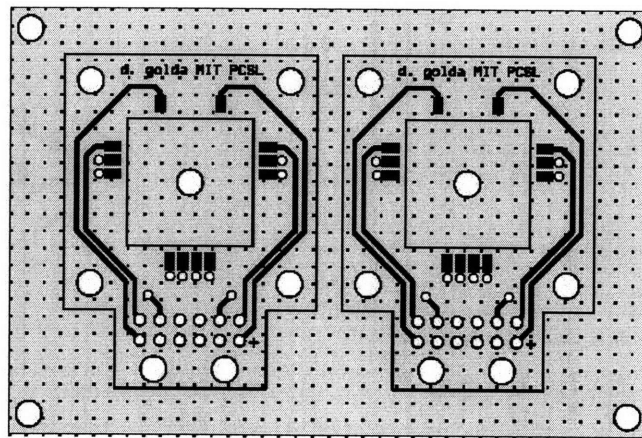


## B.3 PCB Frame

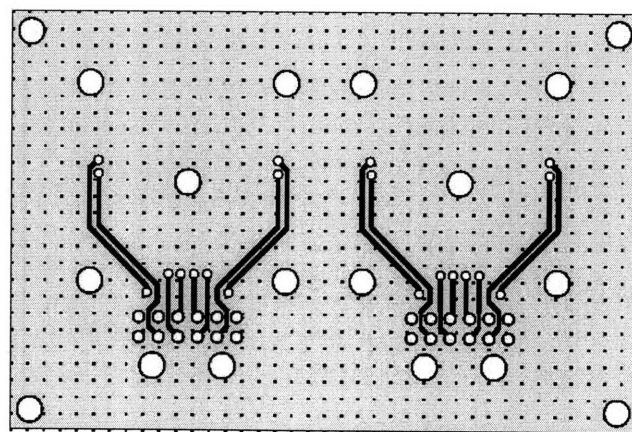


## B.4 PCB Lead Board

The two-sided PCB lead board was waterjet cut to the appropriate shape for mounting on the nanopositioner. The boards will shatter upon initial burst of the waterjet, so that the jetting was started in pre-fabricated holes or on the side of the board. The board was aligned in the waterjet to fixed reference features with a threaded plate. Molex connectors with 12 pins were used to provide current to the lead board from the current amplifier. Lead wires were soldered to the pads. The lead wires were then bent downward to preload against the chip during assembly of the lead frame to the nanopositioner fixture. The circuit board traces are shown in the following figure.



a) Upper trace layer



b) Lower trace layer

## CURRENT AMPLIFIER

This Appendix presents the design of the 6-channel, closed-loop current amplifier that was used to control current in the actuator coils. The input to the current amplifier is an analog voltage with a range of  $\pm 10$  V. Figure C.1 shows a schematic of one channel of the current amplifier.

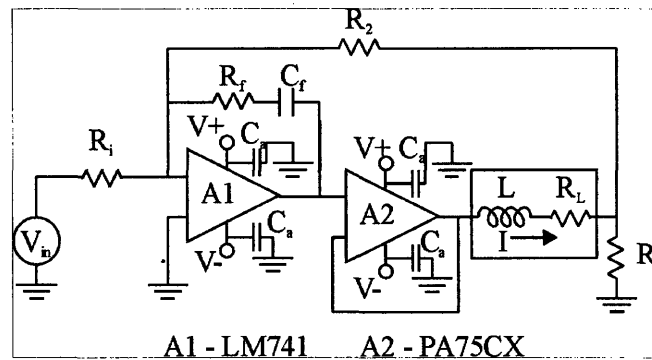


Figure C.1. Schematic of one channel of the closed-loop current amplifier.

The input voltage is represented by  $V_{in}$  and the output is the current,  $i$ , through the coil load inductor,  $L$ , and resistor,  $R_L$ . The LM741 serves as a buffer amplifier that feeds the Apex Microtech PA75CX power amplifier. Each PA75CX is used to drive two amplifier channels. The closed loop transfer function for a single channel of the amplifier is:

$$\frac{I(s)}{V_{in}(s)} = -\frac{R_2}{R_i} \frac{R_f C_f s + 1}{R_f C_f L s^2 + C_f (R_2 R_s + R_2 R_L + R_s R_f) + R_s}$$

The steady state gain, resonant frequency, and damping factor are given by:

$$Gain = -\frac{R_2}{R_i R_s}$$

$$f_n = \frac{1}{2\pi} \sqrt{\frac{R_s}{R_2 C_f L}}$$

$$\xi = \frac{R_2 R_s + R_2 R_L + R_s R_f}{2} \sqrt{\frac{C_f}{R_2 R_s L}}$$

The component values selected for the amplifier are presented in the following table.

**Table C.1. Component values used in the current amplifier.**

Symbol	Parameter	Value	Units
L	Coil Inductance	300	nH
R <sub>L</sub>	Coil Load	5	Ω
R <sub>S</sub>	Power Sense Resistor (10 W)	10	Ω
R <sub>i</sub>	Input Resistor	200	kΩ
R <sub>f</sub>	Feedback Resistor	100	Ω
R <sub>2</sub>	Outer Feedback Resistor	100	kΩ
C <sub>f</sub>	Feedback Capacitor	100	pF

The resulting gain of the system is designed to be  $G = -0.05 \text{ A / V}$ , and was measured to be Gain =  $-0.0495 \text{ A / V}$ . The resonant frequency of the amplifier with the load values in the table is nearly 3 MHz and the damping factor is approximately 30. The circuit boards each contained two channels powered by a single PA75CX amplifier. The circuit board layers are shown in the following figures.



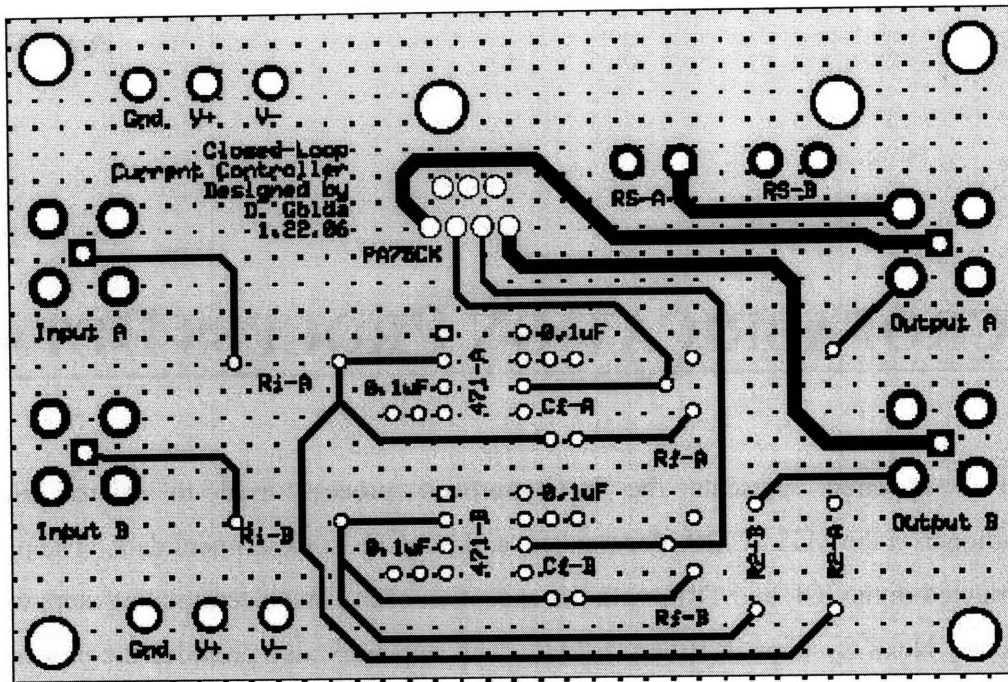


Figure C.2. Upper trace layer of the current amplifier circuit board

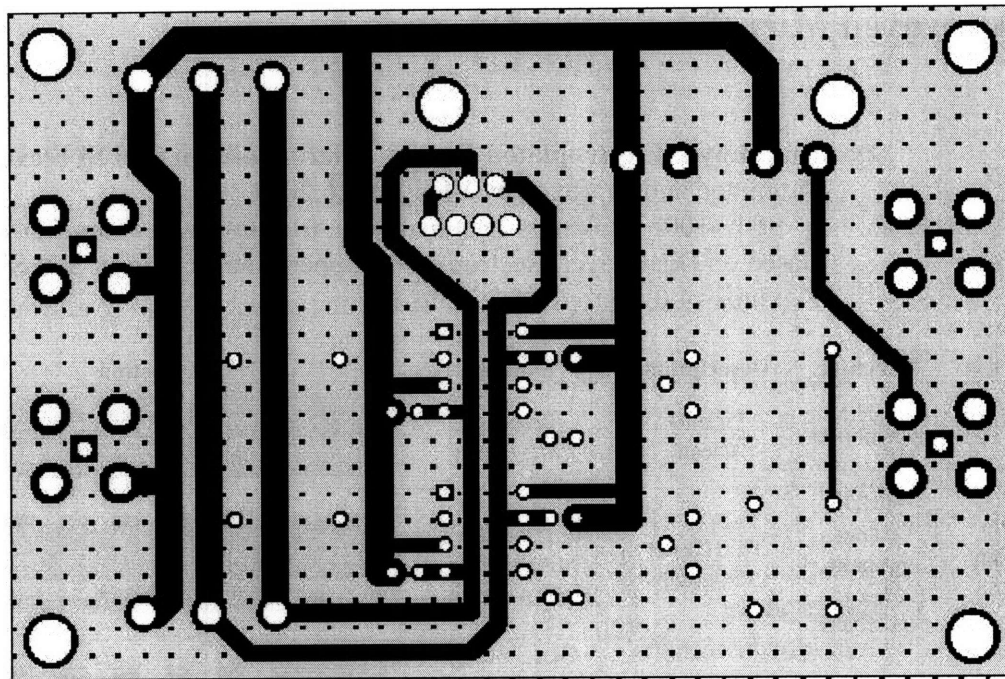


Figure C.3. Lower trace layer of the amplifier printed circuit board.

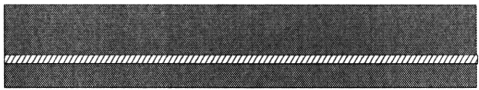
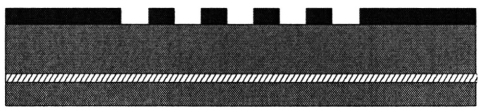
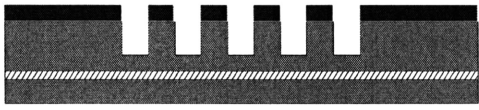
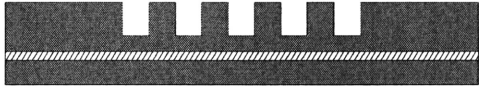
## D

**MICROFABRICATION PROCESS DETAILS**

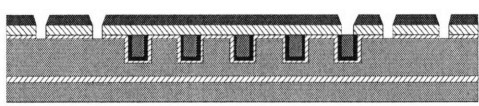
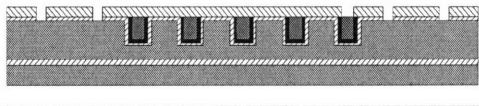
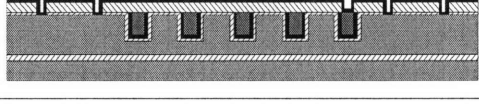
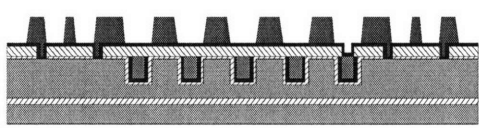
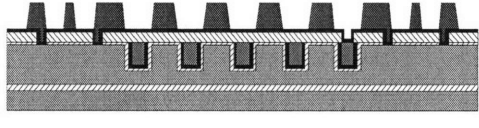
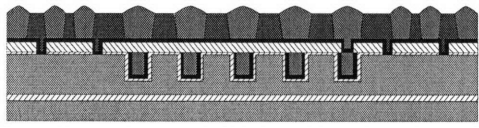
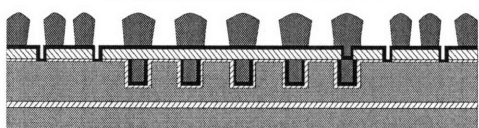
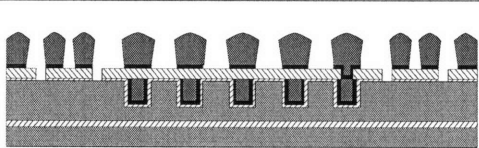
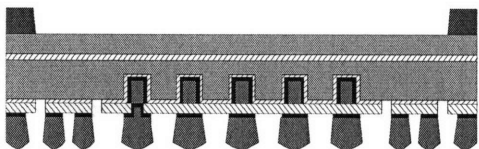
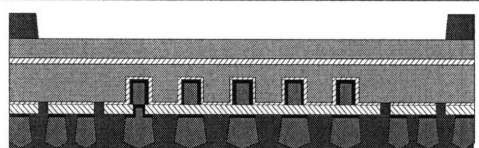
This appendix presents the PTC-approved process used to microfabricate the nanopositioner in the MTL, CMP process data, and photoresist experiment data. The processing was conducted in the ICL and TRL, with the exception of the first electroplating step, which was conducted at Nexx Systems in Billerica, MA. This appendix also provides the process details, such as machine settings and measured etch rates for each step.

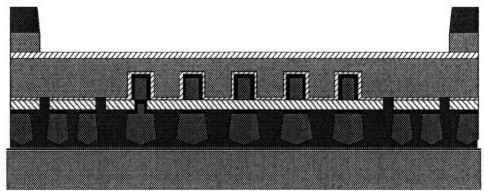
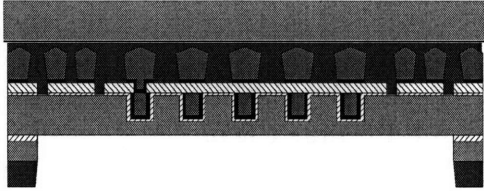
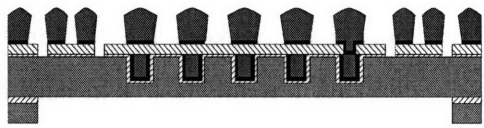
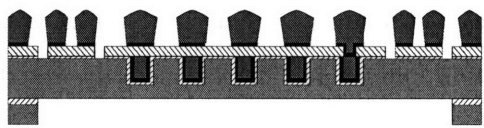
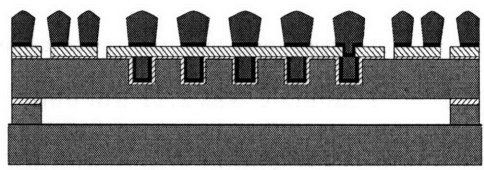
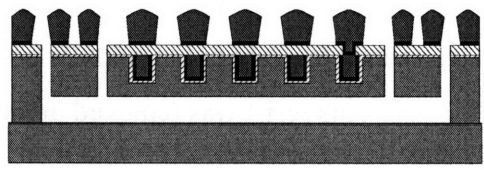
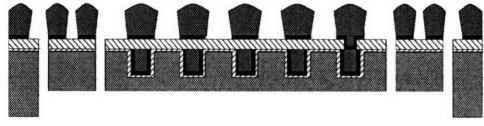
**D.1 Approved Microfabrication Process**

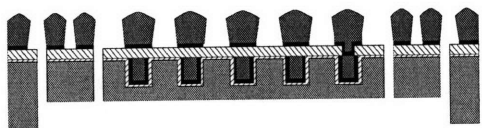
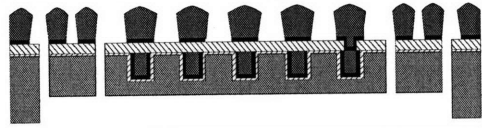
Title: **Dual Layer Electroplated Copper Micro-Coils on SOI Si Flexures v5.0**  
 Status: Submitted and approved by Vicky 10.26.2007  
 Starting Substrate: 6" SOI <100> Si Wafers 100um device, 610um handle, 1um BOX.  
 Comment: Based on Dual Layer Electroplated Copper Micro-Coils on SOI Si Flexures v4.0 approved 5.25.2007.

Step	Lab	Machine	Description	Details	X-Section
1	TRL	Acidhood	Piranha Clean	Prep for Lithography	
2	TRL	HMDS, coater, prebake, EV1, postbake	Thin Resist Lithography	1um thin resist, MASK 1 for DRIE patterning	
3	TRL	STS2	DRIE Trenches	OLE3 30um depth, 1:1 aspect ratio, end on etch. Followed by 1min O2Clean	
4	TRL	AsherTRL	Ash Teflon + resist	1+ hour ash to strip Teflon	

5	TRL	Acidhood	Piranha Clean	Clean wafers for RCA	
6	TRL	RCA	RCA Clean	Prep wafers for thermal oxidation	
7	TRL	TubeA2-WetOx-Bond	Thermal Oxidation	0.2µm oxide as electrical insulator and diff. barrier	
8	TRL	Acidhood	Piranha Clean	Immediately before step 9.	
9	TRL (Au)	Perkin Elmer	Sputter Seed layer for electroplating	Ti-Cu, 20nm/200nm thick,	
10	Nexx Sys.	Nexx Systems	Electroplate Copper	15-20µm thick, on top surface only	
10.1	TRL (Au)	Solvent Hood Au	UltraSonic Solvent Clean	2min Solvent Clean with UltraSonic agitation, followed by Meth/IPA/H2O rinse + SRD	
11	ICL (Au)	CuCMP	Planarization	Polish to oxide surface, followed by 10 sec water polish + sponge clean. Transfer to TRL immersed in transfer bucket. Do not allow to dry before Step 12.	
12	TRL (Au)	Acidhood	Post CMP Clean in Citric Acid	10 min clean to remove slurry residue. 45g Citric : 5L H2O	
13	TRL (Au)	STS-CVD	Deposit Oxide	Interlayer insulator, 1.0µm thick. HFSiO2 Recipe.	
14	TRL (Au)	HMDS, coater, prebake, EV1, postbake	Thin resist lithography	Pattern front of wafer. MASK 2	

15	TRL (Au)	Acidhood	BOE etch oxide	Pattern via to buried Cu coils and mask for downstream DRIE etch	
16	TRL (Au)	Solvent-Hood-Au	Strip Resist	Strip Resist NMP 65C for 20min. Followed by H2O rinse and SRD	
17	TRL (Au)	EBeam-Au	Deposit Seed Metal	Ti-Cu, 20nm/200nm thick	
18	TRL (Au)	HMDS, coater, prebake, EV1	AZ9260 Thick resist lithography	MASK 3, dehydration bake in HMDS, spin photoresist mold 30 micron thick, develop with AZ400K, no postbake	
18.1	TRL (Au)	AsherTRL	Prep for plating	1-2 min ash at 300 W to make resist surface hydrophylic	
19	ICL (Au)	Cu Plating Bench	Electroplate Copper	25-30um thick	
20	TRL (Au)	Solvent-hood-Au	Strip resist in Acetone	Acetone Bath, followed by Meth / IPA / H2O Rinse + SRD	
21	TRL (Au)	Acidhood	Etch seed layer	2 step etch using ultrasonic agitation: 1. 50:1 H2O:Nitric Acid 2. 100:1 H2O:HF	
22	TRL (Au)	HMDS, coater, prebake, EV1	Thick Resist Lithography	Backside double-coat AZ4620, aligned to frontside, 30min postbake	
23	TRL (Au)	Coater, Airbrush, Prebake	Wafer Mount	Spray frontside with thin resist, then wafer target mount on Si using thick resist. Postbake 30min	

24	TRL (Au)	STS1	DRIE backside	Define flexure and stage thickness with buried oxide. Recipe OLE3 followed by 1-2min O2Clean to strip residual Teflon.	
25	TRL (Au)	Acidhood	Vapor HF	Etch backside of wafer w/ Vapor HF. Place wafer right-side-up in horizontal cassette in 50% HF (<1cm deep in Teflon tank). Wafer situated 1 cm above chemistry. Remove from chemistry and spray rinse 5min, follow by SRD.	
26	TRL (Au)	Solvent-hood-Au	Strip Resist	Strip Resist and dismount in Acetone / Meth / IPA / H2O Rinse + air dry	
27	TRL (Au)	AsherTRL	Strip resist	Clean surface with low power oxygen plasma – 300W, 5min cycles in order to minimize Cu oxidation	
28	TRL (Au)	Coater, Prebake	Wafer Mount	Mount on Si using thick resist. No target, but swab 1 vent in resist for pressure equalization. Postbake 30min.	
29	TRL (Au)	STS1	DRIE Frontside etch	Thru etch to release flexures using recipe OLE3	
30	TRL (Au)	Solvent-hood-Au	Wafer Dismount	Acetone / Meth / IPA / H2O Rinse + air dry	

31	TRL (Au)	AsherTRL	Strip resist	Clean surface with low power oxygen plasma – 300W, 5min cycles in order to minimize Cu oxidation	
32	TRL (Au)	Resonetics	Laser ablate chip tethers	Release chips from bulk wafer	

## D.2 Process Details

### Step 1. Piranha Clean

The wafers were cleaned in the Acidhood2 with a 15 min Piranha acid clean (1:3 H<sub>2</sub>O<sub>2</sub> : H<sub>2</sub>SO<sub>4</sub>) followed by 10 minute cascade rinse and spin-dry.

### Step 2. Thin Positive Resist Lithography

The wafers were coated with 1 μm OCG825 resist using HMDS recipe #5, spun at 3000rpm for 30 seconds and prebaked at 95 C for 30 minutes. After prebake, the wafers were exposed for 2 seconds in EV1 with Mask 1 in hard contact mode and then developed 45-50 seconds in OCG 934 developer. The wafers were rinsed and spun dry. The ID markings were appropriately painted on each wafer with thin OCG825 resist, and then the wafers were postbaked at 120 C for 30 minutes. The backsides of the wafers were not cleaned with acetone after post-bake.

### Step 3. DRIE Trenches

STS2 was used to etch the trench molds for the buried copper coils by using recipe OLE3. The measured depth was 32 μm with a “W” bottom profile with less than 1 μm peak-valley. The measured etch rate was 2.21 μm/min.

### Step 4. Strip Residual Teflon and Photoresist

The residual Teflon from DRIE etching and the photoresist was stripped by oxygen plasma in the TRL Asher for 2 hours at 1000W power. Some resist remained around the painted wafer ID regions. This resist was removed in the subsequent acid clean.

### Step 5. Piranha Clean

The remaining photoresist was stripped with a 15 min Piranha clean followed by a 10 min cascade rinse and spin-dry. The wafers were sufficiently clean at this point.

**Step 6. RCA Clean**

The standard RCA clean was used to prepare the wafers for oxidation. This was done in the TRL RCA station.

**Step 7. Wet Thermal Oxidation**

The wafers were transferred to TRL Tube B2 for wet thermal oxidation immediately after completion of the RCA clean. The standard 2000 Å wet thermal oxide recipe was used. The Nanospec was used to measure thickness of the oxide. The oxide was measured to vary by 10% across the 7 wafer batch from 1940 - 2140 Å. Thickness varied across each wafer by about 4%.

**Step 8. Piranha Clean**

The wafers were prepared for seed metal deposition with a 15 minute Piranha clean immediately before metallization in Step 9. The acid clean prepares the oxide surface in order to improve adhesion of the deposited metal and ensure minimal contamination.

**Step 9. Sputter Seed Metal**

The seed metal for electroplating was sputtered with a DC magnetron source. The seed metal consisted of 50 nm Ti adhesion layer and 500 nm Cu. The seed layers were deposited without breaking vacuum. The Ti was deposited at 1kW power for 5 minutes at a rate of 10 nm / min, while the Cu was deposited at 2 kW for 7 minutes at 70 nm / min. The base pressure was  $2.5 \times 10^{-6}$  Torr.

**Step 10. Electroplate at Nexx Systems**

The wafers were transferred from the TRL in double-bag to the Nexx Systems development fab for electroplating. The electroplating system makes contact to the seed layer around the perimeter of the wafer. This limits the seed to be deposited only by sputtering. Evaporated seed metals have an edge exclusion that may lead to problems with the electrode contact in Nexx's tools. Enthone DVF 100 deep via-filling chemistry was used to plate the wafers with Nexx's proprietary agitation system in their developmental Stratus plating tool. The processing parameters were developed at Nexx Systems by Dr. Zhen Liu and his staff. The device wafers were plated on 9/11 – 9/13/2007. The wafers are pre-wet prior to immersion in the plating bath. In order to avoid problems due to seed thinning near the corners at the bottom of trenches, the standard process has two steps:

1. A short, slow DC deposition that builds up the copper seed.

2. A reverse pulse process that results in bottom-up filling by promoting higher accelerator concentration deep in the trenches relative to at the surface of the wafer. The reverse pulse process timing was as follows: a) 200 ms forward current; b) 20 ms reverse current; c) 200 ms off time.

The initial DC step was run with a forward current density of  $4.0 \text{ mA} / \text{cm}^2$  for 10 minutes. The pulse-reverse step was run with a forward current density of  $10 \text{ mA} / \text{cm}^2$  and a reverse current density of  $20 \text{ mA} / \text{cm}^2$  for a total time of 180 minutes. The additive concentrations were as follows: a) 15 ml/L for the DVF100-A accelerator; b) 3.0 ml/L for the DVF100-L leveler; and c) 3.0 ml/L for the DVF100-S suppressor. This is conservative plating recipe that resulted in void-free filling of the  $30 \times 30 \text{ }\mu\text{m}$  coil trenches.

#### **Step 10.1. Ultrasonic Solvent Clean**

The wafers were cleaned in acetone for 2 minutes after plating at Nexx in preparation for continued processing in the TRL, as required by the PTC. Ultrasonic agitation use used to knock off any large contaminant particles during the acetone bath. The acetone bath was followed by 1 minute baths in methanol and isopropanol, and then rinsed and spun-dry.

Note that steps 8-10.1 were repeated due to problems with the electroplated deposit. The repeated steps used Acidhood instead of Acidhood2 for Ti and Cu etches and Piranha cleaning. After detecting problems in the plated deposit in other wafers, the seed metal was etched with 50:1  $\text{H}_2\text{O}:\text{HNO}_3$  for 2 minutes for Cu and 100:1  $\text{H}_2\text{O}:\text{HF}$  for 30 seconds for Ti. The device wafer was then seeded and plated, and voids were detected in wafers that were plated under similar process conditions. The plated copper deposit was stripped with 1:1  $\text{H}_2\text{O}:\text{HNO}_3$  in 8 minutes, and then the Ti seed layer was stripped with dilute HF. The device wafer was seeded and successfully plated on the third attempt.

#### **Step 11. Copper CMP**

The copper overflow on the wafers was polished with the CuCMP and Cabot's iCue copper slurry. This processing step is discussed in detail in Section D.3, along with process suggestions and run data. After CMP, the wafers were cleaned with a polymer sponge and then immersed in water in a container for transfer to the TRL. It is important to prevent the wafer surfaces from drying so that residual slurry does not adhere to the surface. The remaining oxide thickness after over polishing is shown in the following table:



**Table D.1. Oxide thickness after CMP**

Location on Wafer	1	2	3	4	5
Oxide Thickness (Å)	1984	1931	1520	1558	1686

The locations on the wafer are as follows when holding the wafer upright: 1) center, 2) right side, 3) near the flat, 4) left side, and 5) top of the wafer. The dishing of copper features and erosion of the silicon separators was measured with a Dektak profilometer. The results are shown in the following figure.

**Table D.2. Copper dishing and silicon erosion after CMP**

Location	1	3
Dishing (nm)	275	300
Erosion (nm)	275	550

The dishing and erosion are sufficiently small to enable 2  $\mu\text{m}$  thick thin resist processing without shadowing due to the surface topography.

#### **Step 12. Post-CMP Slurry Clean**

Any residual slurry on the wafers is cleaned with a dilute citric acid solution. The solution was created by combining 9 g of anhydrous citric acid powder with 5 L water. The wafers were moved from the transfer container, placed in a cassette, and immersed in the acid before the surfaces dried. The citric acid clean lasted 10 min, and was followed by rinse and spin-drying.

#### **Step 13. PECVD Silicon Dioxide Deposition**

The silicon dioxide was deposited by plasma-enhanced CVD in the STS-CVD using the HFSIO recipe with a platen temperature of 300 C and RF frequency of 13.56 MHz. The target thickness was 1  $\mu\text{m}$ . The measured deposition rate was approximately 9-10  $\text{Å} / \text{sec}$ . The measured total oxide thickness including the underlying thermal oxide is given in the following table:

**Table D.3. Oxide thickness after CMP**

Location on Wafer	1	2	3	4	5
Total Meas Thickness (Å)	12221	12234	11767	11814	12997
Deposited Thickness (Å)	10237	10303	10247	10256	11311

#### **Step 14. Thin Positive Resist Lithography**

The wafers were coated with 2-3  $\mu\text{m}$  OCG825 resist using HMDS recipe #5, spun at 1000rpm for 30 seconds and prebaked at 95 C for 30 minutes. After prebake, the wafers were exposed for 2.6 seconds in EV1 with Mask 2 in hard contact mode and then developed for 2 minutes in OCG

934 developer. The wafers were rinsed and spun dry. The wafers were then postbaked at 120 C for 30 minutes.

#### **Step 15. Wet Etch Oxide**

The oxide was patterned with 7:1 BOE for 7.5 minutes. The etch rate for unannealed PECVD oxide was measured to be 2000 nm / minute and the etch rate for thermal oxide was 800 nm / minute. The wafers were then rinsed in water and spun-dry. The measured lateral over etch was on the order of 1  $\mu\text{m}$ . The 8  $\mu\text{m}$  vias opened to 10  $\mu\text{m}$  because of the over-etching, and were designed to nest within the buried copper lines by more than 10  $\mu\text{m}$  on any side. This eliminated any possibility of BOE attacking the Ti and oxide along the side walls of the trenches. The BOE etched the oxide in the vias down to the buried copper surface without damaging the copper.

#### **Step 16. Strip Resist in NMP**

After BOE etching, the resist mask was stripped with NMP at 65 C for 20 minutes without damaging the exposed copper at the bottom of the vias. Microstrip was also tested at greater than 55 C, but was found to attack any exposed copper. After the NMP resist strip, the wafers were rinsed with water and spun-dry. The resulting wafer surface was free of photoresist debris and suitable for continued processing.

#### **Step 17. Evaporate Seed Metal**

A second electroplating seed metal was evaporated shortly after the previous step. The evaporator chamber was allowed to pump down to the base pressure was  $2.0 \times 10^{-6}$  Torr. The Ti adhesion layer was deposited to a thickness of 20 nm and Cu was deposited to a thickness of 200 nm, both at a rate of 2  $\text{\AA}$  / sec.

#### **Step 18. Photoresist Mold for Electroplating**

The wafers were coated with 32  $\mu\text{m}$  AZ9260 thick positive. Recipe experiments were conducted to optimize the prebake temperature and time, the exposure, and the develop time in order to achieve nearly vertical sidewalls and good adhesion without postbaking. Data from photoresist recipe experiments may be found in Section D.4. HMDS was not deposited since it does not promote adhesion on metal surfaces. The wafer surfaces were dehydrated in the HMDS oven (no deposition) for 20 minutes under vacuum before coating the resist. Photoresist experiments indicate that the ambient humidity is important in obtaining good resist results. The target range is 37 % - 42 %. The resist was coated at 37% RH for this wafer batch. The resist was transferred from refrigeration to a pouring bottle 1 hour prior to use in order to warm to room

temperature. The resist was statically dispensed, spun at 1000 rpm for 60 seconds, and then at 3000 rpm for 5 seconds for edge bead removal with a swab. The wafers were then prebaked at 95 C for 20 minutes. The coating process was then repeated. The wafers were then prebaked at 95 C for 80 min for a total of 100 min. After prebake, the wafers were allowed to rehydrate for 28 hours. The water in the resist is important for promoting the development reaction and for ensuring near-vertical sidewall profile. The resist thickness before exposure was about 32  $\mu\text{m}$ . After rehydration, the wafers were interval exposed for 120 seconds in EV1 with Mask 3 in hard contact mode. The interval exposure used 8 intervals with 15 seconds on and 20 seconds off. The wafers were then developed for 10.5 minutes in AZ 400K 4:1 inorganic developer. The wafers were rinsed and spun dry. No postbake is necessary. The resist thickness after development was near 30-31  $\mu\text{m}$  and the sidewall angle was estimated to be nearly 85°

The photoresist must be coated within a couple weeks of seed layer deposition so that copper oxide does not form on the wafers, which is etched in the plating solution and results in delamination of the resist from the wafers during the first few minutes of electroplating. In this process, the resist was spun onto the seeded wafers after 7 days.

#### **Step 18.1. Low Power Oxygen Plasma**

The resist surface was made hydrophilic by a 1-2 minute oxygen plasma ash at 300 W. This resist preparation step enables the copper plating chemistry in the next step to flow into the molded channels without blocking due to air bubbles. Prior to implementing the ash step, the plated deposits contained missing regions of copper due to air bubbles trapped in the mold features. This ash step did not change the resist thickness or sidewall profile in a measurable way.

#### **Step 19. Electroplate Copper**

The wafers were electroplated in the copper plating bath in the ICL with Enthone's MicroFab SC copper sulfate plating chemistry and with a DC current of  $I = 0.35 \text{ A}$ , which corresponds to a current density of 1.23 ASF (Amp per square foot). The wafers were pre-wet before immersing them in the plating bath. The wafers were plated for  $t = 96 \text{ minutes}$  to result in an average plated thickness of 26  $\mu\text{m}$ . The required plating time may be estimated by Faraday's Law and by using the material properties for copper. It is important to maintain the bath chemistry by adding replenisher during plating (see data sheets). Bath chemistries that are more than 6 months old should be replaced. The plated thickness varied between 25-27  $\mu\text{m}$ .

**Step 20. Strip Resist in Solvent**

After plating, the the photoresist mold was stripped in acetone for 10 minutes, followed by 2 minute baths in methanol and isopropanol, and then rinsed with water and spun-dry.

**Step 21. Wet Etch Seed Metal**

The seed metal was stripped with a two-step wet etch with an ultrasonic bath in degas mode in order to eliminate bubbles between the coils. The wafers were pre-wet in water before placing in the etch chemistry. The Cu seed metal was etched with 50:1 H<sub>2</sub>O:HNO<sub>3</sub> for 130 seconds and then rinsed in water. The Ti seed was then etched in 100:1 H<sub>2</sub>O:HF for 30 seconds and then the wafers were rinsed and spun-dry. The Cu etch rate in 50:1 dilute nitric acid was measured to be 133 nm / min and the Ti etch rate in 100:1 HF was measured to be 60 nm / min. The oxide etch rate in 100:1 HF was estimated to be less than 5 nm / min.

**Step 22. Thick Positive Resist Backside Lithography**

The backsides of the wafers were coated with a double-thick layer of AZ4620 thick positive resist as a mask for backside DRIE etching. The wafers were mounted frontside-down on a custom 6" coater chuck for resist coating. The deposited copper ring on the frontside helped to promote vacuum contact to the chuck. The wafers were prepared with HMDS recipe #4. Resist was dispensed at 500 rpm for 25 seconds, spun at 2000rpm for 60 seconds, and then spun at 2000rpm for 5 second for edge bead removal with a swab. The wafers were then prebaked at 95 C for 20 minutes. The resist coating recipe was repeated, but with a spin speed of 3000rpm. The wafers were prebaked at 95 C for 60 minutes and the resulting thickness was 21 μm. After prebake, the wafers were interval exposed with backside alignment with Mask 4 in EV1 with Mask 4 in hard contact mode. The interval exposure consisted of 3 intervals of 15 seconds on and 20 seconds off. The wafers were then developed for 3-3.5 minutes in AZ440 developer and rinsed and spun dry. The wafers were then postbaked at 95 C for 30 minutes. Final resist thickness was 19 μm.

**Step 23. Wafer Mount**

The wafers were then mounted on an SSP Si mount wafer. The frontside of the device wafer was spray coated with thin positive resist to protect the copper and oxide features and then prebaked at 95 C for 15 minutes. Thick resist was spun onto the mount wafer at 2000rpm and channels were swabs from the edges for ventilation. The device wafer was then mounted frontside-down, the alignment marks were painted with thin resist, and the stack was postbaked at 95 C for 20 minutes. The back of the mount wafer was then cleaned with solvents. The

dummy copper features in Mask 3 were added to promote thermal contact between the device and mount wafers during the subsequent DRIE etch step.

#### **Step 24. Backside DRIE Etch**

The backside cavities were etched in STS1 with recipe OLE3 at 1 hour intervals for a total of 300 minutes. The etch process stopped on the buried SOI oxide. After completion of the etch recipes, residual Teflon was cleaned with recipe O2clean for 2 minutes. The average DRIE etch rate was 2  $\mu\text{m}$  / min, and varied between 1.8-2.2  $\mu\text{m}$  / min across the wafer. The trenches etched 20% faster than the open cavity areas. The remaining buried oxide after completion of the etch process was between 6000-10000  $\text{\AA}$ , and the remaining resist was 14-15  $\mu\text{m}$ .

#### **Step 25. Vapor HF Etch of Buried Oxide**

After DRIE etching, the buried oxide was stripped with vapor HF. The wafer stack was mounted in a cassette with the etch surface facing downward. The wafer stack was positioned approximately 1 cm above the concentrated HF chemistry. The vapor etch was pulsed at 30 second to 2 minute intervals for a total time of 5 minutes until the oxide was cleared. The oxide etch rate was estimated at 200 nm / min. After etching, the wafer was immersed in a water bath for 15 minutes and rinsed and spun-dry. The backside resist peeled off during the water bath and rinse, but this is of no consequence because the silicon etch was already complete.

#### **Step 26. Strip Resist and Wafer Dismount**

After vapor etching of the oxide, the wafer stack was dismounted in acetone for 24 hours, and then cleaned in acetone, methanol, and isopropanol baths for 2 minutes each. The device wafer was then rinsed with water and allowed to air dry.

#### **Step 27. Low Power Oxygen Plasma Clean**

Residual Teflon and resist debris was cleaned with pulsed oxygen plasma at 300 W. The wafers were cleaned at 5 minute intervals for a total of 45 minutes. The resulting wafer surface was sufficiently clean to proceed to the final DRIE etch step. The low-power, pulsed plasma did not oxidize the exposed copper due to the low temperature and limited exposure time. A test wafer was run at 300 W for 15 minutes and showed oxidation of exposed copper. Some cracks were observed in the trenches that separate the chips, but all the chips remained linked to the wafer.

#### **Step 28. Wafer Mount**

The wafers were then mounted frontside-up to a mount wafer in preparation of the final DRIE release etch step. Thick resist was spun at 2000rpm onto the mount wafer and a single vent was

swabbed to the center of the wafer. The device wafer was carefully mounted onto the mount wafer and postbaked for 20 minutes at 95 C. The backside of the mount wafer was cleaned with solvents.

**Step 29. Frontside DRIE Etch**

The mounted device wafer was etched with DRIE in STS1 using recipe OLE3 at 15 minutes for a total of 75 minutes until all chips were released. The oxide and exposed copper was used as the etch mask in this step. The alignment mark etch was used at the end to clean residual Teflon. Some copper coil oxidation was observed after DRIE etching, but the coils were still functional. The etch rate was estimated to vary between 1.3 – 1.7  $\mu\text{m} / \text{min}$ . The remaining oxide after etching was measured with the Nanospec and is presented in the following table.

**Table D.4. Oxide thickness after CMP**

Location on Wafer	1	2	3	4	5
Oxide Thickness (A)	6352	6218	6492	6465	8209
Location on Die	stage	stage	stage	stage	chip

The etch rate was faster on the stage than on the bulk chip because of increased heating of the released structure. The etch selectivity for silicon to unannealed PECVD oxide during this etch step was estimated to be 200:1.

**Step 30. Wafer Dismount**

After etching, the wafer was dismounted in acetone for 24 hours. The mounted wafer was placed frontside-down in a cassette slot and immersed in the acetone bath. The halo cutout pieces fell out of the inverted wafer and drifted to the bottom of the bath due to gravity. This release method enabled the cutouts to fall without damaging the delicate flexure structures. The chip tethers connected the chips to the surrounding wafer and prevented them from falling to the bottom of the bath. After removal from the acetone bath, the wafer stack was carefully placed frontside up in a clean bath of acetone and the device and mount wafer were separated. The device wafer was then transferred to methanol and isopropanol baths for 2 minutes each. The wafer was allowed to air dry.

**Step 31. Low Power Oxygen Plasma Clean**

Residual Teflon and resist debris was cleaned with pulsed oxygen plasma at 300 W. The wafers were cleaned at 5 minute intervals for at total of 50 minutes until 99% of the residues were removed. The low-power, pulsed plasma did not oxidize the exposed copper due to the low temperature and limited exposure time. At this point, the wafer-level processing was complete.

### **Step 32. Laser Ablation to Separate Chips**

The final step in the process was to separate the chips. The 300  $\mu\text{m}$  x 100  $\mu\text{m}$  x 100  $\mu\text{m}$  thick tethers were cut by laser ablation using at 150  $\mu\text{m}$  square mask and 3000 pulses per drill at 100 Hz for a total drill time of 30 seconds. Each tether required 3 drills to cut completely through the tether.

## **D.3 Copper CMP Process Suggestions and Run Data**

CMP is a very complex process, involving many mechanical and chemical factors. Several different parameters control the process, including total down force pressure, differential backpressure, table velocity, head velocity, sweep velocity, slurry type and concentration, pad type and condition, and wafer pattern, material stack and structure, wafer bow, and wafer edge profile. In addition, results are very sensitive to contamination issues such as debris on the pad. It is impossible to optimize all these variables, but minor adjustments to the most important parameters can go a long way towards minimizing wafer and tool damage and obtaining good polishing results.

### **Polishing parameters**

The most important parameters that affect polishing performance are polish pressure and table / spindle speed, and to a lesser extent, differential wafer backpressure. As a rule of thumb, it is always better to polish gently and for longer time in order to prolong pad life, and prevent wafer damage due to pad debris or the possibility of wafers slipping out of the head (catastrophic for wafer and machine). In addition, always check the condition of the pad, head, and wafer, as the interaction of these three components is most important. As the polish pressure, table, or spindle velocity increases, the polish rate will also increase.

There are 2 primary material removal modes – direct “grinding” contact between wafer and pad, and hydroplane gliding of the wafer on a slurry film between pad and wafer. A 3rd mode is somewhere between these two. For very fine and uniform polishing, it is better to polish with light pressure and high table or spindle velocity (high Hersey number), which will result in the wafer mostly sliding on a film of slurry. However, high table velocities result in higher surface friction, and higher probability that the wafer may slip out of the head. There is a limitation to the safe polishing speed due to tool-specific issues.

For heavy grinding, high pressure and slow table and spindles speeds (low Hersey number) leads to more direct “grinding” contact between pad and wafer, but this tends to wear the pad quickly. More importantly, this mode is risky – the wafer could crack due to the pressure if debris is present on the carrier or table pad, and the edges of the wafer (or other structures on the wafer) can catch pad asperities or grooves and drag the wafer out of the carrier head.

**Backpressure and Wafer Slip-out (specific to the MTL 6EG tool)**

The MTL’s 6EG Cu tool lacks the proper hardware to apply pressure to the wafer retaining ring. This capability is critical to obtain uniform polishing because the machine must apply a positive backpressure so that wafer “floats” on the pad. Retaining ring pressure also makes the wafer appear larger to the polishing pad, resulting in better WIWNU. The final function of the pressurized retaining ring is to create a seal on the pad that prevents the wafer from slipping out of the carrier head when operated with positive backpressure (necessary for sufficient uniformity). A fixed ring (on the MTL tool) prevents the wafer from slipping out by means of creating a partial mechanical block. The relative height from wafer surface to retaining ring is set to 0.003-0.005” (75-125um) such that the retaining ring does not impede the application of pressure on the wafer. This results in a finite gap under which the wafer can slide, given enough shear force. Wafers with sharp features such as edges of plated regions can catch pad asperities and pull the wafer out of the head when operating the head with positive backpressure. Reducing the backpressure and table / spindle speeds can reduce the chance of wafer slip-out. Negative backpressure (vacuum) also reduces the likelihood of slip-out, but at the expense of poor WIWNU.

A good strategy minimize the risk of wafer slip-out and still get good uniformity is to initially polish for a few minutes (5-10min) at lower polishing pressures (~3psi) with a negative backpressure (-14psi) to remove any sharp features on the wafer. Then apply no more than 0.5psi mean backpressure and polish at 3-4psi for the duration of the process. Table speed of 30rpm and head speed of 20rpm yield acceptable polish rate and are slow enough to minimize slip-out.

Wafer slip-out is also caused by pressure fluctuations that occur as the head lands on the pad. The down force ramps and fluctuates during this landing period while the backpressure also ramps up. If the backpressure happens to exceed the down force during the pressure fluctuations, the wafer may slip out of the head. Most slip-out incidents occurred during this



phase. This problem was overcome by introducing a 10 second delay step with vacuum backpressure to enable the down force to stabilize before ramping the backpressure. Wafer slip-out was eliminated after implementing this delay.

### **DownForce Drift and Calibration**

The Strasbaugh 6EG CuCMP downforce calibration tends to drift over time, especially when the tool is not used regularly. If the tool has not been used in several weeks, it is a good idea to calibrate the down force. In addition, the tool is designed for 8"+ wafers, and thus the down force capability exceeds 400 lbf. However for normal 6" Cu polishing, only about 80 lbf is necessary. If the tool is not well calibrated, the actual pressure for 6" may fluctuate by more than 30%. Be sure to calibrate if the tool has not been used in many weeks. Always pay attention to the actual pressure gauges while processing.

### **Uniformity**

Differential backpressure can compensate for within-wafer non-uniformity (WIWNU) and lead to more uniform polishing across the wafer. The head has two backpressure zones: inner Zone 1, and outer ring Zone 2. It is possible to adjust the pressures independently for both zones in order to compensate for center- or edge-fast polishing. Uniform copper deposits tend to polish edge fast. However, most plated deposits are thicker near the edge of the wafer, resulting in center-fast polishing. Applying a differential pressure of 0.1-0.2psi can improve wafer-level polishing uniformity. Polish uniformity is important in order to minimize over-polishing time in regions that are already cleared, which reduces dishing and erosion in device and die-level features. Dishing and erosion can also be minimized by polishing at a high Hersey number (high velocities, low pressure)

### **Cleanliness and Pad State**

Contamination is a likely cause of many polishing problems – non-uniformity, scratching, wafer slip-out, and wafer failure. Particles lodged in the carrier head pad can lead to stress concentrations on the wafer, resulting in local pressure gradients and polishing non-uniformity. The stress concentrations can also result in cracking and failure of the wafer if the polishing pressure is sufficiently high. Before polishing, make sure that the carrier head pad and wafer are clean and free of visible debris.

Debris in the polishing pad can lead to local stress concentrations and scratches in the polished surface. It can also result in wafer slip-out if the debris is large enough to impede the

relative sliding of wafer and pad. Always inspect the pad for debris before running wafers, and periodically while running wafers. It is possible for the edge of the wafer to chip and lodge Si debris in the pad. This threat can be mitigated by running short polishing cycles, say 5min max, and then inspecting and cleaning the pad.

In addition to pad debris, the pad state affects polishing rate and polish characteristics. The conditioning head helps to prevent the pad from glazing by roughing in order to maintain pad asperities and pores. In-situ pad conditioning is important for pad maintenance and to ensure a stable polishing rate. The pad should be routinely inspected for signs of wear, such as disappearance of the slurry grooves and pad discoloration.

### CMP Run Data

The following table presents the CMP run data for the wafer that completed the process. The spindle speed and table speed were both 30 Rpm, and the slurry rate was 100 mL / min.

**Table D.5. CMP process run data for Batch 3 Wafer 0-3.**

Run	Recipe	Time (min)	Down Pres (psi)	Back Pres z1/ z2 (psi)	Results / comments
					Change polishing pad and head pad on 9.18.2007. Run 4 pad condition cycles using Dariusz#1. Run dummy oxide wafer 1x 1min 3psi. Looks ok. Wafer 0-3 has shiny finish, small grain structure, and coils appear to be filled from uscope inspection
1	DariuszCuVacBP#1	10	3	-.14	pad looks good. No debris. Couple scratches on wafer
2	DariuszCuFineLong#1	20	4	.5/.5	no debris or new scratches. No pad discolorations
3	DariuszCuFineLong#1	20	4	.5/.5	looks good. Coil outline starting to disappear. No discolorations or pad debris. A couple faint scratches in pad.
4	DariuszCuFine#1	10	4	.5/.5	pad good, no scratches on wafer. Coil outlines are gone
5	DariuszCuFine#1	10	4	.5/.5	everything looks good. Continue
6	DariuszCuFine#1	10	4	.5/.5	pad looks ok, wafer good. Coils completely invisible in center of wafer. Requires more time.
7	DariuszCuFine#1	10	4	.5/.5	pad looks good. 1 particle in pad, and a couple scratches on wafer
8	DariuszCuFine#1	10	4	.5/.5	no debris or new scratches.
9	DariuszCuFine#1	10	4	.5/.5	starting to poke thru - no scratches. Continue. Reduce pressure
10	DariuszCuFine#1	5	3	.5/.5	still requires time. 1 scratch on surface of oxide. Center slow.
11	DariuszCuFine#1	5	3	.6/.4	still need more time. No new scratches
12	DariuszCuFine#1	7	3	.6/.4	center still not done. Continue polishing center fast
13	DariuszCuFine#1	5	3	.6/.4	need to get alignment mark. Polish for 3 more min edge fast
13	DariuszCuFine#1	3	3	.4/.6	needs 1-2min more edge fast to get right AM. No seams visible. Looks great!
14	DariuszCuFine#1	2	3	.4/.6	Run 1x pad condition before continuing. Looks perfect. DONE!

## D.4 AZ9260 Photoresist Experiment Data

Run	Substrate	RH %	HMDS	Coat 1	Prebake 1 Time (min)	Prebake 1 Temp (C)
1	Si+Therm Ox+Ti+Cu Seed	36.5	#4	Static Disp, 2K 60sec, 3K EB	15	95
2	Si+PECVD Ox	37.8	#4	Static Disp, 2K 60sec, 3K EB	20	105? 95 I think
3	Si+PECVD Ox	37.8	#4	Static Disp, 2K 60sec, 3K EB	20	105?
4	(1) Si	37.8	#4	Static Disp, 2K 60sec, 3K EB	20	105?
5	(2) Si+Ti+Cu Seed	37.8	#4	Static Disp, 2K 60sec, 3K EB	20	105?
6	(2) Si, (3) Si+Ti+Cu Seed	??	#4	Static Disp, 1.5K 60sec, 3K EB	15	110
7	Si	36	#4	Static Disp, 1.5K 60sec, 3K EB	15	110
8	Si	36	#4	Static Disp, 1.5K 60sec, 3K EB	15	110
9	Si+Ti+Cu	36	#4	Static Disp, 1.5K 60sec, 3K EB	15	110
12	Si	??	#4	Static Disp, 1.5K 60sec, 3K EB	15	95
13	Si	??	#4	Static Disp, 1.5K 60sec, 3K EB	15	95
14	Si+Ti+Cu	??	#4	Static Disp, 1.5K 60sec, 3K EB	15	95
15	Si+Ti+Cu	??	#4	Static Disp, 1.5K 60sec, 3K EB	15	95
16	Si+Ti+Cu	??	#4	Static Disp, 1.5K 60sec, 3K EB	15	95
17	Sputterd Ti+Cu	30.8	No	Static Disp, 1.5K 60sec, 3K EB	15	95
18	Sputtered Ti+Cu	30.8	#4 Problem	Static Disp, 1.5K 60sec, 3K EB	15	95
19	Ebeam Ti+ Cu	30.8	No	Static Disp, 1.5K 60sec, 3K EB	15	95
20	Ebeam Ti + Cu	30.8	#4 Problem	Static Disp, 1.5K 60sec, 3K EB	15	95
21	Multi	30.8	#4 Problem	Static Disp, 1.5K 60sec, 3K EB	15	95
22	Previous PE dummy	34.1	Dehydrati on	Static Disp, 1.3K 60sec, 3K EB	20	95
23	From Batch 2, virgin	34.1	Dehydrati on	Static Disp, 1.3K 60sec, 3K EB	20	95
24	Si + 5000A them ox from Haifeng	34.1	Dehydrati on	Static Disp, 1.3K 60sec, 3K EB	20	95
25	Si + 5000A them ox from Haifeng	34.1	Dehydrati on	Static Disp, 1.3K 60sec, 3K EB	20	95
26	Si + 4um thermal + concept1 ox From Blaise	34.1	Dehydrati on	Static Disp, 1.3K 60sec, 3K EB	20	95
27	PECVD ox on E-plate	34.1	Dehydrati on	Static Disp, 1.3K 60sec, 3K EB	20	95
28	Si + Ta + Cu	39	Dehydrati on	Static Disp, 1K 60sec, 3K EB with acetone swab	20	95
29	Si + Ta + Cu	39	Dehydrati on	Static Disp, 1K 60sec, 3K EB with acetone swab	20	95
30	Si + Ta + Cu	39	Dehydrati on	Static Disp, 1K 60sec, 3K EB with acetone swab	20	95

Run	Coat 2	Prebake 2 Time (min)	Prebake 2 Temp (C)	Rehydrate Wait Time (hour)	Coat Thick (um)	Exposure (int x on x off)
1	Static Disp, 2K 60sec 3K EB	50	95	15		5x15x20
2	Static Disp, 1K 60sec, 3K EB	50	105?	48	28	5x15x20
3	Static Disp, 1K 60sec, 3K EB	50+30	105?	48	28	5x15x20
4	Static Disp, 1K 60sec, 3K EB	50+20	95	96	28	3x15x20
5	Static Disp, 1K 60sec, 3K EB	50	105?	48	28	
6	Static Disp, 1.5K 60sec, 3K EB	120	110	NA	28	NA
7	Static Disp, 1.5K 60sec, 3K EB	50	110	2	28	7x15x20
8	Static Disp, 1.5K 60sec, 3K EB	50	110	2	28	14x15x20
9	Static Disp, 1.5K 60sec, 3K EB	50	110	2	28	21x15x20
12	Static Disp, 1.5K 60sec, 3K EB	50	95	72	28	14x15x15
13	Static Disp, 1.5K 60sec, 3K EB	50	95	72	28	7x15x20
14	Static Disp, 1.5K 60sec, 3K EB	80	95	96	28	7x15x20
15	Static Disp, 1.5K 60sec, 3K EB	110	95	216	28	7x15x20
16	Static Disp, 1.5K 60sec, 3K EB	80	95		28	5x15x20
17	Static Disp, 1.5K 60sec, 3K EB	80	95	1	28	5X15X20
18	Static Disp, 1.5K 60sec, 3K EB	80	95	1	28	7x15x20
19	Static Disp, 1.5K 60sec, 3K EB	80	95	24	28	7x15x20
20	Static Disp, 1.5K 60sec, 3K EB	80	95	1	28	NO
21	Static Disp, 1.5K 60sec, 3K EB	80	95	1	28	7x15x20
22	Static Disp, 1.3K 60sec, 3K EB	100	95	20	27.5	8x15x20
23	Static Disp, 1.3K 60sec, 3K EB	100	95	120	29	11x15x20
24	Static Disp, 1.3K 60sec, 3K EB	100	95	20	29	9x15x20
25	Static Disp, 1.3K 60sec, 3K EB	100	95	20	29	9x15x20
26	Static Disp, 1.3K 60sec, 3K EB	100	95	20	29	16x7.5x7.5
27	Static Disp, 1.3K 60sec, 3K EB	100	95	144	29	12x15x20
28	Static Disp, 1K 60sec, 3K EB with acetone swab	80	95	50	33 (pre rehyd)	8x15x0
29	Static Disp, 1K 60sec, 3K EB with acetone swab	80	95	50	33 (pre rehyd)	7x15x20
30	Static Disp, 1K 60sec, 3K EB with acetone swab	100	95	50	33 (pre rehyd)	9 x 15 x 20

Run	Developer	Dev Time (min)	Dev Thick (um)	Post-bake (min)	Results / Comments
1	AZ440	5.5	NA	No	Cu lines eroded and pointed, strip resist in Aceton/Meth/IPA than Ash and try again
2	AZ440	3-3.5	27-28	20 @95	Cleave and look at sidewall profile - sloped and eroded dividers!
3	AZ440	3	NA	No	Looks similar to W1 with sloped and pointed sidewalls!
4	AZ440	7	23	No	Features not clear, all dividers are destroyed, toss wafer to garbage
5					
6	NA	NA	NA	No	Resist Cracked upon handling after postbake! Too hot and too long!!! Strip Acetone/Meth/IPA 2min Ash
7	400K 1:4	25	24	No	25min fully developed, some coil dividers have delaminated
8	400K 1:4	21	NA	No	Begin to dev at 17min, complete 21 min, separator width 5um, delamination of separators
9	400K 1:4	25	??		Sharp, pointy coil separators, no delamination?
12	400K 1:4	6.5		No	Bubbling after exposure, lost most coil separators, some ok around edges, inconsistent across wafer
13	400K 1:4	6.5			Bubbling after exp, mostly in large open areas, delamination of separators, vertical sidewalls
14	400K 1:4	8.3			No bubbles, no delamination, vertical sidewalls, slightly sloped in middle of wafer. GOOD. Prebake 2 split 30+ 50
15	400K 1:4	11.5			No bubbles or delam, vertical sidewalls, but slightly sloped on edges of wafer. Noticeable resist debris in trenches. GOOD. Prebake 2 split 50 + 60
16					Prebake split 30+ 50
17	400k 1:4	19			40min 120C dehydration bake b4 coating. Not developed fully. Not enough exposure
18	400k 1:4	12			Full develop. Look great, near vertical sidewalls throughout. GOOD.
19	400k 1:4	12	24		40min 120C dehydration bake b4 coating. Looks good, but perhaps not fully developed after 10min. Dev for 2mor minutes - still looks the same. Some debris in trenches
20					EV1 problem, 1 interval expose only. No development.
21	400k 1:4	9	26		After HMDS, weird spots/colors evident all wafers in HMDS. Sloped Sidewalls!!! Resist cracked above membranes from coater vacuum or EV1 vacuum.
22	400K 1:4	14.5	26-27	No	Fully developed, no delamination, can see thin plateau on 10um lines. Some erosion
23	400K 1:4	15	Must measure	No	
24	400K 1:4	16.5	26-27	No	Clip pads still have residue, 10um lines eroded. Otherwise looks ok.
25	400K 1:4	16	27	No	Better profile, 10um lines have flat tops. Otherwise ok. Clip pads clear. Less time between expose + develop means less diffusion of photopolymerized species. Do develop immediately after expose.
26	400K 1:4	17	27	No	10um lines eroded. Still some residue in large areas. Problem bc exposing large clip pads? Ok otherwise
27	400 1:4	15.33		No	
28	400K 1:4	10.5	31	No	Remove 1mm EDGE bead during spin with Acetone swab. Notice more edge bead on this one. Much feature erosion around perimeter. Some 10um lines have flat tops, but 5um wide. Perhaps over-exposed + edge bead creates gap. Some debris.
29	400K 1:4	10.75	31	No	Remove 1mm edge bead during spin with Acetone swab. Looks really good. All 10um features have fringes on top (flat top). Almost no erosion. Previous wafers likely over-exposed. Very nice sidewall profile. 10um (on mask) tops are 6um wide.
30	400K 1:4	12.5	31	No	Remove 1mm edge bead during spin with acetone swab. Some sloped sidewalls + erosion near bottom left region of wafer. Resist is much thicker at that edge from bead removal. other areas 10um (mask) PR lines are good, width are 4um wide at top.